

IUSS
Scuola Universitaria Superiore Pavia

Scuola Universitaria Superiore IUSS Pavia

ADVANCES IN THE PRACTICAL APPLICATION OF NEXT-GENERATION INTENSITY MEASURES FOR EFFICIENT SEISMIC RISK ASSESSMENT

*A Thesis Submitted in Partial Fulfilment of the Requirements
for the Degree of Doctor of Philosophy in*

**EARTHQUAKE ENGINEERING AND ENGINEERING
SEISMOLOGY**

Obtained in the framework of the Doctoral Programme in

Understanding and Managing Extremes

by

Savvinos Aristeidou

May 2025



Scuola Universitaria Superiore IUSS Pavia

ADVANCES IN THE PRACTICAL APPLICATION OF NEXT-GENERATION INTENSITY MEASURES FOR EFFICIENT SEISMIC RISK ASSESSMENT

*A Thesis Submitted in Partial Fulfilment of the Requirements
for the Degree of Doctor of Philosophy in*

**EARTHQUAKE ENGINEERING AND ENGINEERING
SEISMOLOGY**

Obtained in the framework of the Doctoral Programme in

Understanding and Managing Extremes

by

Savvinos Aristeidou

Supervisor: Prof. Gerard O'Reilly

May 2025

Abstract

Seismic intensity measures (IMs) are crucial for linking seismic hazard with the dynamic response of structures and infrastructures. The peak inelastic displacement of a single-degree-of-freedom (SDOF) system, an efficient IM for estimating seismic demands, has been studied in the past. In this thesis, orientation-independent horizontal component definitions of this IMs such as the median and maximum directional inelastic spectral displacements, $Sd_{i,RotD50}$ and $Sd_{i,RotD100}$, were developed. This was done, first, to examine the directionality of ground motions in the inelastic domain and, second, to mitigate uncertainties related to sensor orientation. Ground motion models (GMMs) for these IMs were constructed using a subset of the next generation attenuation relationships for Western United States (NGA-West2) database. These models highlight the impact of strength ratio and elastic period on response directionality of inelastic SDOF systems, contributing to a more robust understanding of ground motion intensity and its directionality effects on the inelastic response of structural systems.

Bridges present unique challenges in seismic analysis due to their multi-modal and anisotropic response behaviour. The novel IM proposed as part of this thesis, the nn -th percentile inelastic spectral displacement, $Sd_{i,RotDnn}$, was evaluated for its ability to capture both ground motion directionality and structural nonlinearity. A case study on a California highway overcrossing demonstrated its superior performance compared to conventional IMs in characterising the nonlinear response and collapse behaviour. Furthermore, a 17.3% increase in efficiency using the *RotD50* definition over *RotD100* was found.

This thesis also explores the application of artificial neural networks (ANNs) to develop a generalised ground motion model (GGMM) capable of simultaneously predicting various IMs and their cross-correlations. Incorporating classical IMs, such as spectral acceleration, Sa , and significant

duration, D_s and next-generation IMs, such as average spectral acceleration, Sa_{avg} , and filtered incremental velocity, $FIV3$, the GGMM provides a unified framework for estimating those. This model facilitates practical and advanced ground motion selection for nonlinear dynamic analyses and achieves consistent correlation coefficients between IMs. The methodology of developing this GGMM also offers flexibility for incorporating additional IMs or horizontal component definitions with only minor adjustments.

The developed GGMM, based on the NGA-West2 database, was used to quantify correlations between IM residuals, providing insights into the relationships between the aforementioned IMs. Strong correlations between $FIV3$ and Sa , as well as notable negative correlations between Sa and D_s , were observed. Predictive models were developed using ANN to facilitate ease of use and robust interpolation between the correlation coefficients. These correlation models bridge an existing gap in the literature and give the ability of utilising these next-generation IMs for a more holistic approach to ground motion selection and seismic hazard analysis.

Finally, the thesis examines the optimal combination of conditioning and matching IMs to enhance the predictive accuracy in seismic risk assessment. Using the developed GGMM and correlation models within the generalised conditional intensity measure (GCIM) ground motion selection method, employing hazard-consistent records, multiple stripe analysis (MSA) was conducted on seven case study bridges. The results demonstrated that the combination of next-generation and classical IMs improved the representation of seismic hazard characteristics and reduced structural response medians and dispersions. These findings highlight next-generation IMs' role in advancing seismic risk assessment and improving ground motion selection.

Sommario

Le IMs sismiche sono fondamentali per collegare la pericolosità sismica alla risposta dinamica delle strutture e delle infrastrutture. Lo spostamento massimo inelastico di un sistema SDOF, una misura di intensità sismica efficiente per la stima della domanda sismica, è stato studiato in passato. In questa tesi, sono state sviluppate definizioni indipendenti dall'orientazione della componente orizzontale di queste IMs, come gli spostamenti spettrali inelastici mediani e massimi, $Sd_{i,\text{RotD}50}$ e $Sd_{i,\text{RotD}100}$. Questo è stato fatto, innanzitutto, per esaminare la direzionalità dei moti sismici nel dominio inelastico e, in secondo luogo, per mitigare le incertezze legate all'orientamento dei sensori. Sono stati sviluppati GMMs per queste IMs utilizzando un sottoinsieme del database NGA-West2. Tali modelli evidenziano l'impatto del rapporto di resistenza e del periodo elastico sulla direzionalità della risposta nei sistemi inelastici SDOF, contribuendo a una comprensione più approfondita dell'intensità del moto sismico e dei suoi effetti direzionali sulla risposta inelastica delle strutture.

I ponti presentano sfide uniche nell'analisi sismica a causa del loro comportamento di risposta multi-modale e anisotropo. La nuova IM proposta in questa tesi, lo spostamento spettrale inelastico all' nn -esimo percentile, $Sd_{i,\text{RotD}nn}$, è stata valutata per la sua capacità di catturare sia la direzionalità del moto sismico che la non linearità strutturale. Uno studio di caso su un viadotto autostradale della California ha dimostrato le prestazioni superiori di questa IM rispetto alle misure convenzionali nel caratterizzare la risposta non lineare e il comportamento al collasso. Inoltre, è stato riscontrato un incremento del 17.3% nell'efficienza utilizzando la definizione *RotD50* rispetto a *RotD100*.

Questa tesi esplora anche l'applicazione delle ANNs per sviluppare un GGMM capace di prevedere simultaneamente diverse IMs e le loro correlazioni. Incorporando sia le IMs tradizionali, come *Sa* e *Ds*, sia quelle

di nuova generazione, come Sa_{avg} e $FIV3$, il GGMM fornisce un quadro unificato per la loro stima. Questo modello facilita la selezione avanzata dei moti sismici per le analisi dinamiche non lineari e assicura coefficienti di correlazione coerenti tra le IMs. Inoltre, la metodologia utilizzata per sviluppare il GGMM offre flessibilità nell'integrazione di ulteriori IMs o definizioni di componenti orizzontali, con modifiche minime.

Il GGMM sviluppato, basato sul database NGA-West2, è stato utilizzato per quantificare le correlazioni tra i residui delle IMs, fornendo informazioni sulle relazioni tra le misure di intensità considerate. Sono state osservate forti correlazioni tra $FIV3$ e Sa , nonché notevoli correlazioni negative tra Sa e Ds . Per facilitarne l'uso e garantire un'interpolazione robusta tra i coefficienti di correlazione, sono stati sviluppati modelli predittivi basati su ANN. Questi modelli colmano un vuoto nella letteratura e consentono l'uso pratico delle IMs di nuova generazione per un approccio più olistico alla selezione dei moti sismici e all'analisi della pericolosità sismica.

Infine, la tesi esamina la combinazione ottimale di misure di intensità sismica di condizionamento e di matching per migliorare l'accuratezza predittiva nella valutazione del rischio sismico. Utilizzando il GGMM e i modelli di correlazione sviluppati all'interno del metodo GCIM per la selezione di moti sismici coerenti con la pericolosità sismica, sono state condotte analisi MSA su sette punti di caso studio. I risultati hanno dimostrato che la combinazione di misure di intensità sismica tradizionali e di nuova generazione migliora la rappresentazione delle caratteristiche della pericolosità sismica e riduce le mediane e le dispersioni della risposta strutturale. Questi risultati evidenziano l'importanza delle IM di nuova generazione nella valutazione del rischio sismico e nella selezione dei moti sismici.

Acknowledgements

With the completion of this PhD and upon reflecting on this journey, I realise how fortunate I have been to be surrounded by exceptional mentors, colleagues, friends, and family. This thesis is as much a product of their support, kindness, and wisdom as it is of my own efforts. The challenges of this journey were further compounded by the disruptions caused by the Covid-19 pandemic, which brought unexpected setbacks and uncertainties. However, the encouragement and understanding of those around me helped me persevere through these difficulties, making the completion of this work even more meaningful.

In particular, I am deeply grateful to my supervisor, Gerard O'Reilly, whose guidance and unwavering support have been invaluable throughout this process. As Alexander the Great aptly put it, "I am indebted to my parents for living, but to my teachers for living well." His mentorship has profoundly shaped my growth as a researcher and as a person. I especially appreciate his patience as I explored intricate details and ventured into side paths in my research, as well as his ability to gently steer me back toward the broader objectives when needed. For that, and so much more, I am truly thankful.

I also gratefully acknowledge the funding provided by the Italian Ministry of Education, University and Research at IUSS Pavia, within the framework of the project "*Dipartimenti di Eccellenza*".

I am incredibly appreciative of the people with whom I closely collaborated throughout my PhD. Firstly, to Karim Tarbali, whose collaboration in the initial stages of my PhD played a pivotal role in shaping my research. His deep knowledge, keen attention to detail, and kindness made our collaboration both insightful and enjoyable. His bottom-up approach to problem-solving was truly inspiring and has greatly influenced the way I tackle challenges. Our work together led to my first academic publication,

an achievement that laid the foundation for much of what followed. Also, to Davit Shahnazaryan for his invaluable contributions to the machine learning, computational tools, and coding aspects of my thesis. His expertise and willingness to share his knowledge greatly enriched my research and made tackling complex problems both stimulating and rewarding. I would also like to thank the anonymous reviewers of the articles that arose from this thesis. Their insightful and well-targeted comments significantly improved the quality of the papers and, subsequently, this thesis.

I moved to Pavia in 2018 to pursue my MSc degree, which I later continued with my PhD. This city has become a second home, where I have lived some of the most meaningful and vivid experiences of my life to date. Over these past six years—two for my MSc and four for my PhD—I have formed incredible friendships and memories that I will always cherish. On that note, I would like to thank my international classmates—Giorgos, Kenneth, and Besim—from the MSc program, with whom I remained close throughout the PhD. Also, to our Italian classmates of the MSc class of 2020, who taught us so much about Italian culture and helped us navigate the complexities of bureaucracy. I will never forget our late-night study sessions in the Car College study room, when Stelios would often come in at night to continue working and offer us advice on how to thrive in this academically intense environment, while inspiring us with deeper philosophical discussions.

A sincere word of gratitude to all the close friends I made in Pavia for the fun times we shared, for tolerating my sometimes confusing behaviour, and for pushing me to be the best version of myself each day. Volkan, for our discussions on engineering concepts, my research dead ends, and problem-solving approaches, which helped me advance through my PhD more efficiently. Davit, for our endless debates and hilarious conflicts, which somehow always made me see the world in a more pragmatic way—plus, his movie and video game recommendations were top-tier. Pablo, whose witty one-liners and creative stickers in our group chats made the past few years all the more entertaining. Christopher, for our deep conversations in the kitchen about relationships and love, which provided valuable insights (and motivation) in our pursuit of happiness. Lana, my gym buddy, for encouraging me to lift weights with better form, for our deep conversations about all aspects of life, and for our long bike rides that strengthened our bond as we progressed through the PhD. Maithree, for our walks around

Eucentre, catching up on our, admittedly exciting, lives, and gossiping about all the drama around us. Mouayed and Rita, for their patience in teaching me how to ski and for our many unforgettable ski trips in the Alps. Nesma, for the teasing, fights, reconciliations, and all the memorable moments we shared. EYLUL, for her unwavering kindness and support. Deniz, for an amazing trip to Istanbul, where he guided us through his favourite city spots and the best places to eat. Numan, for his invaluable computer hardware support and his caustic humour. Jose, for his kindness and the warm interactions with his lovely family. I am deeply grateful to each and every one of you for making my life in Pavia such a wonderful adventure.

Also, a heartfelt thank you to the Greek community of Pavia—Giorgos, Elvira, Nikos, Evdoxia, and Ioanna—for their companionship and support during my time here. The trips, dinners, drinks, and memories we created while exploring Italy are moments I will cherish for a long time.

I would also like to express my gratitude to my friends back in Cyprus—Lemesios, Charalampis, Antonis, Maratheftis, Stefanos, Giannis, Aris, Pirillas, the Pisinos brothers, and many others. Our gatherings during my Christmas and summer visits were a much-needed recharge, filling me with energy and motivation to return to my studies and push through another semester.

A special thank you to my undergraduate professor in Cyprus, Panayiotis Roussis, whose passion for structural dynamics was truly inspiring. His guidance not only deepened my interest in the field but also played a pivotal role in my decision to pursue this path and continue my studies in Pavia.

Last but most certainly not least, I want to thank my family. To my Mom, who has always been my biggest supporter, there for me whenever I felt anxious, unsure, or discouraged. To my Dad, who always offered realistic solutions to the challenges I faced along the way. And to my sister, who never failed to lift me up with our fun and teasing interactions. I deeply appreciate all that you have done for me. I have finally completed my PhD, and I hope I have made you all proud.

Savvinos Aristeidou
Pavia, Italy
May 2025

Contents

Abstract	iii
Sommario	v
Acknowledgements	vii
Contents	x
List of Figures	xiv
List of Tables	xx
Nomenclature	xxi
1 Introduction	1
1.1 Motivation and Problem Statement	1
1.2 Objectives and Contributions	2
1.3 Theoretical background	3
1.4 Scope and organisation of thesis	6
2 A ground motion model for orientation-independent inelastic spectral displacements from shallow crustal earthquakes	9
2.1 Introduction	9
2.2 Methodology	13
2.2.1 Strong motion database	14
2.2.2 Description of SDOF system	15
2.3 Investigating directional inelastic displacement spectra trends	16
2.3.1 Computation of $Sd_{i,\text{RotDnn}}$ spectra	16

2.3.2	Impact of inelastic behaviour on directionality response	18
2.3.3	Impact of directionality on expected displacement ductility ratio	19
2.3.4	Near- and far-fault ground motions	21
2.4	Fitting of the GMM	22
2.4.1	Functional form	22
2.4.2	GMM performance	25
2.4.3	Median inelastic spectra	30
2.5	Comparison with previous studies	31
2.6	GMM prediction uncertainty	33
2.7	Summary and conclusions	36
3	Exploring the use of orientation-independent inelastic spectral displacements in the seismic assessment of bridges	39
3.1	Introduction	39
3.2	Directionality Effects in the Assessment of Bridges	42
3.3	Case Study Bridge Structure and Numerical Modelling	44
3.4	Ground Motion Records	48
3.5	Intensity Measures	49
3.6	Analysis Results	55
3.6.1	Sufficiency	56
3.6.2	Efficiency	59
3.6.2.1	Comparison of Different Horizontal Component Definitions	64
3.6.3	Bias Against Directionality	65
3.7	Summary and Conclusions	68
4	Artificial neural network-based ground motion model for next-generation seismic intensity measures	71
4.1	Introduction	71
4.2	Strong motion database and filtering	75
4.3	Predictor and response features	77
4.4	Model architecture	81
4.4.1	Fixed-effects with artificial neural network	81
4.4.2	Mixed-effects regression	86
4.5	Model performance	88
4.5.1	Performance metrics	88

4.5.2	Comparison with other GMMs	89
4.5.2.1	Traditional IMs	89
4.5.2.2	Next-generation IMs	93
4.5.3	Response spectra	96
4.5.4	Residuals analysis	97
4.5.5	Model dispersion	99
4.6	Correlation modelling	102
4.7	Summary and conclusions	104
4.8	Code availability	106
5	Correlation models for next-generation amplitude and cumulative intensity measures using artificial neural networks	107
5.1	Introduction	107
5.2	Correlation models developed	109
5.3	Database and ground motion model	114
5.4	Methodology	114
5.5	Artificial neural network architecture	118
5.6	Empirical results and model estimations	124
5.6.1	Correlations between traditional IMs	124
5.6.2	Correlations between traditional and next-generation IMs	127
5.6.3	Correlations between next-generation IMs	130
5.7	Discussion and conclusions	133
5.8	Code availability	136
6	Implications of conventional and next-generation intensity measure-based ground motion record selection for risk assessment	139
6.1	Introduction	139
6.2	Ground motion input for bridge structures	140
6.3	Case study structures	141
6.3.1	General description	141
6.3.2	Numerical modelling and EDP definition	143
6.4	Hazard analysis	146
6.5	Ground motion selection schemes: conditioning IMs, matched spectra and matched IMs	148
6.6	Results	155

6.6.1	MSA results	155
6.6.2	Intensity-based evaluation	157
6.6.3	Demand-based evaluation	161
6.6.4	Risk-based evaluation	164
6.7	Summary and conclusions	165
7	Discussion and Conclusions	171
7.1	Summary of Work	171
7.2	Key Findings and Discussion	172
7.3	Contributions to the state-of-the-art	174
7.4	Limitations and future developments	176
References		181
Appendix A. Influence of database subset selection on correlation coefficients		205
Appendix B. Target and selected intensity measure distributions from the different ground motion selection cases		207

List of Figures

1.1	Analysis stages of PEER-PBEE framework. Adapted from Porter (2003)	4
2.1	Trace response of an elastic SDOF oscillator with $T = 2$ s. (a) Strongly polarized ground motion, SMART1 O07 recording from the 1985 Taiwan SMART1(33) earthquake, RSN: 492; (b) unpolarized ground motion, Dumbarton Bridge West End FF recording from the 1989 Loma Prieta earthquake, RSN: 757; and (c) polar plot of normalized spectral displacement in all horizontal directions for the two considered records in this figure. Dashed lines in (a) and (b) represent the peak SDOF response in each direction	11
2.2	Illustration of the methodology adopted to generate data . .	14
2.3	Distribution of the considered records used in terms of (a) M_w - R_{rup} bins and (b) scatter plot depicting the $V_{s,30}$	15
2.4	Hysteretic behaviour of the bilinear SDOF model	16
2.5	Inelastic spectral displacement defined via the median (solid lines) and 16th and 84th percentiles (dashed lines) for the (a) $RotD50$, (b) $RotD100$, and (c) $RotD00$ components of response	17
2.6	Impact of inelastic behaviour on directionality response shown via the (a) geometric mean and (b) logarithmic standard deviation of the $Sd_{i,RotD100}/Sd_{i,RotD50}$ ratio for different values of T and R . SB14 is the Shahi and Baker (2014) model for the elastic $RotD100/RotD50$ ratio	20
2.7	Comparison of the relationship between R , T , and the ductility demand observed in the SDOF systems when considering the $Sd_{i,RotD100}$ or the $Sd_{i,arb}$ used in conventional models . .	21

2.8	Comparing the impact of near- and far-fault ground motions via the (a) median $Sd_{i,\text{RotD}100}$ spectra, (b) median $Sd_{i,\text{RotD}50}$ spectra, and (c) median directionality measure, $Sd_{i,\text{RotD}100}/Sd_{i,\text{RotD}50}$	22
2.9	Inter-event residuals with respect to M_w for different T and R . Blue dots represent the observed residuals, while black dots and error bars represent the binned mean and \pm one standard deviation, respectively	27
2.10	Total residuals with respect to R_{rup} for different T and R . Blue dots represent the observed residuals, while black dots and error bars represent the binned mean and \pm one standard deviation, respectively	28
2.11	Total residuals with respect to $V_{s,30}$ for different T and R . Blue dots represent the observed residuals, while black dots and error bars represent the binned mean and \pm one standard deviation, respectively	29
2.12	Observed (i.e. measured) versus predicted Sd_i in logarithmic axes. Case of $R = 4$ and $T = 1$ s. Blue dots represent the observed and predicted data points, while the black dash-dotted line represents the perfect fit	30
2.13	Q–Q plot of total residuals. Case of $R = 4$ and $T = 1$ s . . .	31
2.14	Median $\text{RotD}50$ and $\text{RotD}100$ inelastic displacement spectra for different scenarios	32
2.15	Median $Sd_{i,\text{RotD}50}$ and $Sd_{i,\text{RotD}100}$ predicted by the model, along with the empirical data, as a function of M_w and R_{rup} , for $T = 1$ s and $R = 4$	34
2.16	Intra-, inter-event, and total logarithmic standard deviations	36
2.17	Effect of horizontal component definition on intra-, inter-event, and total logarithmic standard deviations	36
3.1	Illustration of the numerical modelling strategy adopted for the case study bridge, along with the pier cross-section fibre discretization	45
3.2	Moment curvature analysis and bilinearization (left). Pushover analysis of just the pier element (right)	46
3.3	Backbone curve of a single abutment spring in (a) longitudinal, (b) transversal, and (c) vertical direction	47

3.4	GMM dispersions of each IM examined for a given rupture scenario	55
3.5	IDA curves with median, 16 and 84 percentiles	57
3.6	Observed trends of IM residuals versus each ground motion parameter investigated. (a) magnitude; (b) rupture distance; (c) scale factor applied during IDA	60
3.7	Dispersion versus pier drift and displacement ductility for each IM investigated	61
3.8	Marginal dispersion of Sa_{avg} with different period ranges	63
3.9	Comparison of dispersion for different horizontal component definitions (a) elastic spectral accelerations and (b) inelastic spectral displacements	64
3.10	Trends of collapse IM residuals versus elastic and inelastic directionality measure. For the $Sd_{i,RotD100}/Sd_{i,RotD50}$, R equal to 3 was used	67
3.11	Trends of collapse IM residuals versus the inelastic directionality measure, $Sd_{i,RotD100}/Sd_{i,RotD50}$, with R equal to 3. Only values of κ_i below 2 are kept	68
3.12	Collapse $Sa(T_1)$ intensities versus the elastic directionality measure, κ , along with the fitted linear trend line	69
3.13	Collapse $Sa(T_1)$ intensities versus the inelastic directionality measure, κ_i , with different R ratios	69
4.1	Flowchart of this chapter's structure	75
4.2	M_w , R_{rup} and $V_{s,30}$ distribution of the filtered ground motion database used to fit the GGMM	78
4.3	Architecture of the ANN ground motion model	82
4.4	Training and testing MSE and R^2 values of the ANN model after the mixed effects regression	89
4.5	Magnitude amplification plots of $Sa(0.01s)$, $Sa(0.1s)$, $Sa(0.5s)$, and $Sa(1.0s)$ for two different rupture distance bins	91
4.6	Distance attenuation plots of $Sa(1.0s)$ for two different magnitude bins	92
4.7	Distance attenuation plots of Ds_{595} for two different magnitude bins	92
4.8	Distance attenuation plot of $FIV3(1.0s)$ for two different magnitude bins	94

4.9	Magnitude amplification plots of <i>FIV3</i> (1.0s) for two different rupture distance bins	94
4.10	Distance attenuation plot of Sa_{avg3} (1.0s) for two different magnitude bins	95
4.11	Magnitude amplification plots of Sa_{avg3} (1.0s) for two different rupture distance bins	96
4.12	Distance attenuation plot of Sa_{avg2} (1.0s) for two different magnitude bins	97
4.13	Magnitude amplification plots of Sa_{avg2} (1.0s) for two different rupture distance bins	98
4.14	Model median estimates of response spectra of <i>FIV3</i> (top) and Sa_{avg3} (bottom)	98
4.15	Inter-, intra-event, and total residuals versus M_w , R_{rup} and $V_{s,30}$, respectively, for three different IMs. Black dots and error bars represent the binned mean and \pm one standard deviation, respectively	100
4.16	Inter-, intra-event and total standard deviations of the proposed model for all IMs, compared with models from the literature	101
4.17	Comparison of inter-, intra-event and total standard deviations of IMs with different horizontal component definitions	102
4.18	Empirical and corresponding predicted correlation coefficients between Sa and <i>FIV3</i>	103
4.19	Empirical and corresponding predicted correlation coefficients between Ds and Sa_{avg3}	104
5.1	Schematic representation of the correlation between total residuals, Δ , (left) predicted and empirical response spectrum of a single record, and (right) residuals of the same IM from a large set of records.	115
5.2	Empirical cumulative distribution of the (a) normalized inter-event and (b) normalized intraevent residuals obtained using the GGMM. Comparison with the theoretical standard normal cumulative distribution and the 5% KS bounds.	116
5.3	Schematic representation of ANN architecture for the case of Sa - <i>FIV3</i> correlation model	121

5.4	Correlation coefficients between $Sa(T_i)$ and $Sa(T_j)$ for four values of T_j	125
5.5	Empirical and predicted $Sa-Ds_{595}$ and $Sa-Ds_{575}$ correlation of the ANN and Bradley (2011a) models	127
5.6	Empirical and corresponding predicted correlation coefficients between Sa and $FIV3$	128
5.7	Empirical and corresponding predicted correlation coefficients between Ds_{595} - $FIV3$ and Ds_{575} - $FIV3$	129
5.8	Correlation coefficients between $Sa(T_i)$ and $Sa_{avg3}(T_j)$ for two values of T_j	130
5.9	Empirical and corresponding predicted correlation coefficients of Sa_{avg3} - Ds_{595} and Sa_{avg3} - Ds_{575}	131
5.10	Empirical and corresponding predicted correlation coefficients between $FIV3$ of different periods	132
5.11	Empirical correlation coefficients between $Sa(T_i)$ - $Sa(T_j)$ and $FIV3(T_i)$ - $FIV3(T_j)$ for three values of T_j	132
5.12	Empirical and corresponding predicted correlation coefficients between Sa_{avg3} and $FIV3$	133
5.13	Empirical and corresponding predicted correlation coefficients between Sa_{avg3} of different periods	134
5.14	Correlation coefficients between $Sa_{avg3}(T_i)$ and $Sa_{avg3}(T_j)$ for two values of T_j	134
6.1	Illustration of structural detailing of the pier cross section (Pinho et al., 2009). The shorter side of the section is placed in the direction of the bridge deck	143
6.2	Illustration of the longitudinal profile of the case study bridge structures. Adapted from O'Reilly (2021b)	143
6.3	Moment curvature analysis of bottom section of the Pier with 7 m height. 10 cycles of unloading/reloading are shown here as an example, with equal curvature increments until the target curvature	145
6.4	Hazard curves of IM* of bridge 1	147
6.5	Hazard disaggregation of Sa at 0.555 s for the nine return periods investigated	148
6.6	Hazard disaggregation of Sa_{avg2} at 0.555 s for the nine return periods investigated	149

6.7	Hazard disaggregation of <i>FIV3</i> at 0.555 s for the nine return periods investigated	150
6.8	<i>Sa</i> spectrum and comparison of the target and selected dispersions for record selection Case 2 of bridge B-1 at 475 years return period	153
6.9	<i>Ds₅₇₅</i> (left) and <i>Sa_{avg3}</i> (right) theoretical and empirical CDF for record selection Case 2 of bridge B-1 at 475 years return period	154
6.10	<i>FIV3</i> theoretical and empirical CDF for record selection Case 2 of bridge B-1 at 475 years return period	154
6.11	Hazard consistency checks for ground motion input Cases 0 (left) and 5 (right) for bridge B-1. Dashed lines represent the hazard curves and solid lines represent the reconstructed hazard curves obtained from the selected ground motions . .	155
6.12	MSA results obtained with the ground motion input 5 on case study bridge B-1. Also depicted is the logarithmic mean and ± 1 standard deviation of the non-collapse cases, and the probability of collapse resulting from each intensity level . .	156
6.13	Median of EDP given IM level given no collapse	159
6.14	Dispersion of EDP given IM level given no collapse	160
6.15	Dispersion of IM given exceedance of EDP	163
6.16	Seismic demand hazard curves of the case study bridges . .	166
A.1	Comparison of correlation coefficients derived from utilising each of the four NGA-West2 GMMs and the one employed for this study	206
A.2	Correlations proposed by BB17, and the ones calculated here with the same GMM (i.e., CY14) and the same ground motion records	206
B.3	<i>Sa</i> spectrum and comparison of the target and selected dispersions. Case 0. Bridge 1. IM level 4	207
B.4	<i>Ds₅₇₅</i> theoretical and empirical CDF. Case 0. Bridge 1. IM level 4	208
B.5	<i>Ds₅₇₅</i> theoretical and empirical CDF. Case 1 (left) and 2 (right). Bridge 1. IM level 4	208

List of Tables

3.1	Modal analysis results of the case study bridge.	48
3.2	Minimum, median, and maximum values of IMs considered in the general sufficiency and efficiency checks	50
3.3	<i>p</i> -values and SRS slopes for the IDA residuals for each IM and parameter investigated	61
4.1	List of predictor features required when using the GGMM .	79
5.1	Correlation models proposed here and corresponding existing ones from the literature. In <i>italics</i> are a few example models in the literature of pairs not examined herein, given for the sake of completeness.	113
5.2a	Key hyperparameters and general architecture of the adopted ANN correlation models	122
5.2b	Key hyperparameters and general architecture of the adopted ANN correlation models	123
6.1	Modal properties of each case study bridge structure	142
6.2	Ground motion input cases	151

Nomenclature

List of abbreviations

<i>tanh</i>	hyperbolic tangent.
2D	two-dimensional.
Adadelta	adaptive learning rate.
Adagrad	adaptive gradient descent.
ADAM	adaptive moment.
Adamax	variation of ADAM.
ANN	artificial neural network.
ASCE	American society of civil engineers.
Caltrans	California department of transportation.
CDF	cumulative distribution function.
CMS	conditional mean spectrum.
CS	conditional spectrum.
EDP	engineering demand parameter.
ELU	exponential linear unit.
ESHM	European seismic hazard model.
Ftrl	follow the regularised leader.
GCIM	generalised conditional intensity measure.
GGMM	generalised ground motion model.
GMM	ground motion model.
IDA	incremental dynamic analysis.
IM	intensity measure.
KS	Kolmogorov–Smirnov.
MAFE	mean annual frequency of exceedance.
MCER	maximum considered earthquake.

MDOF	multi-degree-of-freedom.
MSA	multiple stripe analysis.
MSE	mean squared error.
Nadam	combination of Nesterov accelerated gradient and ADAM.
NEHRP	national earthquake hazards reduction program.
NGA-West2	next generation attenuation relationships for Western United States.
NRHA	nonlinear response history analysis.
PBEE	performance-based earthquake engineering.
PEER	pacific earthquake engineering research.
PSHA	probabilistic seismic hazard analysis.
RC	reinforced concrete.
ReLU	rectified linear unit.
RESORCE	reference database for seismic ground-motion prediction in Europe.
RMSprop	root mean square propagation.
RSN	record sequence number.
SDC	seismic design criteria.
SDOF	single-degree-of-freedom.
SGD	stochastic gradient descent.
SRS	simplified relative sufficiency.
UHS	uniform hazard spectrum.
XGBoost	extreme gradient boosting.

List of symbols

α	windowing factor for the time segment duration for the calculation of IV .
a_s	strain hardening ratio.
b	bias of activation function.
β	scalar that controls the f_c/f_n ratio.
$\beta_{0,s}$	y -intercept of the log-linear interpolation.
$\beta_{1,s}$	slope of the log-linear interpolation.

$\beta_{\text{EDP IM}}$	dispersion of EDP given IM.
$\beta_{\text{EDP IM,NC}}$	logarithmic dispersion of EDP, given IM and no collapse.
$\beta_{\text{IM EDP}}$	dispersion of IM given EDP.
$\beta_{\text{IM rup}}$	dispersion of IM given a set of rupture parameters.
β_{RTR}	record-to-record variability.
b_h	bias of the hidden neuron, h .
b_r	bias of the response neuron, r .
CR_{JB}	centroid Joyner-Boore distance.
Δ	total non-normalised residual.
δ	normalised total residual.
δB	inter-event residual before normalisation.
δb	normalised inter-event residual.
δW	intra-event residual before normalisation.
δw	normalised intra-event residual.
Δ_y	yield displacement.
D_s	significant duration.
D_{s575}	5-75% significant duration.
D_{s595}	5-95% significant duration.
$\varepsilon_{i,j}$	intra-event residual.
ε_s	collapse intensity residuals.
ε_{su}	steel ultimate strain.
$\eta_{\text{EDP IM}}$	median demand for a given intensity.
$\eta_{\text{EDP IM,NC}}$	median demand for a given intensity and given no collapse.
η_i	inter-event residual.
$\eta_{\text{IM EDP}}$	median IM given EDP.
f	frequency of vibration.
F_{basin}	basin-effects correction term.
f_c	cut-off frequency of second-order Butterworth low-pass filter.
F_D	distance function term.
F_{el}	elastic strength (strength of the system if it was to remain elastic).
$FIV3$	filtered incremental velocity.
f_{linear}	<i>linear</i> activation function.

F_M	magnitude scaling term.
F_s	site amplification term.
F_{sof}	style of faulting term.
f_{tanh}	$tanh$ activation function.
F_y	yield strength.
$GMRotD50$	50^{th} percentile of the geometric mean of the two horizontal components rotated to all non-redundant rotation angles sorted by amplitude, with D denoting period-dependent rotation angle.
IVs	incremental velocities.
κ	elastic directionality measure, $Sa_{RotD100}/Sa_{RotD50}$.
κ_i	inelastic directionality measure, $Sd_{i,RotD100}/Sd_{i,RotD50}$.
ξ	damping ratio.
λ	annual rate of exceedance.
m	mass.
μ	ductility.
μ_Δ	displacement ductility.
M_w	moment magnitude.
N	number of spectral accelerations used for the calculation of average spectral acceleration.
PGA	peak ground acceleration.
PGD	peak ground displacement.
PGV	peak ground velocity.
Φ	rotational modal participation factor.
φ	intra-event standard deviation.
$\Phi[\cdot]$	standard normal cumulative distribution function.
ϕ_{max}	maximum pier curvature.
R	strength ratio, also known as force reduction factor.
R^2	coefficient of determination.
ρ	correlation coefficient.
R_{jb}	Joyner-Boore distance.
R_{mod}	modified distance to the source.

$RotD00$	0^{th} percentile of all rotation angles sorted by amplitude, with D denoting period-dependent rotation angle.
$RotD100$	100^{th} percentile of all rotation angles sorted by amplitude, with D denoting period-dependent rotation angle.
$RotD50$	50^{th} percentile of all rotation angles sorted by amplitude, with D denoting period-dependent rotation angle.
$RotDnn$	nn^{th} percentile of all rotation angles sorted by amplitude, with D denoting period-dependent rotation angle.
R_{rup}	rupture distance.
rup	ground motion rupture parameter.
\hat{s}	logarithmic mean of collapse intensities from all the ground motions.
Sa	5% damped spectral acceleration.
Sa_{arb}	arbitrary horizontal component of spectral acceleration.
Sa_{avg}	average spectral acceleration.
Sa_{avg1}	average spectral acceleration over the period range $[0.2T, 1.5T]$ (except in Chapter 3, where the period range is $[0.5T, 1.5T]$).
Sa_{avg2}	average spectral acceleration over the period range $[0.2T, 2T]$ (except in Chapter 3, where the period range is $[0.5T, 2T]$).
Sa_{avg3}	average spectral acceleration over the period range $[0.2T, 3T]$ (except in Chapter 3, where the period range is $[0.5T, 3T]$).
Sa_{gm}	geometric mean of the two as-recorded horizontal components of spectral acceleration.
$Sa_{RotD100}$	100^{th} percentile of spectral acceleration from all rotation angles.
Sa_{RotD50}	50^{th} percentile of spectral acceleration from all rotation angles.
$Sa(T)$	5% damped spectral acceleration at a period T .

Sd_i	inelastic spectral displacement.
$Sd_{i,\text{arb}}$	arbitrary horizontal component of inelastic spectral displacement.
$Sd_{i,\text{gm}}$	geometric mean of the two as-recorded horizontal components of inelastic spectral displacement.
$Sd_{i,\text{RotD}100}$	100 th percentile of inelastic spectral displacement from all rotation angles.
$Sd_{i,\text{RotD}50}$	50 th percentile of inelastic spectral displacement from all rotation angles.
$Sd_{i,\text{RotD}nn}$	nn^{th} percentile of inelastic spectral displacement from all rotation angles.
SF	scaling factor.
s_i	collapse intensity of the i^{th} ground motion.
σ	total logarithmic standard deviation.
SOF	style of faulting.
T	period of vibration.
T_1	first mode period of vibration.
τ	inter-event standard deviation.
t_{end}	last instant of time of the acceleration time series.
T_R	return period.
U	translational modal participation factor.
\ddot{u}_{gf}	filtered ground acceleration time series.
$V_{s,30}$	time-averaged shear-wave velocity for the top 30 m of soil.
$V_{s,\text{max}}$	local maximum IV_s in $V_s(t)$.
$V_{s,\text{min}}$	local minimum IV_s in $V_s(t)$.
$V_s(t)$	incremental velocity time series.
W	weight of activation function.
$W_{h,r}$	weight of the connection between hidden neuro,n h , and response neuron, r .
$W_{p,h}$	weight of the connection between predictor neuron, p , and hidden neuron, h .
X_p	predictor feature.
$Z_{2.5}$	depth to shear wave velocity of 2.5 km/s.

Chapter 1

Introduction

1.1 Motivation and Problem Statement

As the built environment in today's society continues to expand rapidly, so does its exposure to natural hazards. In addition to new structures, ageing structures also exhibit increased vulnerability. Therefore, there is a growing need to refine methodologies and decision-making in seismic risk assessments, which play a pivotal role in safeguarding infrastructure and human lives.

Despite advancements in seismic design, a comprehensive understanding of how to characterise seismic hazard and ground motion input for risk assessments remains a challenge. Traditional approaches often rely on intensity measures (IMs) such as spectral acceleration, Sa , that may not adequately capture key features influencing structural response. Those features include directionality, ground motion duration, velocity pulses, spectral shape, and inelasticity within the IM definition. Next-generation IMs have shown promise in improving the accuracy of seismic risk assessments. However, limitations in their application persist, including the limited number of ground motion models (GMMs) for these IMs and absence of correlation models between them. These gaps hinder the development of holistic ground motion selection frameworks that integrate a broader range of IMs effectively.

Bridges, as critical components of transportation networks, can be significantly affected by seismic events due to their complex structural dynamics. Earthquakes have underscored the significant impacts of bridge

damage, including disruptions to connectivity, economic losses, and threats to public safety. The accurate assessment of their seismic performance requires careful consideration of ground motion directionality, the selection of representative ground motions, and the use of advanced IMs to capture the characteristics of ground shaking expected at a site.

This thesis addresses the need for advanced seismic risk assessment methods that account for directionality and other ground motion characteristics, and their implications on the full range of bridge response. Specifically, it focuses on the development and application of orientation-independent inelastic spectral displacements as a novel intensity measure, and their integration into a framework for more accurate and reliable seismic performance assessment of bridge structures. Additionally, ground motion models and correlation models were developed for next-generation intensity measure and applied on risk assessment of bridge structure to examine their implications. This work contributes to the growing body of knowledge needed to bridge the gap between research and practical implementations.

1.2 Objectives and Contributions

The primary objective of this research is to make available orientation-independent inelastic spectral displacements, directionality models for inelastic spectral displacements, and next-generation intensity measures, such as Sa , average spectral acceleration, Sa_{avg} , and filtered incremental velocity, $FIV3$, for usage and enhancement of seismic risk assessment of structures. These IMs offer a more comprehensive understanding of pertinent ground motion characteristics and more accurate prediction of system's nonlinear behaviour. To this end, the research aims to:

- Explore the directionality effects of ground motions on the basis of inelastic spectral displacements, Sd_i .
- Develop a ground motion model that facilitates the prediction of $RotD50$ and $RotD100$ (and therefore also their ratio) horizontal component definitions of Sd_i from shallow crustal earthquakes.
- Explore the use of Sd_i in seismic assessment, specifically in the context of bridge structures, where traditional methods may fail to capture some elements that affect seismic risk.

- Quantify the impact of ground motion directionality in seismic assessment of bridge structures.
- Develop ground motion models and correlation models for next-generation IMs.
- Investigate advanced ground motion selection and scaling techniques, ensuring that selected ground motions accurately represent the seismic hazard at a given site.
- Integrate advanced IMs into the performance-based assessment of bridge structures, facilitating a more refined evaluation of seismic risk.

The contributions of this thesis include a new approach to quantify ground motion directionality, the development of novel models for next-generation IMs that can be used in seismic hazard assessment, and the integration of these models into a comprehensive framework for bridge performance evaluation.

1.3 Theoretical background

Throughout the years, seismic design and assessment has focused on preventing damage of structural and non-structural elements in frequent low-intensity earthquakes and preventing collapse in rare high-intensity earthquakes. While focusing on life safety and collapse prevention of structures is of utmost importance, it is not sufficient to provide a satisfactory control over the structure's performance. Therefore, a natural evolution was the introduction of performance-based earthquake engineering (PBEE) during the late 1990s with the "Vision 2000" framework (SEAOC, 1995). It provided the desired performance levels to several seismic hazard levels. These hazard levels were called frequent (43 years), occasional (72 years), rare (475 years), and very rare (949 years), and the corresponding performance levels were called fully operational, operational, life-safe, and near collapse, respectively.

These initial manifestations of PBEE were based on discrete hazard levels and expressed the structural performance in terms of global structural response measures, such as inter-storey drift. Yet there was a need to quantify seismic risk in a continuous manner including the propagation

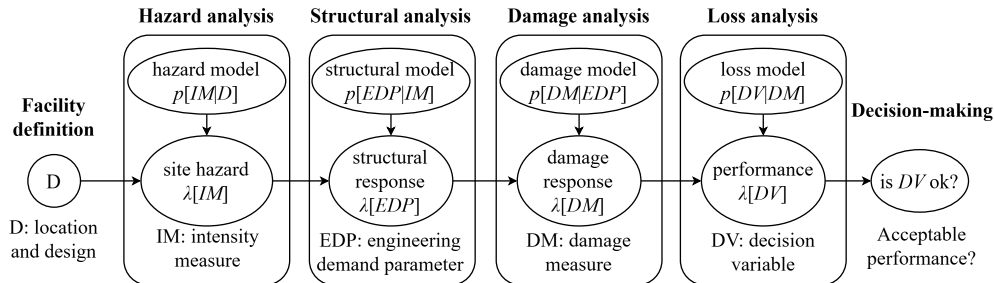


Figure 1.1. Analysis stages of PEER-PBEE framework. Adapted from Porter (2003)

of uncertainty from each calculation segment, while expressing the performance in quantities that are meaningful to building owners, stakeholders, and policy-makers (Porter, 2003). Therefore, a methodology emerged that provides probabilistic estimates of global performance measures (i.e., monetary loss, casualties, and loss of functionality), namely the pacific earthquake engineering research (PEER)'s probabilistic PBEE assessment methodology (Cornell & Krawinkler, 2000). The PEER-PBEE methodology can be used to decide whether the design of a facility at a specific site is acceptable, and the different segmental analysis stages are schematically illustrated in the flowchart of Figure 1.1. The implementation of the PEER-PBEE methodology can be summarised in the form of a triple integral, as shown in Equation 1.1.

$$\lambda[DV] = \iiint p[DV|DM] p[DM|EDP] p[EDP|IM] \lambda[IM] dIM dEDP dDM \quad (1.1)$$

where, $p[X|Y]$ denotes the conditional probability of exceeding X , given a certain value of Y . $\lambda[X]$ refers to the mean annual frequency of exceeding X . dX represents the integration over all possible values of X . This thesis focuses mainly on the hazard analysis and structural analysis segments of the framework, as well as the interface between them.

Seismic hazard analysis typically involves the identification of the expected ground motion characteristics at a region, or site. Intensity measures, such as spectral acceleration, have traditionally been used to quantify the intensity of the ground motion characteristics that have to do with

frequency content and amplitude. However these commonly used measures often fail to capture the more important characteristics of ground motions that affect structural responses, particularly in nonlinear domains. To address this, the use of orientation-independent Sd_i , which are more representative of a structure's inelastic behaviour, can function as an alternative approach.

Shahi and Baker (2014) developed ground motion directionality models that predict the $Sa_{RotD100}$ to Sa_{RotD50} ratio. This is very useful when one wants to perform probabilistic seismic hazard analysis (PSHA) and ground motion selection for the *RotD100* horizontal component definition. Building upon that work, in this thesis the directionality models were extended to Sd_i , with the aim of better understanding its impact on engineering systems that undergo nonlinear behaviour.

The concept of fragility analysis is central to this research. Fragility curves, which represent the probability of exceeding a certain damage state under varying ground motion intensities, are a key tool in assessing the seismic vulnerability of bridge structures. By incorporating advanced IMs, this thesis seeks to refine the fragility curves, providing a more accurate (i.e., with lower dispersion) estimate of the probability of failure under specific seismic conditions.

There is a plethora of GMMs that estimate traditional IMs (e.g., peak ground acceleration, *PGA*, peak ground velocity, *PGV*, and *Sa*) (Douglas, 2022), however there is a shortage of GMMs that estimate next-generation IMs (e.g., Sa_{avg} , *FIV3*, or even significant duration, *Ds*, which could be considered a traditional IM). Additionally there are very few correlation model between all the aforementioned IMs, and for some cases they do not even exist. This hinders the holistic ground motion selection considering different combinations of traditional and next-generation IMs. Therefore, this thesis bridges that gap in literature, and promotes the practical usage of different IM combinations within the framework of risk assessment of structures.

The integration of seismic demand hazard curves with advanced IMs into the seismic risk framework provides a more robust method for estimating the likelihood of structural damage and the associated repair costs.

1.4 Scope and organisation of thesis

Based on what was introduced in the previous sections, the thesis is structured as follows:

- **Chapter 1: Introduction** – Provided an overview of the motivation, problem statement, objectives, and scope of the thesis.
- **Chapter 2: A ground motion model for orientation-independent inelastic spectral displacements from shallow crustal earthquakes** – Explores the ground motion directionality effects on Sd_i , and describes the development of a GMM for $RotD50$ and $RotD100$ horizontal component definitions of Sd_i . Additionally, an inelastic directionality model was developed and described, which can also be estimated more precisely at a site from the GMM.
- **Chapter 3: Exploring the use of orientation-independent inelastic spectral displacements in the seismic assessment of bridges** – Investigates the use of $Sd_{i,RotDnn}$ in the context of seismic assessment of bridge structures, comparing the performance with that of conventional IMs. Also, investigates how much the elastic and inelastic ground motion directionality can bias the bridge's response.
- **Chapter 4: Artificial neural network-based ground motion model for next-generation seismic intensity measures** – Details the development of a generalised ground motion model (GGMM) which includes several conventional and next-generation IMs, and different horizontal component definitions. Compares the resulting estimations with other existing GMMs from the literature.
- **Chapter 5: Correlation models for next-generation amplitude and cumulative intensity measures using artificial neural networks** – Focuses on the development of correlation models between different relevant IMs for seismic risk assessment of structures and comparisons with other existing models.
- **Chapter 6: Implications of conventional and next-generation intensity measure-based ground motion record selection for risk assessment** - Explores the impact of different combinations

of conventional and next-generation IMs into the performance-based assessment of bridge structures. Simultaneously, this chapter demonstrates the practical application of the previously developed GGMM and correlation models in a comprehensive risk assessment framework.

- **Chapter 7: Discussion and Conclusions** – Summarises the key findings of the research and suggests potential avenues for further investigation.

Chapters 2 and 3 can be considered independent from Chapters 4, 5, and 6, although they share a few similar basic principles and comparative procedures. Through this structure, the thesis aims to provide an in-depth exploration of various ground motion characteristics that can significantly impact seismic risk analyses, encompassing ground motion selection, fragility analysis, and risk estimation.

Chapter 2

A ground motion model for orientation-independent inelastic spectral displacements from shallow crustal earthquakes

This chapter is extensively based on the following publication:

Aristeidou, S., Tarbali, K., & O'Reilly, G. J. (2023). A Ground Motion Model for Orientation-Independent Inelastic Spectral Displacements from Shallow Crustal Earthquakes. *Earthquake Spectra*, 39(3), 1601–1624. <https://doi.org/10.1177/87552930231180228>

2.1 Introduction

An accurate representation of the expected damage is needed in any urbanized area for disaster risk management and urban planning. This requires utilizing appropriate ground motion IMs that characterize the response of nonlinear structural systems. Seismic hazard and structural response analyses often use single or multiple IMs (Baker and Cornell, 2005a; Vamvatsikos and Cornell, 2005; Bradley, 2012; O'Reilly, 2021b) to represent shaking intensity. Empirical GMMs provide the probabilistic distributions of these IMs and allow representative ground motions to be selected for nonlinear response history analyses (NRHAs) to estimate structural demands. The most common scalar IM currently used is the

Sa at a given period T of vibration, $Sa(T)$. The notation Sa will be used for brevity herein, implying the spectral acceleration at a period T and 5% of critical damping. Since seismic shaking is felt principally as shaking in three dimensions, there is a need to consider the possible effects of ground motion directionality, which is illustrated graphically in Figure 2.1. Here, “Displacement X” denotes the displacement of the oscillator in the first as-recorded direction as given from the database, and similarly “Y” in the second as-recorded direction. As shown, different ground motions may induce significantly different directional demands on a system, and a given ground motion may induce different directional demands on different systems. Notably, Baker and Cornell (2006c) addressed this question by discussing the regular use of an arbitrary Sa component, Sa_{arb} , or the geometric mean of the two as-recorded Sa components, Sa_{gm} , in seismic analyses.

In recent years, various Sa definitions have been proposed that may be considered more representative of the ground shaking in the entire two-dimensional (2D) horizontal plane. Some of these definitions include the different percentiles of Sa over all non-redundant orientations of elastically responding systems (Boore et al., 2006; Boore, 2010; Rupakhetty and Sigbjörnsson, 2013). Boore (2010) defines the $RotD_{nn}$ component of Sa as the nn^{th} percentile of all rotation angles sorted by amplitude, with D denoting the period-dependent rotation angle. These Sa definitions (e.g. $RotD50$, $RotD100$, and $RotD00$) have been shown to more accurately represent the directional dependency of ground motions in the horizontal plane (Bradley, 2010; Tarbali, 2017; Baker and Lee, 2018). They have been used in several studies to quantify the directional response of both elastic (Bradley and Baker, 2014) and inelastic single-degree-of-freedom (SDOF) systems (Burks and Baker, 2014; Ahdi et al., 2020; Zengin and Abrahamson, 2021). In addition, the next generation attenuation relationships for Western United States (NGA-West2) database (Ancheta et al., 2013) was used to develop an empirical model for the ratio between $Sa_{RotD100}/Sa_{RotD50}$ (Shahi and Baker, 2014) and quantify the directionality measure (i.e., polarisation) of horizontal ground motion pairs, as illustrated in Figure 2.1. This was mainly carried out to enable the estimation of $Sa_{RotD100}$ response spectra from Sa_{RotD50} spectral ordinates via an empirical model proposed by those authors. The vast majority of modern GMMs and the NGA-West2 project GMMs adopt *ad nauseam* the $RotD50$ horizontal component

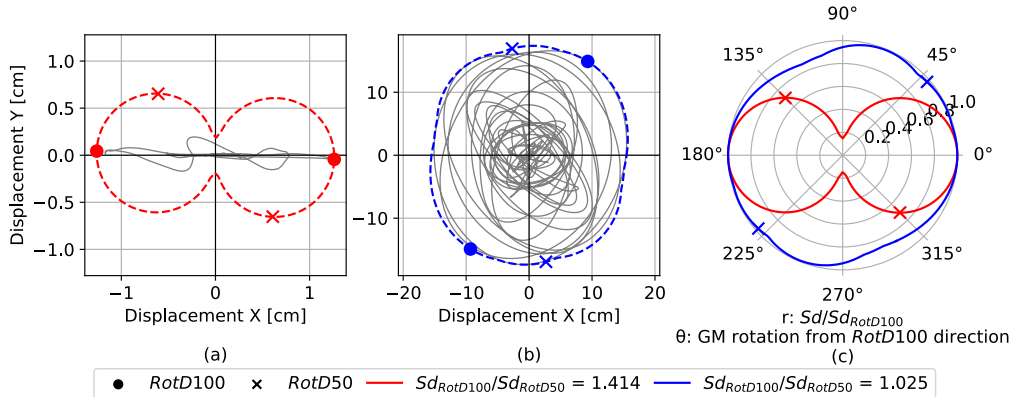


Figure 2.1. Trace response of an elastic SDOF oscillator with $T = 2$ s. (a) Strongly polarized ground motion, SMART1 O07 recording from the 1985 Taiwan SMART1(33) earthquake, record sequence number (RSN): 492; (b) unpolarized ground motion, Dumbarton Bridge West End FF recording from the 1989 Loma Prieta earthquake, RSN: 757; and (c) polar plot of normalized spectral displacement in all horizontal directions for the two considered records in this figure. Dashed lines in (a) and (b) represent the peak SDOF response in each direction

definition (Bozorgnia et al., 2014). Therefore, it was considered thematic to extend and propose herein inelastic response values as an IM with the same horizontal component definition, which to the author's knowledge, does not exist in the literature.

On one hand, many insights have been obtained from these studies concerning the impacts of directionality on linear systems. On the other hand, studies on complex nonlinear systems have drawn many interesting structure-specific conclusions. Several researchers have also developed GMMs for peak inelastic spectral displacements of SDOF systems, Sd_i , (Tothong and Cornell, 2006; Rupakhetty and Sigbjörnsson, 2009; Stafford et al., 2016; Heresi et al., 2018; Huang et al., 2020). Under certain conditions, Sd_i has been demonstrated to be an effective IM to relate ground motion intensity and inelastic structural response and, therefore, the structural and non-structural damage of engineered systems (Aslani, 2005; Luco and Cornell, 2007).

In this study, the RotD_{nn} for the 00th, 50th, and 100th percentiles of Sd_i are investigated for all non-redundant incidence angles for bilinear SDOF systems with a range of T and strength ratio, R , values. The latter parameter is defined as the ratio of the elastic strength demand to the inelastic strength demand (i.e., the reduction due to nonlinear hysteretic behaviour; Miranda and Bertero, 1994), and is discussed in more detail later. From the resulting data, an empirical GMM is developed, with the predictor variables being T , R , and a set of seismological parameters. These are common predictor variables used in many other GMMs, but herein there is the addition of R , which can be challenging to estimate with high degree of accuracy for a building portfolio. In such a case, it is assumed that even approximate values of T and R can still make for an efficient IM for regional risk assessment, which can possibly outperform classic IMs — for example, PGA or $Sa(T_1)$ that do not take into account the nonlinear behaviour of the structure — with a little extra effort. In the case of a single building assessment, knowing the yield/capping horizontal force, the R can in principle easily be obtained for a given return period or shaking scenario. Hence, it is hypothesized that this trade-off between the estimation of one more parameter and the additional benefits gained by using it is worth considering.

The goal of this GMM is not only to predict a useful IM well-correlated with structural demand but also to give an expected measure of directionality for sites under seismic hazard. Hence, it can provide important insights into the maximum directional response of inelastic systems, enabling a more comprehensive quantification of seismic damage to engineered structures. The GMM was also fitted for the RotD_{100} horizontal component definition, as it can be used in important structures where the maximum response in the horizontal plane is of interest. Modern seismic design codes have also included the use of RotD_{100} horizontal component in their provisions, namely (ASCE/SEI 7-16, 2018) in their “risk-targeted maximum considered earthquake (MCER) ground motion hazard analysis.” To give more insight on the importance of these IMs, if the case of a linear isotropic structure is considered and its resultant displacement is the desired output, then the $Sa_{\text{RotD}50}$ would be the best predictor. However, when the system is non-linear and isotropic, the $Sd_{i,\text{RotD}100}$ of the equivalent SDOF system would be a much more representative predictor of the resultant displacement. In addition, when a regular structure is modelled in its two principal directions,

the ground motions can be selected and scaled to represent the median or maximum directional inelastic response proposed in this study. In any case, it is important to distinguish between the *RotDnn* component used to define the IM from the inelastic SDOF system and the *RotDnn* component of the actual structural response. The former refers to the ground motion IM computed based on a given percentile of the response across all horizontal orientations. In contrast, the latter pertains to the structure's response, which is influenced by its dynamic properties, orientation, and nonlinearity. While both are derived from the same mathematical framework, their roles in seismic assessment are fundamentally different: one characterises the input motion, while the other reflects the structural demand.

In the following sections, an overview of the workflow followed is outlined, describing the ground motion database and GMM functional forms used along with the analyses that went into the development of the model. This is then appraised via a performance comparison of the model and the relative differences with different, but similar, models available in the literature.

2.2 Methodology

The methodology employed to generate the data for the model calibration is outlined in Figure 2.2. First, the ground motions within the range of moment magnitude, M_w , and rupture distance, R_{rup} , of interest were extracted from the NGA-West2 database and are discussed in the next section. Then, the range of R and T values, along with the hysteretic behaviour, post-yield stiffness, and the damping of the SDOF system, were defined. For each SDOF system, the ground motions were rotated with an increment of 6° in the range of 0° to 180° and applied to the numerical model developed in OpenSeesPy (Zhu et al., 2018) to obtain the peak displacement. Given the followed methodology, the SDOF system was assumed to be uncoupled and directionally symmetric, which is a simplification since structures are usually asymmetric and torsionally-coupled. However, this simplification is necessary when developing a scalar IM, otherwise the deriving methodology and usability of these IMs would become excessively overcomplicated. The total number of analyses presented in this study amounted to 7139 ground motions $\times 5$ $R \times 13$ $T \times 30$ incidence angles to

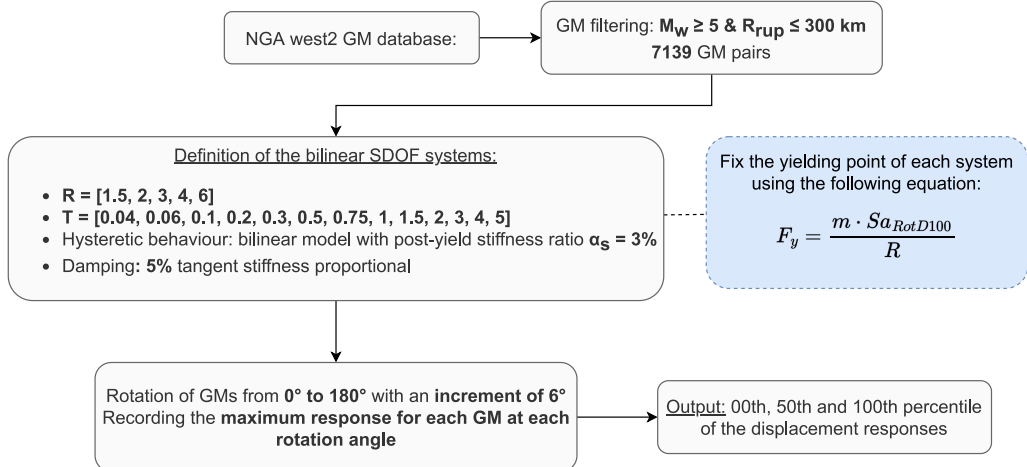


Figure 2.2. Illustration of the methodology adopted to generate data

give 13,921,050 inelastic SDOF analyses. These computational analyses are needed because for inelastic response values, the *RotDnn* component cannot be interpreted in terms of the principal components of the as recorded motion since the linear relationship and transformability breaks down once the system becomes inelastic. It should be noted here that the *R* factor was chosen as the control parameter, even though it is more consistent with a force-based design philosophy. This way the SDOF system could be defined directly for each ground motion, whereas with μ (which is more closely aligned with displacement-based design principles) the SDOF could not be defined directly and iterations would be required.

2.2.1 Strong motion database

The ground motion records used in this study were obtained from the NGA-West2 database (Ancheta et al., 2013), which is a comprehensive database of shallow crustal earthquakes in active tectonic regions. From this database, a subset of ground motions recorded during earthquakes deemed of sufficient intensity to cause structural and/or non-structural damage was selected for the analyses. Specifically, the subset considered was earthquakes whose $M_w \geq 5$ and $R_{rup} \leq 300$ km. The considered earthquakes distributed in different M_w - R_{rup} bins are shown in Figure 2.3a. This subset includes 7139 recordings from 200 earthquake events, whose scatter plot of M_w , R_{rup} , and

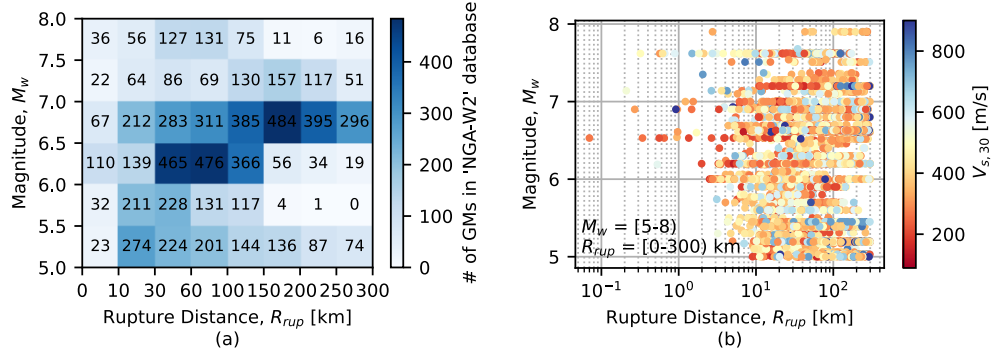


Figure 2.3. Distribution of the considered records used in terms of (a) M_w – R_{rup} bins and (b) scatter plot depicting the $V_{s,30}$

time-averaged shear-wave velocity for the top 30 m of soil, $V_{s,30}$, is depicted in Figure 2.3b. Note that the maximum $V_{s,30}$ value in the selected ground motion pool reached 1289 m/s, but everything above 900 m/s is plotted with the same dark blue colour for clarity. It can be seen that most of the earthquakes had M_w between 6 and 7 and R_{rup} between 30 and 250 km. In addition, ground motions with the maximum usable periods lower than the elastic period of the corresponding system in each case were filtered out of the considered ground motion subset for a given SDOF system.

2.2.2 Description of SDOF system

The SDOF system chosen for this study was a bilinear model with positive strain hardening ratio $a_s = 3\%$, shown in Figure 2.4. The hysteretic behaviour of this system is non-degrading and non-evolutionary. A tangent stiffness proportional damping model was adopted with a ratio of $\xi = 5\%$. The range of elastic periods considered was $T = 0.04, 0.06, 0.1, 0.2, 0.3, 0.5, 0.75, 1, 1.5, 2, 3, 4, 5$ in seconds, and the set of strength ratios was $R = 1.5, 2, 3, 4, 6$ (Figure 2.2). R is defined as the ratio of maximum spectral demand in the elastic system with period T subjected to a given ground motion, F_{el} , to the SDOF yield strength, F_y . In practice, this meant that for a given T and R pair, along with a ground motion whose $Sa_{RotD100}$ is known, F_y is computed from Equation 2.1, where m is a nominal value of mass, meaning that any value can be chosen since it will then be modelled in the numerical model as well.

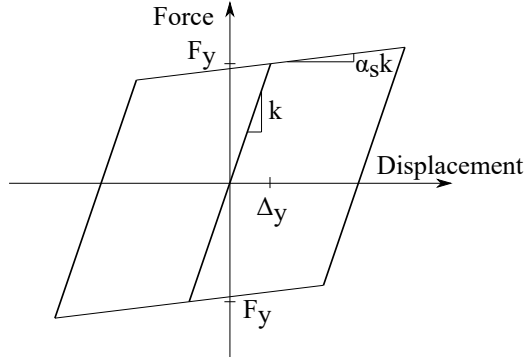


Figure 2.4. Hysteretic behaviour of the bilinear SDOF model

$$F_y = \frac{m \cdot Sa_{RotD100}}{R} \quad (2.1)$$

The aim of using this kind of standardized SDOF system is to represent the inelastic displacement demand of a wide range of first-mode-dominated multi-degree-of-freedom (MDOF) systems and not any specific typology. This gives the opportunity to study the general trends on inelastic response spectra. Future work may consider the response of hysteretic models that represent different structural systems.

2.3 Investigating directional inelastic displacement spectra trends

Following the workflow outlined in Figure 2.2, the data for all SDOF system combinations were generated. To examine these, this section first investigates the trends observed for the directional inelastic displacement spectra to be used in the functional form fitting. In addition, the degree of directionality is discussed along with the observed ductility demands and the impacts of near and far fault ground motions.

2.3.1 Computation of $Sd_{i,RotDnn}$ spectra

The 84th, 50th, and 16th percentiles of the elastic, $Sd_{e,RotDnn}$, and inelastic, $Sd_{i,RotDnn}$, spectral displacements are shown in Figure 2.5. These were

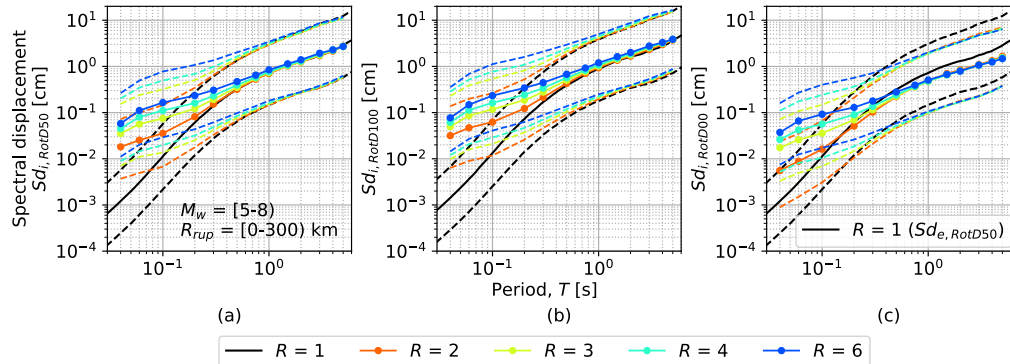


Figure 2.5. Inelastic spectral displacement defined via the median (solid lines) and 16th and 84th percentiles (dashed lines) for the (a) $RotD50$, (b) $RotD100$, and (c) $RotD00$ components of response

generated using the numerous response points obtained from the SDOF analyses but binning the data and computing the relevant percentiles. The $RotD00$ (i.e., the minimum directional response) of the inelastic response is also considered in the comparisons. Generally, it can be seen from Figure 2.5a and b that for $T \leq 1$ s, the median Sd_i increases with R , while for $T \geq 1$ s, the inelastic response is close to the elastic response. This was an expected result, as the nonlinear behaviour of medium to long-period structures typically follows the equal-displacement approximation (Chopra, 2014), where for shorter periods the nonlinear response tends to be higher, as observed. This was also presented in the study by Huang et al. (2020) and holds true for different inelastic $RotDnn$ quantities, hence being reconfirmed here.

Figure 2.5c compares the $RotD50$ elastic displacement spectrum (shown in black) with the $RotD00$ of the inelastic displacement spectrum. This investigated whether the elastic $RotD50$ response, conventionally used in the seismic design process, can be higher than the minimum inelastic response. It is interesting to see that the inelastic $RotD00$ can, in fact, be higher than the elastic $RotD50$ for $T \leq 0.3$ s. For longer periods, the aforementioned inelastic response is always lower than the elastic one, which is the general result that was expected. This shows that the elastic response cannot sufficiently represent the minimum directional response of inelastic systems with short T .

2.3.2 Impact of inelastic behaviour on directionality response

The next aspect of the SDOF system response was the degree to which the nonlinear behaviour can impact the directionality of the response. To do this, a way in which the ground motion directionality could be quantified was needed. From the literature, the $\text{RotD100}/\text{RotD50}$ ratio of Sd_i was identified as a suitable choice as it describes how much the response tends to be polarized and has been illustrated in Figure 2.1. Computing this ratio for all of the cases previously described in Figure 2.5a and b was done and the results are summarized in Figure 2.6.

As a first comparison, Figure 2.6a shows the geometric mean of $\text{RotD100}/\text{RotD50}$ ratio for the elastic (i.e., $R = 1$) systems and compares them with the corresponding values previously published by Shahi and Baker (2014), denoted as SB14. It can be seen that the directionality measure for the selected range of ground motions is in good agreement with the SB14 model. This is also the case for the standard deviations shown in Figure 2.6b. In the case of elastic SDOF systems, the $\text{RotD100}/\text{RotD50}$ ratio can range from 1 for unpolarised ground motions to $\sqrt{2}$ for extremely polarised ones. These limits are derived from basic geometric definitions briefly explained in the following. For an unpolarised (or isotropic) motion, since the Sa would be the same in all directions, $\text{RotD50} = \text{RotD100}$, therefore their ratio will equal to 1. For an extremely polarised (or fully directional) motion, we can assume for simplicity that there is only motion in the x-direction and $Sa_y = 0$ in Equation 2.2. The median Sa will be at $\theta = 45^\circ$, ergo $Sa_{\text{RotD50}} = Sa_x \cos(45^\circ)$ and $Sa_{\text{RotD100}} = Sa_x$, and the ratio $Sa_{\text{RotD100}}/Sa_{\text{RotD50}} = 1/\cos(45^\circ) = \sqrt{2}$.

$$Sa(\theta) = Sa_x \cos(\theta) + Sa_y \sin(\theta) \quad (2.2)$$

Nonetheless, this directionality measure can reach much higher values for inelastic systems, with the lower bound staying the same. Figure 2.6a shows that for $T > 0.3$ s, the geometric mean of $\text{RotD100}/\text{RotD50}$ ratio tends to increase as R increases, meaning the more nonlinearity expected in the structural system, the more its response can be anticipated to become polarized. Furthermore, the $\text{RotD100}/\text{RotD50}$ ratios approach the elastic one for $T > 0.5$ s, especially for low R values. However, for $T < 0.3$ s, the SDOF systems with lower R factors exhibit a more pronounced impact of

directionality, reaching the value of 2.7. This is a notable observation as it essentially means that the trend for shorter periods tends to reverse for medium to long periods, and still returns back to the elastic ratio previously computed by Shahi and Baker (2014). Several R factors were considered, and it was seen that for $R = 1.5\text{--}2.5$ these impacts were most notable. This reversal of the directionality trend at short periods warrants further physical interpretation. A plausible explanation is that low inelasticity in short period systems results in a snap in response in specific direction, while more inelasticity makes the response more smoothed and spread in a range of directions.

The dispersion of the directionality measure, calculated as the standard deviation of the natural logarithm of the directionality measure, is presented in Figure 2.6b. It can be seen that the overall trend is similar to the corresponding geometric mean curves. The logarithmic standard deviation is minimized and approaches the elastic system for long T . Similar to what was done in the study by Shahi and Baker (2014), a mixed-effects regression was fitted to the data to develop directionality models for inelastic spectral displacements. Similar conclusions were drawn by Fontara et al. (2015), where for a structural system of $T = 0.3$ s the variability of structural response to the seismic incidence angle became larger as the level of structural nonlinearity increased. A table is provided as an electronic supplement (<https://journals.sagepub.com/doi/full/10.1177/87552930231180228#supplementary-materials>) containing the inter-, intra-event, and total logarithmic standard deviation, along with the mean of $\ln(Sd_{i,\text{RotD}100}/Sd_{i,\text{RotD}50})$. These can be used to transform the inelastic spectra obtained from other GMMs from the *RotD50* to *RotD100* definition.

2.3.3 Impact of directionality on expected displacement ductility ratio

While the comparisons shown so far have focused on the observations regarding $Sd_{i,\text{RotD}100}$ and $Sd_{i,\text{RotD}50}$ spectra, it is also interesting to note how these inelastic displacements compare to the nonlinear spectra typically used in seismic design and assessment. These are the so-called $R\text{-}\mu\text{-}T$ relationships and can be found in several past studies (Newmark and Hall, 1982; Miranda and Bertero, 1994; Vidic et al., 1994; Vamvatsikos and Cornell, 2006; Nafeh et al., 2020) and implemented in numerous

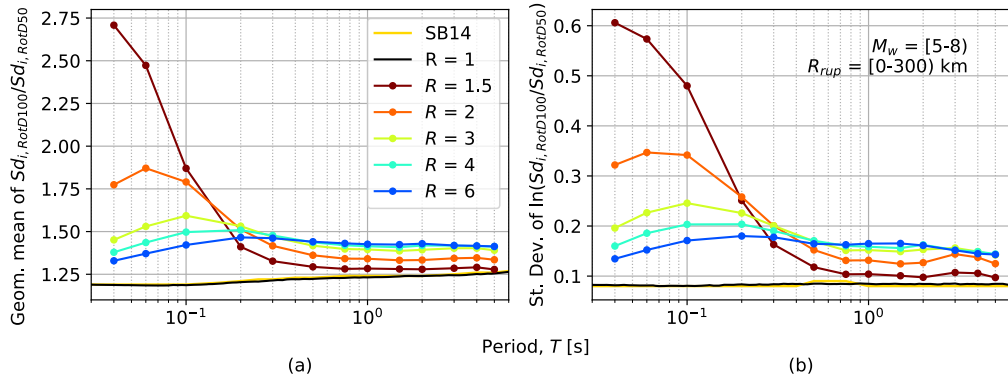


Figure 2.6. Impact of inelastic behaviour on directionality response shown via the (a) geometric mean and (b) logarithmic standard deviation of the $Sd_{i,RotD100}/Sd_{i,RotD50}$ ratio for different values of T and R . SB14 is the Shahi and Baker (2014) model for the elastic $RotD100/RotD50$ ratio

methods and codes of practice. These past models typically adopt an arbitrary component of the ground motion, $Sd_{i,\text{arb}}$, in their definition, so it is interesting to see how much of an impact changing to $Sd_{i,RotD100}$ would have. Figure 2.7(left) depicts the median displacement ductility calculated as $\mu_{\text{RotD}100} = Sd_{i,\text{RotD}100}/\Delta_y$ versus T for the considered R factors. It can be seen that, for a given R factor, μ decreases as T increases until it generally plateaus for $T > 1$ s. This is essentially due to the nonlinear behaviour of the systems converging toward the equal-displacement approximation, meaning that $R \approx \mu$. These results can be used by users who are interested in having the μ parameter as an input by choosing the period of the system and interpolating to estimate R .

Three well-established models relating R , μ , and T from the literature by Newmark and Hall (1982), Nassar and Krawinkler (1991), and Vidic et al. (1994), denoted as NK91, VFF94, and NH82, respectively, are also plotted in Figure 2.7 for comparison. It can be seen that the trend of those models is very close to the trend of the results obtained here. Nonetheless, the median values estimated in this study are somewhat higher, especially for the systems with high R factors and short T . This can be observed in Figure 2.7b via the $\mu/\mu_{\text{RotD}100}$ ratio where for moderate inelasticity and $T < 1$ s, the maximum response can be underestimated by NK91, VFF94, and

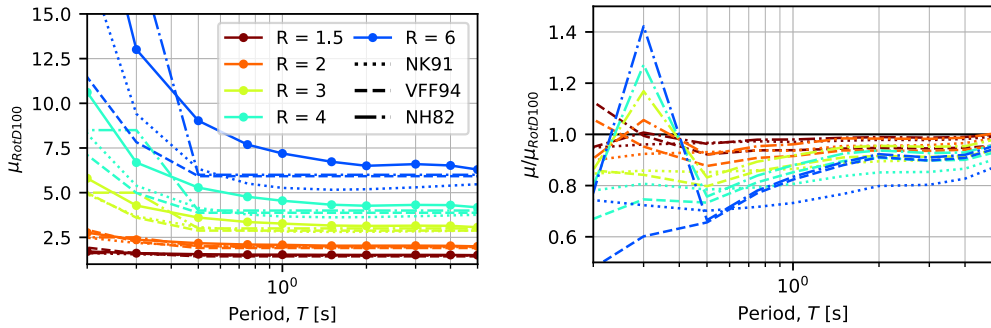


Figure 2.7. Comparison of the relationship between R , T , and the ductility demand observed in the SDOF systems when considering the $Sd_{i,\text{RotD}100}$ or the $Sd_{i,\text{arb}}$ used in conventional models

NH82 by up to 40%, whereas this reduced to 10%–20% for longer periods.

These differences are primarily due to two reasons. First, while the other studies were performed for the arbitrary as-recorded components of ground motions, the ductility presented here is for the system's 100th percentile response direction. Second, although both previous studies used bilinear hysteretic models, there are slight differences in the post-yield stiffness and the assumption of viscous damping modelling. Furthermore, Nassar and Krawinkler (1991) considered 15 ground motions in the western United States and Vidic et al. (1994) considered 20 ground motions recorded in the western United States and the 1979 Montenegro earthquake, as opposed to the 7167 ground motions considered in this study.

2.3.4 Near- and far-fault ground motions

To examine the distinction in nonlinear response observed from near-fault and far-fault ground motions, different bins were examined in terms of the directional inelastic response (i.e., $Sd_{i,\text{RotD}100}$ and $Sd_{i,\text{RotD}50}$) and the directionality measure (i.e., $Sd_{i,\text{RotD}100}/Sd_{i,\text{RotD}50}$) depicted in Figure 2.8. A comparison of the inelastic spectra shows that near-fault ground motions result in higher elastic and inelastic displacements across the entire range of periods. It is also apparent from Figure 2.8c that the near-fault ground motions result in higher directionality in the nonlinear systems. This is especially true for moderate ductility (lower R factor) structures. A similar

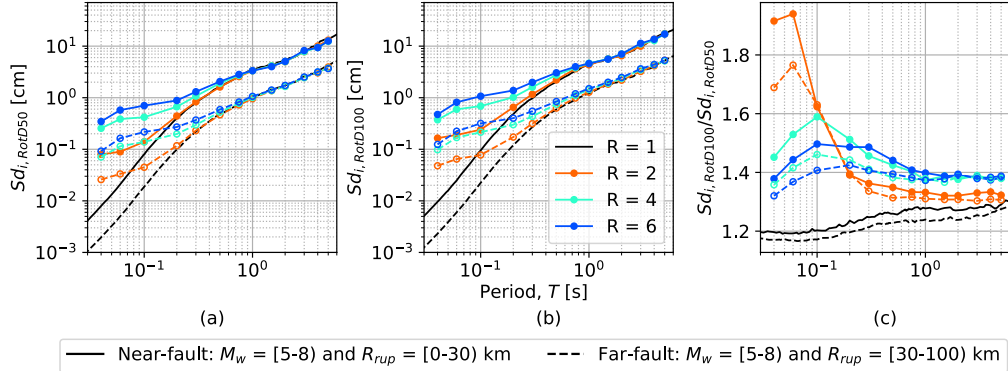


Figure 2.8. Comparing the impact of near- and far-fault ground motions via the (a) median $Sd_{i,RotD100}$ spectra, (b) median $Sd_{i,RotD50}$ spectra, and (c) median directionality measure, $Sd_{i,RotD100}/Sd_{i,RotD50}$

trend is also present for the elastic systems. These observations are to be expected as it is well-known that near-fault ground motions exhibit higher directional effects (Bray and Rodriguez-Marek, 2004; Huang et al., 2009; Tarbali, 2017; Tarbali et al., 2019).

2.4 Fitting of the GMM

2.4.1 Functional form

Utilizing the results presented previously, this section presents a simple, but accurate, model to predict the $RotD50$ and $RotD100$ of the peak inelastic displacement demands of the considered SDOF system for a given T and R using a set of explanatory parameters. The main functional form of this model, which was chosen after many trial combinations of functional forms from past GMMs examining inelastic spectral displacement (Bozorgnia et al., 2010; Heresi et al., 2018; Huang et al., 2020), is given by:

$$\ln Y_{i,j} = a + F_M + F_D + F_{sof} + F_s + F_{basin} + \eta_i + \varepsilon_{i,j} \quad (2.3)$$

where, $Y_{i,j}$ is the nn^{th} orientation-independent component of peak inelastic spectral displacement demand $Sd_{i,RotDnn}$ (in centimetres) at site j in event i ; a is a constant coefficient; F_M , F_D , F_{sof} , F_s , F_{basin} are the magnitude scaling,

distance function, style of faulting, site amplification, and the basin-effects correction terms, respectively. While the nn may refer to any percentile of the $RotDnn$ component, this GMM was limited to predicting only the 50th and 100th. The model given in Equation 2.3 separates the inter- and intra-event residuals (i.e., mixed-effects model). It also considers the inherent correlation of all the samples from the same event, in contrast to a model with a single residual term (i.e., fixed model) that assumes all samples to be independent. η_i is the inter-event term corresponding to event i following a normal distribution with zero mean and standard deviation τ ; $\varepsilon_{i,j}$ is the intra-event error term corresponding to event i at station j following a normal distribution with zero mean and standard deviation φ . It should be noted that η_i and $\varepsilon_{i,j}$ are assumed to be mutually independent; therefore, the total standard deviation of the model is calculated as:

$$\sigma = \sqrt{\tau^2 + \varphi^2} \quad (2.4)$$

The magnitude function in Equation 2.3, which does not consider magnitude saturation is given by:

$$F_M = b_1(M_{w,i} - M_r) + b_2(M_{w,i} - M_r)^2 \quad (2.5)$$

where, M_w is the moment magnitude, M_r is the reference magnitude taken here to be equal to 6, and b_1 and b_2 are unknown model fitting coefficients. The distance function is:

$$F_D = [c_{1k} + c_{2k}(M_{w,i} - M_r)] \ln \left(\frac{R_{\text{mod}}}{R_{h2}} \right) \begin{cases} k = 1; R_{\text{mod}} < R_{h1}, \\ k = 2; R_{h1} \leq R_{\text{mod}} \leq R_{h2}, \\ k = 3; R_{\text{mod}} > R_{h2}, \end{cases} \quad (2.6)$$

where R_{mod} is a modified distance to the source computed given as:

$$R_{\text{mod}} = \sqrt{R_{\text{rup}}^2 + c_3^2} \quad (2.7)$$

where R_{rup} is the closest distance from the rupture plane to the site in kilometres, c_3 is a model coefficient, and c_{1k} and c_{2k} are attenuation coefficients. R_{h1} and R_{h2} are hinge distances to account for the changes in the attenuation rate and are fixed to 15 and 150 km, respectively, and

the index k is introduced to account for the different distance ranges. The style-of-faulting function is given as:

$$F_{\text{sof}} = f_1 F_{N,i} + f_2 F_{T,i}$$

$$(F_{N,i}, F_{T,i}) = \begin{cases} (0,0); & \text{Strike-slip fault} \\ (1,0); & \text{Normal fault} \\ (0,1); & \text{Thrust fault} \end{cases} \quad (2.8)$$

where, f_1 and f_2 are model fitting parameters; F_N and F_T are dummy variables representing the style of faulting. The site amplification function is given by:

$$F_s = s_n \cdot \ln(V_{s,30}) \begin{cases} n = 1; & V_{s,30} < 400 \\ n = 2; & 400 \leq V_{s,30} < 650 \\ n = 3; & 650 \leq V_{s,30} < 1000 \\ n = 4; & V_{s,30} \geq 1000 \end{cases} \quad (2.9)$$

where, s_n is a model fitting coefficient parameter with the index n differentiating between the different $V_{s,30}$ bins, where $V_{s,30}$ is in metres per second. The basin-effects correction is given as:

$$F_{\text{basin}} = \begin{cases} d_1(Z_{2.5} - 1); & Z_{2.5} \leq 1 \\ 0; & 1 < Z_{2.5} \leq 3 \\ d_2[1 - e^{-0.25(Z_{2.5}-3)}]; & Z_{2.5} > 3 \end{cases} \quad (2.10)$$

where, d_1 and d_2 are model fitting coefficients, and $Z_{2.5}$ is the depth to the 2.5 km/s shear wave velocity horizon, typically referred to as basin or sediment depth in kilometres. For the records without registered $Z_{2.5}$, the guidelines suggested in the study by Kaklamanos et al. (2011) were followed, utilizing the formulae given in the studies by Abrahamson and Silva (2008) and Campbell and Bozorgnia (2007) to estimate $Z_{2.5}$ from $V_{s,30}$. Specifically, if $Z_{1.5}$ is known, then the following equation may be used, where all depths are in meters:

$$Z_{2.5} = 636 + 1.549Z_{1.5} \quad (2.11)$$

If $Z_{1.0}$ is known (but $Z_{1.5}$ is unknown), then $Z_{2.5}$ may be estimated by the following extrapolation:

$$Z_{2.5} = 519 + 3.595Z_{1.5} \quad (2.12)$$

When $Z_{1.0}$ is also unknown, the following equation may be used to estimate $Z_{1.0}$ from $V_{s,30}$:

$$Z_{1.0} = \begin{cases} \exp(6.745); & V_{s,30} < 180 \text{ m/s} \\ \exp \left[6.745 - 1.35 \cdot \ln \left(\frac{V_{s,30}}{180} \right) \right]; & 180 \leq V_{s,30} < 500 \text{ m/s} \\ \exp \left[5.394 - 4.48 \cdot \ln \left(\frac{V_{s,30}}{500} \right) \right]; & V_{s,30} \geq 500 \text{ m/s} \end{cases} \quad (2.13)$$

For each SDOF system and combination of R and T , the model parameters required to fit the expressions represented by Equation 2.3 were computed. The standard deviations τ and φ were computed through a series of iterative random-effects nonlinear regressions, following the one-stage mixed-effects regression algorithm proposed by Abrahamson and Youngs (1992). The “trust region reflective” method was used for the fixed-effects regression with least squares, which is the first step of the algorithm. This is particularly suitable for large sparse problems with bounds and is generally a robust method. Different methods for nonlinear least-squares regression were tested, showing a strong agreement among them. Following this approach, the resulting empirical coefficients and standard deviations can be found in the “Supplementary Material” section at: <https://journals.sagepub.com/doi/full/10.1177/87552930231180228#supplementary-materials>.

2.4.2 GMM performance

To assess the performance of the model against the observed data, a visual inspection of the residuals was carried out. A residual is defined as the difference between the “observed empirical” data (i.e., the computed peak inelastic displacements according to the methodology described in Figure 2.2) and the model prediction, both in natural logarithm. Herein, a positive residual indicates under prediction by the proposed model.

Figure 2.9 depicts the inter-event residuals versus the event magnitude for both the $Sd_{i,\text{RotD50}}$ and $Sd_{i,\text{RotD100}}$ component of response and four different combinations of T and R . Plotted in the same figure are also

the binned mean residual values, ± 1 standard deviation. These results clearly indicate that the functional form chosen adequately represents the event term, as no apparent bias against M_w is observed. This trend was also observed across the entire range of T and R used in this study.

Figure 2.10 then shows the total residuals of the same cases with respect to R_{rup} for four different combinations of T and R . Again, the binned means ± 1 standard deviation are plotted to show that they do not consistently deviate from zero as a function of distance. This lack of trend indicates that the functional form adopted is adequate for capturing the data trends.

Figure 2.11 shows the total residuals as a function of $V_{s,30}$ for different combinations of T and R for both $Sd_{i,RotD50}$ and $Sd_{i,RotD100}$. As per Equation 2.9, this site amplification term was separated into four bins in between $V_{s,30} = 400, 650$ and 1000 m/s, which were established based on visually inspecting the total residuals versus $V_{s,30}$ and their deviation from zero in certain ranges. This was necessary to capture the main trends in the response amplification due to the soil conditions, where it can be seen from Figure 2.11 that the model does not exhibit any significant bias with respect to the $V_{s,30}$ of the site.

For a visual inspection of the three aforementioned figures, it can be seen that the model fits well for both the *RotD50* and the *RotD100* components, with the *RotD100* component presenting slightly higher standard deviations.

Overall, the previous figures match the residuals for the different terms in selected cases. In addition, the predictive power of the GMM is also analysed by comparing the observed and median predicted values of Sd_i for each system (i.e. different T and R). The results of this comparison are illustrated in Figure 2.12, where it can be seen that there is a very good match between the predicted and observed values. This is first clear from Figure 2.12 via how close the data points are to the bisector line with no significant bias. Also provided in the same figure is the coefficient of determination, R^2 , which is observed to be around 0.8 for all the cases and no lower than 0.7.

Quantile–quantile (Q–Q) plots compare the quantile of each observation to the same quantity in the theoretical distribution. This is a well-established method to check if the data follow a certain theoretical distribution. If the data are linear and close to the diagonal identity line, then the chosen theoretical distribution is appropriate to describe the actual data. The Q–Q plot of the total logarithmic residuals for the case of $R =$

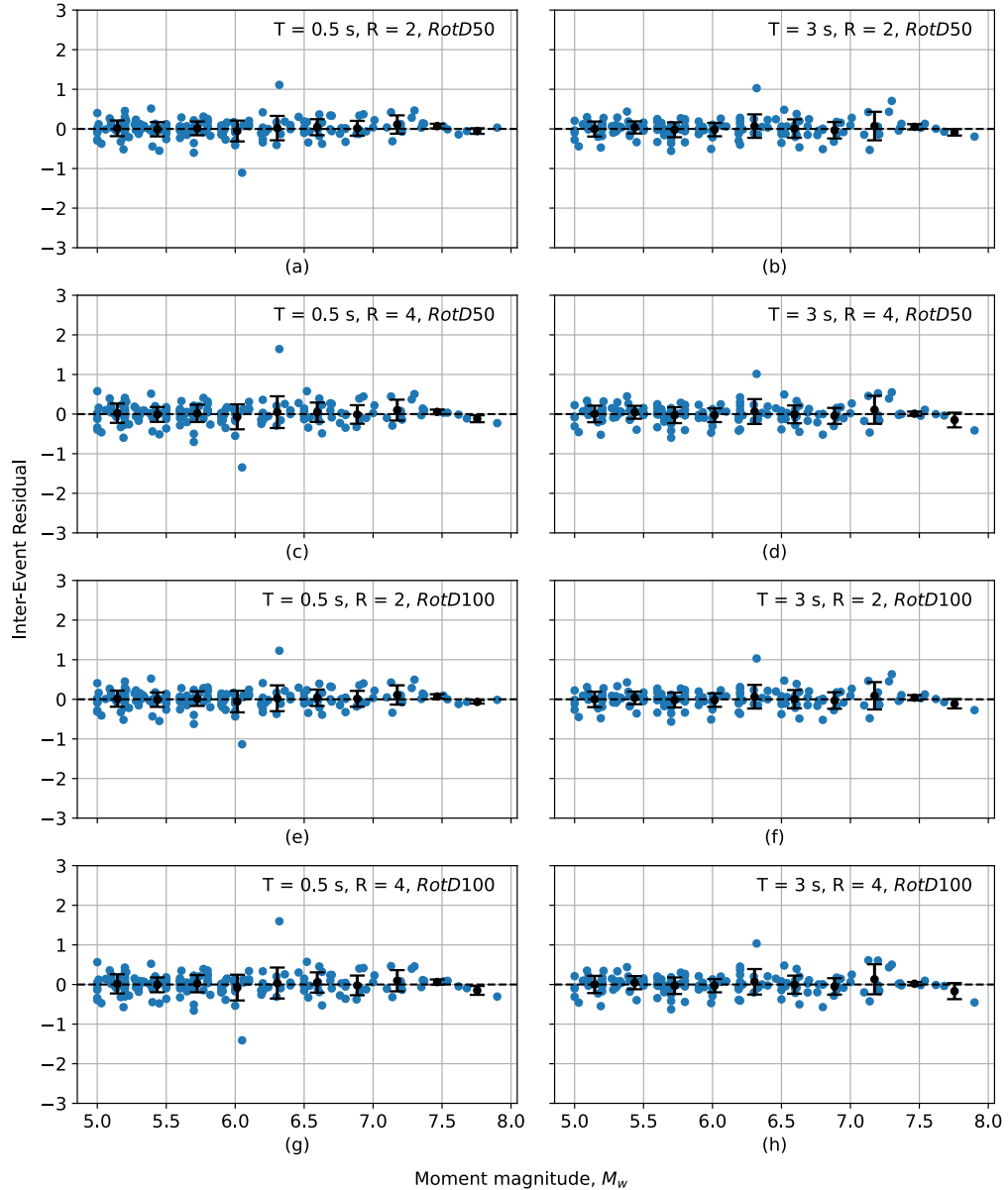


Figure 2.9. Inter-event residuals with respect to M_w for different T and R . Blue dots represent the observed residuals, while black dots and error bars represent the binned mean and \pm one standard deviation, respectively

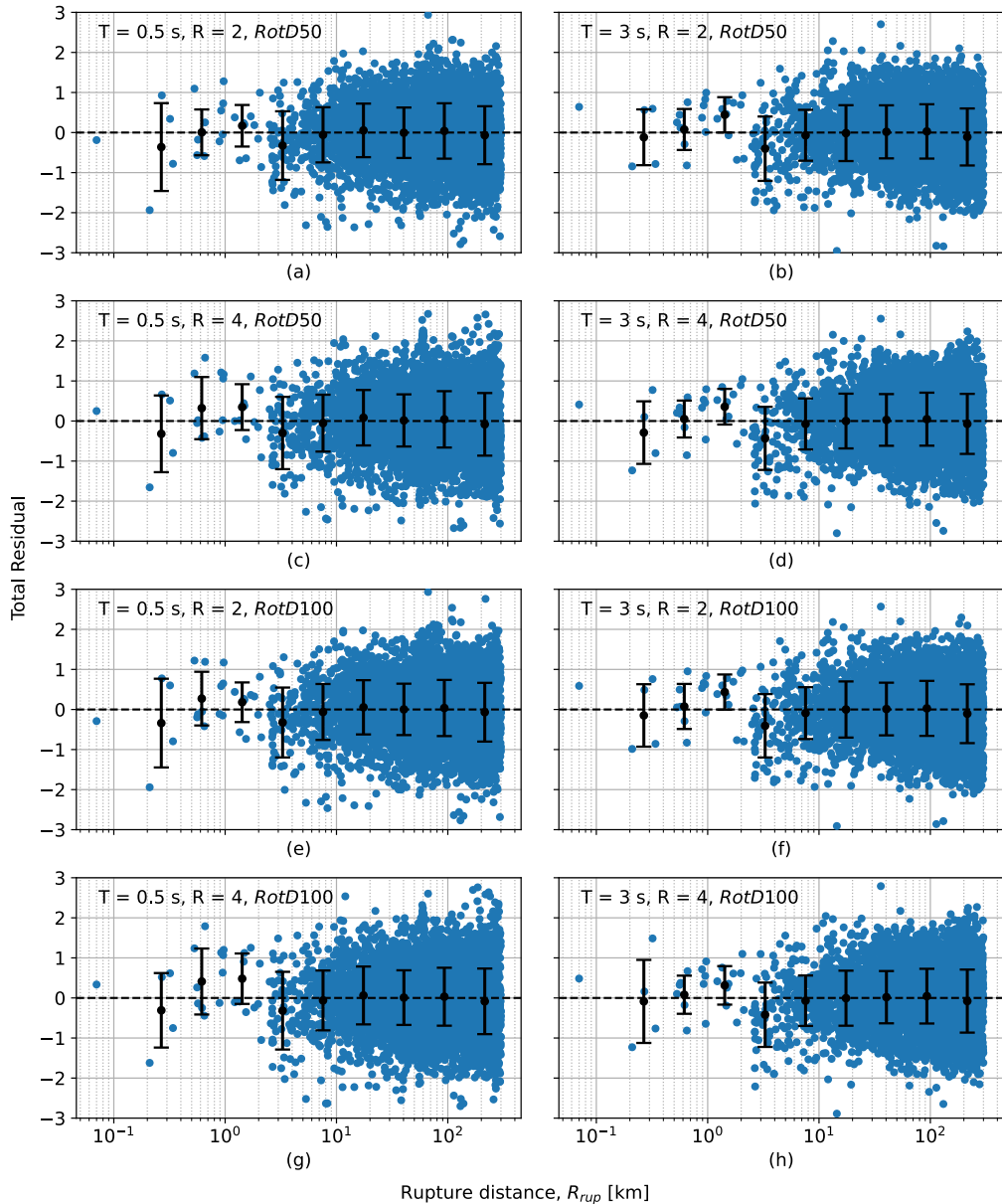


Figure 2.10. Total residuals with respect to R_{rup} for different T and R . Blue dots represent the observed residuals, while black dots and error bars represent the binned mean and \pm one standard deviation, respectively

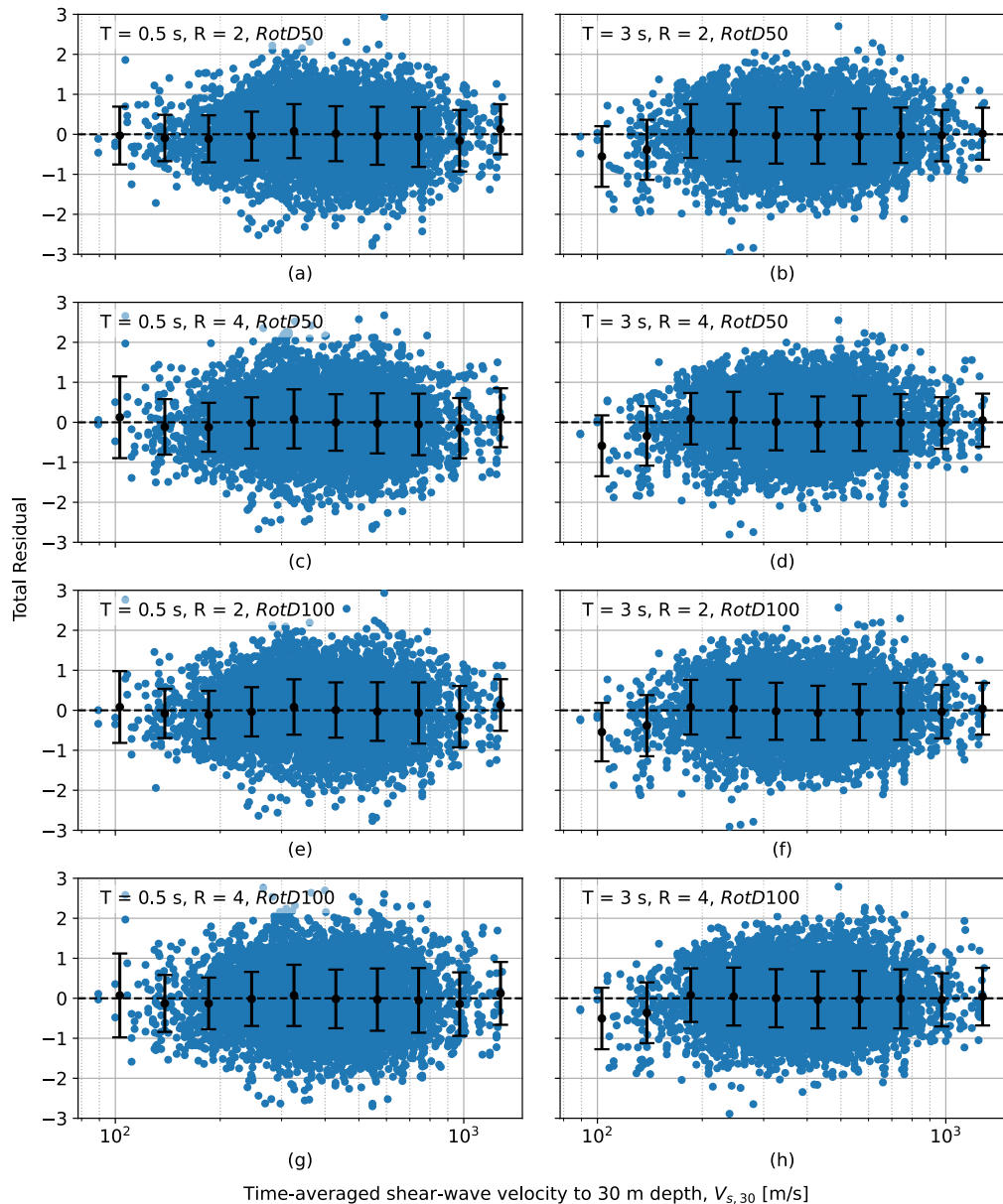


Figure 2.11. Total residuals with respect to $V_{s,30}$ for different T and R . Blue dots represent the observed residuals, while black dots and error bars represent the binned mean and \pm one standard deviation, respectively

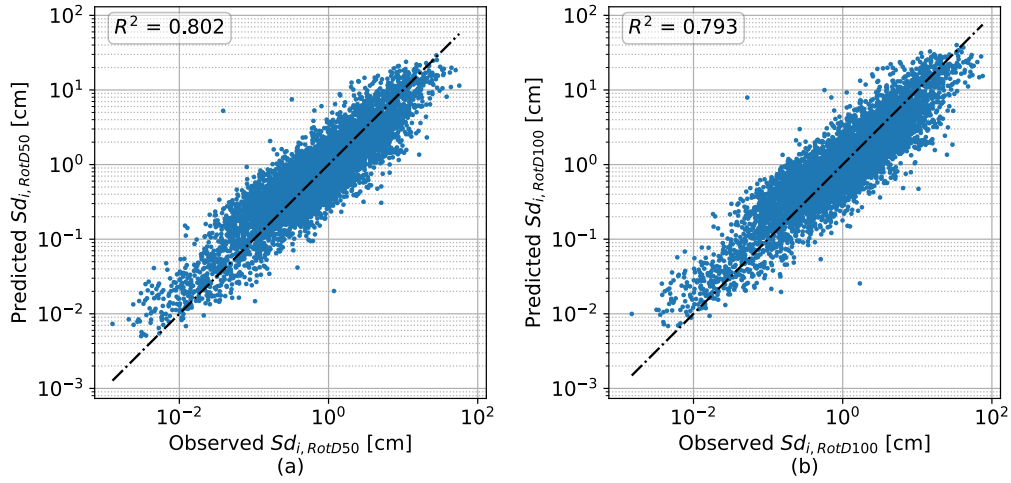


Figure 2.12. Observed (i.e. measured) versus predicted Sd_i in logarithmic axes. Case of $R = 4$ and $T = 1$ s. Blue dots represent the observed and predicted data points, while the black dash-dotted line represents the perfect fit

4 and $T = 1$ s is illustrated in Figure 2.13, where it can be seen that the natural logarithm of the predicted response values follows a normal distribution, confirming the suitability of the GMM developed.

2.4.3 Median inelastic spectra

With the proposed GMM, predictions for the median inelastic displacement spectra can be constructed, given specific ground motion causal parameters. Figure 2.14 shows the median inelastic displacement spectra for different R factors and four rupture scenarios. It can be seen that for short periods, inelastic displacements increase as R increases. This is observed up to a certain period, which changes depending on the scenario. For moderate- and long-period structures, the inelastic displacements are similar across the different R factors, essentially confirming the equal displacement approximation previously discussed. Needless to say, higher magnitudes and shorter distances produce higher spectral displacements, especially for increasing R values and increasing T . It can also be observed from Figure 2.14 that the median values of geometric mean are practically the same as the ones of the *RotD50* definition, with the geometric mean exhibiting

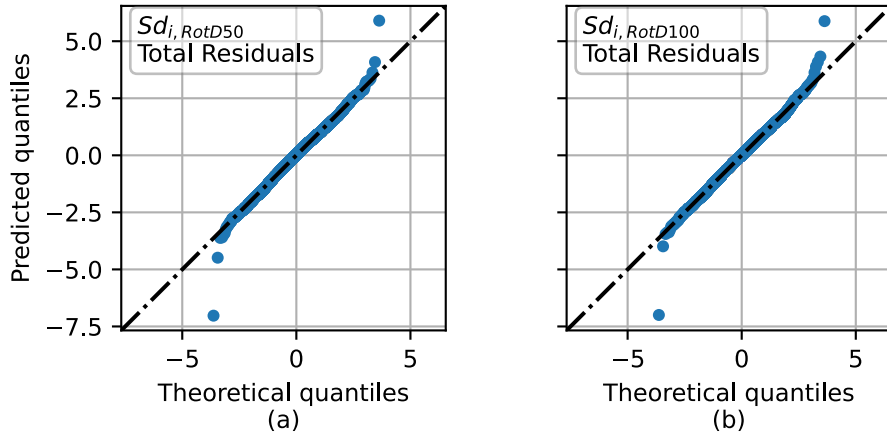


Figure 2.13. Q–Q plot of total residuals. Case of $R = 4$ and $T = 1$ s

slightly lower values in most of the period range.

2.5 Comparison with previous studies

Using the developed GMM, some relative comparisons with existing models available in the literature were explored. Compared to other GMMs, this comparison presented some difficulties since it focused on inelastic spectral displacement. This IM does not have the same research on GMM development as other IMs such as spectral acceleration. Combining this also with the fact that the directionality aspect was incorporated presented some obstacles. Another difficulty was how none of the few available models quantified their inelastic displacement predictions in terms of R , instead using the ductility demand, μ , or the strength coefficient, C_y . Nonetheless, two models from the literature that predict inelastic spectral displacements were used for comparison with the model proposed herein. Namely, the models proposed by Tothong and Cornell (2006) and Huang et al. (2020) denoted as TC06 and HTG20, respectively.

First, starting with Tothong and Cornell (2006), this model uses the outputs of a conventional (elastic) GMM and then converts them to inelastic spectral displacements based on proposed ratios. Hence, the model is actually just any conventional elastic spectral displacement GMM coupled with the TC06 inelastic displacement ratio model, with a proper

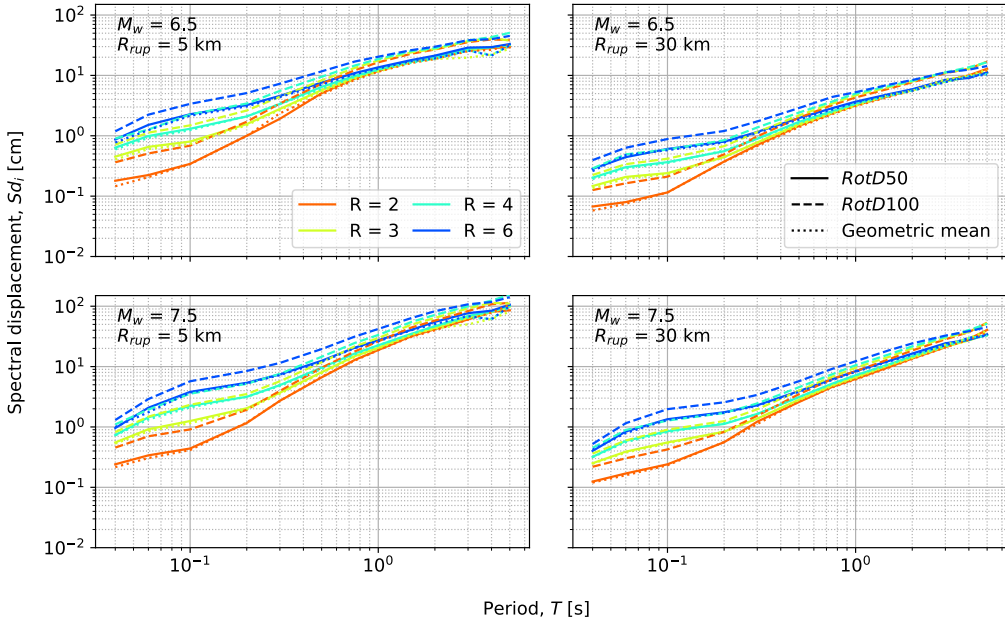


Figure 2.14. Median $RotD50$ and $RotD100$ inelastic displacement spectra for different scenarios

statistical correlation between the two. Herein, the elastic GMM employed in the original article was used (Abrahamson and Silva, 1997), although in principle, any elastic GMM may be used. The predictive parameters are the rupture scenario parameters, the elastic period T , and a yield displacement, Δ_y . Regarding the bilinear oscillator, the main difference with this study is that 5% post-yield stiffness ratio was used. The maximum R_{rup} was limited to 95 km to avoid the potential effects of anelastic attenuation, as reported in the original article (Tothong and Cornell, 2006). The arbitrary horizontal component, $Sd_{i,arb}$, for each recording was selected.

In the study by Huang et al. (2020), they developed a region-specific GMM for northern Italy for inelastic spectral displacements, explicitly accounting for the spatial correlation between intra-event residuals. The strong motion database comprised of 2427 records from 85 events with magnitudes ranging from 4.0 to 6.4 and source-to-site distances less than 200 km. The geometric mean of the two horizontal components, $Sd_{i,gm}$, was used.

Four different comparisons are given in Figure 2.15 for the proposed

GMM and the existing models from the literature. To better understand the quality of the fitting, ground motions were divided into distinct magnitude bins and compared with the median predicted values corresponding to the mean magnitude of ground motions contained in each bin. It can be observed that the median prediction of the proposed GMM generally matches well with the cloud median within the ranges containing a significant amount of data. The only exception is for $6.5 < M_w \leq 7$, where the model presents a little skewness from the cloud median. More amplified differences are observed at large distances since the model does not explicitly account for anelastic attenuation effects and also at lower distances due to the scarcity of the data. The model of HTG20 is close to the proposed model for the two lower magnitude bins, but it was omitted from the comparisons for $M_w > 7$ because the earthquake magnitudes considered in the HTG20 model ranged from $4 < M_w \leq 6.4$. Meanwhile, the model of TC06 is quite close to the cloud median of the data, with the exception of overpredicting the displacements for moderate to long rupture distances. Again it is important to highlight that these models were predicting different ground motion components (i.e., $Sd_{i,gm}$ and $Sd_{i,arb}$) compared to the $Sd_{i,RotD50}$ being evaluated here.

2.6 GMM prediction uncertainty

An important part of any GMM is the variability around the median prediction, which was denoted in Equation 2.4 as τ to represent the inter-event term and φ to represent the intra-event standard deviations. This GMM uncertainty plays a crucial role in both the assessment of existing structures and design of new structures, as it can impact the median IM predictions with small mean annual rates of exceedance. Therefore, accurate quantification of the IM standard deviation is as important as the accurate estimation of its median value. Figure 2.16 shows the logarithmic standard deviations of the $\ln(Sd_{i,RotDnn})$ estimations, where the intra- (φ), inter- (τ) and total (σ) logarithmic standard deviations are given, respectively. This representation adopts the homoscedasticity assumption commonly adopted (Boore et al., 2014; Campbell and Bozorgnia, 2014) in recent GMMs for Sa . It can be seen that the intra-event standard deviation is much higher than the inter-event one, naturally becoming the one principally driving the

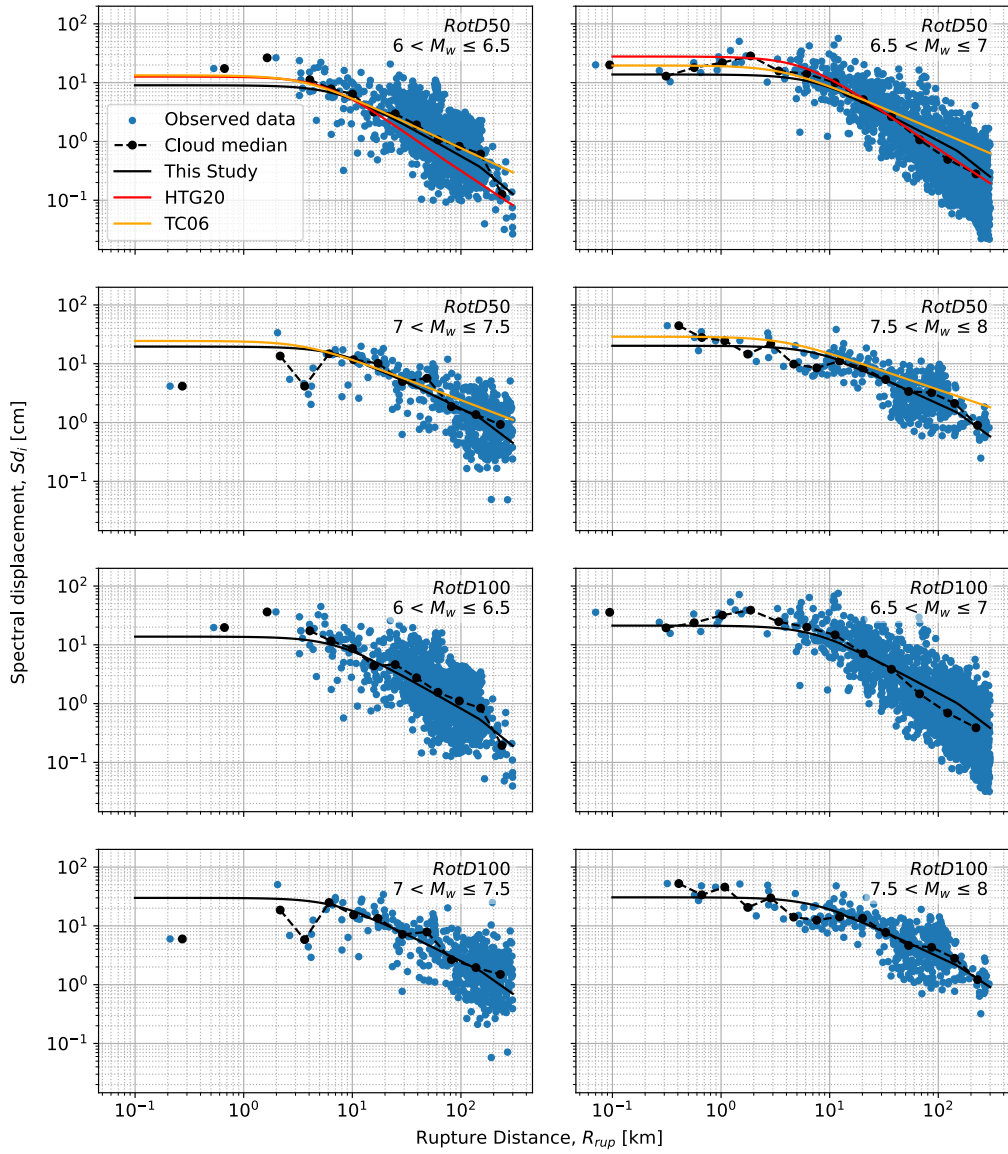


Figure 2.15. Median $Sd_{i,RotD50}$ and $Sd_{i,RotD100}$ predicted by the model, along with the empirical data, as a function of M_w and R_{rup} , for $T = 1$ s and $R = 4$

total standard deviation values. For $T < 1$ s, the total standard deviation increases as T decreases, whereas for $T > 1$ s there tended to be a plateau of about $0.65 \ln(\text{cm})$.

The total standard deviation values are compared with the corresponding ones of TC06. Since the standard deviation of that model depends on the magnitude, the mean value of all the records considered in each case was utilized for relative comparison. It can be observed that for most values of T , the proposed model gives approximately the same order of magnitude of standard deviation as TC06, although slightly lower overall. The only exception is for $T \approx 1$ s, where the proposed model gives somewhat higher values. The lower values obtained here may be partially explained by the different definitions of horizontal component, as here the *RotD50* component was used, while in TC06 the arbitrary component of the recorded ground motion was used. This produces differences in standard deviation estimates as demonstrated in the study by Beyer and Bommer (2006) for elastic spectral ordinates, if the *GMRotD50* is assumed to have the same dispersion characteristics as *RotD50*. It was shown that the arbitrary component exhibits a higher standard deviation than the *GMRotD50*, especially for longer periods.

Regarding the comparison with HTG20, it can be seen that the HTG20 model's intra-event standard deviations are higher than the ones of the proposed model for $T > 0.5$ s, whereas the inter-event standard deviations have about the same values. The difference in total standard deviation is, therefore, primarily due to the difference in the intra-event standard deviation. Overall, the slightly smaller dispersion for most periods is a notable benefit of this GMM.

It should be noted that, according to Beyer and Bommer (2006), for elastic spectral values, the *GMRotD50* component exhibits only very slightly lower dispersion than the geometric mean of arbitrarily oriented components, while the median values are shown to be close, and conventionally equal for practical purposes. However, Figure 2.17 shows that for Sd_i the geometric mean exhibits about the same total standard deviation with the *RotD50*, if not even slightly lower at a few periods. Also illustrated in Figure 2.17 is the comparison with the *RotD100* component, which generally exhibits somewhat higher σ when compared to the *RotD50* component, especially in the middle and low periods.

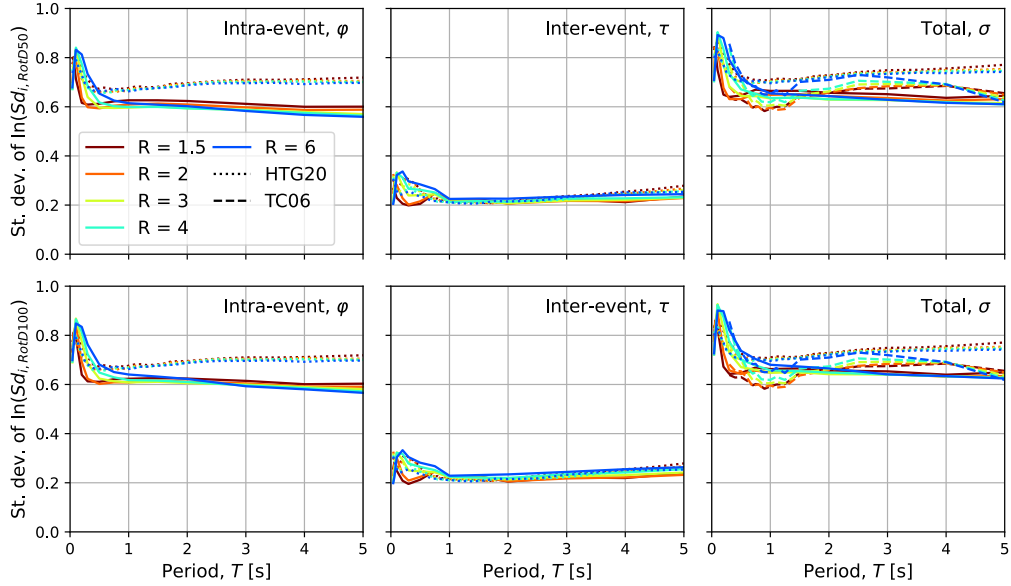


Figure 2.16. Intra-, inter-event, and total logarithmic standard deviations

2.7 Summary and conclusions

This article has looked at the inelastic spectral displacement demands caused by shallow crustal earthquakes considering ground motion directionality effects. The first part of the article examined the general directionality trends of ground motions in the NGA-West2 database for a range of inelastic

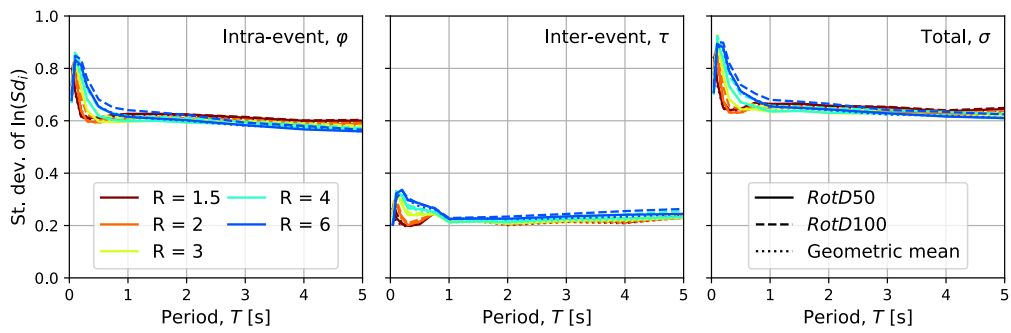


Figure 2.17. Effect of horizontal component definition on intra-, inter-event, and total logarithmic standard deviations

SDOF systems. The inelastic displacement spectra were computed for the *RotD100*, *RotD50*, and *RotD00* definitions of horizontal ground motion and plotted against the corresponding elastic ones. These spectra provided important insights into the response directionality of such systems and their relationship with the elastic ones. A comparison of traditional nonlinear response models with the results obtained herein, which consider the directionality effects, was also demonstrated. The second part of this article presented a new GMM using the previous results to predict the *RotD50* and *RotD00* definitions of horizontal ground motion for SDOF inelastic spectral displacements, namely $Sd_{i,\text{RotD50}}$ and $Sd_{i,\text{RotD100}}$, as a function of the initial elastic period of vibration, T , R , and a set of source, path, and site effect parameters. This model was evaluated and compared with other relatively similar models available in the literature. The proposed GMM can be utilized in scenario and probabilistic seismic hazard analyses to generate inelastic displacement spectra directly. Based on these developments, the following can be noted:

- The effect of directionality, quantified via the *RotD100/RotD50* ratio, on elastic systems was observed to be the same as the results obtained previously by Shahi and Baker (2014). For the inelastic systems, this ratio increased with R for $T > 0.3$ s, whereas the opposite and more pronounced trend was observed for $T < 0.3$ s.
- Examining a subset of near-fault ground motions showed higher elastic and inelastic displacements $Sd_{i,\text{RotDnn}}$ and higher directionality for the entire range of T , which is a somewhat expected result.
- The inelastic SDOF system demands—expressed in terms of strength ratio, ductility, and period—were compared against traditional $R-\mu-T$ relationships from various past studies, methodologies, and codes of practice. As expected, the median $Sd_{i,\text{RotD100}}$ nonlinear demands in the SDOF system were higher than those reported in the literature, which were based on the arbitrary or geometric mean horizontal component definitions. This comparison not only quantified the extent of this difference but also provided valuable insights that could inform future design guidelines.
- For what concerns the GMM developed to represent the *RotD50* and *RotD100* components of inelastic spectral displacement demand, a

mixed-effects regression model was fitted to capture the behaviour with very good accuracy.

- The proposed GMM exhibited reasonably low dispersions when compared with others available in the literature and is not sensitive to the level of nonlinear demand. Compared to past models, this GMM was fitted using a substantially large set of ground motions from the NGA-West2 database. It also does not require any auxiliary elastic GMM to predict the median and dispersion of inelastic displacements.
- The range of applicability of this GMM is the following: moment magnitude, $5 < M_w \leq 8$; rupture distance, $0 < R_{rup} \leq 300$ km; average shear-wave velocity in the top 30 m of the site profile, $90 \leq V_{s,30} \leq 1300$ m/s; tectonically active shallow crustal regions; period of vibration, $0.04 \leq T \leq 5$ s; and strength ratio, $1 < R \leq 6$.

The proposed GMM can be utilized in both deterministic and probabilistic seismic hazard analyses to directly generate inelastic displacement spectra. However, it should be noted that for a regional portfolio assessment it may be challenging to reliably estimate the strength ratio of each building typology, but as it is argued that an approximate yet representative value for a particular building portfolio class would still suffice for practical purposes. Nonetheless, for a single building, whose global behaviour can be easily broken down to a bilinear SDOF system with a specific period and strength ratio, the IMs proposed herein can be very effective in predicting the structural response.

Chapter 3

Exploring the use of orientation-independent inelastic spectral displacements in the seismic assessment of bridges

This chapter is extensively based on the following publication:

Aristeidou, S., & O'Reilly, G. J. (2024). Exploring the Use of Orientation-Independent Inelastic Spectral Displacements in the Seismic Assessment of Bridges. *Journal of Earthquake Engineering*, 28(12), 3515–3538. <https://doi.org/10.1080/13632469.2024.2343067>

3.1 Introduction

Bridges as part of road networks in seismically prone areas provide critical lifelines during substantial seismic events in addition to their fundamental role in the daily operation of society. Therefore, it is essential to maintain their serviceability under a wide range of earthquake intensities. While direct monetary losses can be significant, indirect losses may contribute substantially to the overall impact (Kilanitis and Sextos, 2019) as there might be some degree of re-routing of the traffic demand, causing delays and therefore economic losses, if several bridges close for repairs. For instance, Enke et al. (2008) found for one scenario that indirect losses were about 55% of the direct losses, whereas another study by Abarca et al. (2022) discussed

how because of the bridge's strategic importance the indirect impacts of the 2018 Polcevera bridge collapse in Italy were around ten times those of the direct costs, and another case study investigation in that same work by Abarca et al. (2022) in southern Italy showed the indirect losses to be approximately four times higher than the direct losses. Hence, assessment of bridge network resilience on a regional scale can be more insightful for community impact. Nevertheless, many observations and contributions to these assessment methodologies are first developed on specific issues using smaller case studies.

To evaluate the seismic risk associated with a structure, fragility functions are used to express the probability of the structure being in different damage states. This information is then utilized in decision-making processes. One of the key components of fragility functions is the IM. It connects the level (or intensity) of ground shaking to the structure's damage state. Thus, it is an inseparable link within the PBEE framework (Cornell and Krawinkler, 2000), and should be chosen wisely depending on the type of structure and underlying seismic hazard conditions at hand.

Apart from the IM itself, its horizontal component definition is often overlooked but must also be considered, especially when the directionality effect of ground shaking is notable and is of interest to the particular structure typology being investigated. While the geometric mean has commonly been used to combine the two horizontal as-recorded orientations, more recent studies (Fayaz, Medalla, and Zareian, 2020; Qian and Dong, 2020; Lin et al., 2022) have opted for using the *RotDnn* component as proposed by Boore (2010). The *RotDnn* is defined as the nn^{th} percentile of a response spectral value for all rotation angles sorted by amplitude, where D stands for period-dependent rotation angle. The most commonly used definitions are the *RotD50* and *RotD100*, which are the spectral median value and the spectral maximum over all rotation angles, respectively. These definitions are not to be confused with the *RotDnn* horizontal component definition of the engineering demand parameter (EDP) obtained by rotating the ground motions to different incidence angles, imposing them to the structure, and performing the statistics on the EDP of interest (i.e. the output of dynamic structural analysis as opposed to the input). Herein, these horizontal component definitions were examined only for the IMs, not for the EDPs, in other words, the directionality was considered as solely a property of ground motion and issues relating to the angle of incidence were

not explored.

For bridge structures, PGA , and spectral acceleration-based, $Sa(T)$, IMs have traditionally been popular (Borzi et al., 2015). Still, it was suggested (Huang et al., 2010) that PGV may also be useful. Inelastic spectral displacement has also been considered as an IM, first by Luco and Cornell (2007), and Tothong and Luco (2007), and more recently by Wu et al. (2019) for bridge structures, exploring its potential in probabilistic seismic demand analysis. The use of inelastic spectral displacement seeks to capture the displacement experienced by a simple oscillator proxy structure during an earthquake, which is a critical factor in determining the extent of damage in actual structures. Inelastic deformations are better associated with damage in the piers, such as permanent cracking, concrete spalling, fracture or buckling of reinforcing bars, or crushing of the core concrete due to fracture of the confining reinforcement (Tothong and Cornell, 2006).

Hence, this paper explores a newly developed $Sd_{i,RotD50}$ IM that could be an improved means to accurately estimate inelastic deformation and collapse performance in bridge structures. Its horizontal component definition is the same with the one previously defined, but with inelastic spectral displacement as the spectral value. Also examined is the performance of different $RotDnn$ (and generally horizontal component) definitions, for both elastic and inelastic spectral values, for a case study bridge structure. By performance, it is meant the comparative evaluation based on the relative efficiency and sufficiency of different IMs used for the seismic risk assessment of bridge structures. This research contributes to a better understanding of appropriate IMs for bridge structures, where Sd_i ranks among them, and the relevance of the $RotDnn$ component definitions in capturing the directionality of ground motion shaking. In Section 3.2, a brief literature review of works that studied the effects of directionality in the seismic assessment of bridges is given, along with some critical discussion. In Sections 3.3–3.5, the case study structure, ground motions considered, and intensity measures compared are reported, respectively. In Section 3.6, the different IMs and their horizontal component definitions are compared and ranked based on their sufficiency and efficiency. The extent at which the directionality of ground motions is biasing the seismic response of the bridge is explored specifically in Section 3.6.3. General discussion and conclusions are given in Section 3.7.

3.2 Directionality Effects in the Assessment of Bridges

Directionality effects, as illustrated in Figure 2.1, are especially present in near-fault ground motions with forward directivity (Tarbali, 2017) and fling-step characteristics, which are generally characterized by a unidirectional large-amplitude velocity pulse and a monotonic step in the displacement time history (Kalkan and Kunnath, 2006). It is important to underline here that the characteristics of these motions, typically, have the biggest effect in the fault-normal direction and specifically the spectral acceleration at periods longer than 0.6 s (Somerville et al., 1997). Poulos and Miranda (2023) presented a modification for GMMs to estimate the spectral acceleration at any given azimuth relative to the fault, which is useful when one knows the orientation of a strike-slip fault that governs the seismicity at a site, and also the main orientations of the structure being assessed or designed. However, this information may not always be available. Intensity measures that incorporate spectral values from all the possible rotation angles in the horizontal plane, e.g. *RotD50*, have the advantage of removing the sensor orientation as a contributor to epistemic uncertainty (Boore et al., 2006) and they are state-of-the-art horizontal component definitions of spectral values. Additionally, when combined with the *RotD100* definition in the appropriate manner (i.e. *RotD100/RotD50*) they can create a simple and useful measure of ground motion directionality, as depicted in Figure 2.1 of the previous chapter. It should be noted that there are many proposed formulations of directionality measure in the literature (e.g. Rivera-Figueroa and Montejo, 2022), however there is no common consensus of what scalar value can better describe the ground motion directionality. Nonetheless, the most prevalent in the literature seems to be the *RotD100/RotD50* (Shahi and Baker, 2014), so that was chosen for the comparisons herein. In this study, the elastic and inelastic spectral quantities computed from different horizontal component definitions were compared, in order to draw conclusions on which definition is more suitable as an IM choice for bridges.

Current seismic design methodologies (e.g. (ASCE/SEI 7-16, 2018), Eurocode 8 (CEN, 2005), and JRA (Japan Road Association, 2012)) do not specify the expected degree of directionality of a bi-directional ground

motion shaking (Lin et al., 2022). The latter study imposes a complex combination of forces and displacements on the different components of a bridge structure (e.g. pier elements, shear keys, abutments). On that note, it has been noted in the literature that certain structural typologies, including highway bridges, are sensitive to input records with intense directionality effects (Mackie et al., 2011). That is because these structures often possess asymmetric stiffness, damping and strength characteristics. Several studies have noted and investigated this effect on bridges (Mackie et al., 2011; Torbol and Shinozuka, 2014; Sengupta et al., 2016; Feng et al., 2018). Feng et al. (2018) assessed ten commonly used IMs, in terms of various metrics, to determine which ones better account for the influence of incidence angle variation. This was also examined for various components of the bridge and the bridge system in general. It was found that the seismic excitation direction has a minor impact on the optimal IM rankings. Similar topics were addressed in a subsequent study (Feng et al., 2021), where the basis of comparison was the performance (i.e. monetary repair loss) of a horizontally curved bridge. Also, 20 candidate IMs were investigated and compared. An important finding was that the total bridge loss gradually becomes independent of the seismic excitation direction as the seismic intensity increases and the structure sustains heavier damage. It was also concluded that velocity-related and/or structure-dependent IMs presented superior performance, compared to other categories of IMs. Additionally, for different EDPs in different components, the critical incidence angle can vary significantly. Nevertheless, it was demonstrated in the literature (Mackie et al., 2011) that if the ground motion ensemble is of substantial size and representative of underlying hazard conditions at the site, the incidence angle does not have a significant effect on the response. The three aforementioned studies, though, included both polarized and unpolarized ground motions from both near- and far-field ranges, there was no distinction and direct comparison between polarized and unpolarized ground motions. Additionally, for the incidence angle to have a significant effect, all ground motions could be rotated so that the *RotD100* orientation (or fault-normal orientation for near-fault ground motions) coincides with the weaker principal structural direction. However, a significant bias would be introduced in such case since that would be the worst possible scenario regarding the incidence angle of each ground motion. Nevertheless, comparing that with the structural response obtained under

randomly (or as-recorded) oriented ground motions would yield important insights on the most adverse effects that their directionality can have on a site.

3.3 Case Study Bridge Structure and Numerical Modelling

To illustrate the relative performance of these novel IMs for bridges, a case study structure was numerically modelled and analysed for comparison. The structure adopted in this study was an existing bridge in California constructed in 2001. This bridge is the Jack Tone Road On-Ramp Overcrossing and has been used in several past studies (e.g. Fayaz, Dabaghi, and Zareian, 2020; Otárola et al., 2022). It is used here as a reference structure since much technical documentation is available for sufficiently detailed numerical modelling. It falls under the ordinary reinforced concrete bridge typology, with seat-type abutments, single-pier bent and box-girder deck.

A three-dimensional finite-element model was developed using the open-source software OpenSeesPy (Zhu et al., 2018), whose parameters are described below. For the seismic analysis of bridge structures, it is typically not necessary to model a full three-dimensional model of the superstructure with detailed finite elements. Instead, simple spine models suffice for the scope of seismic analysis, provided that they represent the effective dynamic stiffness characteristics and mass distributions appropriately (Priestley et al., 1996). Figure 3.1 depicts a schematic representation of the three-dimensional finite element model developed.

Since the bridge's superstructure is designed to remain elastic during earthquake-induced ground shaking, the deck was modelled with an elasticBeamColumn element in OpenSeesPy, with gross cross-sectional properties (i.e., $I_{\text{eff}} = I_g$), as recommended by California department of transportation (Caltrans) seismic design criteria (SDC) (Caltrans, 2019). The mass of the superstructure was modelled as a consistent distributed mass acting on the pier element and throughout the length of the deck elements, with each span discretized into ten elements. The bridge pier was modelled using the forceBeamColumn element, with fibre-based cross-sections, employing the HingeRadau integration method (Scott and Fenves, 2006; Scott and

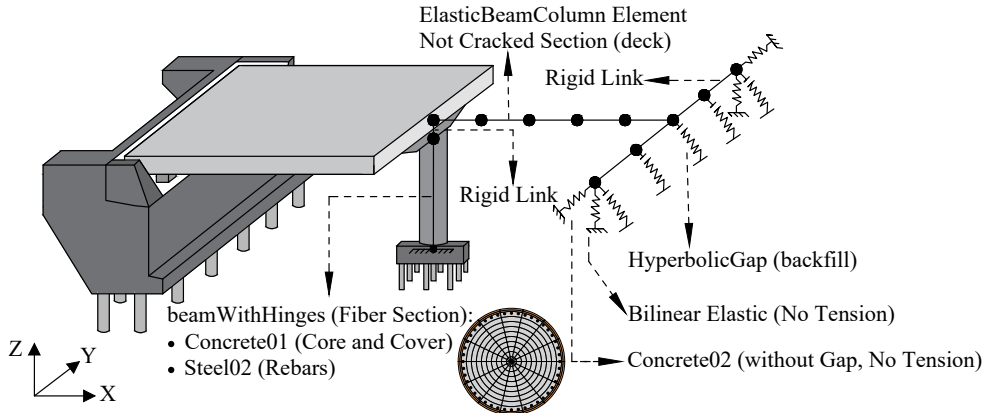


Figure 3.1. Illustration of the numerical modelling strategy adopted for the case study bridge, along with the pier cross-section fibre discretization

Ryan, 2013). The pier was assumed to be fixed at the base for simplicity and monolithically connected to the underside of the deck. Confined and unconfined concrete fibres were modelled using the Concrete01 uniaxial material model, and the steel rebars were represented using the Steel02 (i.e., Giuffre-Menegotto-Pinto) material model, including a MinMax limiting strain of $\varepsilon_{su} = 0.10$ (Priestley et al., 1996) to capture the potential buckling and rupture of the steel reinforcing rebars. The plasticity in the piers was concentrated at the two ends of the pier elements and connected by a linear elastic element with effective cross-section stiffness properties. The shear and torsional behaviour of the pier was modelled elastically using a section aggregator, with the suggested stiffness reduction factors of the report of Kaviani et al. (2014). These were modelled as elastic since failure modes of this type are not expected to occur given the compliance of the case-study bridge with modern seismic design practices. The pier, pier cap and deck are constructed integrally, so a beam-type rigid link was assigned to connect the top end of the pier to the deck element. Figure 3.2 shows the moment-curvature response of the pier section, in addition to the lateral response of the entire element.

For what concerns the bridge ends, a simplified abutment model was adopted, where only three components were explicitly considered: (1)

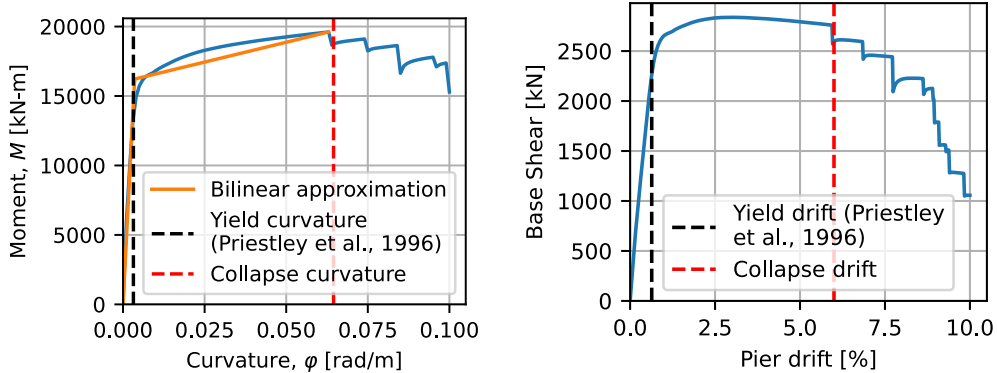


Figure 3.2. Moment curvature analysis and bilinearization (left). Pushover analysis of just the pier element (right)

longitudinal response of the backfill (passive pressure) and the expansion joint; (2) transverse response of the shear keys; and (3) vertical response of the bearing pads and the stem wall. The remaining abutment components were omitted, as their contributions to the overall response have been found to be insignificant (Kaviani et al., 2014). Regarding the longitudinal behaviour of the abutment, five springs were assigned along the deck width, all connected by a rigid beam. The soil backfill response was modelled using the *HyperbolicGapMaterial*. The strength and initial stiffness of the soil springs were obtained from the recommendations provided in Caltrans SDC (Caltrans, 2010), which in turn were derived from a large scale abutment testing (Romstad et al., 1995; Stewart et al., 2007). This material was based on abutment stiffness models for bridge simulation proposed by Wilson and Elgamal (2006) at the University of California at San Diego. The hyperbolic force-displacement model was based on work by Duncan and Mokwa (2001) and Shamsabadi et al. (2007) with calibrated parameters from University of California at San Diego abutment tests. Regarding the transversal behaviour of the abutment, one spring was assigned to each abutment's transversal end. It was assumed that the abutment backwall does not contribute significantly to the longitudinal load-bearing capacity of the abutment, since it fails through a brittle mechanism. The backbone curve response of the different abutment components is given in Figure 3.3. Note that for each component, the response of a single spring was plotted.

Regarding the bearing pads, they were assumed to be frictionless.

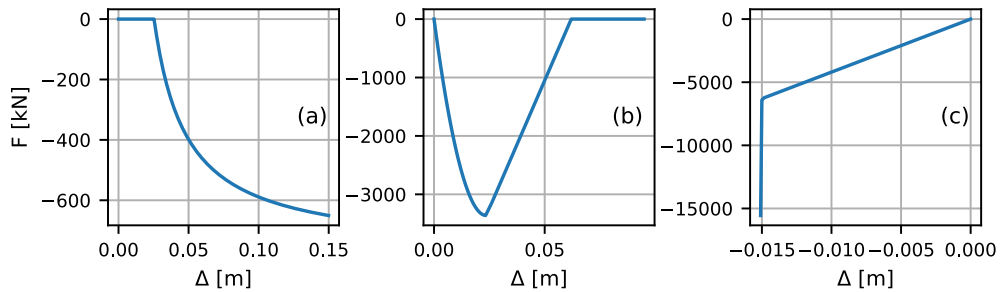


Figure 3.3. Backbone curve of a single abutment spring in (a) longitudinal, (b) transversal, and (c) vertical direction

Thus, their transverse and longitudinal shear capacities, and generally their interaction with the deck were disregarded, except in the vertical direction. The shear keys at the deck ends were modelled using macro-elements that resist only in compression and the *Concrete02* hysteretic force-deformation model was used (Omrani et al., 2017). This hysteretic model was chosen to avoid convergence problems and solve the simultaneous parallel force balance problem by defining a small strength in tension. Further details about this bridge's characteristics and modelling assumptions are given in the "Bridge A" description of Kaviani et al. (2014). With regards to damping, a 5% tangent stiffness proportional Rayleigh damping model was applied to the first mode (Petrini et al., 2008). It should be noted that Sousa et al. (2020) suggest critical damping values ranging from 0.5% to 2% when using fibre-based elements in the model, since most of the energy-dissipation mechanisms are explicitly modelled. They also found that for these small values of critical damping, the differences between mass-proportional or tangent stiffness proportional damping become insignificant. However, since this is a comparative study and not an explicit seismic risk assessment, it is not expected to have notable impact on the final conclusions.

Modal analysis was carried out on the bridge model and the first four modes' periods of vibration and their participating mass in each of the principal directions are listed in Table 3.1. As can be observed through the translational and rotational modal participation factors, U and Φ , respectively, the first two modes are primarily in the X direction, with a small rotation component about the Y axis. It should be noted that these modal properties also closely match those reported by Kaviani et al. (2014)

Table 3.1. Modal analysis results of the case study bridge.

Mode	Period [sec]	Modal participation mass ratios (%)					
		U_x	U_y	U_z	Φ_x	Φ_y	Φ_z
1	0.604	48.5	0	0	0	31.1	0
2	0.363	50.5	0	0	0	34.6	0
3	0.352	0	88.3	0	0.5	0	0
4	0.336	0	0	75.4	0	0	0

for the same bridge typology, therefore giving confidence to the accuracy and representativeness of the case study bridge model.

3.4 Ground Motion Records

To analyse the seismic performance of the bridge model, incremental dynamic analysis (IDA) (Vamvatsikos and Cornell, 2002) was performed to characterize the non-linear dynamic response of the bridge model right up to lateral collapse. To do this, a sufficiently large set of suitable ground motion records was needed to characterize the structure's seismic response adequately and to ensure an accurate marginal distribution of IM for a given EDP threshold (i.e. fragility curves). A set of 200 unscaled ground motion records from shallow crustal earthquakes were selected from the NGA-West2 database (Ancheta et al., 2013) based on a scenario of magnitude, $M_w = 7.5 \pm 0.5$, rupture distance, $R_{rup} = 20 \pm 20$ km and soil conditions, $V_{s,30} = 400 \pm 300$ m/s. Out of those 200 ground motions, the 60 were classified as pulse-like records, and in 57 of them the pulse was caused due to directivity effect. The ground motion directivity effect describes how the intensity and duration of ground shaking can vary depending on the orientation of the earthquake source relative to a particular site. As seismic waves radiate outward from the fault, the ground motion can be stronger in the direction of the rupture and weaker in the opposite direction. This is not to be confused with ground motion directionality, which is a broader term and encompasses the idea that ground shaking can vary depending on the direction from which seismic waves approach a location. Regarding the fault mechanism, 84 records were caused from

strike-slip, zero records from normal and 116 records from reverse faulting. A relatively large number of ground motions was chosen so that the accuracy of seismic demand estimates does not affect the final results and conclusions, which has been studied in the past by Sousa et al. (2016), for example. Also, a quite intense scenario was chosen to minimize the level of scaling required to bring the structure to its collapse limit. This was especially the case since the bridge under consideration was well designed against seismic actions. Table 3.2 reports the minimum, median, and maximum values of the IMs considered in the general sufficiency and efficiency checks, which are presented further below. It should be noted that only the horizontal components of the ground motions were applied to the structure as the bridge was not expected to be susceptible to adverse vertical ground-motion effects. Regarding the application of the ground motion records to the structure, the 1st as-recorded component in the NGA-West2 database was applied to the X (longitudinal) direction of the bridge and the 2nd as-recorded component was applied in the Y (transversal) direction. This was kept constant throughout the analysis since past work (Giannopoulos and Vamvatsikos, 2018) has shown that using an adequately large set of ground motion records is more important and produces more reliable results than a smaller set with varying orientation of each individual ground motion record.

3.5 Intensity Measures

Several studies have focused on investigating IM performance in bridge structures (Avşar and Özdemir, 2013; Mehdizadeh et al., 2017; Monteiro et al., 2019; Abarca et al., 2021; O'Reilly, 2021a) but are typically related to the spectral acceleration-based IMs. Qian and Dong (2020) employed a novel multi-criteria decision-making approach to rank the acceptability of each alternative IM, based on holistic acceptability indices, for different structural components of a case study highway bridge. Many studies have shown how additional considerations are needed for IM selection for bridges compared to buildings. However, none of these studies has so far examined the relative performance of inelastic spectral displacement-based IMs, which have been the focus of recent research (Heresi et al., 2018; Aristeidou et al., 2023; Bahrampouri et al., 2023). Also, the issues of directionality are worth

Table 3.2. Minimum, median, and maximum values of IMs considered in the general sufficiency and efficiency checks

	$Sd_{i,RotD50}$ ($R = 2, T_1$)	$Sd_{i,RotD50}$ ($R = 3, T_1$)	$Sd_{i,RotD50}$ ($R = 4, T_1$)	$Sd_{i,RotD50}$ ($R = 6, T_1$)			
min	0.435 cm	0.519 cm	0.495 cm	0.557 cm			
median	3.387 cm	3.626 cm	4.153 cm	5.512 cm			
max	13.731 cm	24.753 cm	37.011 cm	55.693 cm			
	$Sa(T_1)$	$Sa(1s)$	PGA	PGV	PGD	$FIV3$	Sa_{avg2}
min	0.046 g	0.024 g	0.032 g	5.319 cm/s	0.397 cm	4.425 cm/s	0.046 g
median	0.380 g	0.261 g	0.185 g	37.367 cm/s	25.973 cm	62.365 cm/s	0.334 g
max	1.632 g	1.173 g	0.768 g	256.620 cm/s	365.920 cm	217.256 cm/s	1.333 g

exploring for what concerns bridge structures and are thus examined further here.

Based on the above considerations and also the past literature on this topic for bridge structures, the following intensity measures were employed for the comparisons in this chapter:

- PGA : peak ground acceleration;
- PGV : peak ground velocity;
- PGD : peak ground displacement;
- $Sa(T_1)$: 5%-damped spectral acceleration at the fundamental period, T_1 , of the structure;
- $Sa(1s)$: 5%-damped spectral acceleration at period equal to 1 s;
- $Sd_{i,RotDnn}$: 5%-tangent-stiffness damped inelastic spectral displacement, where two $RotDnn$ definitions were considered: the 50th and 100th percentile of all rotation angles sorted by amplitude (i.e. $RotD50$ and $RotD100$) as defined by Boore (2010);

- $FIV3$: filtered incremental velocity, as defined by Dávalos and Miranda (2019) and Equation 3.1;
- Sa_{avg} : average spectral acceleration as defined by Equation 3.3, which was further subdivided according to the period range as follows:
 - $Sa_{avg1} - T \in [0.5T_1, 1.5T_1]$
 - $Sa_{avg2} - T \in [0.5T_1, 2T_1]$
 - $Sa_{avg3} - T \in [0.5T_1, 3T_1]$

$$FIV3 = \max\{V_{s,max1} + V_{s,max2} + V_{s,max3}, |V_{s,min1} + V_{s,min2} + V_{s,min3}|\} \quad (3.1)$$

$$V_s(t) = \int_t^{t+\alpha \cdot T} \ddot{u}_{gf}(\tau) d\tau, \quad \forall t < t_{end} - \alpha \cdot T \quad (3.2)$$

where $V_s(t)$ is a series of incremental velocities, IVs estimated using time segments of αT , $V_{s,max1}$, $V_{s,max2}$, $V_{s,max3}$ are the first, second, and third local largest IVs in $V_s(t)$, respectively, and $V_{s,min1}$, $V_{s,min2}$, $V_{s,min3}$ are the first, second, and third local minimum IVs in $V_s(t)$, respectively, T is the period of interest, t_{end} is the last instant of time of acceleration time series, and \ddot{u}_{gf} is the filtered acceleration time series using a second-order Butterworth low-pass filter with a cut-off frequency, f_c , equal to βf , where β is a scalar controlling the f_c/f ratio and f is $1/T$. Dávalos and Miranda (2019) presented $FIV3$ as a novel IM that produced promising results for the collapse assessment of buildings. The α and β input parameters required to calculate Equation 3.1 were chosen as 0.7 and 0.85, respectively, as initially proposed by the same study. However, further optimization of these parameters for bridges may be investigated in future work.

Sa_{avg} , is another candidate included in this study for comparison. It is defined as the geometric mean of N -number spectral accelerations at periods within a user-specified range $[T_{lower}, T_{upper}]$, expressed as in Equation 3.3. Different period ranges can be chosen for the definition of this IM depending on the structure and the level of inelasticity that one wants to capture more accurately. This ambiguity was investigated in several past works (Cordova et al., 2000; Vamvatsikos and Cornell, 2005) and also an extensive analysis is conducted in Chapter 7 of Eads and Miranda (2013), where it was

explored how the range, number, and spacing of periods used to compute Sa_{avg} influences the efficiency of collapse risk assessment estimates of SDOF, moment-resisting frames, shear wall, and reinforced concrete systems. To define Sa_{avg} , ten periods (i.e. $N = 10$) equally spanning each chosen period range were used as per Equation 3.3. These alternative period ranges were examined as a simple parametric study to investigate where alternative condition period ranges could improve the IMs performance in this ad-hoc case.

$$Sa_{avg} = \left[\prod_{i=1}^N Sa(T_i) \right]^{1/N} \quad \text{for } T \in [T_{\text{lower}}, T_{\text{upper}}] \quad (3.3)$$

The spectral acceleration at the first mode period has been used in countless studies in recent decades for a variety of bridge structural typologies (e.g., Gardoni et al., 2002; Muntasir Billah and Shahria Alam, 2014; Mangalathu et al., 2017). Recent work by O'Reilly (2021b) has discussed how the first mode period of bridge structures is generally not the dominant mode, and anchoring this IM definition to this period may not be the best solution. In fact, HAZUS (2003) recommends using Sa at period of 1 s, which is not linked directly to the bridge modal properties. Regarding the component definition of $Sa(T_1)$, the *RotD50* horizontal component definition was adopted, unless otherwise stated.

The calculation of $Sd_{i,\text{RotDnn}}$ was based on a bilinear SDOF system with positive strain hardening ratio of 3%, with non-degrading and non-evolutionary hysteretic behaviour. To fully define the inelastic system, the elastic period, T , and R , are needed. The latter was defined as the ratio of maximum spectral demand in the elastic system, to the SDOF yield strength. The set of elastic periods considered was $T = [0.04, 0.06, 0.1, 0.2, 0.3, 0.5, 0.75, 1, 1.5, 2, 3, 4, 5]$ in seconds, and the set of strength ratios was $R = [1.5, 2, 3, 4, 6]$. For the calculation of the different horizontal component definitions, the ground motions were rotated from 0° to 180° with an increment of 6° and recording the maximum response for each ground motion at each rotation angle. More details on the methodology and the definition of SDOF system are given in Aristeidou et al. (2023). The horizontal component definitions examined here are the *RotD50* and *RotD100* definitions. The *RotD50* definition was used as more recent GMMs in the NGA-West2 project have opted to use this horizontal component

definition (Bozorgnia et al., 2014), while the *RotD100* component was chosen because it represents the spectral maximum over all rotation angles and has been used in other models (Shahi and Baker, 2014). For each IM the horizontal component definitions of geometric mean, *RotD50* and *RotD100* were examined and will be compared below in Section 3.6.2.1.

As Bradley (2012) and others have shown, an IM is the interface variable connecting seismological and engineering aspects in seismic analysis. Seismologists employ seismic hazard analysis to determine the probability of exceeding an intensity level for a certain site over a given period of time. Engineers then utilize this IM to examine the structural response and determine the seismic risk performance of a structure. This characterisation of the interface IM between seismology and engineering is meant to avoid associating the structural response to rupture parameters, *rup*, such as magnitude and distance, condensing all pertinent information in the chosen IM for engineering evaluation. To achieve this disassociation of structural response to *rup* parameters to the highest degree possible, the IM needs to be (i) practical in its predictability via GMMs used in hazard analysis, (ii) efficient in its prediction of structural response, (iii) sufficient with respect to the underlying seismic hazard and site characteristics and (iv) unbiased with respect to other ground motion parameters and other unconditioned IMs.

For an IM to be practical, GMMs should be readily available to conduct a seismic hazard analysis for it. This can sometimes restrict the IM choice in seismic risk analysis since research has traditionally focused on peak ground acceleration/velocity/displacement and (pseudo) spectral accelerations. For these IMs, one can choose from a plethora of well-established GMMs, such as Campbell and Bozorgnia (2008), for example, which can predict all of them. For the more recently proposed *FIV3*, the GMM of Dávalos et al. (2020) can be utilised. A newly developed GMM also exists for the novel $Sd_{i,RotD50}$ (Aristeidou et al., 2023) being evaluated as part of this study. Regarding Sa_{avg} , the logarithmic mean and variance for a given rupture scenario can be computed either directly using a GMM (Kohrangi et al., 2018; Dávalos and Miranda, 2021), or indirectly utilizing the $Sa(T)$ values given by other GMMs (Kohrangi et al., 2017).

Efficiency means that the structural response, measured by an EDP, should exhibit low record-to-record variability at any given level of the IM, or reversely low IM level variability at any given structural response (EDP)

level. This IM attribute allows one to accurately evaluate the conditional EDP distribution with relatively few response-history analyses. This can become important when conducting numerous non-linear dynamic analyses for a building class portfolio or in regional assessment. However, it is worth noting that within a risk assessment framework, like the PEER-PBEE framework (Cornell and Krawinkler, 2000), this reduction in response dispersion gained by a more efficient IM, does not necessarily reduce the overall dispersion. A more efficient IM may be more structure-specific and, therefore, present lower EDP dispersion, $\beta_{EDP|IM}$, but this may come at the cost of higher dispersions when defining an appropriate GMM, $\beta_{IM|rup}$ (Kohrangi et al., 2017). Therefore, the eventual risk metric may still result in a high dispersion. This issue is briefly examined in Figure 3.4, where the dispersions (i.e. logarithmic standard deviations) of all the IMs are shown for demonstration purposes for the rupture scenario described in Section 3.4. The GMM of Campbell and Bozorgnia (2008) was used to obtain the dispersions of all spectral IMs, except *FIV3* and *Sd_{i,RotD50}*, and the additional parameters needed for the model input were taken as the mean parameters of the used ground motion suite. It can be seen that all IMs, except peak ground displacement, *PGD*, have $\beta_{IM|rup}$ between 0.5 and 0.7. The elastic spectral values, *PGA* and *PGV* exhibit dispersions between 0.5 and 0.62, while *Sd_{i,RotD50}* exhibit dispersions between 0.64 and 0.7, proportionally to the degree of inelasticity. Generally, it can be said that all the IMs investigated present ground motion prediction uncertainties of a similar order of magnitude, except *PGD*, meaning that the direct comparison of the IM's efficiency is reasonable. However, it should be noted that the logarithmic standard deviations of IMs are slightly changing from GMM to GMM.

The sufficiency criterion mandates that seismological parameters should not influence the seismic response characterized via the IM, eliminating any bias against, for example, magnitude, distance, or fault rupture mechanism. Sufficiency is deemed the most important condition of a good IM because an insufficient IM will leave the EDP response exposed to seismological parameters.

Another desirable property of an IM is for it to be unbiased. Meaning that even if the IM is efficient and sufficient, the structural response should not be impacted by any other unconditioned IM that would otherwise require particular attention during the ground motion selection process.

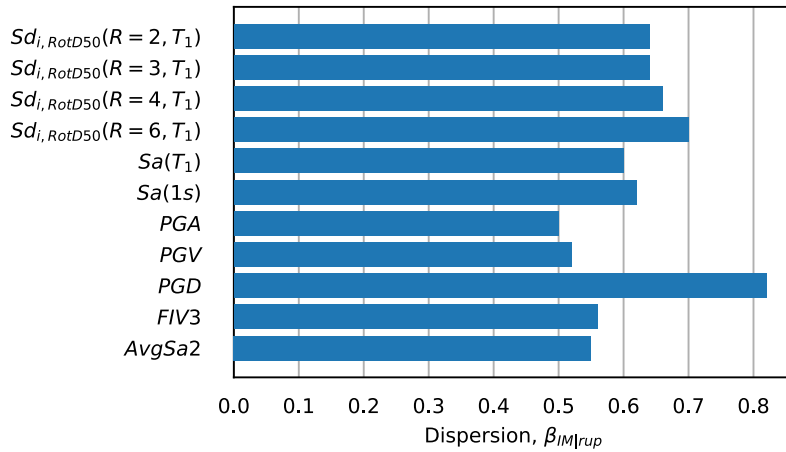


Figure 3.4. GMM dispersions of each IM examined for a given rupture scenario

It is similar to the sufficiency property but with other IMs instead of seismological parameters. However, it is not to say that structural response should be independent of other IMs, as in the case of sufficiency, but rather to say that it would be desirable for the chosen IM for a specific structural typology not to be significantly impacted by other IMs not considered during the ground motion selection process. For example, for the case of non-ductile infilled frames, O'Reilly (2021a) identified that using $Sa(T_1)$ as the IM results in the structural response being notably biased by the velocity-based characteristics of the ground motions used. This would mean that an analyst would need to pay particular attention to these characteristics of the IMs when using $Sa(T_1)$ and ensure that they are indeed representative. However, it was also shown that simply using Sa_{avg} tended to remove this biasing effect, making it a much more attractive IM. The latter situation is a much simpler case to implement in practice.

3.6 Analysis Results

Using the set of 200 ground motion records described in Section 3.4, IDA was performed to quantify the complete response of the bridge structure up to collapse. For computational efficiency, this was done using the hunt

and trace algorithm described in Vamvatsikos and Cornell (2002). The EDP chosen was the pier drift, and the IDA was conducted until a pier drift of 10%. The curves, however, are plotted until 6%, as this was the value at which the pier began to lose lateral strength capacity during the pushover analysis of the pier element, which is depicted in Figure 3.2. The IDA was initially conducted using $Sa(T_1)$ as the IM, as shown in Figure 3.5, and the IDA curves for the other IMs described in Section 3.5 were obtained by simple post-processing of the analysis results to allow for relative comparisons.

Figure 3.5 illustrates an example set of IDA curves for all ground motion records. Also plotted are the median trend of the response along with the 16th and 84th percentiles to graphically illustrate the variability of the structural response. The general trend of the median is a steady increase with intensity before reaching a plateau (i.e. flatline), where the structure is considered to be collapsed. It can be seen that the IM dispersion is relatively low initially and gradually increases. This dispersion is mainly a combined consequence of the record-to-record variability of the ground motions, the IM used, and the multi-modal behaviour of the inelastically responding structure. The response may also be examined in terms of alternative EDPs, for instance, the longitudinal and transversal response at the abutment system. However, these were not considered to be principal elements to examine for the purpose of the present study but whose non-linear response would nonetheless be represented in the numerical model used.

3.6.1 Sufficiency

As previously mentioned in Section 3.5, sufficiency of an IM is a fundamental property to check and verify since it must be independent of the rupture parameters that produced each ground motion and permit widespread application. Here, the sufficiency of the IMs analysed was checked against the M_w , rupture distance, R_{rup} , and level of amplitude scaling applied to the ground motions, SF . To do this, the IM levels required for each ground motion during IDA to induce collapse in the bridge structure were checked. The results of IDA were utilized to characterize the collapse intensity of the selected 200 ground motions (i.e. the red dots in Figure 3.5). The residuals with respect to the logarithmic mean (assuming that the residuals follow a lognormal distribution in the considered range of IMs and EDPs) of

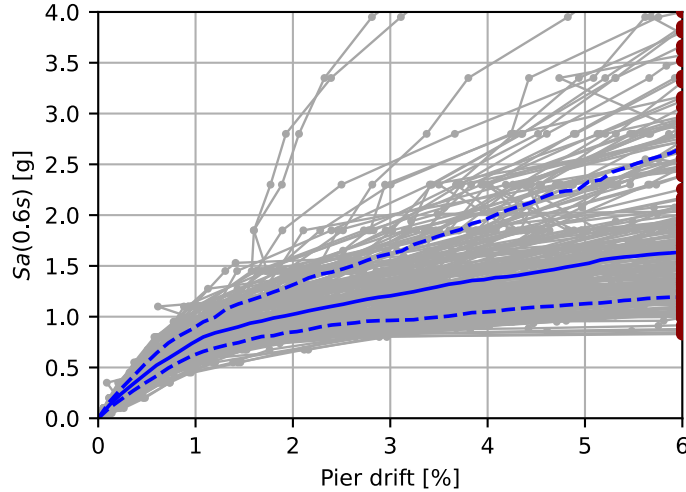


Figure 3.5. IDA curves with median, 16 and 84 percentiles

residuals from all ground motions were examined to determine whether there was any dependency of the collapse intensities, s , on the ground motion rupture parameters. These intensity-based residuals, ε_s , were calculated as per Equation 3.4 for a given ground motion i causing the collapse of the case study structure.

$$\varepsilon_{s,i} = \frac{s_i}{\hat{s}} = \frac{s_i}{\exp\left(\frac{1}{n} \sum_{i=1}^n \ln(s_i)\right)} \quad (3.4)$$

where n is the number of ground motions used in IDA. Note that lower values of ε_s denote more aggressive ground motion records since it means a below-average intensity ground motion was able to induce collapse. The relative trends between the collapse residuals and the ground motion parameters checked were investigated via fitting a log-linear regression trendline to the data, as shown in Equation 3.5. The p values of $\beta_{1,s}$ from that regression were examined.

$$\ln(\varepsilon_s) = \beta_{0,s} + \beta_{1,s} rup \quad (3.5)$$

where $\beta_{0,s}$ and $\beta_{1,s}$ is the y-intercept and slope of the log-linear interpolation, respectively, and rup represents either M_w , R_{rup} , or SF for the scope of this study.

58 While there is no common consensus on the optimal metric of IM sufficiency (Luco and Cornell, 2007), the most widespread is the statistical significance (i.e. p -value) of residuals with respect to the different rupture characteristics. The p -value corresponds to a test hypothesis whose null hypothesis is that the slope is zero, computed using the Wald Test with t -distribution of the test statistic. A low p -value indicates that the data do not conform to what the statistical distribution predicted they should be, which implies that the slope of the regression is probably far from zero and, therefore, there is likely some dependence on the r_{up} parameter under evaluation. Meanwhile, a large p -value would likely indicate that the data are close to the model prediction. That is, there is probably no clear relationship between the residuals and the r_{up} parameter. A significance threshold of 5% is typically adopted in literature and was also used here.

In addition to the common p -value, the simplified relative sufficiency (SRS) evaluation proposed by Dávalos and Miranda (2019) was also used to quantify the sufficiency. The SRS procedure entails a linear regression between the normalized collapse intensities and the ground motion parameter of interest. From that, the slope is computed and used to measure the SRS of each IM by checking how close to zero it is and by comparing it to the slope obtained from the other IMs. Slopes that are zero, or close to zero, indicate that the ground motion parameter being investigated has little to no influence on the structural response. This procedure does not classify an IM as sufficient or insufficient, as it is commonly done using an arbitrary limiting p -value in a null hypothesis test, but rather assesses the sufficiency of an IM relative to the others by using their normalized slopes as a measure of sufficiency.

By adopting these two methods of assessing IM sufficiency, Table 3.3 lists the p -values and the SRS slopes of each IM, with respect to magnitude, rupture distance and scale factor. By visual inspection of Figure 3.6, it can be inferred that almost no IM presents an obvious case of insufficiency with respect to any of the parameters investigated. The only exception is the PGA residuals versus the SF in Figure 3.6c, where the slope is disproportionately higher compared to the other IMs. It was speculated that data with high scale factors may disproportionately influence the calculated slopes and therefore the eventual results. This was checked by eliminating data with scale factors higher than 20 and calculating again the slopes and p -values, where it was found that the ranking of IMs remained the

same. Hence, while it is an important issue to check and scrutinize, it does not impact the conclusions. A clearer comparison can be made from the sufficiency metrics listed in Table 3.3. It can be observed that $Sd_{i,RotD50}$ with $R = 3$ and 4 , $Sa(1s)$ and PGV have p -values above the threshold of 5%, meaning that the observed data pass the test hypothesis prediction and therefore are independent of M_w . The rest of the IMs cannot be deemed independent of M_w from this test. This does not necessarily mean that they are insufficient, but instead that the test cannot provide a decision on whether they are sufficient or not. With respect to R_{rup} , all IMs can be considered statistically independent from it since they all result in p -values greater than 5%. With respect to SF , only $Sd_{i,RotD50}$ with $R = 6$, $Sa(1s)$, PGD and $FIV3$ can be deemed statistically independent. Examining the SRS, however, provides more intuitive guidance on the sufficiency of these IMs. Regarding the second sufficiency metric (i.e. SRS slope), it seems that $Sd_{i,RotD50}$ with $R = 4$, $Sa(1s)$ and $FIV3$ perform the best across all the rup parameters examined. It should be stated that with both methods of assessing IM sufficiency (i.e. p -values and SRS slopes), a major issue is that a poor regression may influence the results. Therefore, a non-regression approach to examine sufficiency such as that utilized by Kazantzi and Vamvatsikos (2015) may be a better alternative.

3.6.2 Efficiency

Considering the IDA response in Figure 3.5 for the case study bridge structure, the efficiency of the IMs was examined. This was done by examining the relative dispersion in the results to evaluate each IM's predictive power. A principal assumption is that the data shown in Figure 3.5 are lognormally distributed and characterized by a median and dispersion value pair, $\{\eta, \beta\}$. For the present study, the dispersion of IM at a given EDP, $\beta_{IM|EDP}$, also known as record-to-record variability, β_{RTR} , was computed for each IM examined over an EDP range, as initially carried out by Vamvatsikos and Cornell (2005). The dispersions for each IM described previously in Section 3.5 were computed and are depicted in Figure 3.7. Also shown is the corresponding pier displacement ductility, μ_Δ , where it can be seen that a ductility well over 8 was obtained before the lateral collapse of the pier element.

Beginning with the spectral acceleration, it can be seen how $Sa(T_1)$ gives

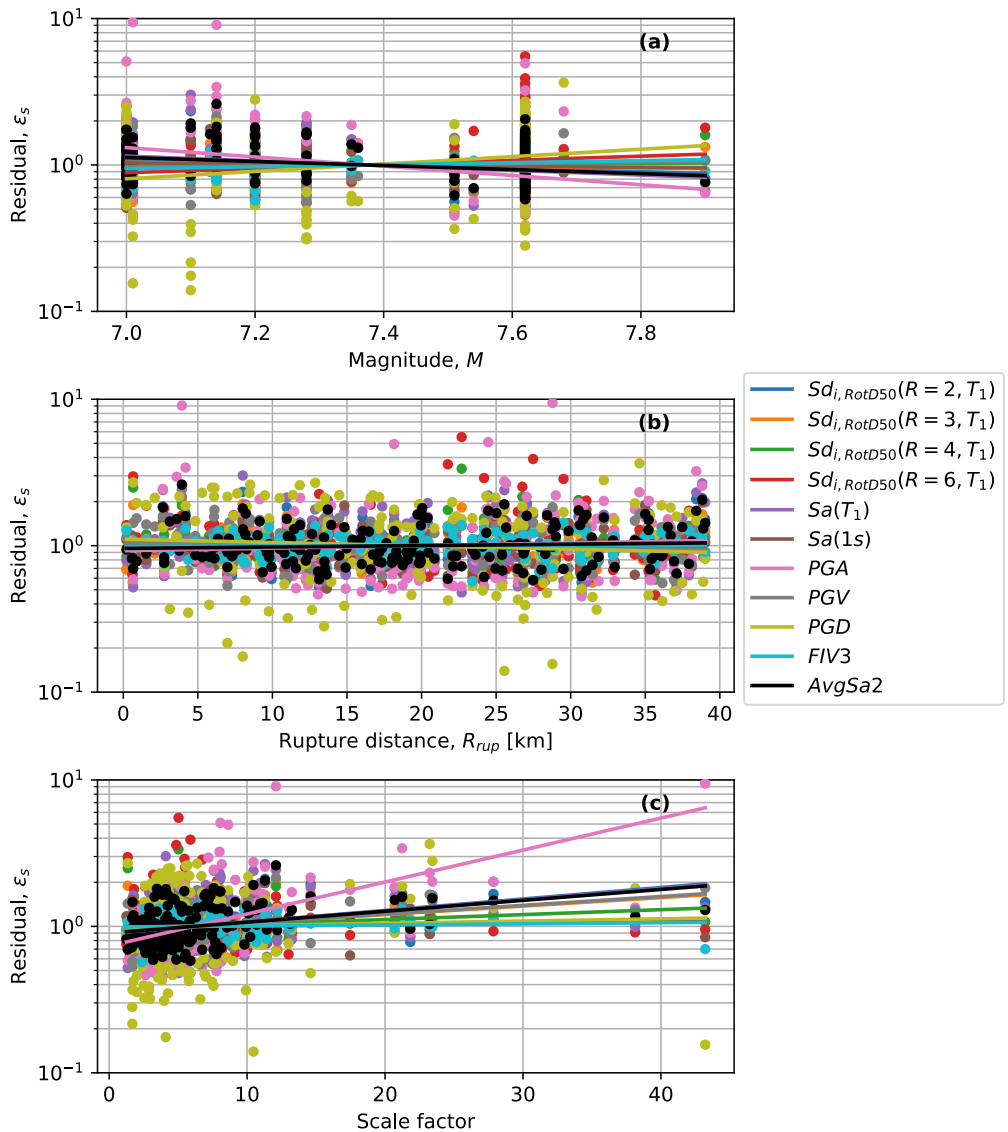


Figure 3.6. Observed trends of IM residuals versus each ground motion parameter investigated. (a) magnitude; (b) rupture distance; (c) scale factor applied during IDA

Table 3.3. p -values and SRS slopes for the IDA residuals for each IM and parameter investigated

Intensity Measure	p -values			SRS slopes		
	M_w	R_{rup}	SF	M_w	R_{rup}	SF
$Sd_{i,RotD50}(R = 2, T_1)$	0.004	0.193	$< 10^{-3}$	-0.248	0.003	0.018
$Sd_{i,RotD50}(R = 3, T_1)$	0.147	0.622	$< 10^{-3}$	-0.111	0.001	0.013
$Sd_{i,RotD50}(R = 4, T_1)$	0.437	0.566	0.031	0.059	-0.001	0.008
$Sd_{i,RotD50}(R = 6, T_1)$	0.001	0.257	0.670	0.324	-0.003	0.002
$Sa(T_1)$	$< 10^{-3}$	0.248	$< 10^{-3}$	-0.365	0.003	0.019
$Sa(1s)$	0.193	0.407	0.355	-0.075	-0.001	0.004
PGA	$< 10^{-3}$	0.250	$< 10^{-3}$	-0.729	0.004	0.050
PGV	0.218	0.117	$< 10^{-3}$	0.096	-0.003	0.014
PGD	$< 10^{-3}$	0.204	0.663	0.581	-0.005	0.004
$FIV3$	$< 10^{-3}$	0.349	0.351	0.161	0.001	0.002
Sa_{avg2}	$< 10^{-3}$	0.264	$< 10^{-3}$	-0.318	0.002	0.017

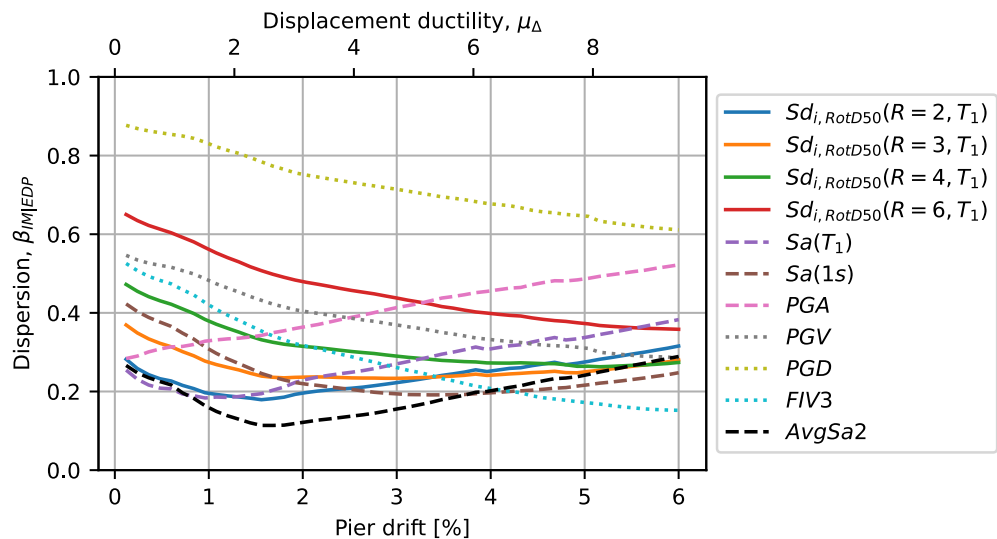


Figure 3.7. Dispersion versus pier drift and displacement ductility for each IM investigated

relatively low dispersion in the elastic range (i.e. $\mu_\Delta < 1$) and close to it, but the dispersion increases significantly as the structure goes well into the non-linear range of response. This is an expected result for any structure since past studies (Shome et al., 1998; Haselton and Baker, 2006; Bradley et al., 2009; Lin et al., 2013b) have shown that $Sa(T_1)$ is well correlated with deformation-based EDPs for first-mode-dominant structures. $Sa(1s)$ presents poor efficiency in the initial elastic and inelastic stages but gets progressively better with displacement ductility and is classified as the second most efficient IM in the collapse limit. PGD exhibits the highest $\beta_{IM|EDP}$ throughout the whole range of structural response, whereas PGA is also seen to increase progressively, making them the worst performers among all IMs.

Meanwhile, in the region with a highly inelastic response and near the collapse limit it is the $FIV3$ which performs the best. This result supports the findings of the original study that proposed this IM (Dávalos and Miranda, 2019). Specifically, this IM has demonstrated the highest efficiency in predicting the seismic collapse intensities of the structure, as evidenced by the smallest record-to-record variability. This effect of $FIV3$ is because, unlike other IMs based on the peak response of one or more linear elastic oscillators, it is defined based on features of severe long-duration acceleration pulses present in the acceleration time series, which are deemed to be the main drivers of collapse.

Among the novel $Sd_{i,RotD50}$ definitions, the most efficient for pier drifts lower than about 3% is the one with $R = 2$, whereas for drifts higher than 3% $R = 3$ performs better. This is expected, since the force reduction factor of the SDOF, with which $Sd_{i,RotD50}$ was developed, is a proxy of the inelasticity that the system is expected to undergo. Ergo, a higher R corresponds to higher efficiency in the high EDP region.

The dispersion of the three definitions of Sa_{avg} investigated was calculated and plotted in Figure 3.8 for the whole range of non-linear responses. The lower bound of the period range was kept the same since it was seen that the dispersion was already low enough for low EDP values. It can be seen that Sa_{avg1} performs the best for pier drifts until about 1.3%, then for drifts of 1.3–2.3%, the Sa_{avg2} is the most efficient and from there until 6% drift the Sa_{avg3} has the best performance. This is expected since the upper bound of the period range accounts for the effects of period elongation during non-linear response. Therefore, the structural response deep into the

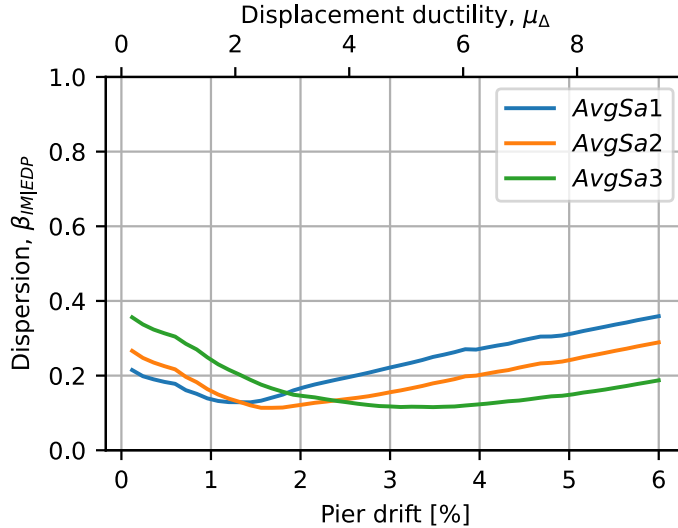


Figure 3.8. Marginal dispersion of Sa_{avg} with different period ranges

non-linear range is better explained using a higher T_{upper} . Taking Sa_{avg2} to be the best overall performer for the case study presented here, it can be seen from Figure 3.7 that it is the most efficient IM in the initial elastic region and, most evidently, in the intermediate inelastic region.

From these observations, it is clear that the choice of IM depends on which part of the structural response is of interest, as no single IM produces the overall best efficiency. For example, if an inefficient IM, such as PGD , PGA , or $Sa(T_1)$, is chosen to estimate the IM at the collapse limit state, it will result in high dispersion in the results and require many more ground motion records to characterize the collapse fragility sufficiently. However, some of these IMs work better at limit states other than collapse. Importantly for what concerns the main aim of this study is that the inelastic spectral displacement definitions of IM have shown promising performance as IMs, with comparable, if not better, efficiency with respect to other notable IMs currently in use. The recent development of the relevant GMM and its implementation into hazard analysis tools, namely OpenQuake, means that it has also become a practical IM to use.

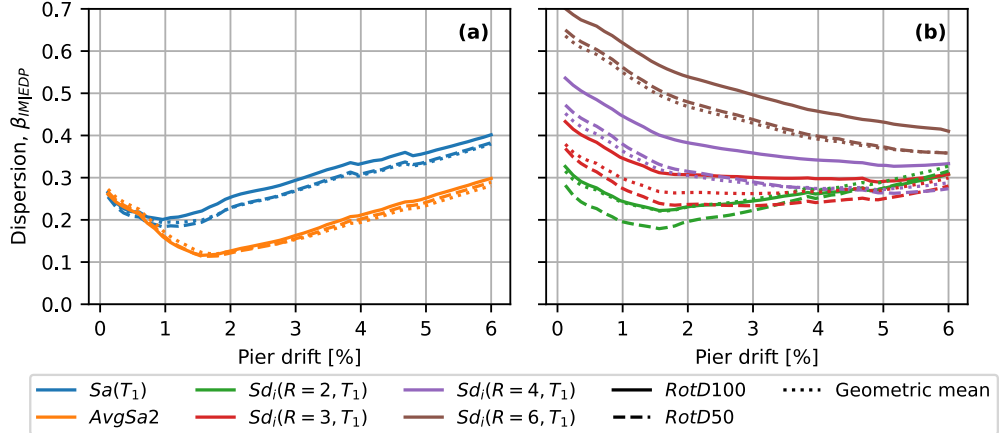


Figure 3.9. Comparison of dispersion for different horizontal component definitions (a) elastic spectral accelerations and (b) inelastic spectral displacements

3.6.2.1 Comparison of Different Horizontal Component Definitions

While the previous section looked at the relative efficiency of the different IMs, this section looks at the impacts the horizontal component definition can have on these results. To do this, the efficiency of three horizontal component definitions of elastic spectral accelerations and inelastic spectral displacements were examined. The results of the relative comparison are shown in Figure 3.9.

It was calculated that the dispersion in the $RotD100$ component definition of the $Sa(T)$ is around 8.1% higher on average than the $RotD50$ component. This is a somewhat expected result when considering the actual definition of these IMs: the $RotD50$ component is the median over all directions; hence, it has a more averaging effect and does not suffer from peaks as much as the $RotD100$ component does, since it takes the maximum over all directions. The same observation is also noted for the Sa_{avg} shown in Figure 3.9(a), but with a less amplified effect as it is only 2.9% higher on average, likely because of the further averaging effect of Sa_{avg} over the predefined period range. The geometric mean definition gives very similar values of dispersion with the $RotD50$ definition for elastic spectral accelerations. Specifically, for pier drift lower than about 2% the geometric

mean gives slightly higher dispersions, whereas for pier drift higher than about 2% it gives slightly lower dispersions. These trends are more apparent in the case of $Sa(T)$ rather than Sa_{avg} .

Regarding the inelastic spectral displacement IMs, Sd_i , the same general trend is observed as in the case of the other IMs, which is conceptually consistent. However, it is worth noting that the ratio of the dispersions between the *RotD100* and *RotD50* definitions is larger, around 17.3% on average. This is because inelastic spectral displacement is used as the IM, where the non-linear cycles produce a maximum displacement that can accumulate more displacement in the non-linear range; hence, the maximum with respect to the median definitions can tend to deviate more, as observed in Figure 3.9(b). From a visual inspection of Figure 3.9(b), this may be the case, but no significant trend is noted, as the average ratios are 10.7%, 23.3%, 22.2% and 13.0% for the $R = 2, 3, 4$ and 6 cases, respectively. Strangely enough, the highest ratios of dispersion are observed for the intermediate R factors, hence there is not an evident trend among the different Sd_i definitions. The geometric mean definition gives generally lower dispersions than *RotD50* for the Sd_i with high inelasticity (i.e. $R = 6$ and 4) and higher dispersions for the Sd_i with lower inelasticity (i.e. $R = 2$ and 3).

3.6.3 Bias Against Directionality

In the previous sections, the focus was solely on the ability of scalar IMs to accurately characterize the non-linear response. Nevertheless, part of that observed record-to-record variability can be explained by separate pertinent but unconditioned ground motion characteristics biasing the response. This hidden bias from different ground motion characteristics (e.g. duration) can introduce a large scatter in the eventual structural response data (e.g. collapse intensities) if not considered properly in the record selection process (Chandramohan et al., 2016). Ground motions selected and scaled to a single conditioning IM, denoted as IM_j here, could depend on, or be biased by another IM, denoted as IM_i . However, this poses no problem if both IM_j and IM_i are consistent with, or match, the site hazard curves obtained from PSHA (Bradley, 2010), which could be cumbersome to take care of in a common performance-based seismic assessment.

In this section, it was investigated whether the ground motion direction-

ality is influencing the sufficiency of the IMs examined here. This was done by checking whether IM_j exhibits any notable statistical dependence on IM_i parameters. The IM_i parameters chosen to represent directionality were the $Sa_{RotD100}/Sa_{RotD50}$ for the elastic case and $Sd_{i,RotD100}/Sd_{i,RotD50}$ for the inelastic case, denoted for brevity as κ and κ_i , respectively. Should a bias be found, it means that the effect of directionality on structural response is not negligible. Due to the format of the analysis (i.e. IDA) the bias was examined upon the collapse cases, where the collapse intensity residuals, ε_s , were used similarly to what was done to check sufficiency in Section 3.6.1. The same functional form of Equation 3.5 was used, but the rup is now replaced by the term $\ln(IM_i)$. For each IM_j , the collapse intensity residuals were computed as previously described in Equation 3.4. The linear trend was fitted using least squares regression. The slopes obtained from each IM_i were graphically examined and compared. The same hypothesis test of $\beta_{1,s} = 0$, which was previously used, can be used again here, to gain some insight on the statistical significance between the collapse intensities and directionality measures. A low p-value (i.e. < 0.05) would suggest that the influence of directionality on collapse capacity is statistically significant. Another relative comparison between the different IMs is simply comparing the slope, $\beta_{1,s}$, of different IM_i and IM_j pairs. These assessment metrics are considered to be theoretically sound, since, in principle, there should not be any notable correlation between $Sa(T_1)$ and κ or κ_i , meaning that a record causing collapse with a certain value of $Sa(T_1)$ does not convey almost any information regarding the directionality of the record.

From Figure 3.10 it can be observed that the collapse residuals of all IM_j are completely independent of κ . However, when the inelastic directionality ratio is used as a metric of ground motion directionality there is an apparent dependency. In other words, ε_s is biased from κ_i , but not from κ , which may be an indicator that the newly proposed directionality measure can be a better proxy to describe the ground motion directionality characteristics rather than the classic elastic κ . There is a negative trend slope of residuals of $Sa(T_1)$, Sa_{avg} and PGA with κ_i , while for the Sd_i it gets from negative to positive for $R = 2$ to $R = 6$, respectively. PGV , PGD and $FIV3$ residuals seem to be unaffected by the degree of inelastic directionality since the slope of their trend lines is close to zero. In order to check for possible issues of linear regression when outliers are present, only κ_i values lower than 2 were kept and the calculations were performed again and shown in Figure 3.11.

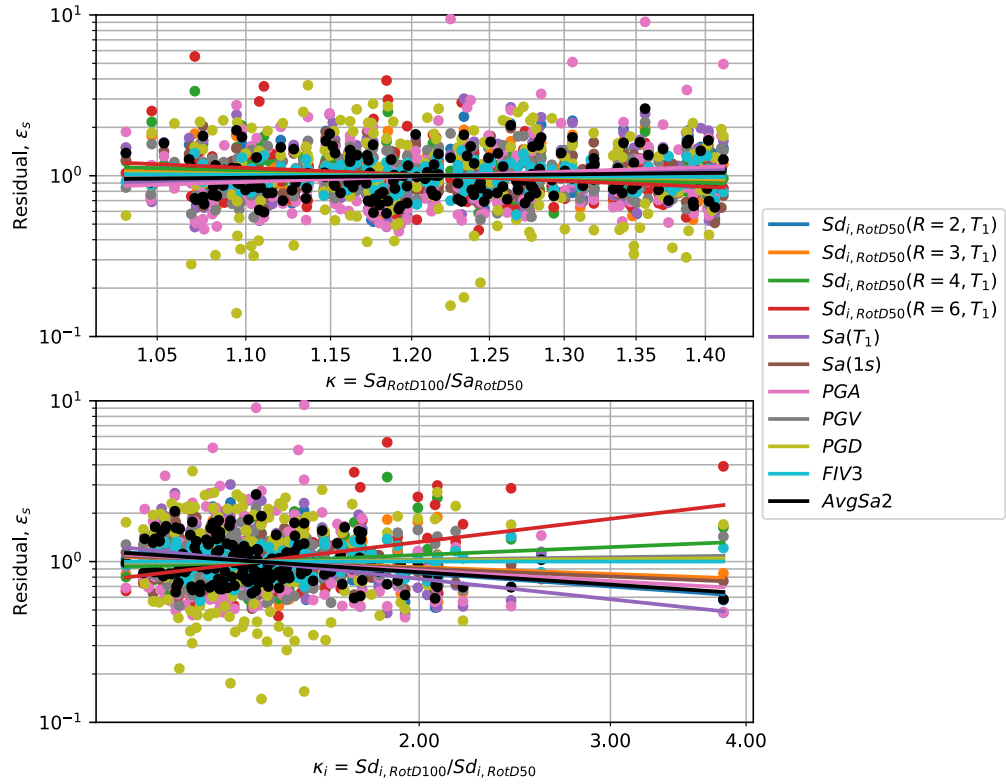


Figure 3.10. Trends of collapse IM residuals versus elastic and inelastic directionality measure. For the $Sd_{i,RotD100}/Sd_{i,RotD50}$, R equal to 3 was used

It can be seen that the relative slopes between the IMs stay about the same, but the absolute slopes become lower and therefore less significant. This suggests that the outliers (i.e. ground motions with high inelastic directionality) are influencing the degree of bias seen in Figure 3.10.

Figure 3.12 confirms that $Sa(T_1)$ collapse intensities are not influenced by κ , where the p -value of 7.4% suggests statistical insignificance (i.e. $> 5\%$) and the low R^2 (0.02) indicates that the collapse intensities cannot be explained from κ . The R^2 statistic is a measure of the capability of $\ln(IM_i)$ to predict the $\ln(IM_j|collapse)$. Meanwhile, collapse intensities are plotted against the κ_i with different R ratios in Figure 3.13. It can be visually observed that the $Sa(T_1)$ are somewhat biased by κ_i , which is also indicated by the slope of the trendline, the low p -values ($< 5\%$) and higher

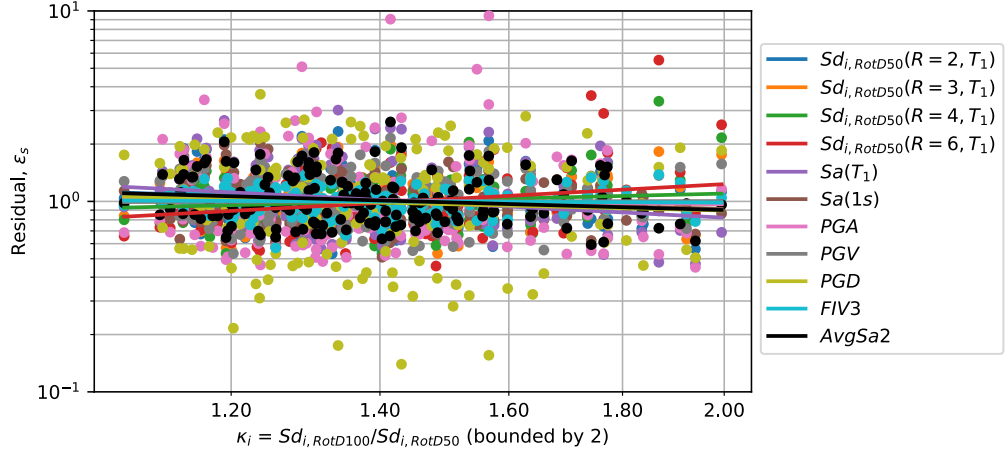


Figure 3.11. Trends of collapse IM residuals versus the inelastic directionality measure, $Sd_{i,RotD100}/Sd_{i,RotD50}$, with R equal to 3. Only values of κ_i below 2 are kept

R^2 values. Comparing the κ_i with different R ratios, the steepest slope is found for $R = 2$, and the lowest for $R = 4$. It can be concluded from the negative trendline slope that, on average, the higher the κ_i , the lower the expected collapse capacity the structure would be expected to exhibit. All in all, this means that this IM_i is a good secondary predictor of the intensity of ground motions, independently of elastic spectral values. Lastly, to check the degree to which the outliers are influencing the regression and consequently the bias results, κ_i values up to 2 were considered. In that evaluation, the slope ranking did not significantly change, the p -values were ranging from 0.0395 to $3.36 \cdot 10^{-5}$, and the R^2 from 0.02 to 0.09. Ultimately, it was decided that the outliers do not significantly affect the bias results and, therefore, only the complete set of data is presented here.

3.7 Summary and Conclusions

In this chapter the use of inelastic spectral displacements, Sd_i , as an IM for the seismic assessment of bridge structures was investigated. A typical reinforced concrete highway bridge in California was employed for the case study comparisons and its dynamic response up to collapse was

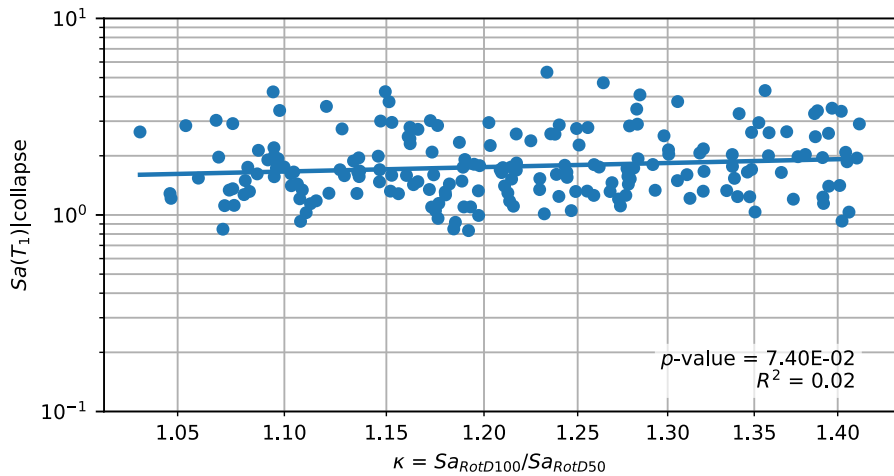


Figure 3.12. Collapse $Sa(T_1)$ intensities versus the elastic directionality measure, κ , along with the fitted linear trend line

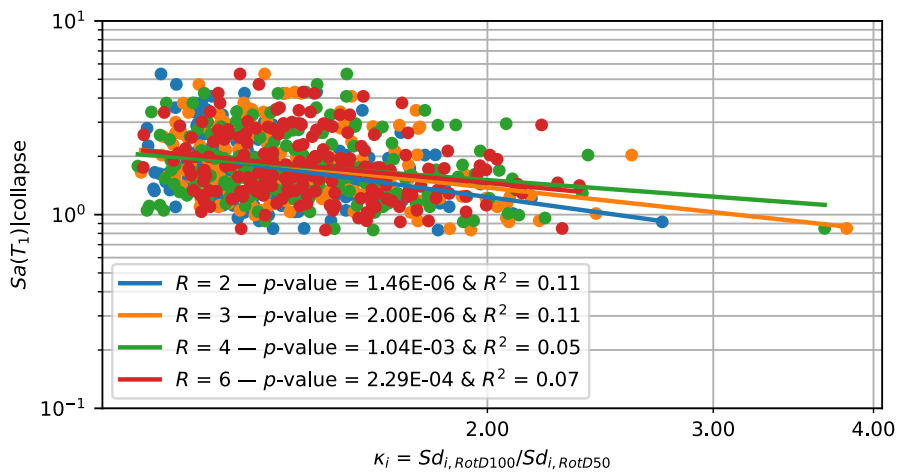


Figure 3.13. Collapse $Sa(T_1)$ intensities versus the inelastic directionality measure, κ_i , with different R ratios

characterized by the ground shaking intensity. A number of traditional and modern IMs were examined and compared on the basis of their efficiency and sufficiency. Based on the outcomes of this study, the following conclusions can be summed up:

- The novel IM $Sd_{i,RotD50}$ performed relatively well in predicting the EDP, both under efficiency and sufficiency checks. An interesting and expected result is that the efficiency of Sd_i with R factors varies with the level of inelasticity. Specifically, for low R factors, the lowest dispersions are found in the elastic or early inelastic ranges, whereas for the higher R factors, the lowest dispersion are found deeper into the inelastic range or near the collapse limit;
- For the widest range of structural response, it was the Sa_{avg2} that was the most efficient (i.e. displayed the lowest dispersion). The period range used to define Sa_{avg} can have a significant impact. It depends on which level of inelastic response the best control over is required for;
- Regarding the sufficiency of IMs checked on the collapse limit, it was found that $Sd_{i,RotD50}(R = 4, T_1)$ and $FIV3$ were the most sufficient of the IMs examined. This is concluded by taking into account all the comparative metrics of sufficiency employed herein;
- The $RotD100$ component falls short in its predictive power of the resultant pier drift response compared to the $RotD50$ component. This is the case for both elastic and inelastic spectral values, with the effect on inelastic spectral values being more amplified;
- An apparent bias of collapse $Sa(T_1)$ intensities was observed against the inelastic directionality measure, but not against the elastic one. The results indicate that the inelastic directionality measure, recently developed as part of this thesis, is a more comprehensive way to quantify the ground motion directionality, rather than the elastic one.

Chapter 4

Artificial neural network-based ground motion model for next-generation seismic intensity measures

This chapter is extensively based on the following publication:

Aristeidou, S., Shahnazaryan, D., & O'Reilly, G. J. (2024). Artificial neural network-based ground motion model for next-generation seismic intensity measures. *Soil Dynamics and Earthquake Engineering*, 184, 108851. <https://doi.org/10.1016/j.soildyn.2024.108851>

4.1 Introduction

GMMs are an essential part of seismic hazard analyses and form the basis for seismic risk assessments, shake maps, loss estimation, seismic design of structures, and more, which comprise both fields of earthquake engineering and seismology. GMMs estimate the distribution of expected ground motion intensity and its associated uncertainty, given a set of causal parameters (e.g., magnitude, source-to-site distance, etc.) at a given site location. Many different IMs can be used to characterise the ground motion shaking intensity at the site of interest. For example, several past studies (Jalayer et al., 2012; Kohrangi et al., 2016; O'Reilly, 2021a, 2021b; Otárola, Gentile, et al., 2023) have examined IMs for different structural typologies to identify the benefits and drawbacks of each in various contexts. There is also a growing interest in using cumulative intensity-based IMs (e.g.,

significant duration) together with peak response amplitude-based IMs (e.g., spectral acceleration), which has sparked the development of a plethora of GMMs to estimate different types of IMs over the years (Douglas, 2022). However, these GMMs (e.g., Bradley, 2011b; Afshari and Stewart, 2016; Campbell and Bozorgnia, 2019; Zafarani and Soghrat, 2023) predict the IMs independently, with each available GMM being based on a different ground motion database (or at least applying different filtering criteria) and different regression models for the fit. This leads to some degree of heterogeneity, which can be mitigated by developing a GGMM to estimate different types of IMs collectively (Fayaz et al., 2021). Using independent GMMs to estimate assorted ground motion IMs for the same earthquake scenario can possibly introduce unwanted bias, since they use different regression datasets, which is then propagated into the seismic analysis and risk assessment results. It is important to note that more consistent correlation models can be produced for the set of output IMs since they are estimated using the same GGMM and, therefore, the same filtered ground motion database, which mitigates these aforementioned potential issues.

GMMs can be divided into two types: parametric and non-parametric. Traditionally, parametric models are employed, where fixed functional forms are used to fit a set of coefficients based on empirical data (e.g., Campbell and Bozorgnia, 2008, 2014; Afshari and Stewart, 2016; Dávalos et al., 2020; Dávalos and Miranda, 2021). These predefined functional forms are derived by observing the ground motion characteristics, like amplification, attenuation and faulting mechanism, leading to increasingly complex functional forms when more effects are considered. Furthermore, these functional forms also differ depending on the IM being estimated, meaning that specific functional forms work better for specific IMs (Baker et al., 2021; section 4.4). Another potential drawback of parametric models is that overly simplistic functional forms may possess limited capability to accurately estimate complex ground motion characteristics. Nonetheless, it should also be stated that parametric GMMs have the advantage of allowing the analyst to maintain some control over the analytical functional forms adopted to ensure that their trends are indeed reflective of the actual physics of the seismological phenomena, as we currently understand them. This is especially helpful where only limited data are available, however with the enriched NGA-West2 dataset researchers can easily opt for machine-learning algorithms.

Meanwhile, researchers have recently been exploring the potential of non-parametric models, where data-driven regression techniques are employed to develop GMMs (Dhanya and Raghukanth, 2018; Fayaz et al., 2021). They have the advantage of not requiring any predefined analytical equations as input. This stemmed from recent applications of advanced non-parametric models, such as machine learning algorithms, artificial neural network (ANN), fuzzy logic, etc., in the field of earthquake engineering. There are many alternative machine learning algorithms that were applied in ground motion modelling through the years, such as Support Vector Machine, genetic programming, Gene expression Programming, ensemble decision tree models (e.g., random forest), and sometimes even combination of different machine learning algorithms. For the development of this model, the ANN algorithm was preferred over the aforementioned methods, since the modeller has more control over the model, by tuning the model parameters and structure. The more recent extreme gradient boosting (XGBoost) algorithm (Chen and Guestrin, 2016) was also tried, but dropped primarily due to the difficulty in adjusting the algorithm to prevent overfitting for this kind of problem, and the difficulty to understand and interpret (Bakouregui et al., 2021). The overfitting problem was subtle during the fixed-effects procedure, but it was very amplified in the mixed-effects. Additionally, the eventual ANN model (see Section 4.8) is much easier and faster to load and use.

The reasons for opting for machine learning algorithms in developing this generalised model were threefold. First, to include all the IMs in a single model using the same fixed- and mixed-effects regression framework and a consistent subset of the database. Second, to enhance the model's predictive capacity and adaptability when incorporating different IMs with different horizontal component definitions. Third, to eliminate the need for predefined functional forms—particularly for next-generation and less common IMs, for which existing GMMs in the literature are scarce. It is acknowledged, however, that relying purely on data-driven approaches is not a perfect solution, as these models work well only where data are available. In ground motion modelling for engineering use, we are typically interested in strong shaking that can potentially cause damage to engineered structures, which requires data from less frequent large-magnitude earthquakes. Hence, there is a danger that inaccuracies may arise when using these data-driven GMMs to predict intensities from scarce

seismological parameters, or even beyond the calibrated range. It is here that robust verification is needed, and, in some cases, the physical meaning of the parametric functional forms may be advantageous because of their transparency, ease of use, and interpretability.

ANNs are generally considered semi-parametric models, because they combine aspects of both parametric and non-parametric models. The parametric aspect is that they have a fixed set of parameters (weights and biases) determined by the network architecture. The non-parametric aspect is that they are highly flexible and capable of approximating complex, non-linear functions. For the case of this study, the ANN is labelled as non-parametric since the parameters were chosen through hyperparameter tuning methods, and they were not fixed. However, it should still be noted that it is still not a non-parametric model in the strictest sense. Derras et al. (2014) used ANN to develop a GMM for Europe, in which a local search algorithm named the quasi-Newton back propagation technique was used to calculate the unknown coefficients. In a subsequent study, Derras et al. (2016) used the same technique on recordings from the NGA-West2 database to model the variability with respect to site conditions. However, that model has the pitfall of getting trapped into local minima and also does not account for the fault mechanism, which is known to have a notable effect on ground motion modelling.

Therefore, in this study, a novel GGMM was developed using a robust ANN algorithm that can be used to estimate a wide variety of IMs. Nine input parameters were chosen to be included in this model to capture as many ground motion characteristics as possible to predict many IMs from the same model. Among them, the most popular are M_w , R_{rup} , Joyner-Boore distance, R_{jb} , $V_{s,30}$, and style of faulting, *SOF*. The output variables are a mixture of traditional and next-generation IMs, which will be explained in further detail in subsequent sections. This is one of the main contributions of the proposed model: the ability to estimate next-generation IMs more accurately than the scarcely available and simplistic models in the literature. The results and predictions of the proposed GGMM are then presented and compared against the aforementioned recent and well-established GMMs available in the literature. Additionally, the GGMM was trained for three different horizontal component definitions of spectral acceleration, namely, the geometric mean, *RotD50* and *RotD100* definitions (Boore, 2010). Therefore, the user has the option of choosing their preferred

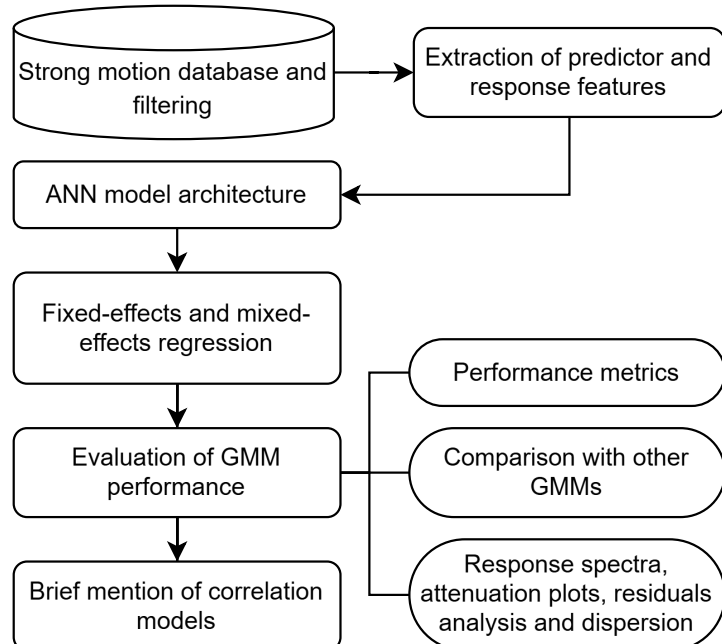


Figure 4.1. Flowchart of this chapter's structure

horizontal component definition or estimating the ratios between them for specific seismic hazard conditions.

The following sections describe the ground motion database utilised and the filtering criteria, the predictor and response features used in the ANN model, the model architecture and methodology employed, followed by an evaluation of the model's performance using different performance metrics, visual representation of the model predictions and spectra, while comparing with other relevant GMMs, and a brief description on the imminent correlation models stemmed from this study. The overall structure of this chapter is illustrated in Figure 4.1.

4.2 Strong motion database and filtering

To utilise ANN to fit a GGMM, a dataset of ground motion recordings was first required. The NGA-West2 database (Ancheta et al., 2013), containing bi-directional ground motion acceleration records with their respective site details, and source information, was adopted. The database was filtered to

remove some of the records that may be deemed unsuitable for general use based on the criteria given below, which indirectly form the recommended usage limitations of the GGMM developed herein:

- Only ground motion records from earthquakes with $M_w \geq 4.5$ were utilised. Earthquakes of lower magnitude were omitted as they were assumed to not be strong enough to induce significant non-linear deformations or structural collapse in engineered buildings without a significant amplitude scaling;
- Recordings with R_{rup} greater than 300 km were discarded. It is worth noting that a few researchers have the source-to-site distance limit to be magnitude-dependent (Zafarani and Soghrat, 2024). This intends to minimise the potential sampling bias, which can occur at large distances and/or low magnitudes, where ground motions are generally weak, and instruments may only be triggered by stronger-than-average ground motions. However, this bias is considered to be insignificant and therefore, no further actions were taken in this regard;
- Recordings from instruments located on the free field, below the surface, or in the first storey of low-rise structures (fewer than four storeys) were utilised. This was based on the Geomatrix 1st letter code of the NGA-West2 flat-file;
- Events with a hypocentral depth greater than 20 km were discarded;
- Events recorded on sites with $V_{s,30}$ higher than 1300 m/s were discarded;
- Recordings from all event mechanisms (i.e., strike-slip, normal, reverse, reverse-oblique, and normal-oblique) from active shallow crustal tectonic environments were included;
- Only records whose minimum useable frequency of both components was less than 0.25 Hz were considered;
- Earthquakes with $M_w < 5.5$ and fewer than five recordings were discarded. Earthquakes with $5.5 \leq M_w < 6.5$ and fewer than three recordings were discarded. This was because those earthquakes could

be considered to have insufficient number of recordings, and therefore unreliably recorded;

- Recordings were considered only if both horizontal components were available. This was necessary to characterise the different horizontal components of shaking;
- Recordings from aftershocks were excluded since most seismic hazard analyses are performed based on the (Poissonian) recurrence of mainshocks. Therefore, including aftershocks in the regression dataset of the GGMM could introduce an unwanted bias. In this study, a recording is classified as an aftershock if it is defined as a “Class 2” event with centroid Joyner-Boore distance, $CR_{JB} < 10$ km according to the criteria given in Woodell and Abrahamson (2014), although other classification criteria could have been used.

Based on the above filtering criteria, the final ground motion database included 4135 recordings from 102 earthquakes. The earthquakes were classified into five *SOFs*, including strike-slip (58 earthquakes and 1819 recordings), normal (9 earthquakes and 74 recordings), normal oblique (4 earthquakes and 247 recordings), reverse (21 earthquakes and 1077 recordings) and reverse oblique (10 earthquakes and 918 recordings). Figure 4.2 displays the M_w , R_{rup} and $V_{s,30}$ distributions of the filtered database. Additionally, the depth to shear wave velocity of 2.5 km/s, $Z_{2.5}$, when missing for some ground motion recordings, was estimated following the prediction equations of Kakkamanos et al. (2011).

4.3 Predictor and response features

Before developing and training the ANN model, it is essential to identify the predictor and response features. The informed selection of predictor features is essential to the robustness and accuracy of the subsequent modelling process. Within the scope of GMMs, past research (Cornell C. Allin, 1968; Fayaz et al., 2021; Baker et al., 2021 - Section 4.5) has highlighted the substantial predictive power of magnitude, M , and source-to-site distance, R , for most IMs of engineering interest. In addition, several other causal parameters were included to train the ANN models. The full list of predictor

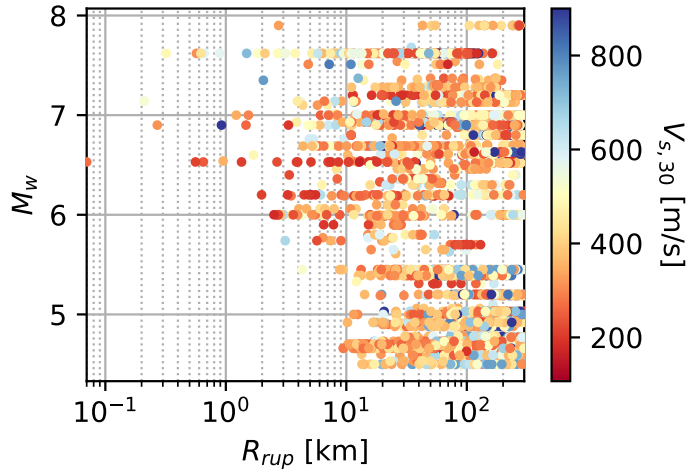


Figure 4.2. M_w , R_{rup} and $V_{s,30}$ distribution of the filtered ground motion database used to fit the GGMM

features within this study are listed in Table 4.1, where the associated response features are PGA , PGV , PGD , Ds_{595} , Ds_{575} , $Sa(T)$, $FIV3(T)$, $Sa_{avg2}(T)$, and $Sa_{avg3}(T)$, which are described in detail below. Users must provide a value for each of the predictor features shown in the first column and can obtain predictions for any of the response features listed just above, essentially making it a generalised GMM due to the variety of IMs that can be predicted. Also, the minimum and maximum values of each parameter in the filtered database are listed in Table 4.1. These values also reflect the recommended usage limits of the model. We note that the GGMM considers multiple depth-related predictor features, which is not necessarily an issue and several models available in the OpenQuake library, for example, follow a similar approach. The inclusion of three different distance metrics may seem peculiar, but it was seen to produce more accurate and reliable predictions, which is in line with the observations of other researchers (e.g., Campbell and Bozorgnia, 2014; Fayaz et al., 2021). It is worth noting that users must also be aware that there may be physical limits to the input predictor features can take with respect to each other (e.g., $V_{s,30}$ and $Z_{2.5}$); hence, care is required when using such models.

Response features, or IMs, include the PGA , PGV , PGD , two definitions of Ds , given by Equation 4.1, 22 definitions of Sa at periods ranging

Table 4.1. List of predictor features required when using the GGMM

Description	Min value	Max value
Moment magnitude, M_w	4.5	7.9
Rupture distance, R_{rup} [km]	0.07	299.59
Hypocentral depth, D_{hyp} [km]	2.3	18.65
Time-averaged shear-wave velocity to 30 m depth, $V_{s,30}$ [m/s]	106.83	1269.78
Style of faulting, SOF^a	0	4
Depth to the 2.5 km/s shear-wave velocity horizon (a.k.a. basin or sediment depth), $Z_{2.5}$ [m]	0	7780
Depth to top of fault rupture, Z_{tor} [km]	0	16.23
Joyner-Boore distance, R_{jb} [km]	0	299.44
Distance measured perpendicular to the fault strike from the surface projection of the up-dip edge of the fault plane, R_x [km]	-297.13	292.39

^a Encoding for the SOF is as follows: 0 for strike-slip, 1 for normal, 2 for reverse, 3 for reverse-oblique, and 4 for normal-oblique.

from 0.01 s to 5.0 s, 14 definitions of two different definitions of average spectral acceleration, $Sa_{\text{avg}2}(T)$ and $Sa_{\text{avg}3}(T)$, at periods ranging from 0.1 s to 4.0 s given by Equation 4.3 (Vamvatsikos and Cornell, 2005; Eads et al., 2015), 14 definitions of $FIV3$, at periods ranging from 0.1 s to 4.0 s given by Equation 3.1 (Dávalos and Miranda, 2019). The equations and definitions of some of the output IMs are given below in this section.

There are many ways to describe the duration of a strong ground motion (Bommer and Martínez-Pereira, 1999); the two most common definitions are bracketed duration and significant duration (Afshari and Stewart, 2016). The scope here is limited to the significant duration since it is often the preferred definition used in the literature (Chandramohan et al., 2016). It is defined as follows:

$$Ds_{xy} = t_y - t_x \quad (4.1)$$

$$x = \frac{100\%}{I_a} \int_0^{t_x} [a(t)]^2 dt \quad (4.2)$$

where t_x and t_y are the time stamps on a Husid plot (Husid, 1969) at which x and y per cent of the total Arias intensity, I_a , occurs (as defined in Equation 4.2 for x and similarly for y). $a(t)$ stands for the acceleration time history. The most common values of x and y adopted in the literature, which are also included in this study, are $\{x, y\} = \{5\%, 75\%\}$ and $\{x, y\} = \{5\%, 95\%\}$, subsequently referred to as D_{S575} and D_{S595} , respectively.

Average spectral acceleration, $Sa_{avg}(T)$, has been shown in the literature to be a better overall predictor of structural response, than the classic IM of $Sa(T)$ for the majority of structural typologies (Kazantzi and Vamvatsikos, 2015; O'Reilly, 2021a, 2021b). It can be easily calculated from the geometric mean, which is the log-average, of a range of $Sa(T)$ values as follows:

$$Sa_{avg}(T) = \left(\prod_{i=1}^N Sa(c_i T) \right)^{1/N} \quad (4.3)$$

where $Sa(c_i T)$ corresponds to the 5%-damped pseudo-spectral acceleration value, c_i is a factor ranging uniformly, $N = 10$ times, from 0.2 to 2.0 and 0.2 to 3.0 for $Sa_{avg2}(T)$ and $Sa_{avg3}(T)$, respectively. Previous research has shown that this spacing scheme is more efficient than a logarithmic one and that the difference between using 10 or 100 periods is negligible, on average (Eads and Miranda, 2013).

A novel IM, named *FIV3*, proposed by Dávalos and Miranda (2019), has shown promising results regarding its efficiency and sufficiency in characterising the collapse performance of buildings. It is mathematically summarised as previously presented in Equations 3.1 and 3.2. The parameters α and β were chosen to be equal to 0.7 and T , respectively, in the context of this chapter, based on Dávalos et al. (2020)'s findings.

In addition to the IMs themselves, ground motions are usually recorded in three orthogonal directions in space, so combining these recorded directions into a scalar value with a specified horizontal component definition is necessary. Several horizontal component definitions have been used in the literature to quantify the intensity of a ground motion on single-degree-of-freedom systems based on the two orthogonal horizontal components, such as arbitrary component, maximum of the two, average, square-root-of-sum-

of squares, geometric mean, $GM RotI50$, $RotD50$, etc. Most modern GMMs use the $RotD50$ definition (Boore, 2010), as it is considered to be the state-of-the-art horizontal component definition, at least for spectral acceleration IMs, however, also other definitions maybe of interest in a seismic risk analysis. In this model, the $RotD50$, $RotD100$ and geometric mean were adopted for Sa and Sa_{avg} ; only the $RotD50$ was adopted for PGA , PGV , and PGD ; whereas for more advanced IMs (i.e., $FIV3$) and other IMs (i.e., Ds_{575} and Ds_{595}) only the geometric mean definition was adopted.

4.4 Model architecture

4.4.1 Fixed-effects with artificial neural network

A feed-forward ANN was employed to predict the IMs outlined in Section 4.3. ANN is a subset of deep learning composed of artificial neurons interconnecting an input layer, one or more hidden layers, and an output layer (McCulloch and Pitts, 1943). Each neuron performs a simple computation, receiving a signal, applying an activation function, and passing the result through the hidden layers to the output layer, hence the term feed-forward. While the neurons in the hidden layers process the information, the neurons in the input layer transmit the input data, and the neurons in the output layer provide the final outputs, or within the scope of this study, the predictions of IMs of interest. Each connection has an associated synaptic weight representing the strength of the connection. Similarly, network neurons are associated with a bias term, which adjusts the point at which the neuron becomes significantly active or inactive based on the total input received, thus influencing the neuron's overall activation behaviour. The synaptic weights of the connections, along with the neurons' biases, represent the neural network's parameters, which are adjusted during the training process to optimise the network's performance. The synaptic weights are used as the multipliers of the outputs of the previous layer, and the bias is a constant added to the outputs before passing through the activation function. The training is typically done through a technique called back-propagation, which uses a gradient descent optimisation (Kiefer and Wolfowitz, 1952), where the network tries to minimise the difference between its predictions and the actual target values in the training dataset by adjusting its weights and biases. For a detailed description of neural

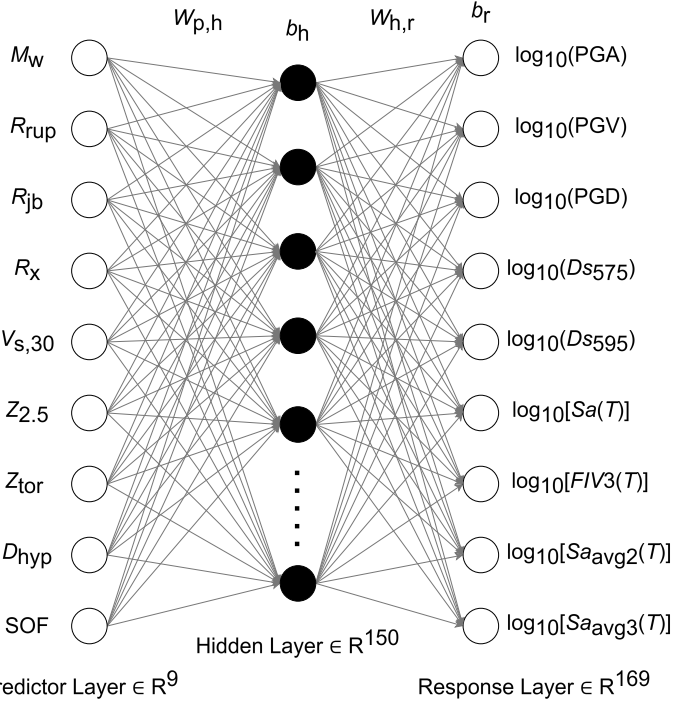


Figure 4.3. Architecture of the ANN ground motion model

networks, readers are referred to Haykin (2009). The schematics of the chosen ANN architecture are shown in Figure 4.3, and the general expression to predict each IM is as per Equation 4.4.

$$\log_{10}(IM_r) = f_{linear} \left[b_r + \sum_{h=1}^{150} W_{h,r} \cdot f_{tanh} \left(b_h + \sum_{p=1}^9 W_{p,h} X_p \right) \right] \quad (4.4)$$

where X_p is the predictor feature p (Table 4.1), $W_{p,h}$ is the weight of the connection between predictor neuron, p , and hidden neuron, h , b_h is the bias of the hidden neuron, h , $W_{h,r}$ is the weight of the connection between hidden neuron, h , and response neuron, r , b_r is the bias of the response neuron, r (from 1 to 169), f_{tanh} and f_{linear} are the activation functions of the hidden and response layers, respectively. It should be noted here that the standard deviation term is not shown in Equation 4.4, since the focus here is the fixed-effects regression model. The treatment of dispersion is covered in Section 4.4.2.

The ANN training was performed in Python, using the open-source TensorFlow library (Abadi et al., 2015). The step-by-step implementation, including dataset processing, training of ANNs, and generation of predictions, is outlined here. Dataset feature processing and selection of ANN parameters and functions are described as follows:

- **Predictor feature engineering:** *MinMax* normalisation is adopted to ensure that predictor features are on a similar scale and, hence, have a comparable influence on the model's learning process (e.g., magnitude ranges between $M_w = 4.5 - 8$, but soil properties can vary between $V_{s,30} = 200 - 1200$ m/s). This can improve the convergence of the training process and make it less sensitive to the scale of predictor features. Additionally, the initialisation of weights can be more effective, which will facilitate faster convergence and prevent gradients' vanishing or exploding issues. The scaling was done using a range of - 3 to 3 instead of 0 and 1, as this range was found to increase the predictive power of this specific model architecture. For what regards *SOF*, one-hot encoding was applied. A lognormal transformation of the predictor features was also tried, but it was seen through manual cross checking with the results of the model that the *MinMax* normalisation worked better;
- **Response (IM) feature engineering:** Similar to predictor features, the response features are scaled to span similar ranges. A \log_{10} transformation was applied to the vector of IMs, as it is sometimes adopted in GMMs in the literature, instead of the natural logarithm (e.g., Bindi et al., 2011; Dhanya and Raghukanth, 2018; Kalakonas and Silva, 2022; Zafarani and Soghrat, 2024). The \log_{10} transformation limits the response parameter range more than a natural logarithm transformation, and therefore, a more robust fit could be achieved (i.e., better performance metrics);
- **Number of hidden layers and neurons:** A single hidden layer was employed following a trial-and-error approach, demonstrating that using just one hidden layer was adequate for making predictions. The input layer consisted of 9 neurons, matching the number of predictor features, while the output layer consisted of 169 neurons, corresponding to the number of considered IMs. Concerning the

number of neurons in the hidden layer, 150 neurons were chosen, as it produced the model’s optimal predictive performance (considering the chosen performance metrics and eventual model dispersion described later). It was observed that using fewer or more neurons led to either underfitting or overfitting, respectively;

- **Activation functions:** Calculates the output of a neuron. Given the nature of this regression problem, *softmax*, *tanh*, and *linear* activation functions were considered in the input, hidden and output layers, respectively, based on the hyperparameter tuning described later. The *tanh* proved to work better with the range of predictor features, given the *MinMax* normalisation together with passing through the *softmax* activation function. Furthermore, *tanh* in the hidden layer introduces the necessary non-linearity, which enables the network to learn complex patterns from the data. Additionally, *linear* activation function was used for the output layer as it prevents the output values from having an upper or lower limit and can also output negative values to take care of the contradicting effects of some predictor features on different response features;
- **Optimisation algorithm and loss function:** The loss function employed for optimisation was the mean squared error (MSE) given by Equation 4.5, and its minimisation was accomplished through the use of the adaptive moment (ADAM) optimisation algorithm (Kingma and Ba, 2014). Additionally, the R^2 , given by Equation 4.6, was used to determine how well the variation of response features is explained by predictor features in a regression model, where y_i is the i -th observed value, \hat{y}_i is the i -th predicted value, and \bar{y} is the mean value of n data points;
- **Training and testing sets:** Before model training, the filtered dataset from Section 4.2 was randomly split into training and testing sets using an 80:20 ratio.

$$MSE = \frac{1}{n} \sum_{i=1}^n (y_i - \hat{y}_i)^2 \quad (4.5)$$

$$R^2 = 1 - \frac{\sum_{i=1}^n (y_i - \hat{y}_i)^2}{\sum_{i=1}^n (y_i - \bar{y})^2} \quad (4.6)$$

The next step of the implementation involves training the ANN. To assess the model's performance, a five-fold cross-validation (Picard and Cook, 1984) was employed. The training set was randomly partitioned into five equal-sized sets. Five separate ANNs were trained, each using four of the subsets for training and the remaining fifth subset for model prediction validation. The procedure ensures that each subset takes on the role of the validation set for its respective training. The fixed-effect regression metrics for cross-validation were computed as the average of the results from five ANNs. Furthermore, Bayesian optimisation (Močkus, 1975) was employed to determine the optimal hyperparameters for the ANN regression model. The objective within the context of this study was to minimise the MSE of the fixed-effects regression by exploring a range of hyperparameters. A summary of the hyperparameters considered is provided below:

- **Batch size from 8 to 128:** helps balance computational efficiency and model performance. With smaller batch sizes, better model generalisation can be achieved. However, it can be computationally insufficient, as more updates are needed to process the entire dataset. In contrast, larger batch sizes accelerate the training but can hinder model generalisation. Hence, the model is more prone to overfitting;
- **Training epochs from 50 to 200:** during each epoch, the model passes through all training samples and updates its parameters (weights and biases) based on the loss incurred when making predictions. The updates try to minimise the error and improve the model's performance. While the optimal number of training epochs can improve the model's ability to generalise, with the increasing number of epochs, overfitting may incur. Therefore, early stopping was implemented as a preventive measure against overfitting, which automatically halts training if the model stops improving for 20 consecutive epochs;
- **Optimisation algorithm:** The following optimisation algorithms were considered: ADAM; root mean square propagation (RMSprop);

stochastic gradient descent (SGD); adaptive gradient descent (Adagrad); adaptive learning rate (Adadelta); a variation of ADAM (Adamax); a combination of Nesterov accelerated gradient and ADAM (Nadam); follow the regularised leader (Ftrl);

- **The learning rate of the optimisation algorithm from 0.5×10^{-3} to 0.05:** controls the step size during weight updates and influences the convergence speed and stability of the model;
- **The activation function of hidden layer:** The following activation functions were considered: linear; rectified linear unit (ReLU); leaky ReLU; exponential linear unit (ELU); scaled ELU; *softmax*; hyperbolic tangent (*tanh*).

The approach was utilised to comprehensively evaluate the model's performance while mitigating the potential risks associated with overfitting (high variance) and underfitting (high bias). The hyperparameters that yielded the best model performance are as follows: *tanh* and *linear* activation functions for the hidden and response layers, respectively; learning rate of 1.04×10^{-3} ; a batch size of 32; and 100 training epochs.

4.4.2 Mixed-effects regression

The functional form of the GGMM is given as:

$$\log_{10}(IM_i) = f_i(\mathbf{X}, \boldsymbol{\theta}) + \delta b_i \tau_i + \delta w_i \varphi_i \quad (4.7)$$

where $\log_{10}(IM_i)$ is the logarithm with base 10 of the i-th IM; $f_i(\mathbf{X}, \boldsymbol{\theta}) = \mu_{\log_{10} IM_i | \mathbf{X}, \boldsymbol{\theta}}$ is the predicted mean output from the ANN model, taking as input a set of causal features (e.g., M_w , R_{rup} , etc.), denoted as \mathbf{X} ; $\boldsymbol{\theta}$ are the 'calibrated coefficients' of the ANN model (i.e., synaptic weights and biases); δb_i and δw_i are the normalised inter- and intra-event (or between- and within-event) residuals of IM_i , respectively; τ_i and φ_i are the inter- and intra-event logarithmic standard deviations. Note that herein, the normalised residuals are denoted with lowercase letters (i.e., δb_i and δw_i) and the residuals before normalisation with uppercase letters (i.e., δB_i and δW_i). The main metric to evaluate the model's performance is the total standard deviation, σ . Most recent GMMs have the inter- and intra-event standard deviation models, or just the inter-event standard deviation

models, to be magnitude-dependent (Kotha et al., 2020; Boore et al., 2021). However, for the sake of simplicity and to not over-complicate this study, the dispersion model was assumed to be magnitude-independent since also a few other studies noticed only minor dependencies on M_w and only for $M_w < 5.5$ (Boore et al., 2014; Campbell and Bozorgnia, 2014). To calculate σ , one must first segregate the total residuals between inter- and intra-event residuals, which can be treated as normal variables that ideally should follow a normal distribution with zero mean and standard deviations τ and φ , respectively (Atik et al., 2010). If the inter- and intra-event residuals are assumed to be mutually independent, then the total standard deviation can be calculated as the square root sum of their variances, as given in Equation 4.8.

$$\sigma = \sqrt{\tau^2 + \varphi^2} \quad (4.8)$$

Taking advantage of this assumption and a better understanding of these two different sources of uncertainty, Abrahamson and Youngs (1992) proposed a one-step mixed-effect regression algorithm, using the maximum likelihood approach, to compute the variances τ^2 and φ^2 . This algorithm is an iterative procedure in which mixed-effects, variances, and model parameters are computed successively. This procedure is now widely applied for the development of GMMs and is hence adopted for the ANN model development here. The adopted algorithm is based on the procedure proposed by Abrahamson and Youngs (1992), which is similar to the one used in Derras et al. (2014), and can be summarised as follows:

1. Estimate the initial set of ANN model parameters (i.e. $[W]$ and $\{b\}$ in Equation 4.4), using a fixed-effect training procedure.
2. Estimate τ^2 and φ^2 from $[W]$ and $\{b\}$, by maximising the log-likelihood function as given in Abrahamson and Youngs (1992), and specifically their Equation 7.
3. Given $[W]$, $\{b\}$, τ^2 and φ^2 , estimate the random inter-event residuals, δB , as given in Abrahamson and Youngs (1992), and specifically their Equation 10.
4. Estimate the new $[W]$ and $\{b\}$ using a fixed-effects training procedure for $(\log_{10} IM - \delta B)$.

5. Repeat steps 2, 3, and 4 until the termination criterion is satisfied. The adopted termination criterion was 0.15 % in terms of the difference between two successive likelihood values.

4.5 Model performance

4.5.1 Performance metrics

The performance of the ANN model can be evaluated by comparing the empirical (i.e., recorded) values of IMs with their corresponding model estimations using various metrics. In this study, two of the most common ones (i.e., MSE and R^2) are reported, as described in Equations 4.5 and 4.6, while acknowledging that there exist several other metrics in the literature (e.g., ANOVA, LLH, and Akaike information criterion) to test and evaluate a GMM's performance. The resulting average MSE of the (fixed-effects) model, determined through five-fold cross-validation with the optimal parameters, obtained as described in Section 4.4.1, was found to be 0.080 for the training set and 0.079 for the validation set, showing an overall very low value, with the validation set giving a slightly higher value, as anticipated. Finally, the model corresponding to the optimal parameters, after passing through the mixed-effects regression, was evaluated using the 20 % unseen testing set, and the regression metrics MSE and R^2 associated with each IM are reported in Figure 4.4. The eventual average MSE of all IMs were 0.078 for the training set and 0.079 for the test set, again exhibiting high accuracy. It is noteworthy that the average training and validation set MSE after cross-validation with the optimal parameters have very close values to the average training and validation set MSE after passing through the mixed-effects regression, respectively, further validating the model's accuracy. From Figure 4.4, it can be seen that the R^2 of the testing set is at times slightly higher or equal to that of the training set, which can be expected but the overall comparison is nonetheless encouraging. At the same time, both values are not excessively low, indicating that while the model has high predictive power, it also avoids overfitting. In the case of MSE, the testing set presents both lower and higher errors than the training set, depending on the IM. For IMs with relatively high MSE, it is the testing set that is higher than the training set. The inverse happens in the case of IMs with low MSE, but to a lesser extent. Reasons for these

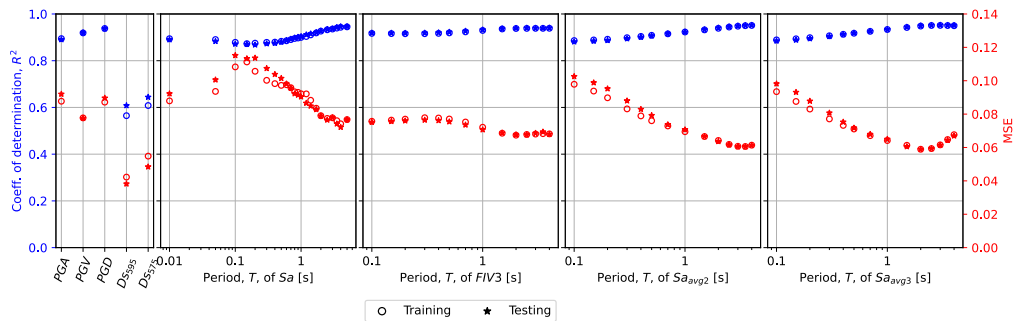


Figure 4.4. Training and testing MSE and R^2 values of the ANN model after the mixed effects regression

latter case may include situations where the training data were harder to predict, or had inherently more dispersion than the testing data. Generally, the MSE values are considered to be low, which is another indicator of the model's predictability, and allows the ANN model's performance to be deemed sufficient for general application.

4.5.2 Comparison with other GMMs

4.5.2.1 Traditional IMs

To evaluate the quality of GGMM's estimations visually with respect to the available data and other comparable GMMs available in the literature, a few graphical representations were plotted and are described below. To do this, different combinations of input causal parameters were used to illustrate relative trends with respect to other causal parameters. Strike-slip rupture style was assumed, and the average of the observed data was taken for the rest of the features needed for this study and the compared models, except for R_{jb} whose value was indirectly calculated from R_{rup} . Figure 4.5 shows the magnitude amplification of $Sa(0.01s)$, $Sa(0.1s)$, $Sa(0.5s)$, and $Sa(1.0s)$ for two different rupture distance bins and are compared with the GMMs of Campbell and Bozorgnia (2014) (CB14), Dhanya and Raghukanth (2018) (DR18), and Fayaz et al. (2021) (FXZ21). The horizontal component definitions for Sa of these models are $RotD50$ for CB14 and FXZ21 and unspecified for DR18. The $RotD50$ definition of the proposed model is used for the comparisons. These models are well-established models based

on either a classical approach to GMM fitting (i.e., CB14) or machine learning-based approaches (i.e., DR18 and FXZ21). These GMMs were selected to provide a relative comparison but of course, many more models could have been chosen here. The comparison was limited to three to avoid overcrowding in the plots that would inhibit the visualisation.

It can be seen that the estimated values of the proposed GGMM are generally close to the cloud mean, with a minor deviation in short distances (i.e., $0 \text{ km} \leq R_{\text{rup}} \leq 50 \text{ km}$) in high magnitudes, which is mainly because of the data sparsity. Also, minor deviation from the empirical data is observed in longer distances (i.e., $50 \text{ km} \leq R_{\text{rup}} \leq 100 \text{ km}$) for moderate magnitudes (i.e., $6 \leq M_w \leq 7$), again due to data sparsity. The differences between the compared models and the proposed model are more pronounced in the Sa values of longer periods. Generally, all of the compared models give values close to each other and to the proposed model, while also keeping the same trends, giving confidence to the proposed model. For the same IM, the distance attenuation for two different magnitude bins is shown in Figure 4.6, along with the comparison of the three previously mentioned models. The FXZ21 model is limited to $R_{\text{rup}} \leq 100 \text{ km}$ (and $R_x \geq 0 \text{ km}$) and is hence not plotted beyond that limit. The estimations of this study capture well the trends of the cloud mean, with the CB14 model also being very close. The other two models are somewhat deviating from the observed mean in some sections of the plot.

It is noted that the mean hypocentral depth of the observed data was used here, which for the two bins of Figure 4.5 were 9.80 and 9.83 km, respectively, and for the two bins of the Figure 4.6 were 10.10 and 8.13 km, respectively.

In Figure 4.7, the distance attenuation of Ds_{595} is illustrated. While amplitude-based quantities decrease with source-to-site distance, the significant duration of ground motion increases due to different waves (e.g., P-, S-, and surface waves) travelling at different velocities and the effect of scattering of those. The estimations of the proposed model are compared with Afshari and Stewart (2016) (AS16) and FXZ21 models. For Ds_{595} , both of these models and the proposed model estimate the geometric mean from the two as-recorded horizontal components. While the trends between the proposed model and AS16 are similar, the AS16 model predicts somewhat lower values of significant duration than the proposed model. This difference is thought to be because of the different database filtering

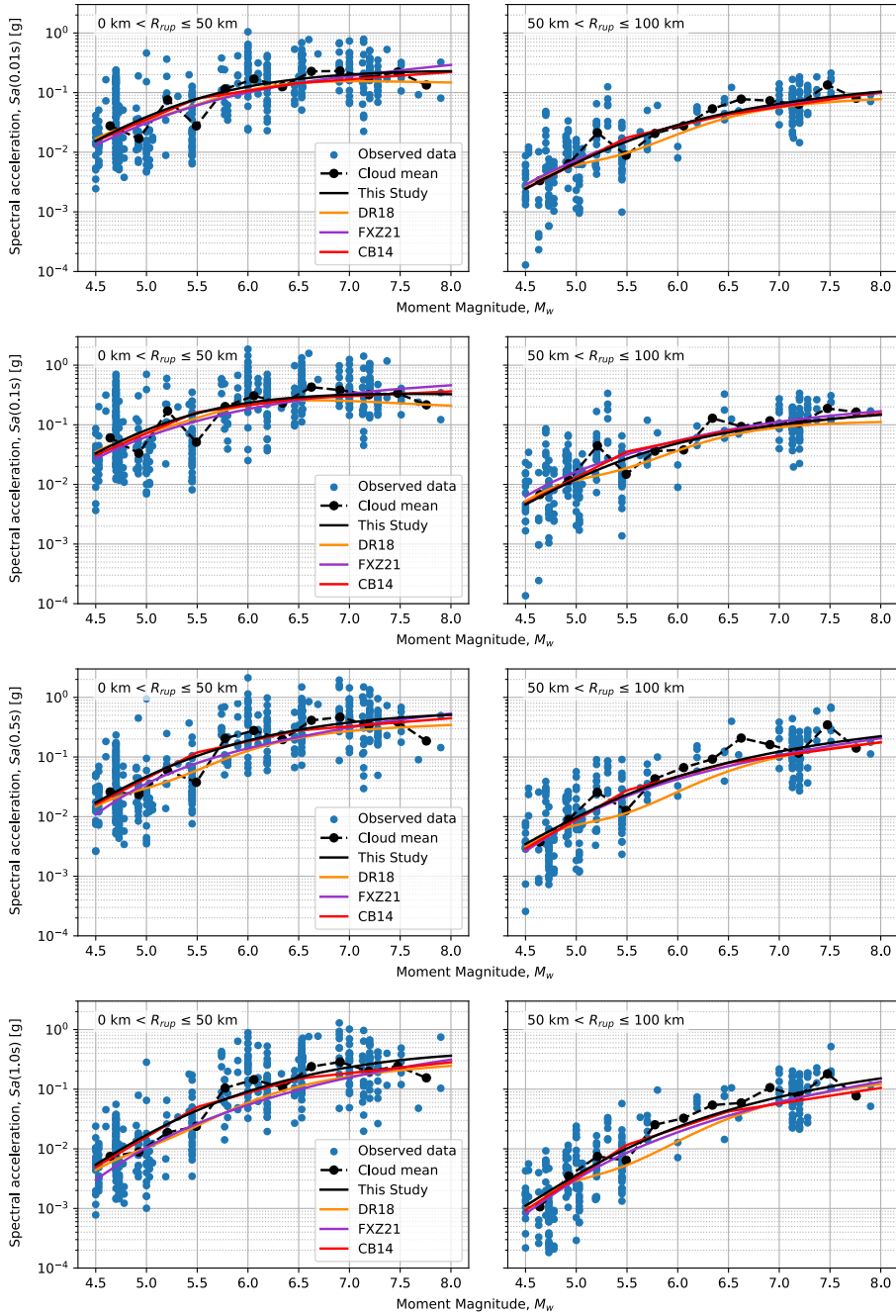


Figure 4.5. Magnitude amplification plots of $Sa(0.01s)$, $Sa(0.1s)$, $Sa(0.5s)$, and $Sa(1.0s)$ for two different rupture distance bins

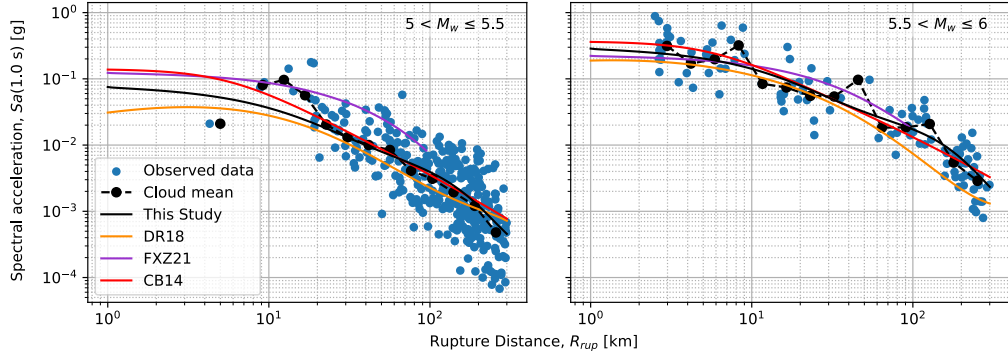


Figure 4.6. Distance attenuation plots of $Sa(1.0s)$ for two different magnitude bins

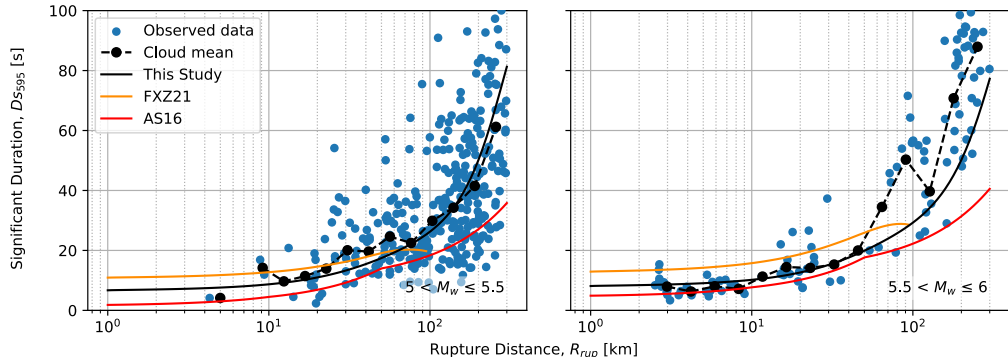


Figure 4.7. Distance attenuation plots of Ds_{595} for two different magnitude bins

criteria of the AS16 model to exclude recordings with unreasonably large durations polluted by high-frequency noise, even though the same database with the proposed model was used (i.e., NGA-West2). The FXZ21 model on the other hand tends to estimate slightly higher values of duration compared to the proposed model.

Overall, the GGMM developed here seems to have good predictability against the observed data when compared to the other models currently available for these traditional IMs of spectral acceleration and significant duration. Similar comparisons were done for the other traditional IMs listed in Section 4.3 (i.e., PGA , PGD , PGV , Ds_{575} and spectral acceleration at other periods), but were not included here due to space limitations.

4.5.2.2 Next-generation IMs

The previous section focused on the comparison of traditional IMs, for which several models already exist in the literature. It showed the GGMM proposed here to be of similar quality and bolsters confidence in its general use. In this section, we examine some next-generation IMs that have emerged in recent years that tend to have a small number of GMMs available. Hence, while these IMs have been shown in several studies to be quite efficient and sufficient when performing seismic vulnerability and risk analysis, the lack of robust GMMs to predict them is extremely problematic as it means the hazard component of risk is lacking. This study directly addresses this need.

Available GMMs estimating more advanced and complex IMs tend to be more simplistic and can sometimes have limited ranges of application. However, with the proposed model the trends of those next generation IMs are captured more accurately and for a wide range of ground motion causal parameters. For instance, Figures 4.8 and 4.9 present the distance attenuation and magnitude amplification of *FIV3(1.0s)* for two different magnitude and distance bins, respectively, and it is compared with the recently developed model of Dávalos et al. (2020) (DHM20), which to date is the only other GMM available for this IM. The DHM20 model estimates the arbitrary horizontal component definition, whereas the proposed model estimates the geometric mean definition. The DHM20 model is limited to $V_{s,30}$ values between 180 m/s and 360 m/s and takes just two input parameters (i.e., rupture distance and magnitude). Here, the strike-slip mechanism was examined and $V_{s,30}$ was between 180 and 360 m/s for the sake of equal comparison. For the other input parameters, the average was taken, except R_{jb} whose value was calculated from R_{rup} . It can be seen that the proposed model does well in capturing the trends of the cloud mean, while the DHM20 model generally predicts higher values at near and far distances from the source, especially in lower magnitudes.

Another IM that can be classified as next generation is the average spectral acceleration, whose attenuation with distance is illustrated in Figure 4.10 for the Sa_{avg3} definition of the IM described in Equation 4.3 and at a period of 1s. The estimations of the proposed model are compared directly with the model of Dávalos and Miranda (2021) (DM21), and with the ‘indirect method’ to compute the Sa_{avg} values. Regarding the latter

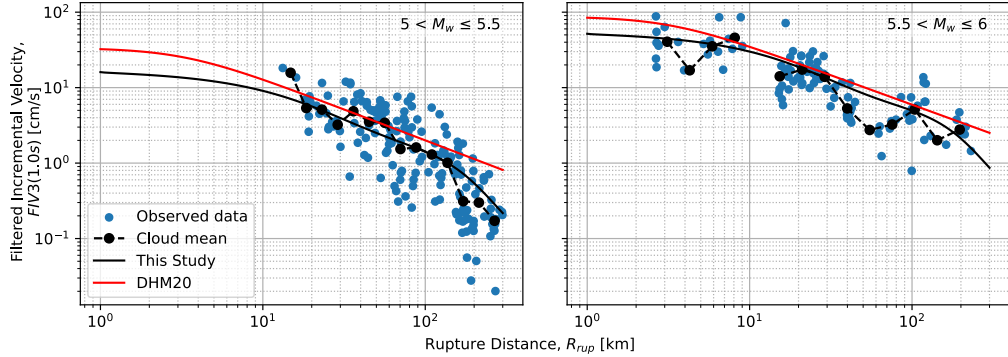


Figure 4.8. Distance attenuation plot of $FIV3(1.0s)$ for two different magnitude bins

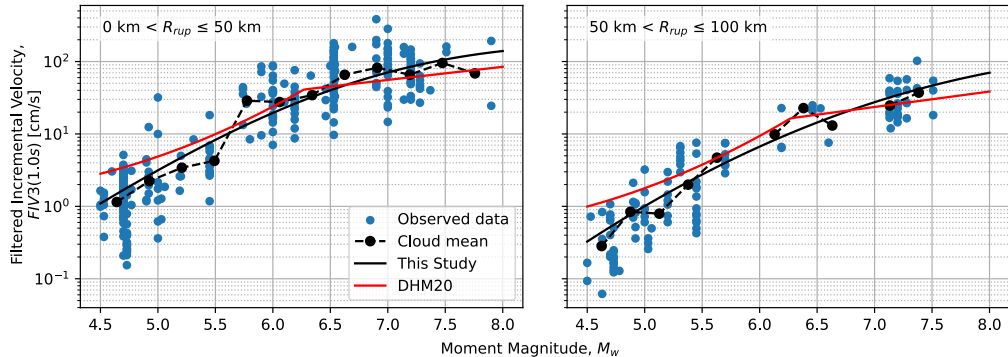


Figure 4.9. Magnitude amplification plots of $FIV3(1.0s)$ for two different rupture distance bins

method, Kohrangi et al. (2017) report the equations that can be used to calculate the mean and standard deviation of Sa_{avg} , denoted $\mu_{\ln Sa_{avg}|rup}$ and $\sigma_{\ln Sa_{avg}|rup}$, respectively, and they are formulated as follows:

$$\mu_{\ln Sa_{avg}|rup} = \frac{1}{N} \cdot \sum_{i=1}^N \mu_{\ln Sa(T_i)|rup} \quad (4.9)$$

$$\sigma_{\ln Sa_{avg}|rup} = \sqrt{\left(\frac{1}{N}\right)^2 \cdot \sum_{i=1}^N \sum_{j=1}^N \rho_{\ln Sa(T_i), \ln Sa(T_j)} \cdot \sigma_{\ln Sa(T_i)|rup} \cdot \sigma_{\ln Sa(T_j)|rup}} \quad (4.10)$$

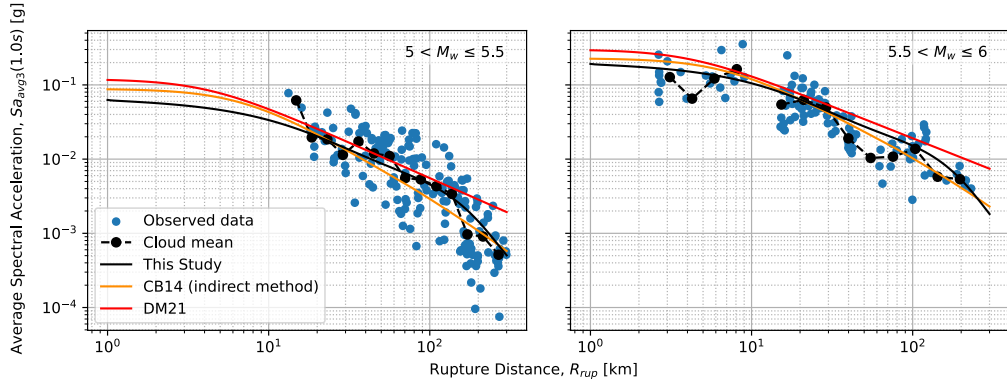


Figure 4.10. Distance attenuation plot of $Sa_{avg3}(1.0s)$ for two different magnitude bins

where N refers to the number of $Sa(T)$ values being averaged. $\mu_{\ln Sa(T_i)|rup}$ and $\sigma_{\ln Sa(T_i)|rup}$ are the logarithmic mean and standard deviation of Sa at the i -th period in the selected range for a given rupture scenario as obtained from a standard GMM. $\rho_{\ln Sa(T_i), \ln Sa(T_j)}$ is the correlation coefficient between $\ln Sa(T_i)$ and $\ln Sa(T_j)$. Herein, the CB14 model is used as the GMM and the Baker and Jayaram (2008) model is used as the correlation model to compute the mean and variance of logarithmic Sa_{avg} values with the ‘indirect method’ and compare with the output of the proposed model.

It should be noted that the DM21 model estimates the arbitrary horizontal component definition of Sa_{avg} , whereas the $RotD50$ definition is chosen for the proposed model. Additionally, since the DM21 model is limited to $V_{s,30}$ values between 180 and 360 m/s, only recordings from sites abiding to those limits were used for the comparisons. It can be observed from Figure 4.10 that the indirect method does well in capturing the trends of the observed data, since both the GMM and the correlation model come from similar databases (NGA-West2 and NGA, respectively) and have similar filtering criteria. Meanwhile, the direct estimations of DM21 tend to deviate from the binned cloud mean of the data for short and long distances. However, it is important to mention that DM21 suggest that the model should be used between $0 \text{ km} \leq R_{jb} \leq 150 \text{ km}$, which could explain some of these minor discrepancies. It is worth noting that the indirect method may also be used with the proposed GGMM, where the individual values of $\mu_{\ln Sa(T_i)|rup}$ and $\sigma_{\ln Sa(T_i)|rup}$ are estimated and the

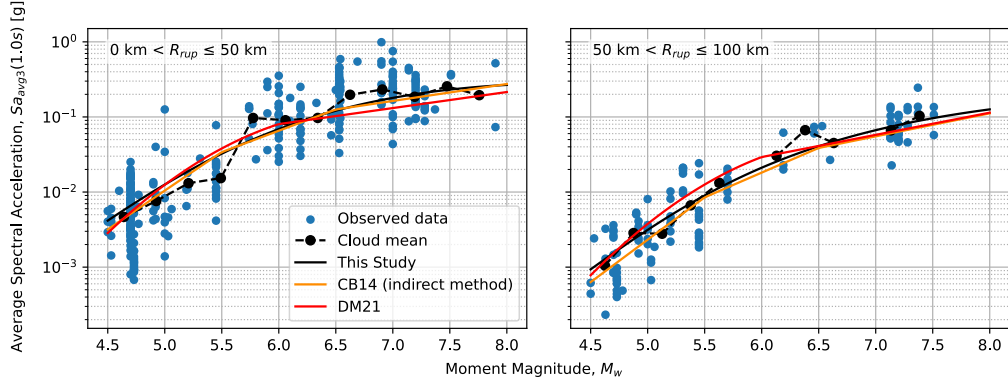


Figure 4.11. Magnitude amplification plots of $Sa_{avg3}(1.0s)$ for two different rupture distance bins

correlations are estimated with the ANN-based correlation model briefly presented in Section 4.6 and in Aristeidou et al. (2025).

Figure 4.11 presents the estimations of the proposed GGMM of Sa_{avg3} as a function of magnitude for two different rupture distance bins, along with the empirical data and the comparison with DM21 and the indirect method. It can be observed that the estimations of the proposed model are very close to the ones of the indirect method. The model of DM21 is also close to the proposed model for low, average, and high magnitudes, but slightly deviates in-between. Figures 4.12 and 4.13 present the same information as Figures 4.10 and 4.11, but for Sa_{avg2} . The DM21 is not included in the comparison, because of the different period range used in their calculation of Sa_{avg} , hence only the indirect method is included. It can be seen that the proposed model gives very similar estimations with the calculated values with the indirect method, and both do well in capturing the cloud mean. The only minor exception is the places where data are scarce.

4.5.3 Response spectra

While the previous sections evaluated the comparisons of the GGMM to available data and other available GMMs, this section provides some brief illustrations of the response spectra that may be obtained for these next-generation IMs investigated and how they are impacted by the main causal

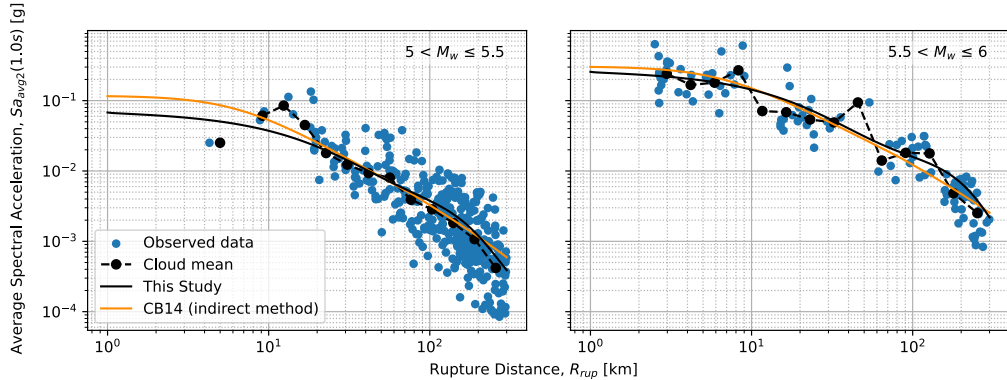


Figure 4.12. Distance attenuation plot of $Sa_{avg2}(1.0s)$ for two different magnitude bins

parameters. The response spectra, as estimated by the proposed model for *FIV3* and Sa_{avg3} , are presented in Figure 4.14 for different ground motion scenarios. On the left panels of the plots, the distance is kept constant while the magnitude is varied, and on the right panels, the magnitude is kept constant while the distance is varied. It can be seen that the *FIV3* is generally monotonically increasing with period and plateaus after a period of around 0.7 s, suggesting that for medium-to-long-period structures, the *FIV3* IM is almost period-independent. There is an exception for low magnitudes (i.e., 4.5), where there is a mild decrease for long periods. It can also be observed how the effect of the earthquake magnitude is more important than the effect of the source to-site distance. Similar observations can be made for Sa_{avg3} , but with the difference that it decreases in value with increasing period, which is an expected observation given the similarity in definition to the well known Sa IM.

4.5.4 Residuals analysis

To ensure that the proposed model did not contain any potential bias with respect to any input parameter, an analysis of the inter-, intra-event, and total residuals was performed. Here, the residuals are defined as $\log_{10}(\text{observations}) - \log_{10}(\text{predictions})$ and are plotted in Figure 4.15 for the inter-, intra-event, and total residuals against three ground motion causal parameters (i.e., M_w , R_{rup} and $V_{s,30}$), respectively, for three IMs (i.e.,

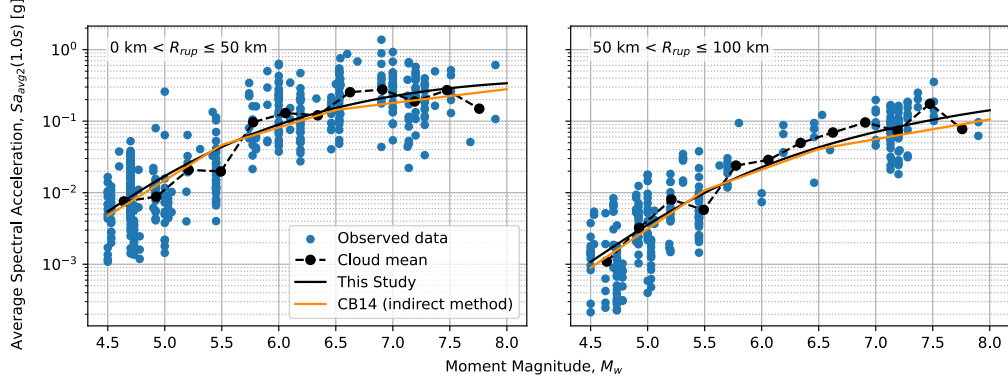


Figure 4.13. Magnitude amplification plots of $Sa_{avg2}(1.0s)$ for two different rupture distance bins

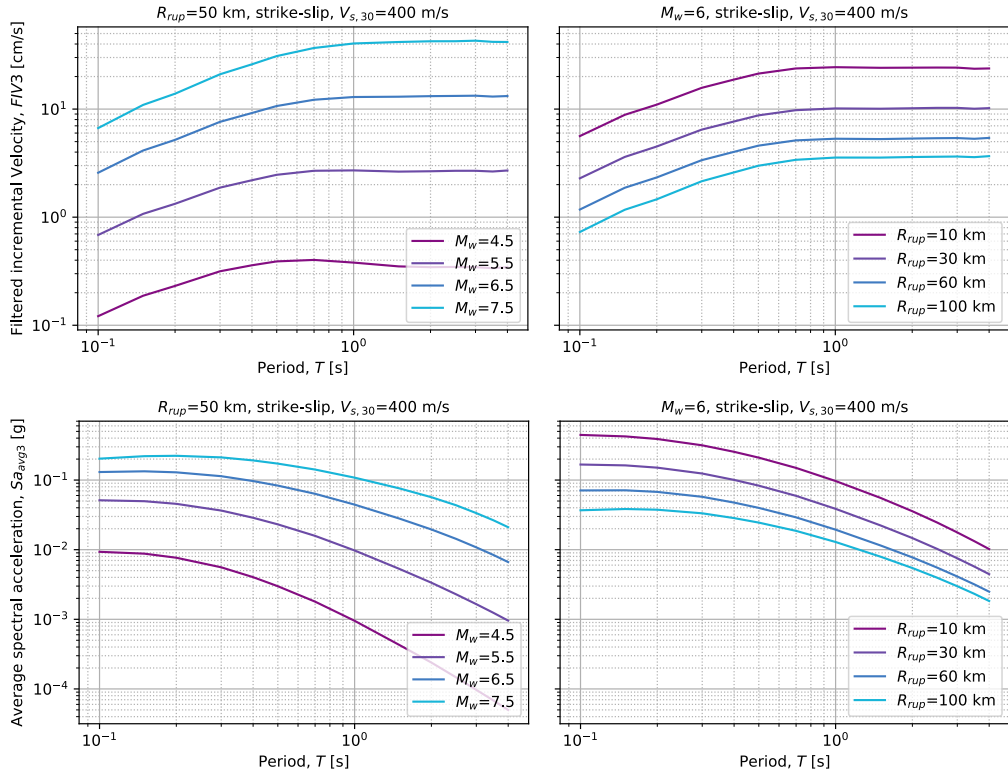


Figure 4.14. Model median estimates of response spectra of $FIV3$ (top) and Sa_{avg3} (bottom)

$Sa(1.0s)$, $FIV3(1.0s)$, Ds_{595}). It can be observed that there is no notable bias in the binned mean of residuals. Also, there is no significant change in standard deviations versus the ground motion causal parameters, further corroborating the homoscedasticity assumption for the dispersion model of the proposed GGMM. This assumption suggests that the variability of predicted IM is consistent across different levels of the predictor variables, such as M_w , R_{rup} or $V_{s,30}$. All the observations in Figure 4.15 were checked to be valid for all the combinations of IMs, ground motion causal parameters and residual types.

4.5.5 Model dispersion

The residuals between the values estimated from the proposed GGMM and those observed from the recorded ground motions were used to calculate the inter- and intra-event logarithmic standard deviations. The final standard deviations of all the IMs included in this study are presented in Figure 4.16, along with their respective counterparts given from other GMMs available in the literature for relative comparison. All standard deviations were transformed into natural logarithm (i.e., ln) units to have an equal basis for comparison since the fitted GGMM was in terms of log with base 10 and other models have used natural logarithm. It can be seen that the total standard deviation of the GGMM is the lowest for most IMs compared to other GMMs available in the literature. This is the case, especially for long-period IMs, although a slight difference was observed at shorter periods, where the intra-event term is slightly higher than CB14, for example, meaning the overall uncertainty is a little higher. Similar trends were observed in the recent GMM of Sedaghati and Pezeshk (2023), developed with machine-learning methods. This was investigated, and no specific reason was found to be causing it. It could be argued that previous models used much larger datasets, which could influence the overall variability, but it must be recalled that strict filtering criteria were applied here, as outlined in Section 4.2, which are expected to decrease the aleatory variability and increase the within-model epistemic uncertainty. In any case, it is noted here that while the mean predictions shown in Figure 4.5 may be satisfactory at a shorter period, the uncertainty shown in Figure 4.16 is slightly higher using the proposed GGMM. If the analyst is focusing solely on this short period range, other existing models may be more suitable,

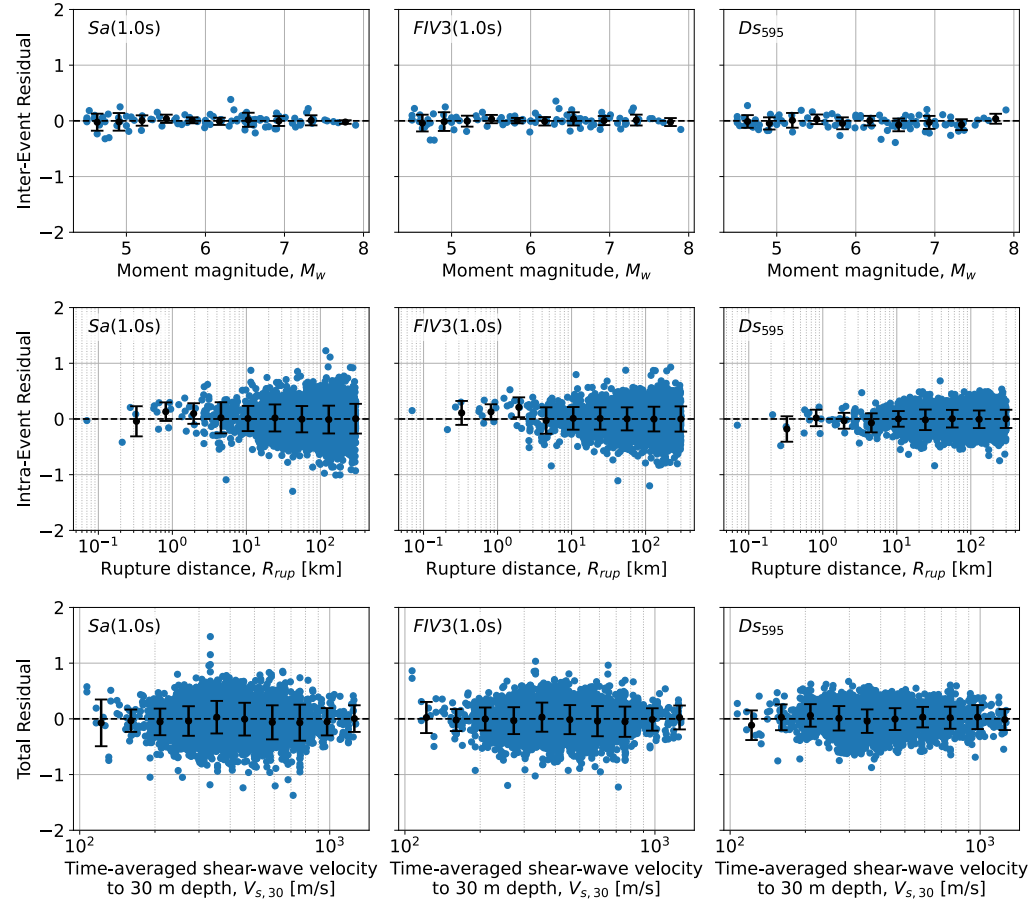


Figure 4.15. Inter-, intra-event, and total residuals versus M_w , R_{rup} and $V_{s,30}$, respectively, for three different IMs. Black dots and error bars represent the binned mean and \pm one standard deviation, respectively

but from a broader and more generalised perspective, the proposed GGMM tends to have lower uncertainty across several IMs.

Additionally, the proposed model maintains a low inter-event standard deviation and is almost constant throughout all IMs. The high difference between intra- and inter-event standard deviations in this model is likely because of the better characterisation of source effects in comparison to path and site effects. Another reason could be the generally strict filtering criteria applied on the initial strong motion dataset, allowing only recordings from

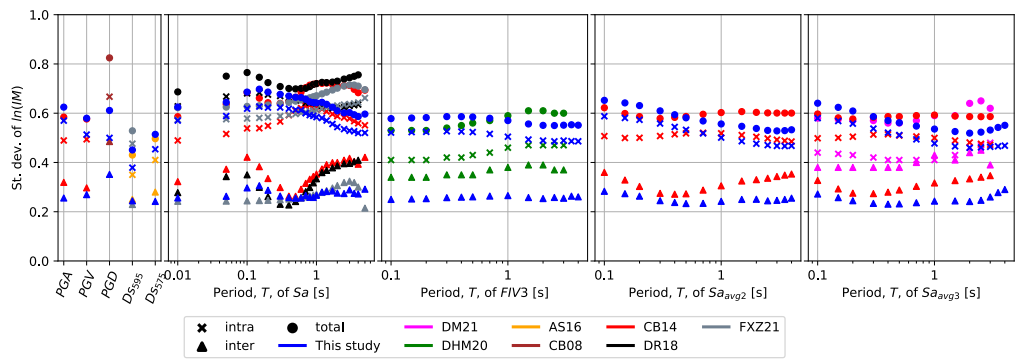


Figure 4.16. Inter-, intra-event and total standard deviations of the proposed model for all IMs, compared with models from the literature

earthquake magnitudes above 4.5, while the source-to-site distance limit was loose, allowing distances from 0 to 300 km.

The comparison of the dispersion of IMs with different horizontal component definitions is illustrated in Figure 4.17. It can be seen that the *RotD100* definition presents the highest logarithmic standard deviation from the three, followed by the *RotD50* and then the geometric mean definition. This difference is more pronounced in *Sa* IMs, rather than *Sa_{avg2}* and *Sa_{avg3}*, which is an expected result due to the inherent averaging effect of *Sa_{avg}*. Nonetheless, all horizontal component definitions present very similar standard deviations. The standard deviation of different horizontal component definitions of *Sa* was also studied by Beyer and Bommer (2006), but they did not include the *RotD50* definition, as it was not available at the time. The closest definition to *RotD50* would be the *GMRotD50*, for which they found about the same or slightly lower dispersion, than the geometric mean definition. Regarding the *RotD100* definition, denoted as ‘*MaxD*’ in Beyer and Bommer (2006), they found its dispersion to be slightly higher than the geometric mean definition, which is aligned with what has been observed here.

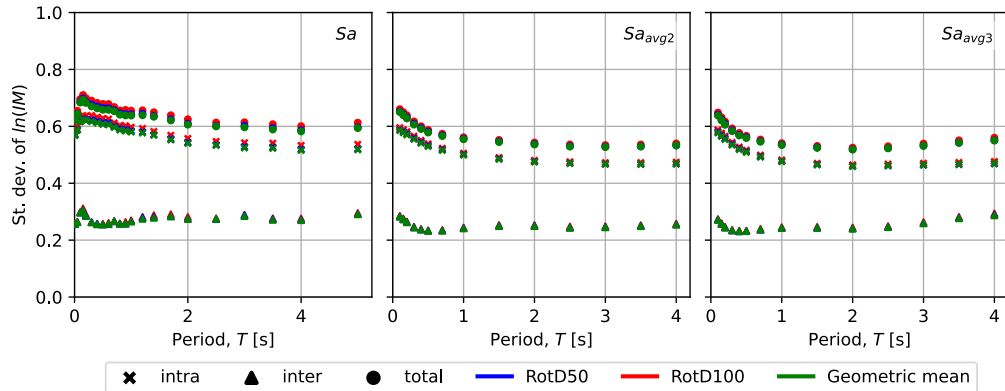


Figure 4.17. Comparison of inter-, intra-event and total standard deviations of IMs with different horizontal component definitions

4.6 Correlation modelling

As previously stated, this GGMM, which includes several IMs, finds good utility in creating consistent (i.e., from the same database and GMM) correlation models, which are needed for ground motion record selection and identification of ground motion field used in regional analysis. The general procedure to get those correlation models is outlined in the following. From Equation 4.7, the total normalised residual, δ_i , and total standard deviation, σ_i , can be expressed as the sum of inter- and intra-event residuals as:

$$\delta_i \sigma_i = \delta b_i \tau_i + \delta w_i \phi_i \quad (4.11)$$

This means, by implication, that $\log_{10} IM_i$ and δ_i exhibit a linear relationship. Therefore, the correlation between two IMs is equal to the correlation between the normalised residuals, which in mathematical expression translates to:

$$\rho_{\log_{10}(IM_i)|\mathbf{X},\theta, \log_{10}(IM_j)|\mathbf{X},\theta} = \rho_{\delta_i, \delta_j} \quad (4.12)$$

Then, the correlations of residuals between different IMs can be estimated using the Pearson product-moment correlation coefficient formula:

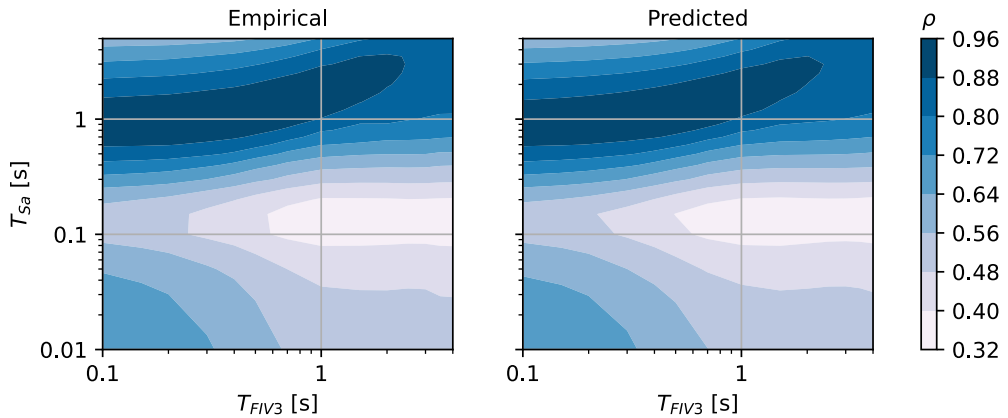


Figure 4.18. Empirical and corresponding predicted correlation coefficients between Sa and $FIV3$

$$\rho_{x,y} = \frac{\sum_{m=1}^M [(x_m - \bar{x})(y_m - \bar{y})]}{\sqrt{\sum_{m=1}^M [(x_m - \bar{x})^2] \sum_{m=1}^M [(y_m - \bar{y})^2]}} \quad (4.13)$$

where x and y are generic variables, corresponding to δb_i and δb_j for inter-event correlation for IMs i and j , and to δw_i and δw_j for intra-event correlation in this application; \bar{x} and \bar{y} are the sample means and $\sum_{m=1}^M$ is the summation of all M ground motion records. From the definition of correlation coefficient, the correlation between total residuals can be estimated from the inter- and intra-event correlations as follows:

$$\rho_{\delta_i, \delta_j} = \frac{\rho_{\delta b_i, \delta b_j} \tau_i \tau_j + \rho_{\delta w_i, \delta w_j} \phi_i \phi_j}{\sigma_i \sigma_j} \quad (4.14)$$

Correlation models between PGA , PGV , Sa , $FIV3$, Ds_{595} , Ds_{575} , Sa_{avg2} and Sa_{avg3} were developed using this GGMM and are derived, presented, and discussed in detail in Chapter 5. Readers interested in these correlations and their modelling are referred to the subsequent chapter for further details and discussion. As an example, the correlation coefficients between Sa and $FIV3$ and between Ds and Sa_{avg3} are illustrated in Figures 4.18 and 4.19, respectively.

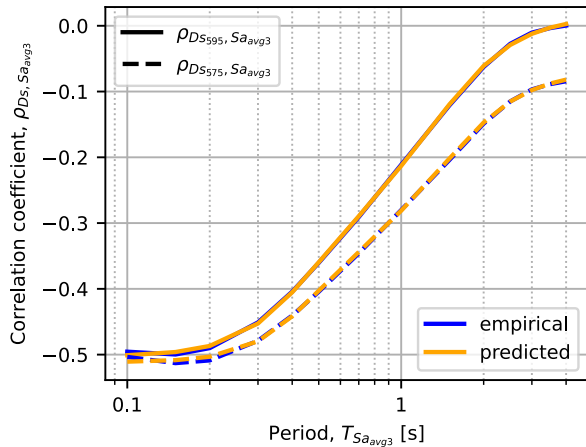


Figure 4.19. Empirical and corresponding predicted correlation coefficients between Ds and Sa_{avg3}

4.7 Summary and conclusions

This study proposed a GGMM to estimate different types of amplitude and cumulative-based IMs for active shallow crustal earthquakes. These IMs include the PGA ; peak ground velocity, PGV ; PGD ; spectral acceleration $Sa(T)$; two definitions of significant duration, Ds_{575} and Ds_{595} ; filtered incremental velocity, $FIV3(T)$; and two definitions of average spectral acceleration, $Sa_{avg2}(T)$ and $Sa_{avg3}(T)$, meaning a total of 169 output IMs were presented here. Testing and training data were collected from a stringently filtered subset of records from the NGA-West2 strong motion database.

Thorough validation exercises and comparisons with other GMMs were carried out to demonstrate the suitability of the GGMM. It shows how this framework can effectively capture the complex relationships and interactions between different IMs, which is one of the advantages of this GGMM, as it estimates various IMs in a single model. This helps develop more consistent correlation models between the estimated IMs since they come from the same database and GMM. Meanwhile, more IMs of interest can be seamlessly added to the model's outputs with only minor modifications (e.g., increase of hidden layer neurons). Another advantage observed was that it minimises the dispersion of residuals (aleatory uncertainty) while keeping

the two fitting performance metrics (i.e., R^2 and MSE) at an optimal level. The logarithmic total standard deviations were low, especially in long-period IMs.

A few limitations of the approaches and methods adopted for the development of this model are that these types of models work well only where data are available, the analyst has less control over the analytical functional forms, which ideally reflect the actual physics of the seismological phenomena, and maybe the homoscedasticity assumption for treatment of dispersion. The reason for not opting for heteroscedastic dispersion model, is there are already a lot of output IMs from the same model, so adding heteroscedasticity would overcomplicate the model, for small potential benefit.

Overall, the results and comparisons suggest that the proposed model performs excellently in estimating a variety of traditional and next generation IMs, without any bias against the input features. The proposed model can be used in seismic hazard analysis to derive site specific uniform hazard spectra, hazard curves for the IM of choice, scenario-based shake maps, and more. This model represents a very useful addition in many situations where more advanced intensity measures, such as filtered incremental velocity or average spectral acceleration, are required. Recent research has highlighted the potential of these intensity measures for a better characterisation of structural response (i.e., sufficiency, efficiency etc.) but to date, there has been little work done to provide suitable models to quantify their hazard (i.e., hazard computability) (O'Reilly, 2021a). This paper has directly aimed at filling that gap. Furthermore, the use of this single GGMM has allowed consistent correlation models to be quantified by Aristeidou et al. (2025) which paves the way for more refined record selections following the generalised conditional intensity measure approach (Bradley, 2010).

Following the finalisation and peer-review of the model, this GMM was implemented in the well-known PSHA tool OpenQuake. Also, there is a code available online for this GMM takes inputs the nine seismological parameters and outputs the mean and sigma of a specific IM. Therefore, even if the model is non-parametric, it can be used like any other classical GMM and easily adapted to any other PSHA package.

4.8 Code availability

The relevant files and functions that can be used to get estimations from the generalised ground motion model presented in this chapter are available on GitHub at: <https://github.com/Savvinos-Aristeidou/ANN-GGMM.git>.

Chapter 5

Correlation models for next-generation amplitude and cumulative intensity measures using artificial neural networks

This chapter is extensively based on the following publication:

Aristeidou, S., Shahnazaryan, D., & O'Reilly, G. J. (2025). Correlation Models for Next-Generation Amplitude and Cumulative Intensity Measures using Artificial Neural Networks. *Earthquake Spectra*, 41(1), 851–875. <https://doi.org/10.1177/87552930241270563>

5.1 Introduction

Earthquake-induced ground motion severity can be quantified via a plethora of proxies describing the amplitude, frequency content, and duration of ground shaking, termed IMs. Traditionally, the ground motion amplitude and frequency content are explicitly considered by examining acceleration-based response spectrum quantities. However, other types of IMs, like duration, average spectral acceleration, or *FIV3*, have received less attention due to their relative novelty, despite being efficient predictors of structural response (Bojórquez et al., 2012). These “secondary” features of ground motion shaking (i.e., duration, average spectral intensity, energy content, and velocity-based IMs) are generally assumed to be implicitly

accounted for by limiting the causal parameters (e.g., magnitude and source-to-site) of the selected ground motion record set (e.g., Bommer and Acevedo, 2004; ASCE, 2017; Spillatura et al., 2021).

To perform a NRHA, a set of ground motion records must be selected, which usually depends on the definition of a target spectrum. The set of records that is as close as possible to a target spectrum and its anticipated dispersion are usually chosen as input records for the NRHA. Earlier proposals and a few current seismic provisions (e.g., ASCE 7–10 and Eurocode 8) recommended using a uniform hazard spectrum (UHS) for Sa as the target spectrum. More recently, improved approaches introduced the concept of the conditional mean spectra and conditional spectra (conditional mean spectrum (CMS), and conditional spectrum (CS), respectively) (Baker and Cornell, 2006a, 2006b; Abrahamson and Al Atik, 2010; Baker, 2011), which provides median spectral ordinates and logarithmic standard deviations conditioned to the intensity at a certain period of vibration having a certain probability of exceedance level. More holistic ground motion record selection methods like the generalised conditional intensity measure (GCIM) method that considered the conditional distribution of IMs beyond spectral acceleration made it possible to explicitly consider several IMs during the selection process (Bradley, 2010). These methods require not only an available GMM of each IM but also knowledge of correlations between the residuals of all IMs (or spectral ordination of the same IM) that are under consideration.

The GMM provides the marginal, or unconditional, distribution of an IM given specific causal parameters (Baker et al., 2021). To obtain conditional distributions of an IM with other relevant IMs, the correlations between them are needed. Despite several recent studies illustrating their appreciable predictive power and efficiency in seismic risk assessments, to the authors' knowledge, there are no correlation models of *FIV3* with itself or with other IMs, nor is there a direct correlation model for Sa_{avg} with other IMs. Therefore, this study attempts to close this gap while also refining a few conventional correlation models using machine learning-based techniques. In addition, these correlation models can find use in specialized performance-based hazard and risk assessments, where it is often required to estimate the joint probability of occurrence of different IMs through a vector-based PSHA (Bazzurro and Cornell, 2002). Further details on the general procedure of said vector-PSHA are formalized for the case of two

IMs in Baker et al. (2021) for interested readers.

First, the IMs and their cross-correlations are described in more detail. Then, a brief description of the estimation of residuals is given, along with the adopted GMM and strong-motion database. Subsequently, the methodology for computing the correlation coefficients is outlined, and the architecture of ANN models is presented. Finally, the quantified empirical correlations are appraised, and their comparisons with the fitted ANN models and other existing models are discussed.

A novelty of this article is the exploration of machine learning-based techniques, namely ANN, for the regression models of correlations. This is in contrast with the traditional approach of identifying functional forms, which in some cases might even deviate from empirical values in their estimations, thus introducing fitting errors. To the authors' knowledge, no such ANN models currently exist in the literature. This is the case for cross-IM correlations at a single site, although an advanced approach has been applied to the spatial correlation of IMs in a recent study (Bodenmann et al., 2023). Another (and most important) novelty of this study is bridging the gap in the correlations of *FIV3* and direct estimation of Sa_{avg} with themselves and other conventional IMs. These IMs have been studied in many past works to demonstrate their utility in seismic response assessment, but often lack the necessary GMMs or correlation models to fully leverage them for ground motion selection, vector-PSHA, or generally account for these IMs in a site or regional assessment. In addition, the procedure adopted is modular in the sense that it could be easily extended to other IMs or horizontal component definitions through simple repository and model versioning and updating. These are the main novelties of this work, while at the same time, it was aimed to complement the existing body of literature regarding the more well-established IMs.

5.2 Correlation models developed

There are many different IMs that are of interest to seismic engineers, which generally depend on the type of structure under examination and the extent of the investigation. The IMs used for the correlations in this study, and the definitions of those IM are given in the following:

- ***PGA***: peak ground acceleration.

- **PGV** : peak ground velocity.
- **$Sa(T)$** : 5%-damped spectral acceleration at a vibration period, T .
 List of periods: $T = [0.01, 0.05, 0.1, 0.15, 0.2, 0.3, 0.4, 0.5, 0.6, 0.7, 0.8, 0.9, 1, 1.2, 1.4, 1.7, 2, 2.5, 3, 3.5, 4, 5]$ s.
- **Ds_{xy}** : $x\% - y\%$ significant duration, defined as the time interval over which $x\%$ to $y\%$ of the integral $\int_0^{t_{max}} [a(t)]^2 dt$ is accumulated (Trifunac and Brady, 1975), as per Equation 4.1. The proposed models include $\{x, y\} = \{5\%, 75\%\}$ and $\{x, y\} = \{5\%, 95\%\}$.
- **Sa_{avg}** : average spectral acceleration as defined in Equation 4.3, for two different period ranges defined below. List of periods: $T = [0.1, 0.15, 0.2, 0.3, 0.4, 0.5, 0.7, 1, 1.5, 2, 2.5, 3, 3.5, 4]$ s.
- **$FIV3$** : defined by Dávalos and Miranda (2019) and summarized in Equation 3.1. List of periods: $T = [0.1, 0.15, 0.2, 0.3, 0.4, 0.5, 0.7, 1, 1.5, 2, 2.5, 3, 3.5, 4]$ s.

PGA and PGV are included in the proposed models as they have traditionally been popular and are still used in simplified and/or regional seismic assessments (Kaka and Atkinson, 2004; Akkar and Özen, 2005; Borzi et al., 2015).

Regarding the importance of duration, Hancock and Bommer (2006) summarized how different conclusions have been drawn in the literature, depending on the structural demand parameters considered in each study. A few studies that considered only the peak structural deformations (Saried-dine and Lin, 2013) found that duration has little effect. Meanwhile, most other studies (Iervolino et al., 2006; Oyarzo-Vera and Chouw, 2008; Raghunandan and Liel, 2013; Chandramohan et al., 2016; Gentile and Galasso, 2021; Otárola, Sousa, et al., 2023) found that, while duration does not influence the peak deformations, it does influence the cumulative engineering demand parameters, and, therefore, the damage due to cumulative effects. Overall, it is generally important to consider the correlation of duration with Sa when examining the effects of duration on structural response, especially in degrading systems. Even though there are many ways to describe the duration of a strong ground motion (Bommer and Martínez-Pereira, 1999), the two most common definitions are bracketed duration and significant duration (Afshari and Stewart, 2016). The scope

herein is limited to the significant duration since it is often the preferred definition used in the literature (e.g., Chandramohan et al., 2016). The significant duration is defined as presented in Equation 4.1 of the previous chapter.

Average spectral acceleration, Sa_{avg} , has been shown in the literature to be a better overall predictor of structural response, rather than the classic IM of Sa for the majority of structural typologies (e.g., Bianchini et al., 2009; Eads et al., 2015; Kazantzi and Vamvatsikos, 2015; O'Reilly, 2021a, 2021b). Different period ranges can be chosen for the definition of this IM depending on the structure and the level of inelasticity that one wants to capture more accurately. This ambiguity was investigated in several past works (Cordova et al., 2000; Vamvatsikos and Cornell, 2005), and also, an extensive analysis was conducted in Chapter 7 of Eads and Miranda (2013), where it was explored how the range, number, and spacing of periods used to compute Sa_{avg} influences the efficiency of collapse risk assessment estimates of SDOF, moment-resisting frames, shear wall, and reinforced concrete systems. Sa_{avg} was also included in the correlation models developed in this study. It is defined as the geometric mean of N -number spectral accelerations at periods within a user-specified range $[T_{lower}, T_{upper}]$, as expressed in Equation 4.3. Hence, 10 periods (i.e., $N = 10$) equally spanning each chosen period range were used (Eads et al., 2015). Two different period ranges were used for the proposed correlation models, $[T_{lower}, T_{upper}] = [0.2T, 2T]$ and $[0.2T, 3T]$, based on Kohrangi et al. (2017) and Eads et al. (2015) recommendations, respectively. The two Sa_{avg} metrics derived from different period ranges (i.e., $[0.2T, 2T]$ and $[0.2T, 3T]$) were treated as separate IMs, denoted as Sa_{avg2} and Sa_{avg3} , respectively. These different period ranges were adopted based on the different focus of the aforementioned articles. Eads et al. (2015) focused on the collapse prediction. In contrast, Kohrangi et al. (2017) were also interested in the floor-acceleration response and economic losses.

Dávalos and Miranda (2019) proposed *FIV3* as a novel IM that showed promising results regarding its efficiency and sufficiency in characterizing the collapse performance of buildings. In addition, some recent studies further highlighted the value of this IM in estimating seismic collapse in buildings and bridges (Dávalos and Miranda, 2019, 2020; Aristeidou and O'Reilly, 2024). To date, there is just one empirical GMM for estimating this IM (Dávalos et al., 2020), whereas the other IMs tend to be better represented with several different GMM options. *FIV3* is briefly

summarized mathematically as previously presented in Equation 3.1. The α and β input parameters required to calculate Equation 3.1 were chosen as 0.7 and $1/f$ (or T), respectively, as these were the parameters chosen in the original study (Dávalos et al., 2020).

The $RotD50$ horizontal component definition (Boore, 2010) was adopted for PGA , PGV , Sa , and Sa_{avg} , whereas the geometric mean of the two as-recorded horizontal components was adopted for Ds and $FIV3$, since other definitions have not been studied for these IMs so far. Baker and Bradley (2017) computed the spectral acceleration correlations for two horizontal component definitions ($RotD50$ and $RotD100$) and concluded that they are essentially identical. This finding suggests that correlation models can be used interchangeably for the different common horizontal component definitions.

Table 5.1 summarizes the correlation models developed in this study, denoted as ASO24. Also summarized are a few pre-existing correlation models used for the comparisons herein. It should be noted that it is not an exhaustive list of pre-existing models, but rather a selection of models that used herein for comparative purposes. Listed in *italics* are a few existing models (given as example) of the correlation pairs not examined herein. These pairs are not examined since first they do not find much use in contemporary seismic risk analysis applications, and second, they are already well documented in the literature (Turbali and Bradley, 2015; Baker and Bradley, 2017; Turbali et al., 2023). Cases noted as the “indirect method” for Sa_{avg} refer to the indirect method of estimating correlations, using the mathematical definition of Sa_{avg} , from Sa and exploiting the available models for that IM, which is described by Kohrangi et al. (2017).

Table 5.1. Correlation models proposed here and corresponding existing ones from the literature. In *italics* are a few example models in the literature of pairs not examined herein, given for the sake of completeness.

$IM_i \backslash IM_j$	Sa	Sa_{avg2}	Sa_{avg3}	PGA	PGV	Ds_{575}	Ds_{595}	$FIIV3$
Sa	ASO24, BJ08, ASA14, BB17	ASO24, CB14 and BJ08*, CB14 and ASA14*	ASO24, CB14 and BJ08*, CB14 and ASA14*	<i>BB17,</i> <i>TBB23</i>	<i>BB17,</i> <i>TBB23</i>	ASO24, B11, BB17	ASO24, B11, BB17	ASO24
Sa_{avg2}	ASO24	ASO24	ASO24	ASO24	ASO24	ASO24	ASO24	ASO24
Sa_{avg3}		ASO24, DM21	ASO24	ASO24	ASO24	ASO24	ASO24	ASO24
PGA				<i>BB17,</i> <i>TBB23</i>	<i>BB17,</i> <i>TBB23,</i> B11	<i>BB17,</i> <i>TBB23,</i> B11	<i>BB17,</i> <i>TBB23,</i> B11	ASO24
PGV					<i>BB17,</i> <i>TBB23,</i> B11	<i>BB17,</i> <i>TBB23,</i> B11	<i>BB17,</i> <i>TBB23,</i> B11	ASO24
Ds_{575}							<i>BB17,</i> <i>TBB23,</i> B11	ASO24
Ds_{595}								ASO24
$FIIV3$								ASO24

ASO24: This study; BJ08: (Baker and Jayaram, 2008); ASA14: (Akkar et al., 2014); DM21: (Dávalos and Miranda, 2021); B11: (Bradley, 2011a); BB17: (Baker and Bradley, 2017); *: indirect method; TBB23: (Tarbali et al., 2023).

5.3 Database and ground motion model

Regarding the GMM adopted in this chapter for the estimation of IM distributions, a single GGMM applicable to active shallow crustal tectonic regions was utilized. This model is presented in Chapter 4, and, therefore, not discussed in detail here. It was developed using the strong-motion database from NGA-West2 (Ancheta et al., 2013) using an ANN framework. Although a combination of GMMs could have been used, only one was considered here to compute the residuals regarding these predictions. Studies such as Baker and Bradley (2017) have examined the impact of considering different GMMs and strong-motion databases when computing residuals and noted that while there is some difference, it is not considered to have a significant impact on the computed correlation coefficients. Therefore, it was deemed acceptable, and possibly advantageous, to use a single GGMM for all IMs examined herein. The ground motion database used is the same as the one used to develop the GGMM, namely the NGA-West2 database (Ancheta et al., 2013), and the same filtering criteria as described in Aristeidou et al. (2024) and Chapter 4 are applied. The basis of those filtering criteria was to remove some of the records that may be deemed unsuitable for general engineering use. The filtering criteria also indirectly form the recommended usage limits of the correlation models. In total, 4,135 ground motion records from 102 earthquakes were chosen.

5.4 Methodology

To estimate the correlations between the aforementioned IMs, two important inputs are needed: a ground motion database and a GMM to predict the expected shaking intensity each rupture parameter. For each ground motion record in the database adopted, the residuals are computed as the difference between the actual observation (i.e., the ground motion record's actual value of IM) and the predicted median value from the GMM; as illustrated in Figure 5.1 for two values of a spectral IM. These residuals are computed for all IM definitions, the correlations between them are quantified, and predictive models were developed to estimate these correlations.

Inter-event, intra-event, and total residuals obtained from the GGMM

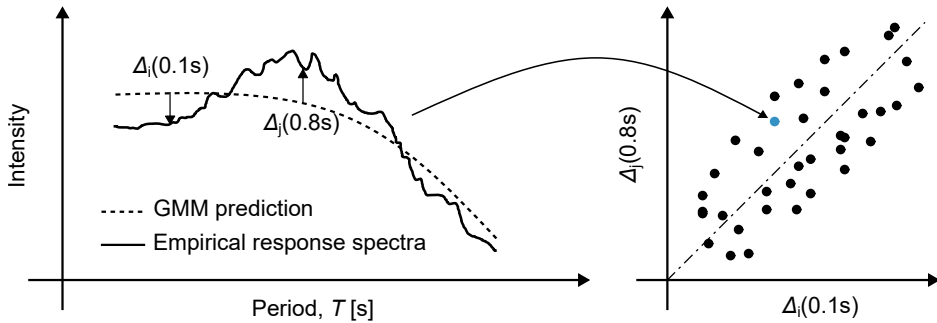


Figure 5.1. Schematic representation of the correlation between total residuals, Δ , (left) predicted and empirical response spectrum of a single record, and (right) residuals of the same IM from a large set of records.

were passed onto this study to compute the empirical cross-correlation of the IM residuals. Figure 5.2 depicts the empirical distributions of the normalized inter- and intra-event residuals for Ds_{595} , $Sa(T = 1s)$, and $FIV3(T = 1s)$. They are compared with the theoretical standard normal distribution and the Kolmogorov–Smirnov (KS) goodness-of-fit bounds at a 5% significance level. The compatibility of the GGMM with this data set is demonstrated by the observation that both inter- and intra-event empirical distributions lie within the KS goodness-of-fit bounds. Figure 5.2 depicts just three IMs but similar results were obtained for the other IMs considered, meaning that the natural logarithm of the residuals can generally be expected to be normally distributed, as is adopted in other past studies.

Even though Figure 5.1 focused on total (non-normalized) residuals, correlations are separately estimated for the normalized inter- and intra-event residuals, which are estimated from the mixed-effect regression of the GMM. Then, they are combined to derive the correlations of the normalized total residuals. The general methodology to achieve this is described below, beginning with the general form of the GGMM, given as:

$$\log_{10}(IM_i) = f_i(\mathbf{X}, \boldsymbol{\theta}) + \delta b_i \tau_i + \delta w_i \varphi_i \quad (5.1)$$

where $\log_{10}(IM_i)$ is the logarithm with base 10 of the i-th IM; $f_i(\mathbf{X}, \boldsymbol{\theta}) =$

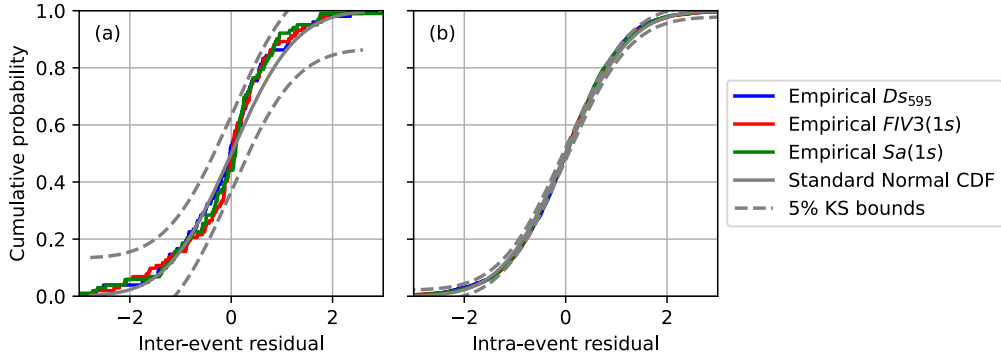


Figure 5.2. Empirical cumulative distribution of the (a) normalized inter-event and (b) normalized intraevent residuals obtained using the GGMM. Comparison with the theoretical standard normal cumulative distribution and the 5% KS bounds.

$\mu_{\log_{10}(IM_i)|\mathbf{X},\boldsymbol{\theta}}$ is the predicted mean output from the ANN model, taking as input a set of causal parameters (M_w , R_{rup} , etc.), denoted as \mathbf{X} ; $\boldsymbol{\theta}$ are the “calibrated coefficients” of the ANN model (i.e., synaptic weights and biases); δb_i and δw_i are the normalized inter- (between) and intra- (within) event residuals of IM_i , respectively; τ_i and φ_i are the inter- and intra-event logarithmic standard deviations. Here, lowercase δ is used to denote normalized residuals, and uppercase Δ is used to denote non-normalized residuals. The total normalized residual, δ_i , and total standard deviation, σ_i , can be expressed as the sum of inter- and intra-event residuals as:

$$\delta_i \sigma_i = \delta b_i \tau_i + \delta w_i \varphi_i \quad (5.2)$$

Combining Equations 5.1 and 5.2, and rearranging, the total normalized residual for a specific ground motion g , $\delta_{i,g}$, can be thought of as the number of standard deviations that the empirical IM is above the predicted mean value from the GMM, as illustrated in Figure 5.1 (albeit normalized with the total standard deviation) and formally described as:

$$\delta_{i,g} = \frac{\log_{10}(IM_{i,g}) - \mu_{\log_{10}(IM_i)|\mathbf{X},\boldsymbol{\theta}}}{\sigma_i} \quad (5.3)$$

It can be seen that $\log_{10}(IM_{i,g})$ and $\delta_{i,g}$ exhibit a linear relationship in Equation 5.3; therefore by extension, the correlation between two IMs,

for given causal parameters \mathbf{X} , is equal to the correlation between the normalized residuals, which in mathematical form translates to:

$$\rho_{\log_{10}(IM_i)|\mathbf{X}, \boldsymbol{\theta}}, \log_{10}(IM_j)|\mathbf{X}, \boldsymbol{\theta} = \rho_{\delta_i, \delta_j} \quad (5.4)$$

Herein, for the sake of brevity, the correlation between two IMs will be simply referred to as ρ_{IM_i, IM_j} , where the conditioning on the causal parameters is implied but is generally taken as independent. Baker and Bradley (2017) studied the dependence of IM correlations on causal parameters such as magnitude, distance, and time-averaged shear wave velocity to 30 m depth. They found no systematic variation of these correlations with any of these GM causal parameters and corroborated this typical assumption that IM correlations are independent of these parameters (Baker and Cornell, 2005b, Appendix B; Huang and Galasso, 2019; Kohrangi et al., 2020; Tarbali et al., 2023), although other studies such as Kotha et al. (2017) have noted correlations to be magnitude-, region-, and database-dependent. Having the correlation coefficients to be depended on seismological and site-specific parameters can definitely enhance the robustness of the correlation models, but it would compromise their easy of use. It should be noted here that the correlations arising from \log_{10} transformations of IMs are eventually the same with the ones arising from natural logarithm transformations. In the literature, usually the natural logarithm transformation is used, thus the ln denotation can be used interchangeably.

Since δb_i and δw_i are generally assumed to be independent (Abrahamson et al., 2008), which was also the case in the recently developed GGMM used for this study, the correlations of inter- and intra-event residuals between different IMs can be estimated using the Pearson product-moment correlation coefficient formula (Ang and Tang, 1975), described as:

$$\rho_{x,y} = \frac{\sum_{m=1}^M [(x_m - \bar{x})(y_m - \bar{y})]}{\sqrt{\sum_{m=1}^M [(x_m - \bar{x})^2] \sum_{m=1}^M [(y_m - \bar{y})^2]}} \quad (5.5)$$

where x and y are generic variables, corresponding to δb_i and δb_j for inter-event correlation for IMs i and j , and to δw_i and δw_j for intra-event correlation in this application; \bar{x} and \bar{y} are the sample means, and $\sum_{m=1}^M$

is the summation of all M ground motion records. Therefore, Equation 5.5 was used to compute the $\rho_{\delta b_i, \delta b_j}$ and $\rho_{\delta w_i, \delta w_j}$ correlations separately. From this definition of the correlation coefficient, the correlation between total residuals can be estimated from the individual inter- and intra-event correlations as follows:

$$\rho_{\delta_i, \delta_j} = \frac{\rho_{\delta b_i, \delta b_j} \tau_i \tau_j + \rho_{\delta w_i, \delta w_j} \phi_i \phi_j}{\sigma_i \sigma_j} \quad (5.6)$$

To account for the GMM uncertainty in the computed correlation coefficient, more than one GMM for active shallow crustal tectonic regions could be used with a logic tree; however, this was not applied here, and only a single GMM was used for simplicity. Past studies, such as Bradley (2011b), for example, have shown that the distribution of the correlation coefficient, which includes both finite sample size and GMM uncertainty, can be represented by the normal distribution. Herein, only point-estimate results for the mean correlation coefficients are presented. Finally, as previously mentioned, only the correlations between the total residuals are presented.

5.5 Artificial neural network architecture

The results of the empirical correlations calculated were then used to fit predictive models. Traditionally, these regression models (or predictive equations) are analytical functions with no strong physical basis and are developed simply to fit the observed data (e.g., Baker and Cornell, 2006a; Baker and Jayaram, 2008; Baker and Chen, 2020). Because of this lack of physical basis, these analytical models may somewhat deviate from the empirical correlation data in some parts. To address this potential shortcoming of sub-optimal fitting due to analytical functional form constraints, machine learning techniques were employed here. In particular, ANN (McCulloch and Pitts, 1943) was used to fit the data, eliminating the need to find suitable functional forms and keeping the misfit between observed and predicted data to a minimum. To the authors' knowledge, this technique has not been used to date for fitting predictive IM cross-correlation models. It must be clarified here, that the regression of the empirical data with ANN was done simply to provide a method to interpolate between the distinct

correlation coefficients and disseminate those, not to provide any additional insights into the underlying physical phenomena.

To adopt this technique, an ANN architecture first needs to be set up and the optimal hyperparameters for each model need to be chosen. The general mathematical expression to predict the correlation between an IM_i - IM_j pair for the case of a neural network with one hidden layer is given as:

$$\rho_{\log_{10}(IM_i), \log_{10}(IM_j)} = f_{activation2} \left[b_r + \sum_{h=1}^{n_h} W_{h,r} \cdot f_{activation1} \left(b_h + \sum_{p=1}^{n_p} W_{p,h} X_p \right) \right] \quad (5.7)$$

where X_p is the predictor feature p , $W_{p,h}$ is the weight of the connection between predictor neuron p and hidden neuron h , n_p is the number of predictor features, n_h is the number of hidden layer neurons, b_h is the bias of the hidden neuron h , $W_{h,r}$ is the weight of the connection between hidden neuron h and response neuron r , b_r is the bias of the response neuron r , $f_{activation1}$ and $f_{activation2}$ are the activation functions of the hidden and response layers, respectively. A natural logarithm transformation was applied to the predictor feature of only the following IM correlation pairs: $Sa-Ds_{595}$, $Sa-Ds_{575}$, $Sa_{avg2}-Ds_{595}$, $Sa_{avg2}-Ds_{575}$, $Sa_{avg2}-PGA$, $Sa_{avg2}-PGV$, $Sa_{avg3}-Ds_{595}$, $Sa_{avg3}-Ds_{575}$, $Sa_{avg3}-PGA$, and $Sa_{avg3}-PGV$.

A schematic representation of the network is illustrated in Figure 5.3 for the example case of the Sa -FIV3 correlation model, where the weights, W , and biases, b , of the activation function are also depicted. It is noted here that the T_{IM} notation means period of the period-dependent IM, for example T_{Sa} means period of Sa . Meanwhile, the chosen hyperparameters for each model are listed in Table 5.2a and 5.2b. Two hidden layers were required in most of the models to represent well the trends of the empirical data, with a high number of neurons per layer. Fewer neurons might also be adequate, but the goal was to resemble the empirical data as closely as possible, so having high number of neurons is more desirable, even though it creates relatively larger/heavier models. The activation functions are listed in Table 5.2a and 5.2b in the order of input, hidden, and output layers, respectively. *Softmax*, *linear*, *sigmoid*, and *tanh* activation functions were employed, as they were found to be optimal for the problem at hand.

Despite the fact that the *softmax* activation function is primarily used for classification problems, it found usage here, as it was seen that for the regression problems at hand, in conjunction with other activation functions, to capture the empirical values very well. In addition, it was seen that the fit was very similar when either *softmax* or *sigmoid* was used. Also, large numbers of epochs were chosen, as the goal here was to have the model predict values that are as close to the empirical ones as possible. In other words, overfitting here is desirable. Regarding the batch size, small numbers were chosen in these models, since the training data set is exceptionally small (i.e., one correlation coefficient per unique IM pair). The hyperparameter selection for the predictive models was done manually for each model. This is because the regression problems at hands were relatively easy to tackle, so there was no need for automated hyperparameter selection methods (i.e., Bayesian optimization or grid search). The goal was to reduce the MSE metric as much as possible, while also observing visually the mismatch between empirical data and predictions. The first model fitted was the correlation between *Sa-FIV3*, for which the optimal hyperparameters, reported in Table 5.2a, were found after a few attempts. For every subsequent correlation model, these parameters were tweaked accordingly to obtain a good fit for each case. It can be observed from the same table that each correlation model between different IM has different hyperparameters. This is because of different data size, different trends, and generally different values to fit. The MSE was selected as the loss function metric, which was minimized by the ADAM estimation algorithm (Kingma and Ba, 2014). Table 5.2a and 5.2b also report two common indicators to assess the “goodness of fit” (i.e., MSE and R^2) for each correlation model. It can be seen that the all the MSE values are lower than 10^{-4} , and all the R^2 values higher than 0.98, which both indicate that the match between empirical values and predictions is good.

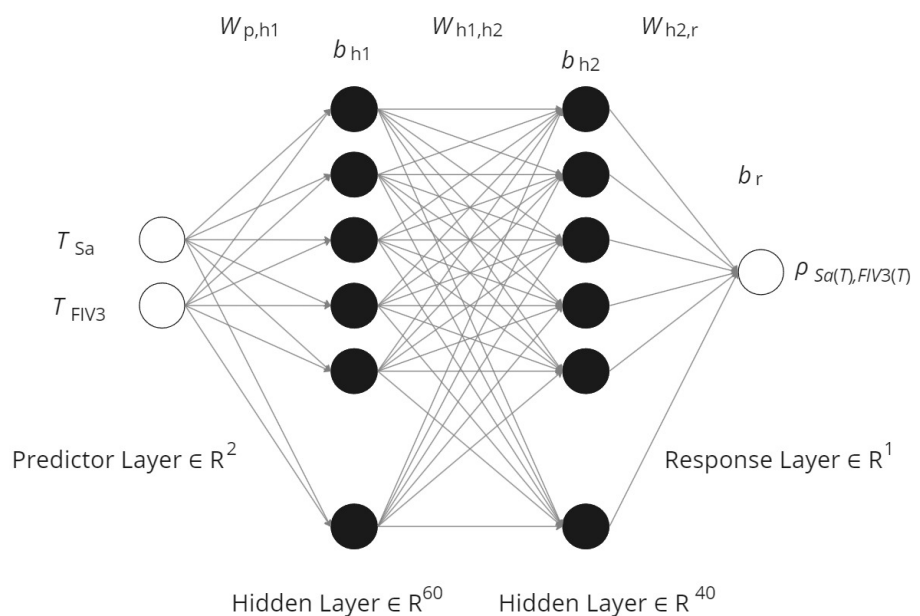


Figure 5.3. Schematic representation of ANN architecture for the case of *Sa-FIV3* correlation model

Table 5.2a. Key hyperparameters and general architecture of the adopted ANN correlation models

Correlation model	<i>Sa-FIV3</i>	<i>Sa-FIV3</i>	<i>FIV3-FIV3</i>	<i>FIV3-Ds595</i>	<i>FIV3-Ds575</i>	<i>Sa-Ds595</i>	<i>Sa-Ds575</i>	<i>Sa-Saavg3</i>	<i>Sa-Saavg2</i>	<i>Saavg3-Saavg3</i>	<i>Saavg3-FIV3</i>
Number of hidden layers	2	2	1	2	2	2	2	2	2	2	2
Activation functions	linear, sig-moid, tanh, linear	linear, soft-max, linear	linear, soft-max, linear, linear	linear, soft-max, linear, linear	linear, sig-moid, soft-max, linear	linear, sig-moid, soft-max, linear	linear, tanh, sig-moid, linear	linear, sigmoid, linear	linear, sigmoid, linear	linear, sigmoid, linear	linear, sigmoid, linear
Number of neurons per hidden layer	60 and 40	60 and 30	300	30 and 30	30 and 30	40 and 60	40 and 60	60 and 40	60 and 40	60 and 30	60 and 30
Epochs	800	1000	3000	400	400	1500	1500	1000	1000	1300	1000
Batch size	8	8	16	4	4	4	4	8	8	8	8
MSE	3.04E-05	3.94E-05	4.32E-06	6.55E-06	5.38E-06	2.56E-05	2.66E-05	2.83E-05	4.12E-05	3.21E-05	4.64E-05
R ²	0.9989	0.9991	0.9974	0.9990	0.9990	0.9994	0.9990	0.9990	0.9987	0.9988	0.9984

Table 5.2b. Key hyperparameters and general architecture of the adopted ANN correlation models

Correlation model	$S_{avg3-DS595}$	$S_{avg3-DS575}$	$S_{avg2-S_{avg3}}$	$S_{avg3- PGV}$	$S_{avg3- PGV}$	$S_{avg2- PGV}$	$S_{avg2- PGV}$	$S_{avg2-FIV3}$	$S_{avg2-Ds555}$	$S_{avg2-Ds575}$	$FIV3-PGV$
Number of hidden layers	2	2	1	2	2	2	2	2	2	2	2
Activation functions	linear, soft-max, soft-max, linear	linear, sig-moid, soft-max, linear	linear, sig-moid, soft-max, linear	linear, sig-moid, soft-max, linear	linear, soft-max, soft-max, linear	linear, soft-max, soft-max, linear	linear, soft-max, tanh, linear				
Number of neurons per hidden layer	60 and 40	60 and 40	300	60 and 40	50 and 50						
Epochs	1500	1500	3000	1500	1500	1500	1500	1500	1500	1500	1800
Batch size	4	4	16	4	4	4	4	8	4	4	4
MSE	4.60E-06	1.02E-05	2.00E-05	1.04E-06	5.82E-07	3.97E-06	4.81E-06	1.75E-05	9.89E-06	2.52E-05	9.44E-06
R^2	0.9999	0.9996	0.9993	1.0000	0.9998	0.9999	0.9989	0.9993	0.9997	0.9990	0.9983

5.6 Empirical results and model estimations

5.6.1 Correlations between traditional IMs

Of the 24 total IM cross-correlation models developed within this study, three are well documented in the literature. Many past studies investigated and proposed parametric models and/or empirical tabulated values for the estimation of correlation between Sa of different periods (Baker and Jayaram, 2008; Akkar, Sandikkaya, and Ay, 2014; Baker and Bradley, 2017), which is also examined here. The other well-documented models are $Sa-Ds_{575}$ and $Sa-Ds_{595}$, for which the works of Bradley (2011a) and Baker and Bradley (2017) were used for the comparisons. The correlations estimated here are discussed further in this subsection and compared with the aforementioned existing models.

Correlation coefficients between $Sa(T_i)$ and $Sa(T_j)$ for four distinct values of T_j are illustrated in Figure 5.4, where any differences between the empirical and predicted values, or differences between this and past studies, can be appreciated. First, it can be seen that the correlations predicted by the ANN model developed in this study are almost identical to the empirical data. This is seen throughout the range of values of the correlation model. This was very encouraging to see since it illustrates the utility of ANN models in this regard, which have yet to be employed for this purpose.

It can be observed that the correlations predicted by the Baker and Jayaram (2008) model somewhat deviate from the ones computed here, primarily where the inter-period “distance” increases. The BJ08 model generally underpredicts the correlations compared with the empirical data of this study. The impact of this underprediction on ground motion selection via conditional spectrum (Baker, 2011) would be that the variance around the target mean would be slightly higher, meaning that the selected ground motions would be more dispersed than they would be with using the proposed correlations. For structures where this spectral content at periods away from the conditioning period is relevant, it may result in an overprediction of structural demands. The difference of BJ08 model may be due to several factors. The most dominating factor was found to be the filtering of the ground motion records. Specifically, it was seen from background analyses, presented briefly in Appendix A, that the limits on

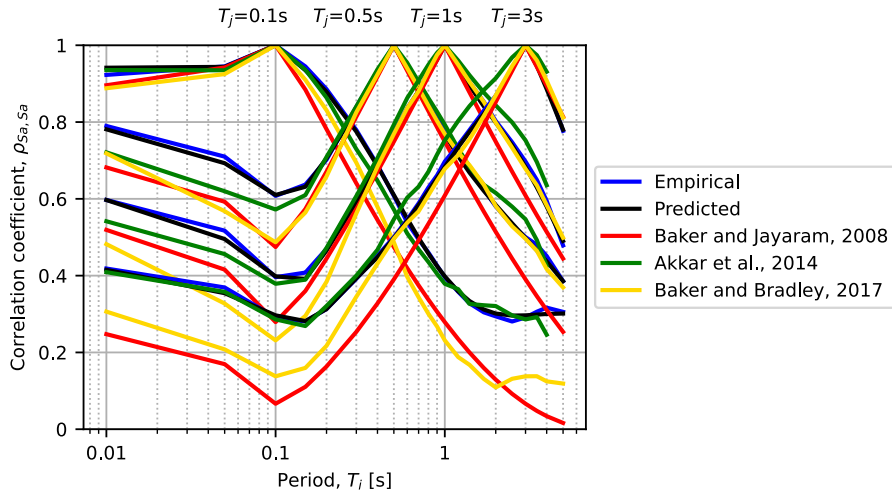


Figure 5.4. Correlation coefficients between $Sa(T_i)$ and $Sa(T_j)$ for four values of T_j

magnitude and distance ranges play the most important role. Other less important factors include first the difference in ground motion databases used, where BJ08 used the NGA-West database with approximately 2,500 recordings available at moderate periods, whereas the proposed models utilized a subset of NGA-West2 database containing 4,135 records. Second, small changes occur from the different GMM from which the residuals are computed. Finally, the expected errors involved in functional form identification can also be anticipated to have a minor impact.

The model of Baker and Bradley (2017) is very close to BJ08, because of their very similar filtering criteria (i.e., the ones of Chiou and Youngs (2008)). However, BB17 presents higher correlations, in most period ranges, than BJ08, but still lower than the proposed values. Even though the same base database as the proposed model is used (i.e., NGA-West2), the filtering criteria are different, and that is the main cause of differences in the correlation values.

The model of Akkar, Sandikkaya, and Ay (2014) utilized strong-motion accelerograms from the reference database for seismic ground-motion prediction in Europe (RESORCE) database (Akkar, Sandikkaya, Senyurt, et al., 2014). It consists of 1,041 accelerograms from 221 shallow active crustal earthquakes, most of which have epicentral locations in the Mediterranean

region and the Middle East. The correlation coefficients for Sa up to 4 s are plotted, as this represents the maximum period input that the model can accommodate. The ASA14 correlations appear closely aligned with the ones calculated here and exhibit very similar trends. In addition, there is no sign of consistent underprediction or overprediction in any period ranges. Nevertheless, there is still a small deviation from the values of this study in specific parts. The main reason that the ASA14 model is closer to the proposed model is because they considered only events with magnitude larger than 4, from a data set which includes mostly events with magnitudes between 5 and 6. Meanwhile, the models of BJ08 and BB17 include much wider magnitude (>3) and distance (<400 km) filtering limits, from events and sites of assorted regions, resulting in higher aleatory variability, and, therefore, lower correlations. These are decisions that can potentially affect the eventual correlation coefficients.

In the case of significant duration, Figure 5.5 shows that the empirical correlation with Sa increases (i.e., takes less negative values) with increasing vibration period. The coefficients are monotonically increasing, except for the period range between 0.1–0.3 s, where the slope is transiently negative. This is caused by a sudden small increase in correlation for $Sa(0.1s)$, which is considered insignificant from a practical viewpoint. The same observations were also noticed by previous studies (Bradley, 2011a; Baker and Bradley, 2017), but can be a consequence of the available data rather than an underlying physical feature. Nevertheless, this behaviour is regressed by a smooth, monotonically increasing, curve. Correlation of Sa with Ds_{575} is slightly more negative than the one with Ds_{595} , especially in longer periods of Sa . The fact that the correlation between Ds and high-period IMs (i.e., $Sa(T > 2$ s) and $FIV3(T > 1$ s) discussed later) is relatively small (i.e., weak linear relationship) suggests that ground motions with more energy concentrated in high periods do not translate to higher significant duration, or vice versa. Generally, duration exhibits a negative correlation with low-period IMs. This is an expected result since ground motions with longer-than-predicted durations tend to have their energy scattered over a longer period of time and are, therefore, less likely to cause large peak responses in a short-period damped oscillator. This is in contrast with long-period oscillators that resonate with longer duration of shaking and, therefore, present little or no negative correlation.

Regarding the comparison with the B11 model, the trend is very similar,

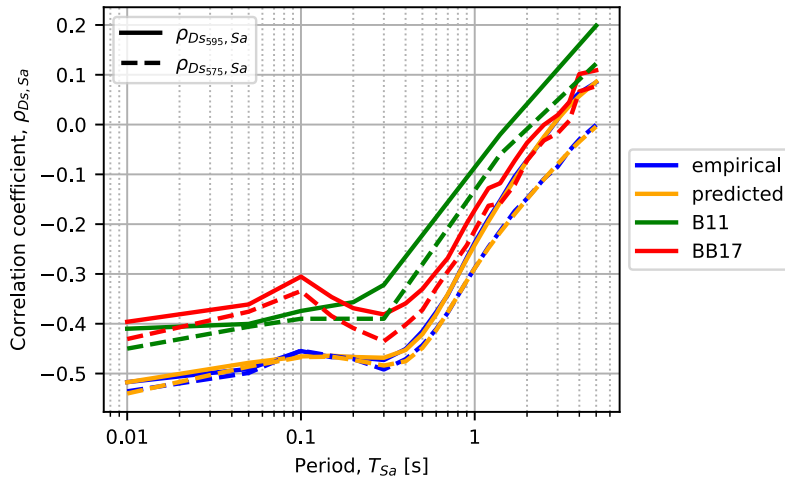


Figure 5.5. Empirical and predicted Sa - Ds_{595} and Sa - Ds_{575} correlation of the ANN and Bradley (2011a) models

but the correlations computed here are shifted downward by about 0.1 across the whole range of Sa periods. This is primarily due to the different filtering criteria and secondarily due to the difference in the ground motion database used (NGA-West versus NGA-West2), and the different GMMs employed. Also, the total number of ground motions utilized in that study was 1,842. The BB17 correlations are more in line with the B11 correlations for low periods, and they converge to the proposed $\rho_{D_{595}, Sa}$ for long periods. As stated above, the difference is mostly due to the filtering of the ground motion database, since BB17 also used the NGA-West2 database.

5.6.2 Correlations between traditional and next-generation IMs

To select ground motions via the CS or GCIM methods that match the distribution of next-generation IMs conditioned on traditional IMs, which is often the goal of a more advanced ground motion record selection, the correlations between those traditional and next-generation IMs are needed. A few of those models are presented in this subsection. For instance, Figure 5.6 presents the observed/empirical and predicted correlations between Sa and $FIV3$. The empirical coefficient values range from 0.35 to 0.95. The

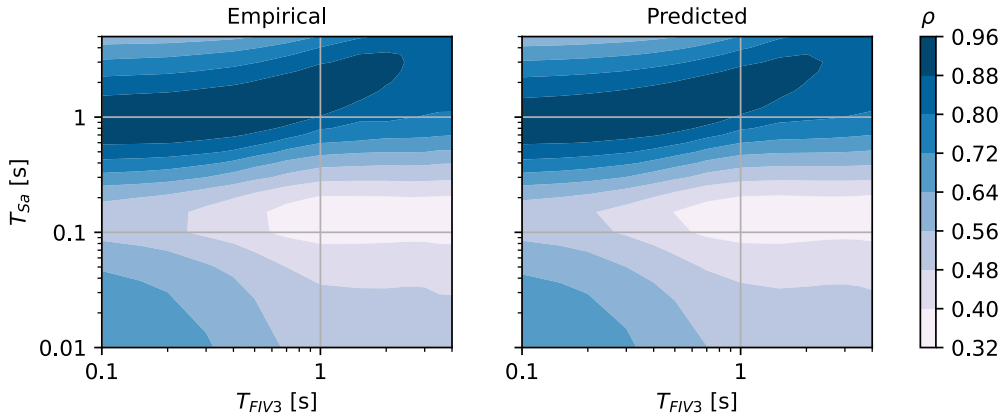


Figure 5.6. Empirical and corresponding predicted correlation coefficients between Sa and $FIV3$

results indicate that $FIV3$ of most periods is highly correlated with $Sa(1s)$, which is the IM recommended by HAZUS (2003) to be used for seismic assessment of bridges in the United States. Also shown in Figure 5.6 are the corresponding predictions by the proposed ANN model, which capture the empirical data very well, as can be concluded by a visual inspection.

Figure 5.7 illustrates the empirical and predicted correlation coefficients of Ds_{595} - $FIV3$ and Ds_{575} - $FIV3$. First, it can be observed that the correlation of Ds_{595} - $FIV3$ is negative for all periods of $FIV3$, with values ranging from -0.3 for the lowest period $FIV3$ to about -0.08 for the highest period $FIV3$. The trend is monotonically increasing and plateauing after an $FIV3$ of period 2 s. The negative correlation coefficients suggest that a ground motion with a higher-than-predicted $FIV3$ will, on average, have a lower-than-predicted duration. This was suspected to be attributed to the ground motion releasing all of its energy within a few strong velocity pulses rather than over a long duration; however, the work of Tarbali et al. (2023) studied the effect of near-fault directivity pulses on correlations between Ds and other IMs and found that the effect was essentially negligible. Any differences found in that study were mainly attributed to the data set ground motion distribution and sample size, rather than the inherited characteristics of directivity pulse-like records. Overall, the trend of Ds - $FIV3$ correlations is very similar to the correlation trend between Sa and Ds , shown previously in Figure 5.5. For the case of Ds_{575} , the coefficients

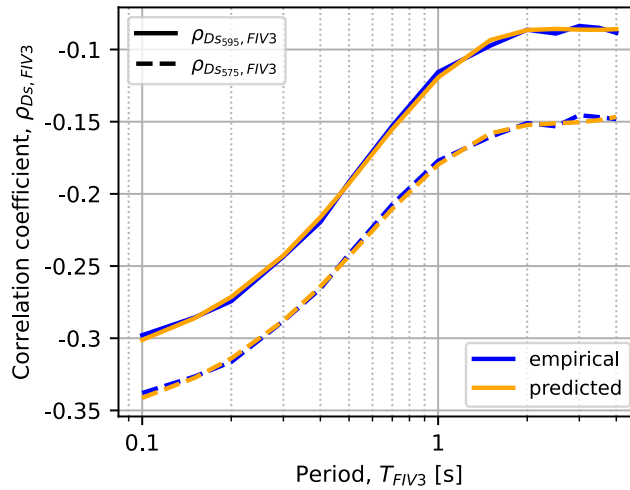


Figure 5.7. Empirical and corresponding predicted correlation coefficients between Ds_{595} -FIV3 and Ds_{575} -FIV3

are shifted down by about 0.05. The empirical results suggest that FIV3 is more correlated with Sa than Ds_{595} .

Regarding the correlation between Sa and Sa_{avg3} , the difference or similarity between empirical and predicted coefficients can be assessed visually in Figure 5.8, where slices of two different periods of Sa_{avg3} are presented as demonstrative examples. From that, it can be concluded that the match between empirical and predicted values is excellent. As expected, the Sa_{avg3} of period T_i best correlates with Sa of period somewhat higher than T_i . Very similar results were found for the case of Sa_{avg2} , but not presented here due to space limitations. Kohrangi et al. (2017) presented an approach to develop a CS for Sa conditioned on a specific value of Sa_{avg} at the period of interest. This was done with the so-called “indirect” and “direct” methods, while comparing the two. The indirect method included in Figure 5.8 uses the CB14 GMM and BJ08 correlation model for the first case and the CB14 GMM and ASA14 correlation model for the second case. The main difference in the indirect methods here comes from the correlation models, rather than the GMM since it was generally found that the CB14 model predicts almost identical Sa values as the GMM used here (Aristeidou et al., 2024). Thus, the indirect method that uses the ASA14 correlation model results in about the same correlation coefficients as the

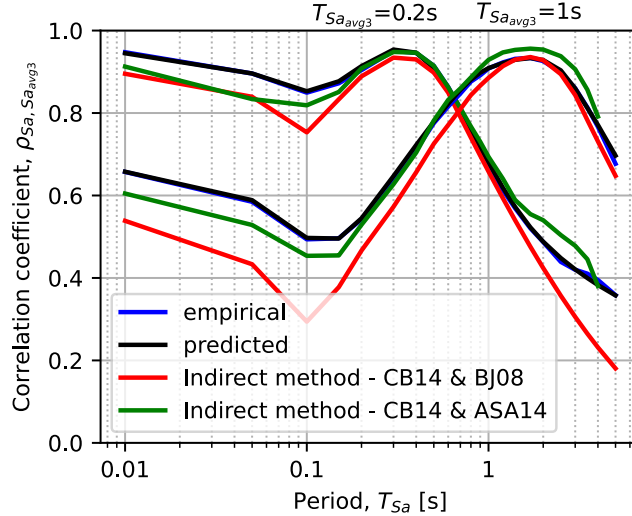


Figure 5.8. Correlation coefficients between $Sa(T_i)$ and $Sa_{avg3}(T_j)$ for two values of T_j

proposed model, which is an encouraging result as it also provides a sort of validation to that theoretical development. That is because the ASA14 model itself is closer to the $Sa-Sa$ correlation model proposed here than the BJ08 correlation model.

Figure 5.9 illustrates the empirical and predicted correlation coefficients of $Sa_{avg3}-Ds_{595}$ and $Sa_{avg3}-Ds_{575}$. They are closely resembling the ones between Sa and Ds . The most negative correlation is found in the shortest period of Sa_{avg3} , while for long periods of Sa_{avg3} , the correlation with Ds takes smaller negative values and eventually approaches zero at a period of 4 s for the case of Ds_{595} . Meanwhile, the correlation with Ds_{575} is generally more negative, with the difference getting amplified in longer periods of Sa_{avg3} . The predicted coefficients almost overlap the empirical ones.

5.6.3 Correlations between next-generation IMs

Next-generation IMs showed improved performance in predicting different levels of nonlinear behaviour and collapse estimation in several past studies. Therefore, one may utilize one of the most recent record selection methodologies to consider the conditional distribution of a set of next-generation

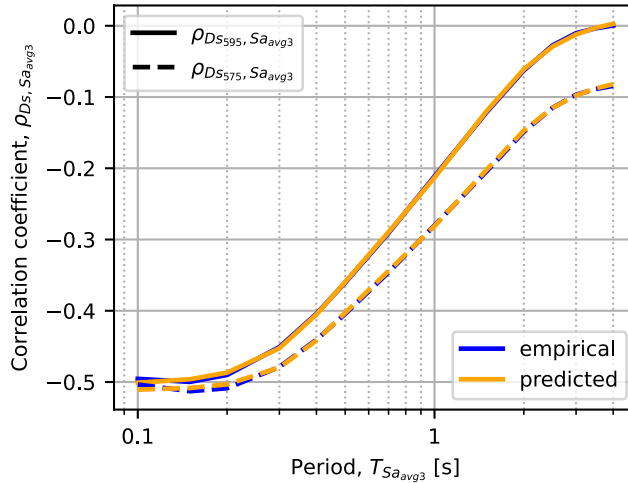


Figure 5.9. Empirical and corresponding predicted correlation coefficients of Sa_{avg3} - Ds_{595} and Sa_{avg3} - Ds_{575}

IMs when performing seismic risk studies.

Figure 5.10 shows the inter-IM correlations of $FIV3$ at different periods, with empirical correlation coefficients ranging from about 0.86 to 1, which suggests that $FIV3$ is strongly correlated between itself at different periods. This can be better appreciated in Figure 5.11, illustrating these same data slightly differently whereby specific slices of Figure 5.10 are shown. Also shown are the Sa - Sa correlations that were discussed in a previous subsection. This relative comparison affirms that $FIV3$ is much more correlated to itself across different periods than Sa . This signifies that $FIV3$ can be treated as almost a period-independent IM, in a similar way that PGA has been used traditionally, but with the added value of much-improved efficiency in its near-collapse response prediction, as past studies have noted. Also noted are the close predicted coefficients to the empirical ones, confirming the precision of the model. To the best of the authors' knowledge, there are no available correlation models of $FIV3$ with any other IM or with itself, which constitutes a novelty of this study.

The empirical and predicted correlation coefficients between Sa_{avg3} and $FIV3$ are presented in Figure 5.12, and they closely resemble the ones between Sa and $FIV3$. It can be noticed that the Sa_{avg3} at a period of about 1 s is well-correlated with $FIV3$ of most periods.

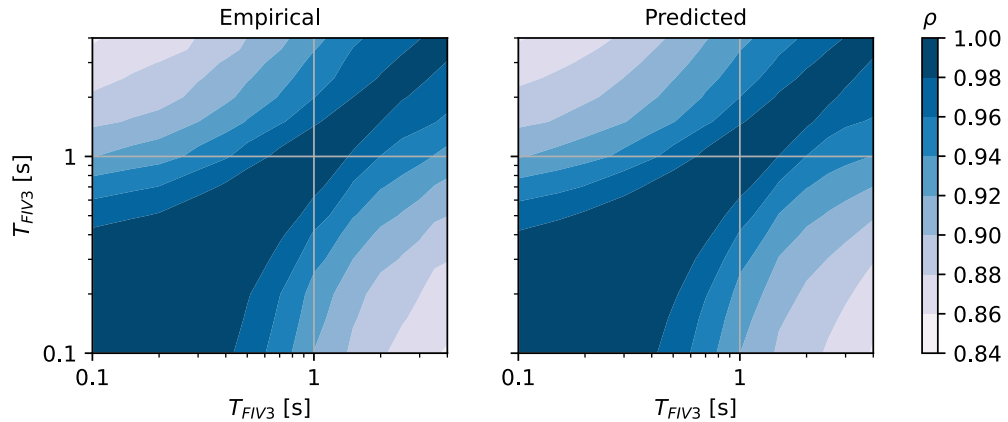


Figure 5.10. Empirical and corresponding predicted correlation coefficients between $FIV3$ of different periods

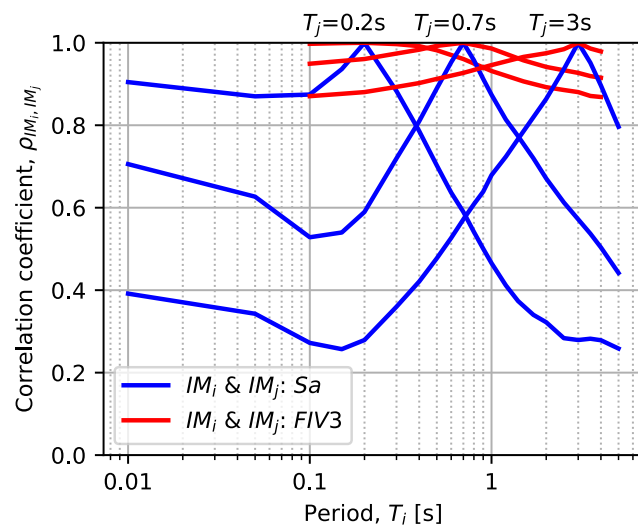


Figure 5.11. Empirical correlation coefficients between $Sa(T_i)$ - $Sa(T_j)$ and $FIV3(T_i)$ - $FIV3(T_j)$ for three values of T_j

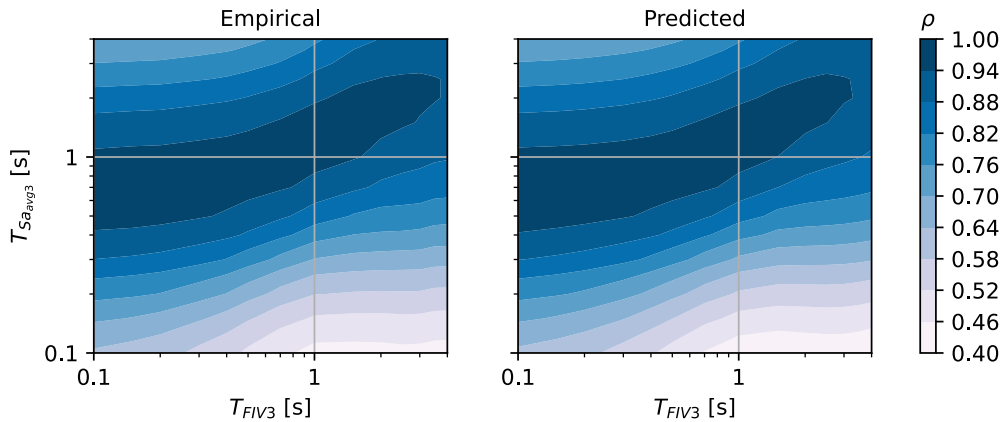


Figure 5.12. Empirical and corresponding predicted correlation coefficients between Sa_{avg3} and $FIV3$

Figure 5.13 illustrates the contours of empirical and predicted correlation coefficients between Sa_{avg3} of different periods. Figure 5.14 presents two slices of correlation coefficients between Sa_{avg3} for the case of periods 0.2 and 1 s. Also superimposed is the corresponding model proposed by Dávalos and Miranda (2021), which features the same period range for Sa_{avg} as the one used here for Sa_{avg3} . The DM21 model under predicts the correlation coefficients calculated here, which could be attributed to the different filtered data set used for the regression of the GMM and for the correlation model. For instance, one difference could be the filtering of the $V_{s,30}$ values, which were limited between 180 and 360 m/s, corresponding to national earthquake hazards reduction program (NEHRP) site class D. In any case, further investigations would be needed to identify the precise cause of this difference.

5.7 Discussion and conclusions

This study presented the empirical correlations between assorted IMs of various types, namely PGA , PGV , Sa , Ds , Sa_{avg} , and $FIV3$. The residuals, which are used for the calculation of correlations, were obtained from a previously developed GGMM and the same filtered ground motion database. This is believed to produce more consistent correlation coefficients

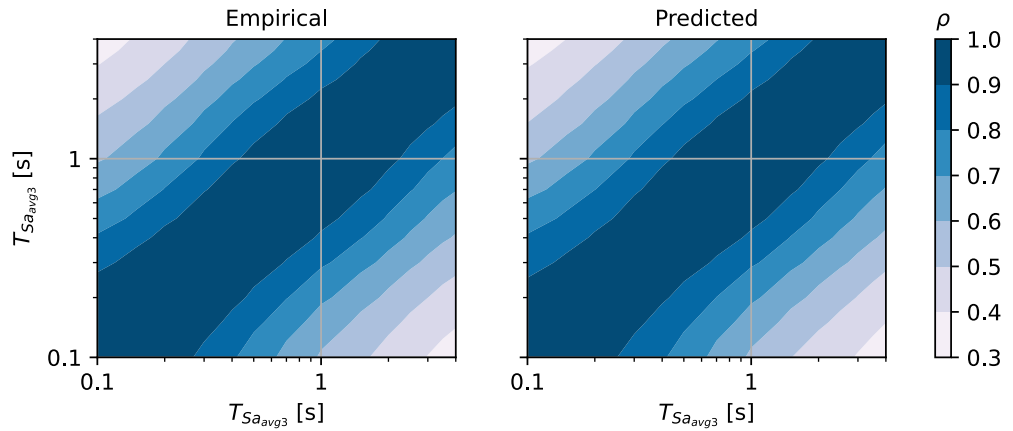


Figure 5.13. Empirical and corresponding predicted correlation coefficients between Sa_{avg3} of different periods

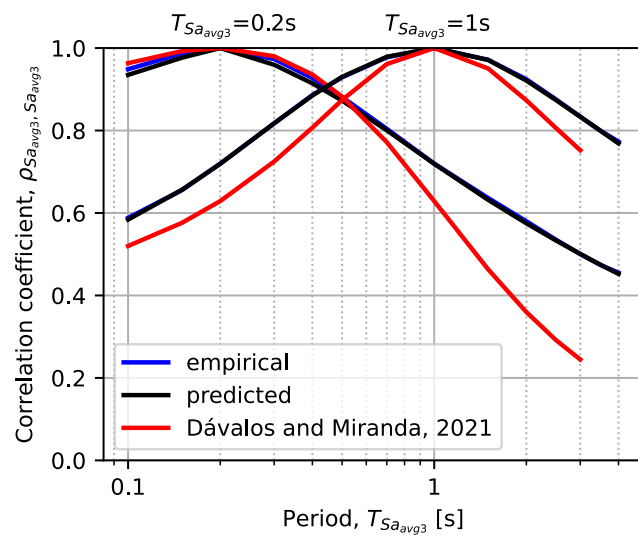


Figure 5.14. Correlation coefficients between $Sa_{avg3}(T_i)$ and $Sa_{avg3}(T_j)$ for two values of T_j

since the same filtered database is used for the development of the GMM and the calculation of residuals used for the calculation of empirical correlation coefficients.

In total, 24 correlation predictive models were developed based on a novel approach via ANNs for the regression. It was shown how these models could excellently and adaptively fit the empirical data. Well-established correlation models from the literature were used to compare with the empirical and ANN-based correlation models proposed here. Based on the results, the following conclusions can be drawn from this research:

- Comparing correlations between traditional IMs with pre-existing models instills confidence in the empirical correlation coefficient computations and the sensibility of estimated residuals. That stems from the close alignment of their values to the empirical data, or at least their consistent adherence to the same trends.
- The *FIV3* presented a relatively strong correlation with *Sa*, especially in the range of $Sa(T = 0.6s)$ to $Sa(T = 3s)$, which indicates that *FIV3* is best correlated with moderate- and long-period IMs and less correlated with short-period IMs.
- The correlation between *Ds* and *FIV3* showed the same trend as that of *Ds* and *Sa* but with a slightly weaker negative correlation (i.e., taking values closer to 0).
- The direct correlation between *Sa* and *Sa_{avg}*, developed here as a novel correlation model, will allow for more consistent ground motion record selection procedures when both of these IMs are considered, as several studies have already been carried out via an indirect method.
- The correlation between *Ds* and *Sa_{avg3}* closely resembles that of *Ds* and *Sa*.
- It was found that *FIV3* is strongly correlated with itself, with the correlation values not dropping below 0.86, essentially making this IM almost period-independent, which could be useful for more general and regional studies.
- Correlation between *FIV3* and *Sa_{avg}* exhibits similar behaviour to that of *FIV3* and *Sa*.

- The correlation models between Sa_{avg} spectral ordinates of different periods can be used to create a conditional spectrum based on Sa_{avg} , instead of Sa . The higher inter-IM correlations and lower dispersions of Sa_{avg} will produce spectra with less pronounced pinching at the conditional period and smaller spectral ordinates than CS based on Sa .
- The empirical results obtained in this study present some differences when compared to existing models, which were attributed mainly to the differences in the filtered database, and secondary to the utilized GMM and base database. It was seen that the fitting methodology of the existing models has negligible effect.
- The proposed predictive ANN models estimate the empirical data with high precision, as confirmed by the reported low MSEs, and high coefficients of determination. Simultaneously, it facilitates a seamless application since the models are readily available online.

Finally, a few correlation models have not been presented here graphically due to information redundancy. Nevertheless, their coefficients can be obtained from the data provided online, as described in Section 5.8. The period range of applicability of these correlation models spans from 0.01 s to 5 s for Sa , 0.1 s to 4 s for Sa_{avg} , and 0.1 s to 4 s for $FIV3$. The ground motion causal parameters' range of applicability can be taken as the minimum and maximum value of each predictor feature used in the development of GGMM (Aristeidou et al., 2024). The same methodology and similar network architectures can be adapted to seamlessly come up with correlation models between other IMs or other horizontal component definitions. Overall, the models presented in this study represent a notable step toward allowing seismic risk analysts to adopt these next-generation IMs in their studies and account for their cross-correlations during ground motion record selection.

5.8 Code availability

The relevant files and functions that can be used to get the correlation models' estimations presented here are available on GitHub at: <https://>

github.com/Savvino-Aristeidou/ANN_correlation_models.git. The user has the option of choosing whether they want to get the correlation values from the raw empirical tabulated values, via linear interpolation, or from the predictive model fitted with ANN. It is worth noting that there is no need to load any specific Python package to use the ANN models, but rather the code loads a file with all the fitted coefficients (i.e., weights and biases) and the activation functions and uses the ANN analytical functional form to output the correlation values.

Chapter 6

Implications of conventional and next-generation intensity measure-based ground motion record selection for risk assessment

6.1 Introduction

Seismic risk assessment of structures, particularly bridges, has evolved significantly over the years with advancements in ground motion modelling and the development of next-generation IMs. Traditional approaches often relied on simpler IMs, such as PGA , which, while convenient, is insufficient in capturing the complex response of multi-modal and multi-component systems like bridges (Luco & Cornell, 2007; Huang et al., 2010). Recent research has highlighted the importance of utilising advanced IMs that better reflect the underlying seismic hazard that can be of higher engineering interest (e.g., Kohrangi et al., 2019; Dávalos and Miranda, 2020). These advanced (or next-generation, as dubbed here) IMs not only improve the accuracy of seismic hazard representation but also enhance the reliability of risk predictions, addressing the limitations of older approaches. Building on this foundation, some IMs of engineering interest were integrated herein with advanced modelling and evaluation techniques to assess the level to which they enhance seismic risk for bridge structures.

This final chapter of the thesis leverages the developed GGMM and correlation models, presented in Chapters 4 and 5, to demonstrate the potential

of next-generation IMs in enhancing seismic risk assessment. These models enabled improved predictive power and more accurate representation of seismic hazard. This chapter also shows the practical applicability of the aforementioned models in ground motion record selection and risk assessment.

This chapter begins with a review of the evolution of ground motion record selection for structures, with a particular focus on bridges, positioning this work within the context of state-of-the-art in the field. Next, the case study bridge structures and their numerical models are described. Ground motion selection strategies and seismic hazard analysis of the conditioning IMs are then introduced, setting the stage for the subsequent multiple stripe analysis (MSA), for which a few example results are presented. Finally, the chapter concludes with a comparison and critical evaluation of the structural response statistics and risk estimates, highlighting the significance and practical implications of the findings.

6.2 Ground motion input for bridge structures

The selection and scaling of ground motion input are critical steps in the seismic analysis of bridge structures. Ground motions are typically selected and scaled based on seismic scenarios that match the site-specific hazard, coming from either PSHA, or design code requirements. Scaling is usually done to achieve a specific IM value, and subsequent selection to match the spectral shape (or distribution in the probabilistic case). Many studies continue to rely on IM definitions, such as PGA or Sa at a fixed period (HAZUS, 2003; Del Gaudio et al., 2017; Villar-Vega et al., 2017) for regional risk assessments. Although they recognise that IMs like PGA are not ideal, they are often used as a baseline standard due to their simplicity and widespread adoption for convenience.

There are several ground motion selection approaches listed and briefly described in the following. The UHS-based approach, commonly employed in seismic design codes such as Eurocode 8 (CEN, 2005) and ASCE 7 (ASCE, 2017), involves selecting and scaling ground motions to match the UHS for a given return period. However, the UHS does not really represent the physical characteristics of individual earthquakes, but instead

aggregates the seismic hazard across all potential magnitudes, distances, and fault mechanisms, selecting the maximum intensity at each period for a given return period. This tends to overestimate hazard at certain periods and lead to conservative design requirements. While UHS-based selection remains prevalent due to its simplicity and alignment with design code requirements, advanced methods such as the CS (Baker, 2011) and GCIM (Bradley, 2010) offer a more rigorous probabilistic framework, with a more nuanced representation of ground motion variability. They offer the capability of conditioning the selection process on a specific intensity measure or multiple IMs. These methods ensure consistency with PSHA and are particularly suited for performance-based assessments. Scenario-based assessment (Tarbali and Bradley, 2015), on the contrary, selects ground motions that represent specific seismic events, such as characteristic earthquakes from a known nearby fault. While this approach provides realistic inputs for scenario-specific studies, which can sometimes be easier to communicate, it lacks the versatility required for probabilistic risk evaluations.

For bridge-specific analyses, considerations such as long-period motions for flexible structures, site effects, and multi-support excitations due to varying soil and pier conditions can provide additional insights. These factors may influence the development of fragility curves and the assessment of seismic risk. However, for the purposes of this study, these considerations were omitted to focus on the primary objective of assessing the impact of different ground motion selection schemes on the response of the bridge. While these factors could affect the absolute values of fragilities and risk estimates, they are not expected to significantly alter the conclusions and relative comparisons of the different ground motion selection schemes examined here. Future work could incorporate these additional factors to enhance the robustness and generalisability of the findings.

6.3 Case study structures

6.3.1 General description

To examine the influence of the different combinations of conditioning and matching the different IMs on the fragility assessment of bridges, seven multi-span bridges, each comprising either of 4 or 8 spans of 50 m, were

Table 6.1. Modal properties of each case study bridge structure

ID	Type	T_1 [s]	T_2 [s]	T_3 [s]	% M_1	% M_2	% M_3	$\Sigma\%M$
B-1	Irregular	0.555	0.447	0.277	30	8	27	65
B-2	Irregular	0.555	0.474	0.253	30	19	5	53
B-3	Regular	0.483	0.475	0.223	32	0	66	98
B-4	Regular	0.508	0.475	0.307	6	0	77	94
B-5	Regular	0.479	0.479	0.225	16	0	76	92
B-6	Irregular	0.494	0.474	0.360	3	10	29	42
B-7	Irregular	0.556	0.436	0.387	11	7	35	53

analysed. These bridges, previously studied by Pinho et al. (2009) and O'Reilly (2021b) are representative of typical European bridge designs, featuring reinforced concrete (RC) piers designed according to Eurocode 8 (CEN, 2005). The piers have a hollow rectangular cross-section, while the deck is continuous, with reinforcement details depicted in Figure 6.1. Pier heights are either 7 m, 14 m, or 21 m, and the bridges were categorised as regular or irregular based on the pier height variations along their length. Table 6.1 summarises the modal properties of the bridge structures and their classification as either regular or irregular, with additional illustrations shown in Figure 6.2.

The longitudinal reinforcement is consisted of 20 mm diameter bars evenly spaced at 110 mm along the shorter dimension, 310 mm along the longer dimension, and 600 mm for the innermost bars. The concrete cover thickness is 20 mm, with reinforcement yielding at 500 MPa and a concrete compressive strength of 42 MPa. As noted by Pinho et al. (2009), the piers were modelled as fixed at their bases and rigidly connected to the underside of the deck, while the deck ends rest on linear bearings at the abutments. By considering bridges with varying span number and pier height arrangement, and consequently different stiffness distributions, the study aimed to (1) evaluate the effects of period elongation resulting from damage to the pier elements, (2) explore the relevance of regularity/irregularity of the bridge, (3) investigate the influence of multiple significant response modes of bridge structures, and (4) achieve a level of generalisation for different structural configurations of bridge structures.

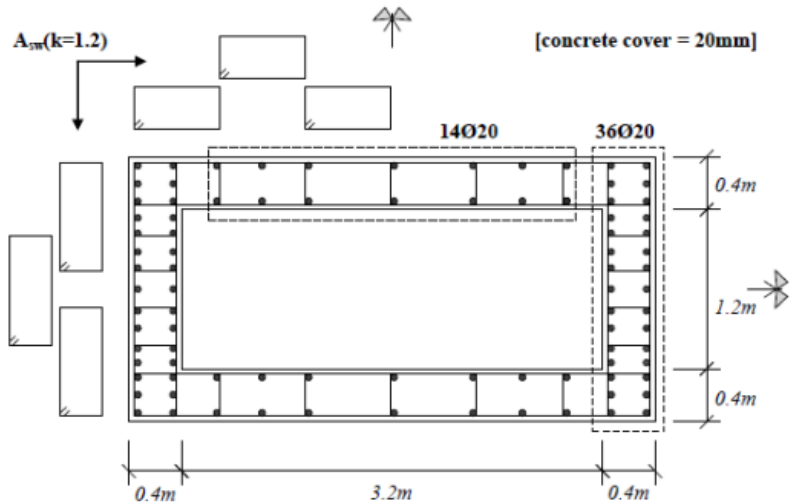


Figure 6.1. Illustration of structural detailing of the pier cross section (Pinho et al., 2009). The shorter side of the section is placed in the direction of the bridge deck

6.3.2 Numerical modelling and EDP definition

A numerical model for each bridge was adapted to OpenSeesPy (Zhu et al., 2018) from the existing OpenSees model detailed in O'Reilly and Monteiro (2019). The deck system was modelled as a continuous elastic beam-column element with effective cross-sectional properties and distributed mass. For simplicity, the piers were assumed to have fixed bases, and the deck ends

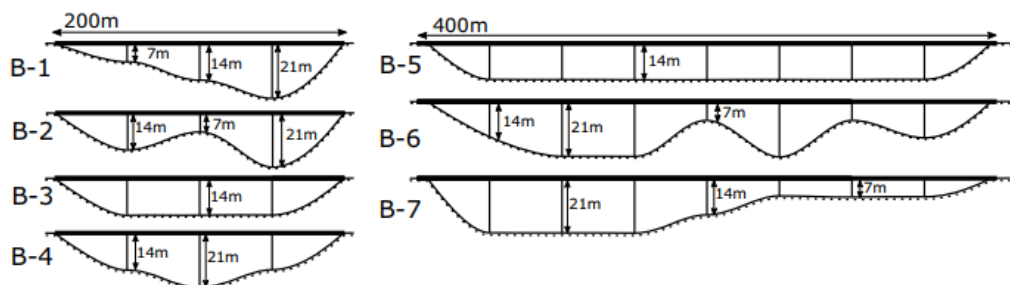


Figure 6.2. Illustration of the longitudinal profile of the case study bridge structures. Adapted from O'Reilly (2021b)

were supported by pot bearings. Although a more refined foundation model could have been implemented, it was deemed unnecessary for the focus of this study, which focusses on the relative comparison of different ground motion selection strategies.

The pier elements were represented using lumped plasticity models, with their parameters derived from moment–curvature analysis of the corresponding fibre-based section. To capture the rupture of the reinforcement bars and the subsequent loss of strength in the pier sections, the *MinMax* criterion was applied in OpenSeesPy, which simulated the loss of strength in the rebars when a predefined strain threshold was exceeded. This rupture strain was set at 0.10, based on Priestley et al. (1996) for reinforcement steel in European bridges. The only difference from the modelling parameters described in O'Reilly and Monteiro (2019) and O'Reilly (2021b) is the use of the *HystereticSM* material for the lumped plasticity hinges. This material was implemented with a pinching factor for deformation during reloading of 0.8, a pinching factor for force during reloading of 0.2, a damage parameter due to ductility of 0.001, and a damage parameter due to energy of 0.0001. Incorporating cyclic and in-cycle stiffness and strength degradation was essential here for two main reasons: firstly, to capture the effects of matching (or not) the theoretical GCIM distribution of D_s and the implications of matching and/or conditioning to *FIV3*; and secondly, to ensure the model exhibits behaviour that more closely approximates real-world structural response.

As one of the objectives of this study was to evaluate the dispersion in response due to record-to-record variability and its relationship to different ground motion inputs, epistemic uncertainties related to numerical modelling parameters were not considered. A single deterministic model was utilised for each bridge structure.

Modal analysis was performed to determine the dynamic properties of each bridge structure. Table 6.1 presents the periods, T , and modal mass participation factors, M , for the first three modes of vibration, as well as their cumulative sum for each structure, focusing exclusively on the transverse direction of response. It is evident that some periods are closely spaced, and none of the first modes capture a significant portion of the modal mass. This highlights that, unlike building structures, bridges generally lack a dominant first mode that adequately represents the entire dynamic response.

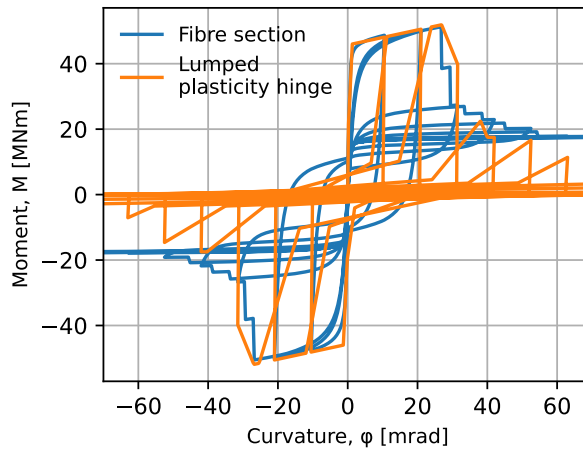


Figure 6.3. Moment curvature analysis of bottom section of the Pier with 7 m height. 10 cycles of unloading/reloading are shown here as an example, with equal curvature increments until the target curvature

Additionally, it is worth noting that for regular bridge structures, the first three modes account for most of the modal mass (over 92%), whereas in irregular bridge structures, the first three modes collectively represent less than 65% of the modal mass, indicating a much more disperse modal mass distribution.

To characterise the structural response under increasing intensity, an appropriate structural demand parameter, or EDP, was required. In bridges, the absence of a dominant mode or a clearly critical element complicates the selection of a suitable EDP. While global EDPs, such as peak deck displacement, can be employed, they may fail to adequately capture the extent of damage in piers with varying heights. Given the structural configuration of the bridges, the piers were identified as the critical elements susceptible to structural damage. Since piers were fixed at their base and rigidly connected to the deck, the largest inelastic demand occurs at their base.

Considering the simplicity of the bridge models used in this study, element-specific EDPs were preferred. Specifically, the peak transient section curvature at the base of the piers was monitored during the ground shaking. The maximum curvature among all piers, ϕ_{max} , was then selected

as the EDP. The curvature direction was the transversal, since in the records were applied only in the transversal direction. The collapse limit was assumed to be when the first pier reached 60 mrad of base curvature, since as seen in Figure 6.3 there is almost no moment resisting capacity in the pier at that level of deformation. Other failure mechanisms, such as pier shear failure, deck unseating, and foundation or abutment failure, could also be considered in more detailed studies. For instance, Borzi et al. (2015) highlighted these mechanisms for older Italian bridges, where shear failure and deck unseating were observed in past seismic events, and the two limit states were subsequently incorporated into a global demand-capacity envelope EDP, as described by Jalayer et al. (2007).

6.4 Hazard analysis

PSHA was carried out for a site in Erzincan, Turkey using the OpenQuake (GEM, 2022) open-source software for seismic hazard and risk assessment developed by the Global Earthquake Model Foundation. The source model input was the ESHM20 model (Danciu et al., 2021) and the GMM was the one previously described in Chapter 4 by Aristeidou et al. (2024). Erzincan was selected as the case study site as it exhibits one of the highest seismic activities in Europe and Middle East and has been struck by a devastating $7.8 M_w$ earthquake in 1939, among others. This high seismicity facilitates the characterisation the bridges' performance throughout the whole range of nonlinear response without needing to reach very high return periods.

The hazard curves of each IM used to analyse bridge 1 are shown in Figure 6.4. The hazard curves of the IMs at other periods are omitted here for brevity, but would be similar and were characterised the same way. Additionally the hazard disaggregation for the IMs of bridge 1 are given in Figures 6.5, 6.6, and 6.7. It can be seen that most of the hazard is controlled by source-to-site distances below 30 km and magnitude mostly above 6.5. There are many scenarios contributing to the hazard, especially in low return periods, but for simplicity only the modal rupture scenario was used to select ground motions at each return period as a first-order representation of the full disaggregation distribution. This is an approximation that is only appropriate when the seismic hazard disaggregation shows that only a single rupture scenario, *rup*, strongly dominates the hazard (Baker et

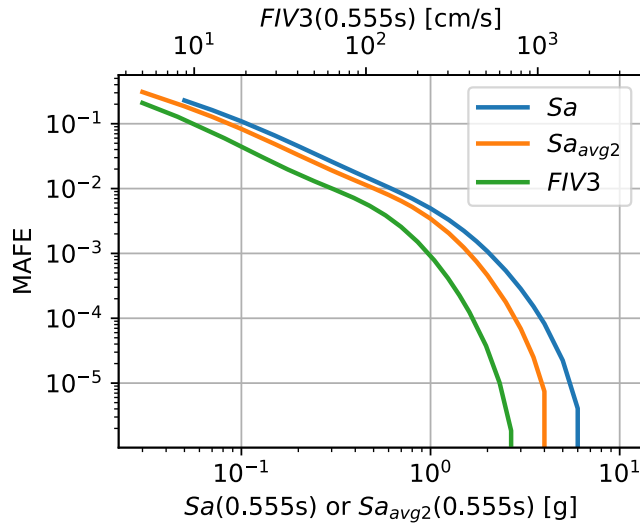


Figure 6.4. Hazard curves of IM* of bridge 1

al., 2021). An alternative choice for this approximation could be the mean rupture scenario, which involves computing a weighted mean of all the causal parameters (i.e., magnitude, and distance) or directly including all contributions in the ground motion selection. However, based on the observation of Lin et al. (2013a) the impacts of these nuances to the record selection are not deemed critical enough to have a notable impact on the comparative assessment carried out herein.

It is also important to have a sense of the dispersions of $IM|rup$ for the different conditioning IMs used in this study. In this case, the input rupture parameters used in the estimation of $\sigma_{IM|rup}$ are irrelevant, because the GGMM used is homoscedastic (i.e., dispersion of IMs is independent of rupture parameters). Therefore, the $\sigma_{IM|rup}$ calculated for a period of 0.5 s (which is an intermediate period between the T_1 of the analysed structures) was 0.66, 0.58, and 0.58 for Sa , Sa_{avg2} , and $FIV3$, respectively. The lower GGMM dispersion of $FIV3$ and Sa_{avg2} indicates a better predictability with respect to other IMs and further encourages their usage in risk analyses. Indicative dispersions of other commonly used IMs (e.g., PGA , PGV , and $Sa(1s)$ (HAZUS, 2003)) is presented in Figure 3.4. It can be seen that PGA and PGV present lower, and $Sa(1s)$ presents higher $\sigma_{IM|rup}$ than $FIV3$ and Sa_{avg2} . Nevertheless, they are all have comparable values, since the

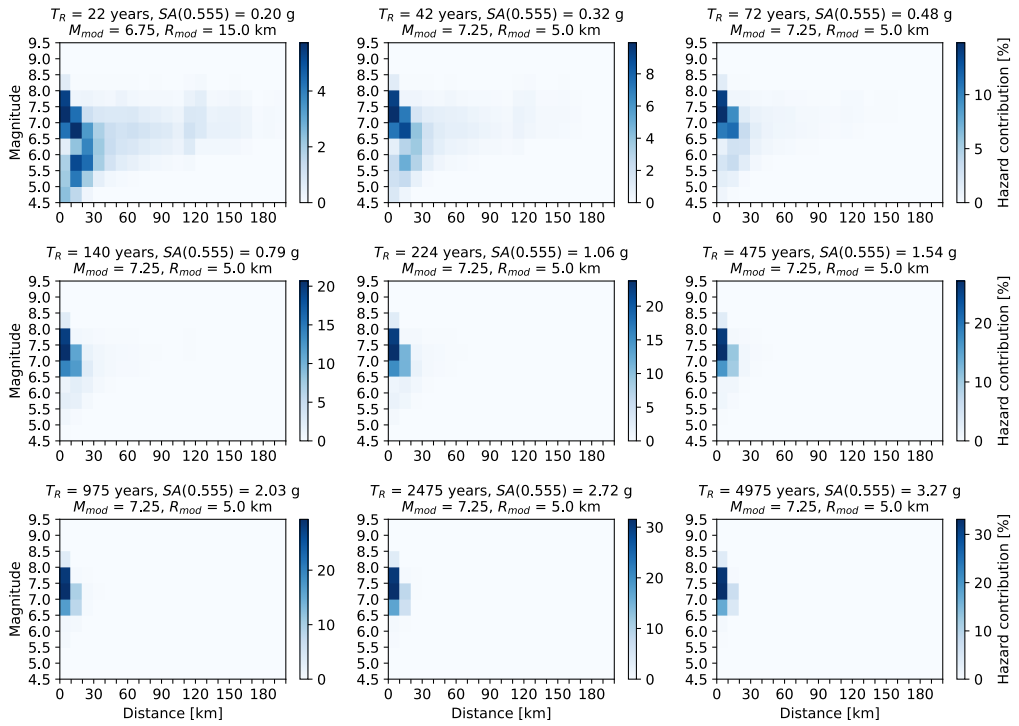


Figure 6.5. Hazard disaggregation of Sa at 0.555 s for the nine return periods investigated

difference of all these IMs is within about 0.1 unit of dispersion.

6.5 Ground motion selection schemes: conditioning IMs, matched spectra and matched IMs

The GCIM ground motion selection approach, introduced by Bradley (2010) extends the principles of the CS approach (Baker, 2011) by allowing the matching IMs to differ from the conditioning IM. This addresses a key limitation of the CS approach, which exclusively focuses on spectral accelerations while neglecting other characteristics of ground motions which may or may not be pertinent to the structural system studied. It is well-established that the severity of a ground motion in non-linear systems

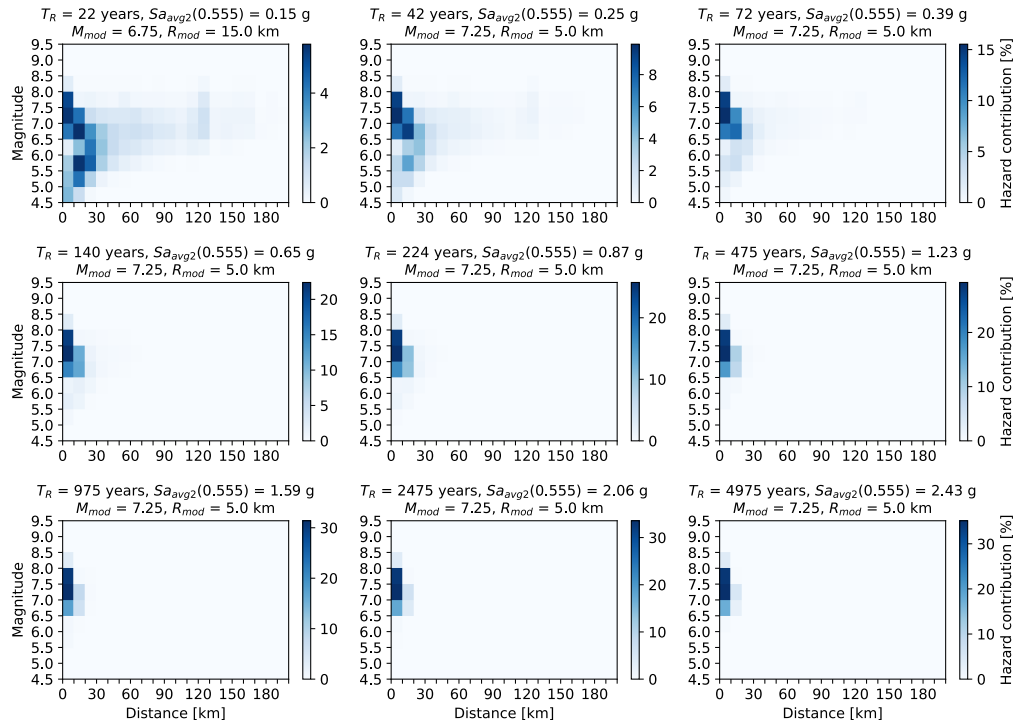


Figure 6.6. Hazard disaggregation of Sa_{avg2} at 0.555 s for the nine return periods investigated

depends not only on its spectral accelerations but also on its frequency content, velocity, duration, and energy. Spectral acceleration, by definition, represents the peak response of an elastic SDOF oscillator at a specific period and therefore fails to account for other important ground motion features.

The CS approach is based on the assumption that spectral accelerations follow a multivariate lognormal distribution. Building on this, the GCIM approach generalises this concept by proposing that any arbitrary vector of IMs, for a given seismic scenario, follows a multivariate lognormal distribution. This vector can include any scalar IMs, making the GCIM approach more versatile. Regarding the validity of this assumption, it is widely recognised that most IMs exhibit marginal lognormal distributions, as supported by regression analyses on $\ln(\text{IM})$ in empirical GMMs.

The conditional mean and standard deviation of the included IMs are

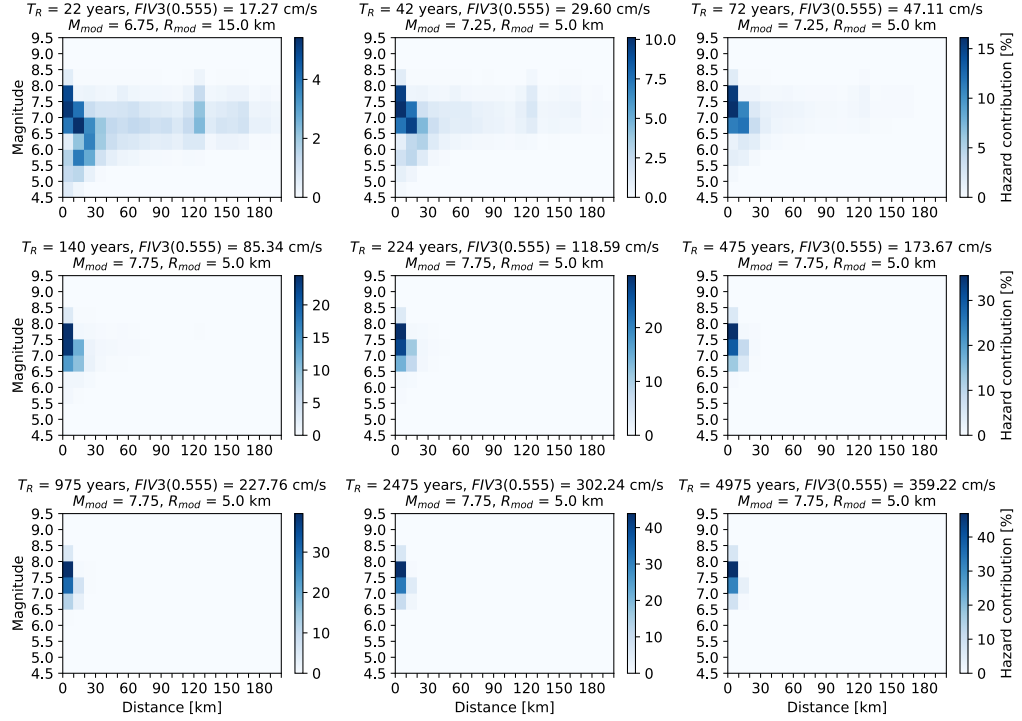


Figure 6.7. Hazard disaggregation of *FIV3* at 0.555 s for the nine return periods investigated

therefore expressed in Equations 6.1 and 6.2.

$$\mu_{\ln \text{IM}_i | \ln \text{IM}^*, \text{rup}} = \mu_{\ln \text{IM}_i | \text{rup}} + \sigma_{\ln \text{IM}_i | \text{rup}} \cdot \rho_{\ln \text{IM}_i, \ln \text{IM}^*} \cdot \epsilon_{\ln \text{IM}^*} \quad (6.1)$$

$$\sigma_{\ln \text{IM}_i | \ln \text{IM}^*, \text{rup}} = \sigma_{\ln \text{IM}_i | \text{rup}} \cdot \sqrt{1 - \rho_{\ln \text{IM}_i, \ln \text{IM}^*}^2} \quad (6.2)$$

where, IM_i is the matched IMs, IM^* is the conditioning IM, μ is the target mean, σ is the target standard deviation, ρ the cross-correlation coefficient, and ϵ the normalised residual (Baker and Cornell, 2006b).

In the ground motion selection schemes investigated here, three different conditioning IMs (IM^*) were included, namely $Sa(T_1)$, $Sa_{\text{avg}2}(T_1)$, and $FIV3(T_1)$. Also, a combination of several IMs, for which the theoretical distribution was also conditionally matched (IM_i), namely $Sa(T)$, Ds_{575} ,

Table 6.2. Ground motion input cases

Case No.	IM*			IM _i	
0	$Sa(T_1)$	—	—	—	—
1	$Sa(T_1)$	$Sa(T)$	—	—	—
2	$Sa(T_1)$	$Sa(T)$	Ds_{575}	$Sa_{avg3}(T_1)$	$FIV3(T_1)$
3	$Sa(T_1)$	$Sa(T)$	—	$Sa_{avg3}(T_1)$	$FIV3(T_1)$
4	$Sa(T_1)$	$Sa(T)$	Ds_{575}	—	—
5	$Sa_{avg2}(T_1)$	$Sa(T)$	—	—	—
6	$FIV3(T_1)$	$Sa(T)$	—	—	—
7	$Sa_{avg2}(T_1)$	—	—	$Sa_{avg2}(T)$	—
8	$FIV3(T_1)$	—	—	—	$FIV3(T)$
9	$Sa_{avg2}(T_1)$	—	Ds_{575}	$Sa_{avg2}(T)$	—
10	$FIV3(T_1)$	—	Ds_{575}	—	$FIV3(T)$

$Sa_{avg3}(T)$, $FIV3(T)$, and $Sa_{avg2}(T)$, were included. All the different ground motion record selection cases along with their conditioning and matched IMs are listed in Table 6.2. For the period-dependent IMs, where ‘ T ’ is denoted it means that the whole spectrum at a range of periods was matched, and ‘ T_1 ’ means that the IM at the first period of each structure was matched.

Listed in the following is the description and motivation behind defining each case, and what was sought to be achieved. Typical example applications of some cases are given as well.

- Case 0 is the simplest case, where the records were just scaled to each $Sa(T_1)$ value from PSHA, without matching the distribution of any other IM_i. This case was included to check what could be the implications of not matching (at least) the Sa , and how they can affect the eventual risk estimates. This is typical, for example, in situations where one reads the value of an IM from a hazard map, and scales a set of ground motions to that IM level to obtain a quick estimate of the response distribution but without much care or precision in how the ground motion characteristics actually match the hazard. This approach is typical of what is done in IDA, where only a single IM is focused on.

- Case 1 is the classic conditional spectrum approach outlined by Baker (2011). It is the main and most popular method of selecting ground motions for MSA and conducting a seismic risk analysis in research and industry. It is mostly applied on single-building seismic risk assessments.
- Cases 2-4 is an extension of the CS to GCIM, because of the additional IM_i (i.e., Ds_{575} , Sa_{avg3} , and $FIV3$). These three cases are included to explore whether the differences between Case 1 and 2 come primarily from Ds_{575} . They are employed when features other than spectral acceleration need to be considered, for example in situations where cumulative effects like fatigue, degradation, or liquefaction are critical.
- Case 5 is the conditional spectrum-based approach, but having $Sa_{avg2}(T_1)$ as the conditioning IM*. It is a scheme similar to Case 1, but with a superior (i.e., more sufficient and efficient) IM*. Similarly, Case 6 is the CS approach, but with $FIV3(T_1)$ as the IM*. While the capabilities of $FIV3$ as an IM were checked in a few previous studies (Dávalos and Miranda, 2019, 2020; Aristeidou and O'Reilly, 2024), a rigorous performance-based assessment is still not carried out in the literature with that as the conditioning and/or matched IM. Hence, exploring that via an MSA is a novel aspect explored here.
- Case 7 is the conditional spectrum of Sa_{avg2} , instead of the classic Sa . Similarly, Case 8 is conditional spectrum of $FIV3$. These two cases are added to explore the difference (if any) with the Cases 5 and 6, respectively. Cases 9 and 10 are the extension to GCIM of the Cases 7 and 8, respectively, with the additional matching of Ds_{575} . The duration matching was added to the last cases, as it was expected that these would be the best cases, and by adding duration most of the relevant characteristics of ground motion would be accounted for.
- It should be stated here that Cases 2, 3, 5, 6, 8, and 10 were only made possible after the development of GGMM and correlation models presented in Chapters 4 and 5 of this thesis. Case 5 was possible from before, but with an indirect method (Kohrangi et al., 2017), whereas now it is possible with a direct GMM and direct correlation model between Sa and Sa_{avg} (i.e., $\rho_{Sa,Sa_{avg}}$).

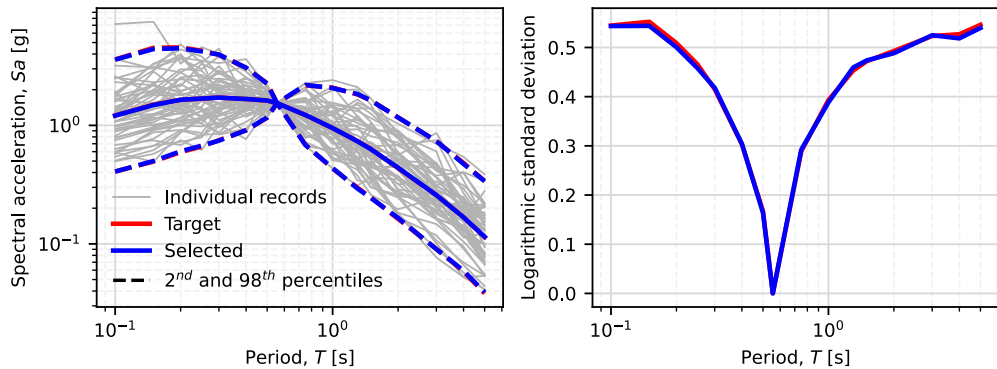


Figure 6.8. S_a spectrum and comparison of the target and selected dispersions for record selection Case 2 of bridge B-1 at 475 years return period

No rupture parameter limits were applied in the selection of ground motions, but a maximum scale factor of 8 was set. Both horizontal components of the pool of recorded motions were included in the selection pool, in other words the amount of possible ground motions to be used for the analysis were double the amount of available recordings. This is done because the bridge is excited unidirectionally. However, in the hazard calculations and in generating the target IM distributions, the *RotD50* or the geometric mean horizontal component definitions were used. It should be noted that the ideal scenario would be to use the $S_{a\text{arb}}$ horizontal component definition for hazard and ground motion selection targets. Nevertheless, the difference is expected to be small and would not affect the relative conclusions drawn in this study. A set of 50 records were selected for each stripe. As an example, the target and selected spectra and cumulative distribution function (CDF) distributions of selection Case 2 for the structure B-1 at 475 year return period are illustrated in Figures 6.8, 6.9, and 6.10. This case is chosen to be presented here as it has the most IM_i . It is clear how the selected records match the target distributions very well, for all IM types explored.

The hazard consistency was checked for the ground motion selection cases and two examples are illustrated in Figure 6.11. The checks are shown for four different periods of S_a , a shorter period than the conditioning one, a period that is close to the conditioning, and two longer periods than the

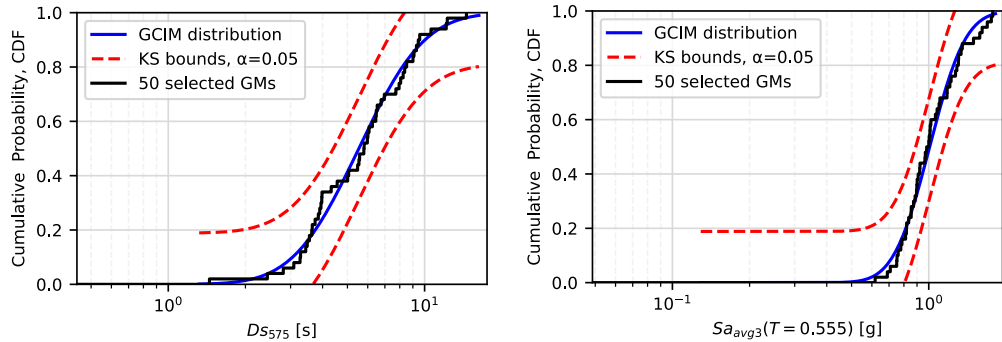


Figure 6.9. Ds_{575} (left) and Sa_{avg3} (right) theoretical and empirical CDF for record selection Case 2 of bridge B-1 at 475 years return period

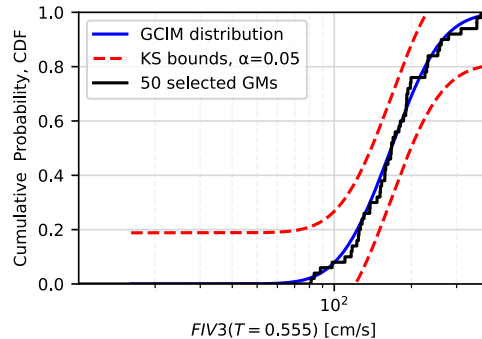


Figure 6.10. $FIV3$ theoretical and empirical CDF for record selection Case 2 of bridge B-1 at 475 years return period

conditioning one. Firstly, it can be observed that the selection Case 0 gives a good match with the seismic hazard curves, except for $T = 0.2$ s, which is an unexpected result since no effort was made in the selection to achieve hazard consistency. It seems to be a circumstantial result, emanating from the interaction between the lower medians and higher dispersions of the selected records of Case 0. This is the case for longer periods than the conditioning one (Figure B.3). For shorter periods than the conditioning, it can be seen that the selected records present higher hazard curve than that from PSHA. This is because, while the median of selected records is close in value to the target median, but the dispersion of the selected records is

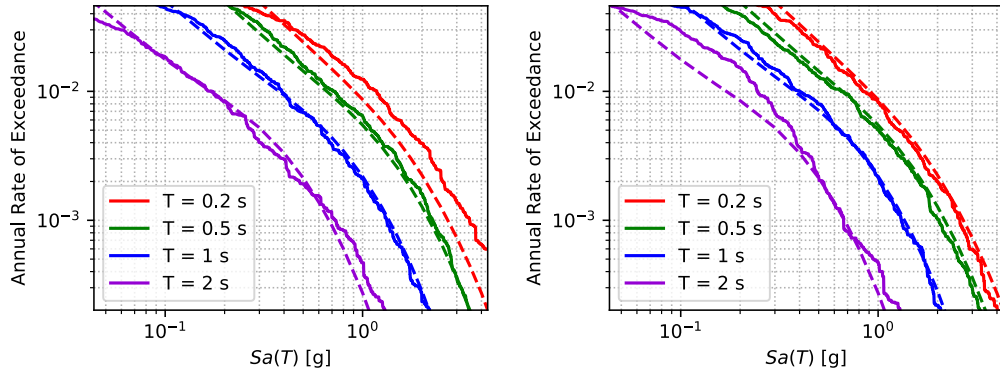


Figure 6.11. Hazard consistency checks for ground motion input Cases 0 (left) and 5 (right) for bridge B-1. Dashed lines represent the hazard curves and solid lines represent the reconstructed hazard curves obtained from the selected ground motions

higher than the target dispersion (Figure B.3).

Figure 6.11(right) illustrates the hazard consistency check of ground motion record selection Case 5, which is conditioned on Sa_{avg2} . It can be seen that there is a good match with the hazard curves obtained from PSHA, except for the high annual rate of exceedance part of $T = 2$ s. The source of this mismatch is due to the fact that not all input parameters of the GGMM could be extracted from the hazard disaggregation, only magnitude and distance, therefore some assumptions had to be made for other parameters. Another reason is the choice of the modal scenario of the hazard disaggregation, and not the inclusion of all the scenarios that significantly contribute to hazard.

6.6 Results

6.6.1 MSA results

With the ground motion record sets identified in Section 6.5 for each selection case, return period, and bridge structure, MSA was carried on the numerical model of each bridge structure. The output of this analysis is an empirical distribution of the bridge response, characterised via an EDP (in this case ϕ_{max}), versus an IM level corresponding to a specific return period.

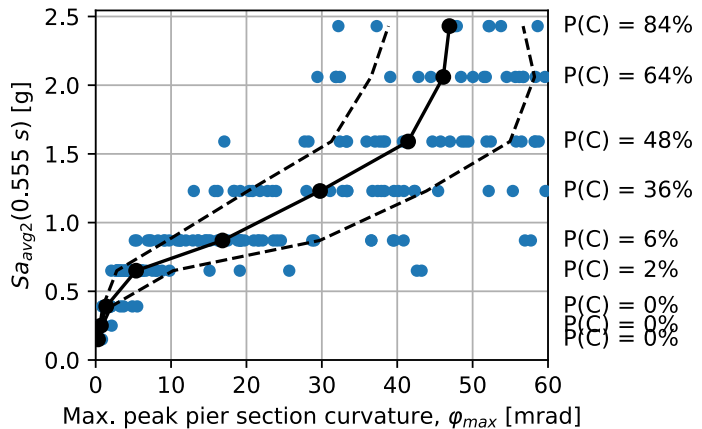


Figure 6.12. MSA results obtained with the ground motion input 5 on case study bridge B-1. Also depicted is the logarithmic mean and ± 1 standard deviation of the non-collapse cases, and the probability of collapse resulting from each intensity level

As an example, the MSA results for the case study bridge B-1 and ground motion selection Case 5 are illustrated in Figure 6.12. Each scatter point represents an individual response ordinate from a ground motion record scaled to a specific intensity stripe, which amount to a total of 9 intensity levels. The response ordinates of only the non-collapse cases are shown in the plot, for which the logarithmic mean and ± 1 standard deviation are also illustrated. Also shown in the right-hand side of the figure is the probability of collapse in each intensity level. The logarithmic mean non-collapse response values, along with the denoted probability of collapse, indicate the increase in bridge demand with increasing shaking intensity. It can be also observed from Figure 6.12 the increased standard deviation of EDP response with increasing IM level, but it should be noted that the axes are not logarithmic. O'Reilly (2021b) confirmed that the response data at each intensity stripe follow a lognormal distribution using the Kolmogorov–Smirnov goodness of fit test at the 5% significance level, and this assumed to hold also here.

6.6.2 Intensity-based evaluation

One of the points of comparison can firstly be the dispersion in demand for a given intensity, $\beta_{EDP|IM}$, which can help in gaining insights into the predictive capability of each ground motion input case. Another point can be the median demand for a given intensity, $\eta_{EDP|IM}$, which is also reported in this section and discussed, since it is important to investigate the impact of employing ground motions with different characteristics in each case on the structural response. Although demand-based evaluations are more relevant for risk assessment purposes, intensity-based evaluations remain commonly prescribed in design codes (Lin et al., 2013b; Poveda and O'Reilly, 2025). Consequently, accurately characterizing the structural response of a bridge for a given return period of seismic shaking is of interest. Furthermore, intensity-based evaluations serve as the foundation for the structural analysis inputs required in loss estimation, as exemplified by Mackie et al. (2010).

It is important to recognise that the median and dispersion observed in these structural analysis results is significantly influenced by the ground motion selection methodology employed at each IM level. For instance, the use of a conditional spectrum CS-based approach, or a generalized conditional intensity measure GCIM-based approach, is substantially affecting the outcomes of loss assessments. Therefore, it is critical for one to ensure that the methods employed are appropriate for the specific objectives of the analysis.

Figure 6.13 depicts the $\eta_{EDP|IM,NC}$ for all the bridge structure and all the ground motion input cases as a function of return period. It should be mentioned that the median is conditioned on no collapse. In the legend of the plot, the code name for each case is also given. The first IM is the conditioning one, while the IMs after the dash symbol are the ones whose theoretical GCIM distribution is been matched by the record selection. The IMs after the dash that are denoted with “(T)” are the ones whose spectrum is matched, whereas for the other period-dependent IMs, without “(T)”, only at the 1st period of each structure was matched. Bridge 4 presents the lowest EDP medians, and therefore has the lowest vulnerability and also the lowest probability of collapse for a given return period. This is because of the regular distribution of pier heights along the length of the bridge, the same with B-3 and B-5. The most obvious observation in Figure 6.13

is Case 0, which gives the lowest response medians. This is simply because the selected mean spectrum of the selected ground motions is notably lower than the target mean spectrum for the site, since the Sa spectrum was not matched, as can be seen for example in Figure B.3, although the conditional variability is slightly higher and not matching the target distribution either. In addition to that, the duration of records obtained in Case 0 are shorter than the one obtained in Case 1, as seen in Figures B.4 and B.5, which further decreases the severity of the selected ground motion on degrading systems (Chandramohan et al., 2016). Another point that stands out is the higher $\eta_{EDP|IM}$ obtained in regular bridges with the cases that have *FIV3* as the conditioning IM. The reason for this has not been identified yet, therefore further investigations are necessary to understand the source of this difference but it is an interesting observation regardless.

Furthermore, it should be noted in Figure 6.13 that Cases 2 and 3 present lower EDP medians than Case 1. This is mostly because Case 1 includes records with higher-than-expected durations, whereas Cases 2 and 3 match the duration distribution expected at the site. This is where the majority of the difference comes from, since distribution of other IMs are very similar in these cases.

Figure 6.14 presents the $\beta_{EDP|IM,NC}$ as a function of return period for all the bridges and ground motion input cases. It can be seen that the general trend of this dispersion is that it starts from a low dispersion in low T_R , gets higher in the intermediate T_R and get even lower in high T_R . The reason for having lower dispersion in higher return periods is because many records cause collapse in the case study structures, since for the scope of this exercise is located in high seismicity area, and additionally degradation is added in the models. This causes the more severe records to cause collapse, and therefore excluded from the dispersion calculation, since it is conditioned on no collapse.

It can be observed that for most return periods, Case 9 (i.e., Sa_{avg2} GCIM with matching Ds_{575}) exhibits the lowest $\beta_{EDP|IM,NC}$. Meanwhile, in regular bridges (i.e., B-3, B-4, and B-5), Cases 6, 8, and 10 (i.e., the ones with *FIV3* as the conditioning IM) are the most efficient ones for return periods of 475 years and above, which corroborates past observations for these IMs (e.g., Kazantzi and Vamvatsikos, 2015; Dávalos and Miranda, 2019; O'Reilly, 2021b; Aristeidou and O'Reilly, 2024).

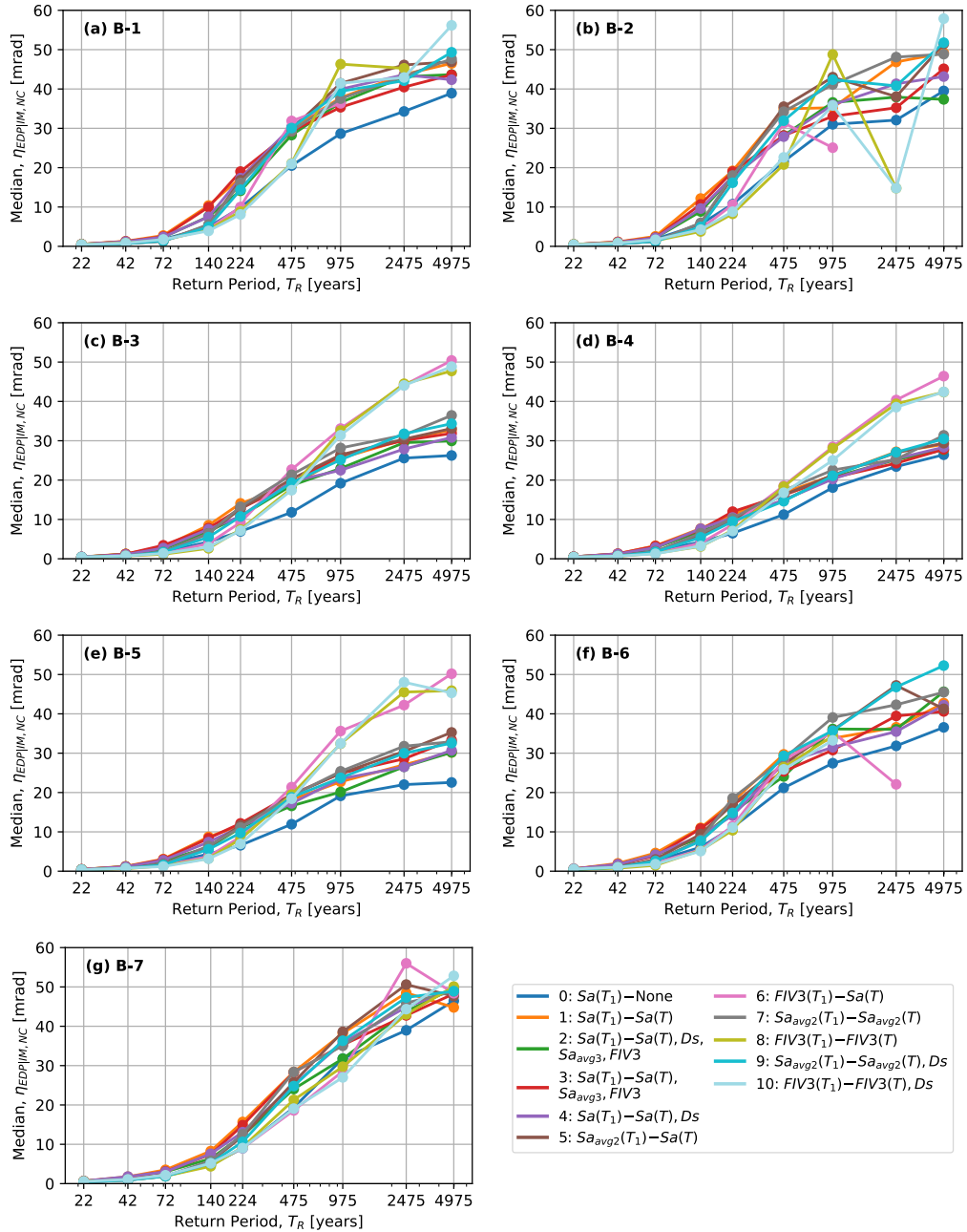


Figure 6.13. Median of EDP given IM level given no collapse

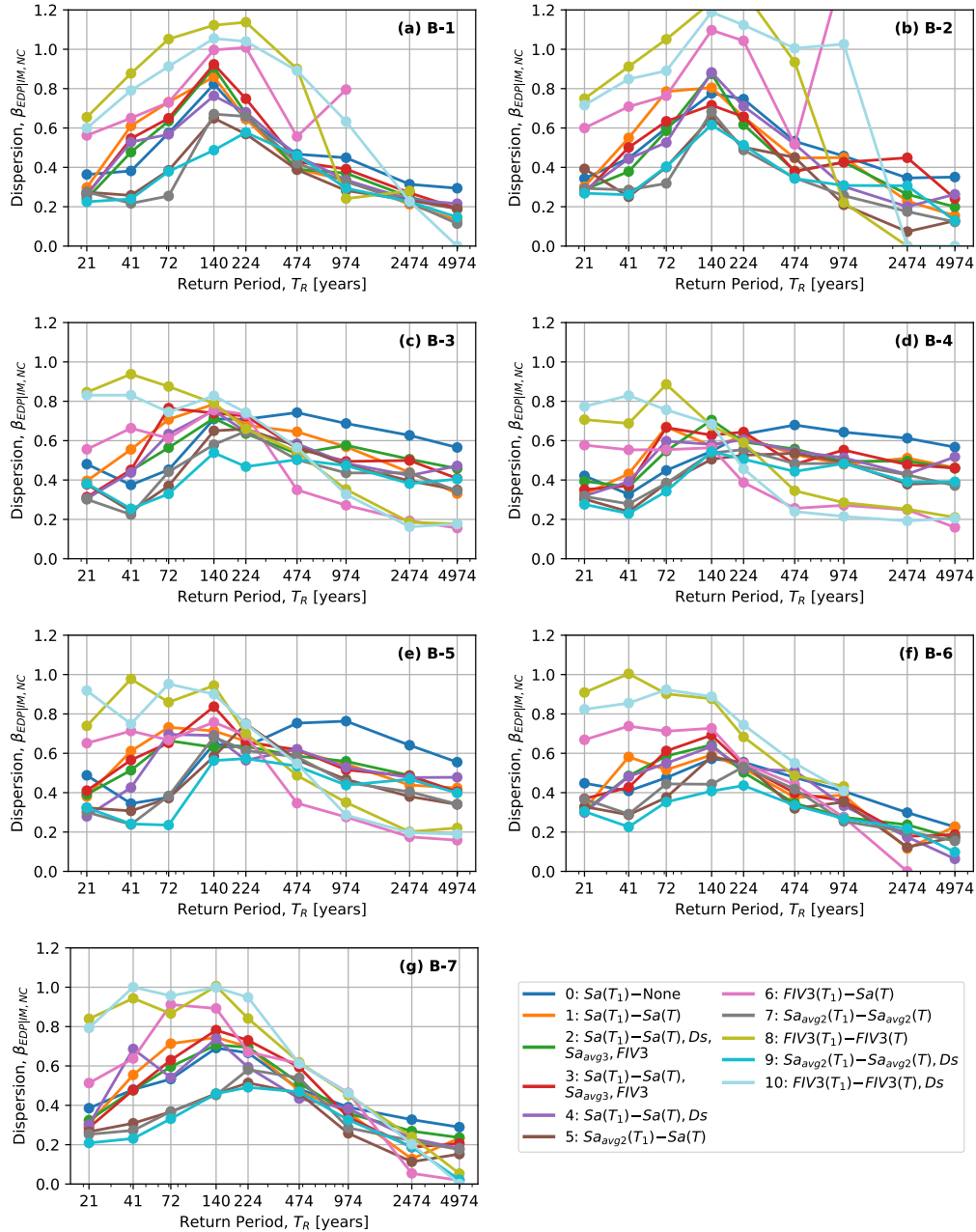


Figure 6.14. Dispersion of EDP given IM level given no collapse

6.6.3 Demand-based evaluation

The capacity limit of a structure, represented as C , and the seismic demand, represented as D , are used to assess the likelihood of exceedance of a certain damage limit (i.e., $D > C$). Given the inherent uncertainty in ground motion records and structural response, it is appropriate to quantify this exceedance probabilistically. Thus, the conditional probability of $D > C$ for a given intensity measure level, im , denoted as $P(EDP > edp | IM = im)$, is typically employed. This probability is often modelled using a lognormal distribution characterised by a median, $\eta_{IM|EDP}$, and dispersion, $\beta_{IM|EDP}$, forming what is known as a seismic fragility function. By integrating this function with the mean hazard curve derived from PSHA, $H(im)$, the mean annual frequency of exceedance (MAFE) of C is obtained, offering a more comprehensive and consistent measure of seismic risk. The calculation of this MAFE is given in Equation 6.3, where $\Phi[\cdot]$ represents the standard normal cumulative distribution function.

$$\lambda = \int_0^{+\infty} \Phi \left[\frac{\ln im - \eta_{IM|EDP}}{\beta_{IM|EDP}} \right] |dH(im)| \quad (6.3)$$

An important characteristic often sought in a conditioning IM is efficiency (Luco and Cornell, 2007). This implies that the IM should serve as a reliable predictor of the structural response, characterized by a low dispersion, $\beta_{IM|EDP}$, and thereby accurately reflect the overall performance. This is a characteristic that can be achieved, not only with the conditioning IM, but also with matching the theoretical distributions of “secondary” IMs. By that last part, also the median of structural response gets affected for different return periods.

In this study, the sufficiency for the chosen conditioning IMs is assumed and not investigated in detail, as supported by existing literature (Shome et al., 1998; Bradley, 2010; Aristeidou & O'Reilly, 2024). Sufficiency implies that the structural response is independent of other ground motion characteristics once conditioned on the selected IM. While efficiency and sufficiency has been extensively studied in the context of next-generation IMs, efforts to fully address the challenges of hazard computability and practical implementation have often been overlooked. This thesis bridged this gap by proposing a GGMM and correlation models to ensure that the IMs not only exhibit efficiency and sufficiency but are also computationally

viable and straightforward to integrate into hazard assessments.

The parameter $\beta_{IM|EDP}$ in Equation 6.3 is plotted in Figure 6.15 versus the whole range of EDP response of the structure. For the regular bridge structures (B-3, B-4, and B-5), Cases 6, 8, and 10 exhibit the lowest dispersion $\beta_{IM|EDP}$ for ϕ_{max} values exceeding 10 mrad, which spans most of the response range. These cases employ *FIV3* as the IM*. Among these, Case 10 clearly achieves the lowest dispersion overall by conditioning on *FIV3* and matching both the *FIV3* spectrum and Ds_{575} , demonstrating its superior efficiency for these regular bridges, especially for the higher levels of EDP when the structure is responding in its nonlinear range since the yield curvature is approximately 1.25 mrad.

In contrast, for the irregular bridge structures, Cases 5, 7, and 9 show the lowest dispersion, particularly in the first half of the structural response range. These cases condition on $Sa_{avg2}(T_1)$. While the differences among these cases are not pronounced, Case 9 stands out as slightly more efficient. This can be attributed to its matching of the expected duration distribution at the site, which additionally ensures more accurate median response estimates.

For cases using Sa as the conditioning IM, dispersion remains low in the initial stages of the response but increases significantly as the structural response becomes more nonlinear. Cases 1 and 3 exhibit the highest dispersion, although they differ little from Cases 2 and 4. Interestingly, Case 0—the most basic scenario—exhibits lower dispersion than the other Sa -conditioned cases, despite its higher dispersion of the selected records (Figure B.3). This unexpected outcome can be explained by the inclusion of records with lower spectral ordinates in longer periods and also lower durations, which artificially raises the efficiency of Sa as a conditioning IM. However, this comes at the expense of not adhering to hazard-consistent selection rules, as Case 0 fails to represent the site-specific hazard and underestimates risk, particularly at higher EDPs where structural nonlinearity and longer-period motions dominate, as discussed in section 6.5.

Finally, it is worth noting that cases incorporating Ds as a matched IM consistently achieve lower dispersion compared to corresponding cases where Ds is not matched. This highlights the value of including duration-based IMs, like Ds , in reducing variability and improving the accuracy of seismic demand predictions.

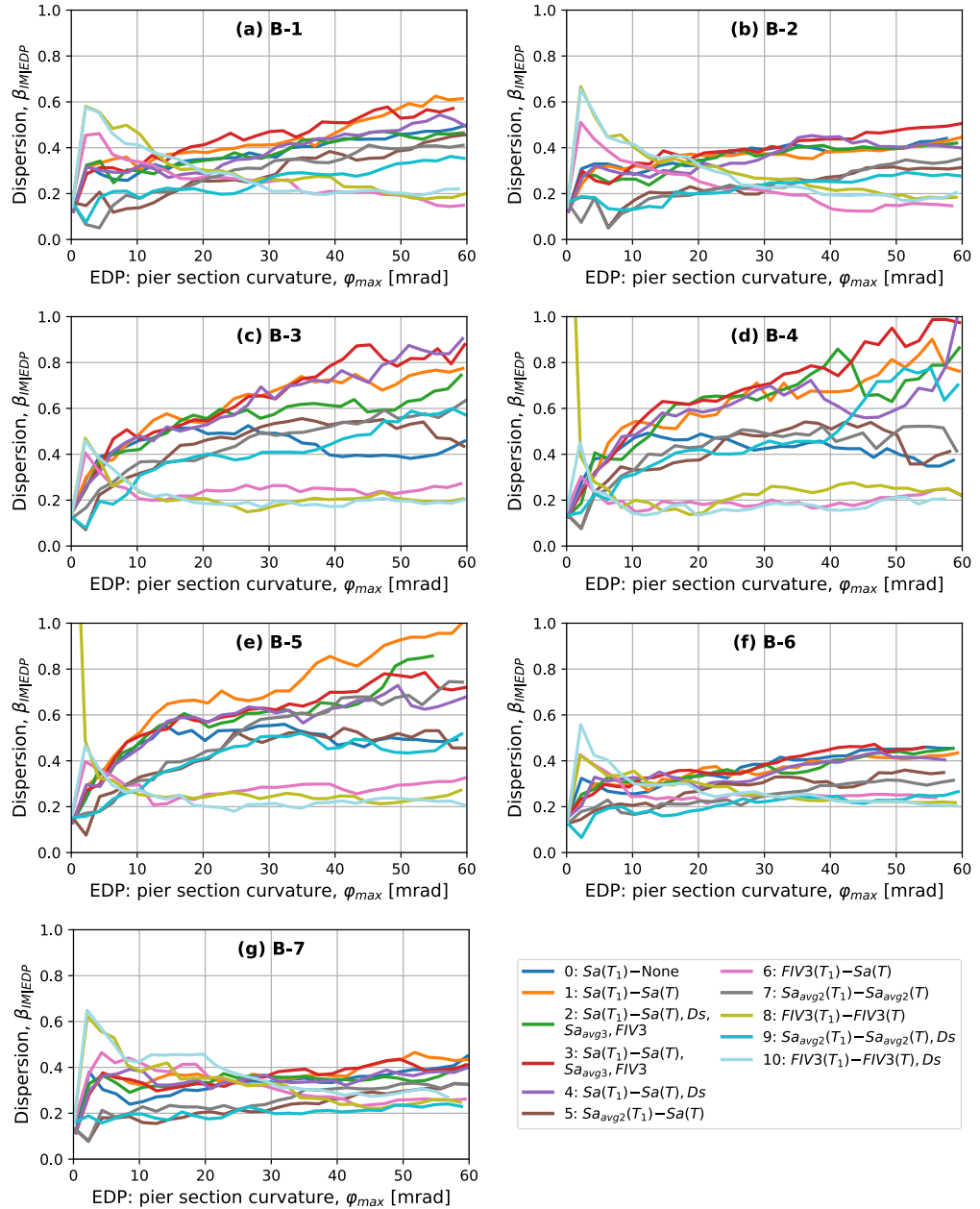


Figure 6.15. Dispersion of IM given exceedance of EDP

6.6.4 Risk-based evaluation

In the demand-based evaluation, the $\eta_{IM|EDP}$ and $\beta_{IM|EDP}$ of the lognormally distributed IMs required to exceed a given level of EDP were determined for each input case at increasing levels of structural demand. This distribution was then directly integrated with the mean hazard curves of each conditioning IM to calculate the MAFE as a function of EDP, λ , calculated as shown in Equation 6.3. Computing the MAFE in this manner accounts only for record-to-record variability, though additional sources of uncertainty can also be incorporated. Since the mean hazard curves used in this analysis were derived from the hazard results provided by the OpenQuake engine described in Section 6.4, the integration of the seismic fragility functions for a range of EDP thresholds, yields a mean estimate of the annual exceedance frequency for that EDP range. While it is possible to include the uncertainty associated with the hazard curves, as discussed by Cornell et al. (2002) and Vamvatsikos (2013), this study focuses solely on MAFE for the comparisons. By directly integrating the fragility functions with the hazard curves shown in Figure 6.4 using Equation 6.3, the seismic demand hazard curves for the case study structures were obtained for the different ground motion input cases, and are illustrated in Figure 6.16.

Before discussing the results, it is important to establish the theoretical basis for evaluating the seismic demand hazard curves. The MAFE, λ , begins at zero demand and corresponds to the baseline hazard for an infinitesimally small intensity. As structural demand increases, λ decreases, eventually approaching the structure's mean annual collapse frequency for extreme levels of demand.

To assess the accuracy of each ground motion selection case's estimates of λ , consistency among the hazard-consistent selection cases is typically used as a benchmark. While it is not possible to experimentally verify the exact value of λ , agreement between the different observations suggests that the computed values reflect the unique seismic risk of the structure at a given demand level. This interpretation aligns with the findings of Bradley (2012) and Lin et al. (2013a), who demonstrated that risk-based quantities like MAFE are largely independent of the chosen IM when specific conditions are met: (1) the ground motion records used are hazard-consistent, (2) the IM* employed is sufficient to represent the structural response, and (3) the IM* is an efficient and unbiased predictor of structural demand.

It is expected that for the hazard-consistent selection cases the resulting MAFE estimates converge to a similar values for each bridge. These curves can be compared and, in some cases, validated against results from detailed physics-based simulations, as discussed by Bradley et al. (2015). However, such validations would be beyond the scope of this study.

From Figure 6.16, there are a number of observations that can be made. Regular bridges have lower MAFE, than the irregular bridges, especially in higher EDPs. B-4 has the lowest risk. Cases 1 and 3 consistently gave higher estimates of λ in all the bridge structures. It is interesting to note the Cases 2 and 4 (i.e., conditioning on Sa and matching the Ds_{575}) result in MAFE closer to the rest of the cases, which indicates that matching the Ds_{575} GCIM distribution alleviates part of the incompetencies of Sa as a conditioning IM. Case 0 gives one of the lowest risk estimates because of its lower-than-expected Sa spectrum and Ds_{575} of the records, as already discussed above, hence deeming it the “worst” case for what concerns risk estimation.

The difference between Cases 5 and 7 is negligible. The same applies to Cases 6 and 8, which indicates that there is no practical difference in matching the Sa or Sa_{avg2} spectrum along with conditioning on Sa_{avg2} , or matching the Sa or $FIV3$ spectrum along with conditioning on $FIV3$. This is likely due to the high level of correlation between each of these IMs (see Chapter 5), meaning that these cases are slight variations of each other. It also underlines the importance of hazard-consistent ground motion record selection when compared to Case 0, for example.

Additionally, Cases 9 and 10 give similar MAFE estimates, which are relatively low in value compared to the rest of the cases. All in all, it can be concluded that matching the Ds_{575} distribution makes a notable difference in the risk estimates and should be considered by analysts when dealing with nonlinear systems with some form of strength degradation.

6.7 Summary and conclusions

In this chapter, a comprehensive analysis was conducted to evaluate the impact of next-generation IMs on the seismic risk assessment of bridge structures. The developed GGMM and correlation models, presented in Chapters 4 and 5, were employed to facilitate the selection of ground

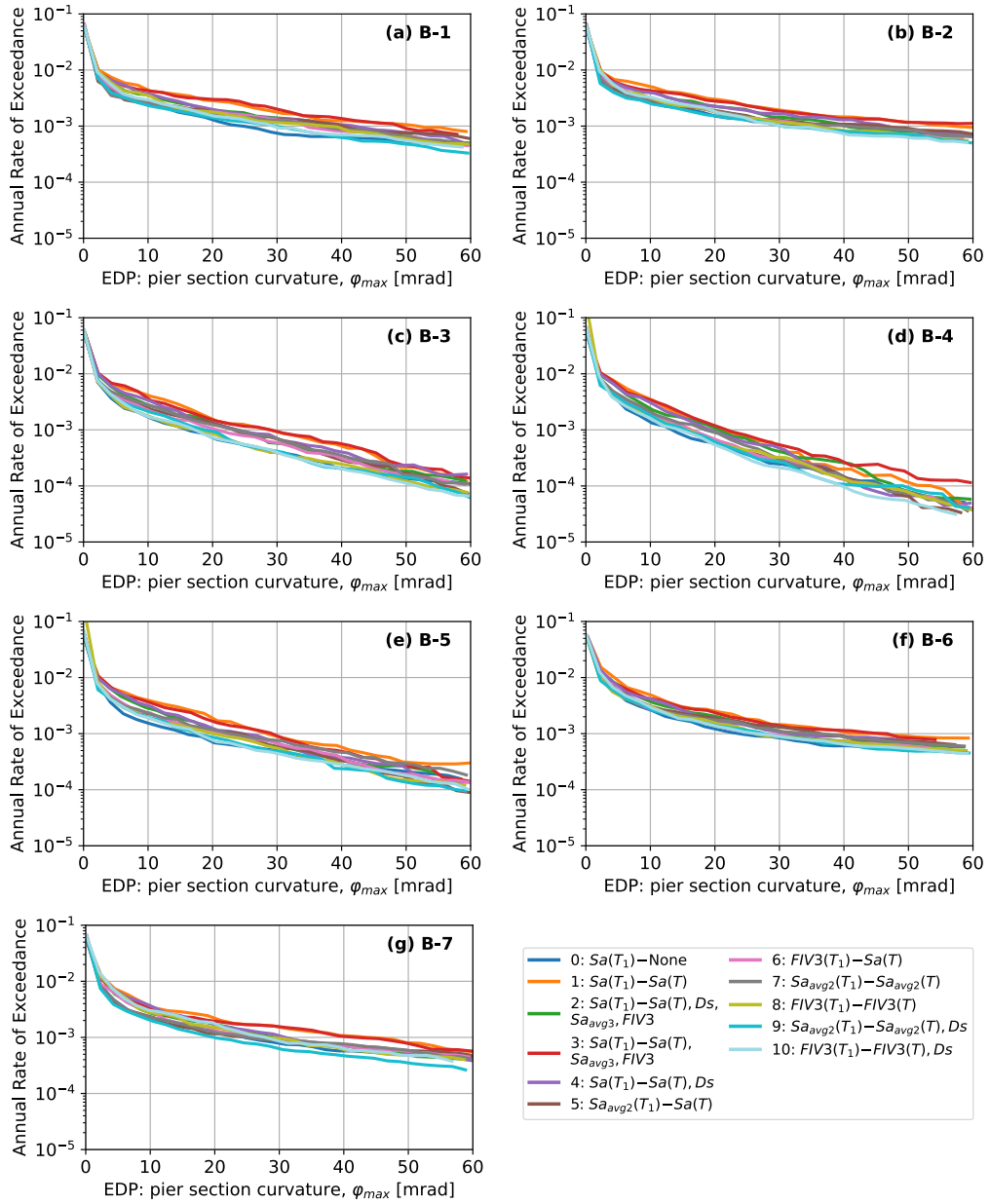


Figure 6.16. Seismic demand hazard curves of the case study bridges

motions using advanced approaches, such as the GCIM method. This approach ensures that key features of ground motions beyond spectral acceleration, such as spectral shape, duration and velocity, are appropriately represented and matched during selection.

A suite of multi-span bridge structures with varying pier heights and span configurations was analysed using numerical models built in OpenSeesPy. Ground motion records were selected and scaled according to different strategies, including just scaling to the conditioning IM, CS-based and GCIM-based selection. The MSA method was used to quantify structural demands, and risk estimates were derived for the case study bridges.

Several ground motion selection cases were investigated and the conclusions regarding the comparisons between them are outlined as follows:

- Cases 0 and 1: Impact of just scaling the ground motions to $Sa(T_1)$, in comparison to also matching the Sa spectrum (i.e., conditional spectrum). Case 0 gave lower structural response for the same IM level, because of the lower-than-expected Sa spectrum of the selected ground motions. The impacts of this were also evident in the dispersions and risk estimates, which highlighted the importance of matching the target distribution of a wide range of Sa spectrum, and not just the conditioning one.
- Cases 1 and 2: Comparison between conditional spectrum of Sa and GCIM. The CS approach gave ground motions with higher-than-expected Ds_{575} , which resulted in higher EDP medians. The dispersions were somewhat lower in Case 2, and therefore presented higher efficiency. Nevertheless, the differences in dispersion were small.
- Cases 1, 2, 3, and 4: They are included to check whether the differences between Cases 1 and 2 come mainly from the duration. In fact, Cases 2 and 4 give similar results, while Cases 1 and 3 also exhibit similar results between them. Therefore we can conclude that the differences between Cases 1 and 2 come primarily from matching the Ds_{575} or not.
- Cases 1, 5, and 6: Comparison of the different conditioning IMs (i.e., Sa , Sa_{avg2} , and $FIV3$, respectively) while matching the Sa spectrum.

Case 1 resulted in low dispersion only in the initial stages of EDP response, which is the elastic and mildly inelastic stage, and then the dispersion quickly rises. Case 5 was more efficient in the irregular bridges, while Case 6 dominated with regards to efficiency in most of the non-linear response range of the regular bridges.

- Cases 5 and 7: This is to investigate the difference between conditioning on Sa_{avg2} and matching the Sa spectrum, with the CS of Sa_{avg2} . Dispersions, medians and risk estimates are very similar between the two cases. This suggests that one can select any of the two schemes and obtain very similar results.
- Cases 6 and 8: This is to investigate the difference between conditioning on $FIV3$ and matching the Sa spectrum, with the CS of $FIV3$. Dispersions, medians and risk estimates are very similar between the two cases, with Case 6 resulting in slightly lower dispersions.
- Cases 9 and 10, versus the all rest: The GCIM method of conditioning on Sa_{avg2} and $FIV3$, while matching their corresponding spectrums and the Ds_{575} theoretical distribution at the site, seem to be best cases. Case 9 is better for the initial and intermediate stages of nonlinearity, while case 10 is better for the deeper stages of nonlinear response and near collapse. Furthermore, Case 9 is a better selection strategy for irregular bridges, while Case 10 is a better selection strategy for regular bridges.

In addition to the key conclusions presented, this chapter provided significant advancements in applying ground motion selection methodologies for performance-based seismic risk assessment of structures. By utilising the developed GGMM and correlation models described in Chapters 4 and 5, respectively, we have demonstrated the practical benefits of next-generation IMs, such as $FIV3$ and Sa_{avg} , in improving both the accuracy and consistency of seismic demand estimations.

Specifically, the GCIM-based approach proved highly effective in reducing the dispersions and providing more accurate median estimates of structural response, while ensuring hazard consistency—a critical factor often overlooked in traditional selection methods. The findings further highlighted the sensitivity of IM efficiency to structural regularity, with

velocity-based IMs like *FIV3* excelling for regular bridges and Sa_{avg2} exhibiting superior performance for irregular structures.

Overall, this work bridges the gap between state-of-the-art ground motion selection techniques and practical applications, offering a robust and hazard-consistent framework for fragility analysis and risk estimation. The comparisons and conclusions drawn here can serve as a foundation for future research and considerations in performance-based design and assessment, ensuring greater resilience of critical infrastructure under seismic loading.

Chapter 7

Discussion and Conclusions

7.1 Summary of Work

The primary focus of this thesis was divided into two main aspects. First, the phenomenon of ground motion directionality through the study of inelastic spectral displacements, Sd_i , was examined. This provided deeper insights into the intrinsic characteristics of ground motions, specifically their polarisation, commonly referred to as directionality. It involved the calculation and analysis of the $RotDnn$ horizontal component definitions for the 00th, 50th, and 100th period-dependent percentiles of Sd_i . This was achieved by calculating the Sd_i values for all non-redundant incidence angles in bilinear single-degree-of-freedom (SDOF) systems, covering a range of elastic periods, T_s , and, strength ratios, Rs . This approach allowed for a more comprehensive understanding of the directionality effects of ground motions originating from various underlying seismic conditions, which builds upon previous studies focusing on elastic systems. Ground motion records from the next generation attenuation relationships for Western United States (NGA-West2) database were used in the analysis. For the SDOF systems, a non-degrading, non-evolutionary bilinear hysteretic behaviour was adopted. Inelastic displacement spectra were computed for the $RotD100$, $RotD50$, and $RotD00$ definitions and compared with their corresponding elastic counterparts, providing valuable insights into how the response directionality of inelastic systems contrasted with that of elastic systems. The measure of directionality was chosen to be the $RotD100/RotD50$ ratio, which is the most widely adopted. Additionally, key differences and the impacts

of incorporating directionality to traditional nonlinear response estimation models (i.e., R - μ - T relationships) were revealed. Another notable point was that the near-fault ground motions exhibited higher inelastic and elastic directionality across the entire range of T .

The second part involved the development of a generalised ground motion model (GGMM) and correlation models for various intensity measures (IMs) and horizontal component definitions, addressing gaps in the existing literature. The GGMM estimates a wide range of traditional and next-generation IMs, including peak ground acceleration, PGA , peak ground velocity, PGV , peak ground displacement, PGD , two definitions of significant duration, Ds_{595} , Ds_{575} , spectral acceleration, Sa , filtered incremental velocity, $FIV3$, and two definitions of average spectral acceleration, Sa_{avg2} , and Sa_{avg3} . Consistent correlation models, coming from the same ground motion model (GMM) and filtered database, between the aforementioned IMs were also developed. These advancements enable more accurate and comprehensive ground motion selection, incorporating critical ground motion characteristics such as duration and velocity, which are often overlooked in conventional methods. The practical relevance of these contributions was demonstrated through the application of the GGMM and correlation models in advanced ground motion selection frameworks, such as the generalised conditional intensity measure (GCIM) approach, on a suite of seven bridge structures. This analysis highlighted the potential of next-generation IMs to reduce dispersion in structural response predictions, improve fragility curve accuracy, and provide more reliable seismic risk estimates.

7.2 Key Findings and Discussion

Several critical challenges in the domain of seismic hazard and risk assessment have been addressed, with a focus on advancing the understanding of the impact of ground motion directionality, and the application of next-generation IMs in ground motion selection strategies. The key findings of the research are summarised and discussed in the following.

The first two main body chapters introduced and explored the concept of orientation-independent inelastic spectral displacements, offering a novel approach to ground motion directionality representation. Chapter

2 presented the development of a ground motion model specifically for estimating orientation-independent inelastic spectral displacements from shallow crustal earthquakes. This model addressed gaps in existing ground motion models by incorporating inelastic effects with the a simple addition of R factor as an input parameter, in comparison to conventional GMMs that estimate elastic spectral quantities.

To evaluate the usefulness and practical application of the previously developed GMM, Chapter 3 explored the use of those IMs and horizontal component definitions for the seismic assessment of bridges. The analyses demonstrated improved sufficiency and efficiency in predicting the bridge's response in the different stages of nonlinearity. Also, the inelastic ground motion directionality was seen to introduce some level of bias in the bridge response. These contributions highlight the potential to enhance seismic risk assessments by addressing limitations in traditional IMs that do not account for inelastic behaviour or for a more informed directionality measure at a site.

The GGMM presented in Chapter 4 represents a significant advancement in ground motion modelling of unconventional IMs, while also providing a unified framework for estimating a wide range of IMs, including traditional ones like PGA , PGV , Sa , and significant duration, D_s , as well as next-generation IMs such as Sa_{avg2} and $FIV3$. The use of artificial neural networks (ANNs) enabled the simultaneous fitting of the model for all the aforementioned IMs, without the need to come up with functional forms for each one, which is very useful for the IMs that do not have many legacy functional forms in the literature. Also, the ANNs accommodate accurate and efficient estimations with reduced dispersion and high predictive performance. Additionally, the presented methodology for developing the model allows for the seamless addition of new IMs (and/or horizontal component definitions) and provides more consistent correlation coefficients by using the same subset of the strong motion database. These features make the GGMM a valuable tool for seismic hazard analysis and an important component in hazard-consistent ground motion selection frameworks.

The correlation models developed in this study provide a comprehensive characterisation of the relationships between the examined IMs. One key finding of these models was the demonstration that $FIV3$ exhibits strong correlations with Sa , particularly in its moderate- and long-period ranges. The consistency between GMMs and correlation models is important for ad-

vanced ground motion selection methodologies, as it enables the creation of hazard-consistent conditional spectra and target distributions. The findings also highlighted the strong correlation between *FIV3* of different periods, making it a nearly period-independent IM, which can be particularly useful for regional seismic studies.

Through comprehensive analyses of multi-span bridge structures, this thesis demonstrated the benefits of using next-generation IMs in seismic risk assessment. The GCIM-based selection approach was shown to effectively capture critical ground motion characteristics, such as duration and velocity pulses, resulting in reduced dispersion of structural response predictions and improved fragility curve accuracy. The findings further indicated that the efficiency of conditioning IMs changes based on structural regularity, with *FIV3* excelling for regular bridges and Sa_{avg2} performing better for irregular bridges. These insights underline the importance of tailoring ground motion selection strategies to the specific characteristics of the structures being assessed. Furthermore, the comparisons between various ground motion selection strategies revealed that hazard-consistent approaches, such as GCIM and conditional spectrum (CS)-based selection, offer significant advantages over just scaling to match the $Sa(T_1)$ from hazard analysis. The ability to match key IM distributions, beyond just the conditioning one, was shown to have a substantial impact on both median structural response and dispersion. Notably, the GCIM approach demonstrated superior performance in maintaining hazard consistency and improving the reliability of seismic risk estimates. The developed GGMM and correlation models provide tools that can be readily adopted in performance-based seismic design and risk assessment frameworks.

7.3 Contributions to the state-of-the-art

This thesis has made several contributions to advancing the state-of-the-art in seismic risk assessment, particularly in understanding the implications of ground motion directionality, and the development of models that allow the practical application of next-generation IMs. The key contributions are summarised in the following.

Valuable insights were provided regarding the maximum directional response of nonlinear systems, enabling a more comprehensive quantification

of damage in engineered structures. This can inform the design of new structures, based on the most adverse directional case. The findings showed that the effect of directionality on inelastic systems, quantified via the $RotD100/RotD50$ ratio increased with increasing R for systems with $T > 0.3$ s, whereas the opposite trend was observed for $T < 0.3$ s. These results highlight the importance of considering directionality in seismic design and risk assessments, particularly for structures with shorter periods as they present the highest directionality measures overall.

The GGMM developed in this thesis represents a novel contribution to ground motion modelling of less conventional IMs that are still of engineering interest. By reducing residual dispersion and ensuring consistent cross-correlations, the GGMM enables hazard-consistent selection and facilitates the integration of advanced IMs, such as $FIV3$ and Sa_{avg2} , into seismic risk frameworks.

The correlation models developed here constitute a clear contribution to the state-of-the-art, since some of them were not existing in the literature to date. They contribute to a deeper understanding of the relationships between IMs. Additionally, they support the use of the included IMs in advanced ground motion selection methods, such as GCIM, and enable the creation of hazard-consistent conditional spectra. The novel correlations between Sa , Ds , Sa_{avg} , and $FIV3$ are particularly impactful for improving the accuracy of seismic risk analyses.

By integrating the GGMM and correlation models into advanced selection frameworks, such as GCIM, this work demonstrated the potential of next-generation IMs to reduce dispersion in structural response predictions and improve fragility curve accuracy. These advancements provide a robust foundation for future research and practical implementation in performance-based seismic design and risk assessment.

Beyond the immediate contributions, this work lays the groundwork for further advancements in the field. The methodologies presented here can be extended to include additional IMs, develop heteroscedastic dispersion models, and explore applications for other structural typologies and hazard scenarios. Moreover, the findings on directionality and inelastic response showed potential for continuing the research into the complex interactions between ground motion characteristics and structural behaviour.

In summary, this thesis represents a substantial step forward in the field of seismic risk assessment, providing innovative tools and methodologies

that address critical gaps in ground motion modelling, correlation, and selection, while paving the way for future advancements in both research and practice.

7.4 Limitations and future developments

Despite the advancements made in this thesis, some limitations remain, suggesting opportunities for future research. Regarding directionality and inelastic spectral displacements, the key limitations and potential areas for further investigation are outlined below.

- Further studies may be conducted using different inelastic SDOF systems, each representing a distinct structural typology;
- The GMM is based on the NGA-West2 database, which focuses on shallow crustal earthquakes in tectonically active regions, this hinders its application to different tectonic environments. Similar analyses and GMM development may be conducted for ground motions from subduction earthquakes, given the inherent differences in their duration and cumulative intensity measures compared with ground motions from shallow crustal earthquakes. Extending the model to subduction and stable continental regions could improve its applicability for global seismic hazard assessments;
- The model assumes constant variance (homoscedasticity) across different input seismological parameters (e.g., moment magnitude, M_w , rupture distance, R_{rup}), which may not capture variability accurately across the range of these parameters. This simplification could affect model precision. Future studies could explore a model that accounts for varying dispersion (heteroscedasticity), offering more refined uncertainty quantification;
- While the model incorporates inelastic spectral displacements using orientation-independent measures ($RotD50$ and $RotD100$), it only addresses two specific percentiles. Future models could include more refined directionality measures to more comprehensively capture variations in ground motion incidence angles from the fault-normal direc-

tion. This can allow a more nuanced understanding of directionality in seismic risk.

- Similar methodology and calculations can be performed by having T and μ as the input parameters of the GMM. This would require some iterations in the initial stages of preparing the empirical data, but it would be more consistent with displacement-based design approaches.

Regarding the application of $Sd_{i,RotD50}$ and $Sd_{i,RotD100}$ for the seismic risk assessment of bridges and the directionality bias on the response, the following limitations and recommended future work can be stated.

- The study is based on a specific California bridge model. Results might not generalize to other bridge typologies, especially those with different configurations and structural vulnerabilities. Future research could apply the methods to different bridge types and configurations to assess the robustness of the inelastic spectral displacement approach across various structures;
- The difference that polarised or non-polarised ground motions can have on the response of structures can be investigated in a more detailed and targeted manner. For example, explore if polarised motions have different impact in different sites, or in different types of structures;
- While the study uses the $RotD100/RotD50$ definition of directionality measure, future research might investigate different directionality measures and evaluate their influence on structural response;
- Further exploration of inelastic directionality effects could refine our understanding of how they affect bridge response and improve the risk analyses under highly directional ground motions.

Regarding the GGMM developed with ANN for a range of IMs, the limitations and recommended future work are as follow.

- Future research could explore the inclusion of additional IMs and horizontal component definitions;

- The model works effectively only in regions where sufficient data is available. This can lead to inaccuracies when applied to data-scarce regions, particularly for large-magnitude and short-distance events that are less frequent but critical for assessing seismic risk. Addressing the scarcity of strong ground motion data from large earthquakes could enhance the model's accuracy for critical seismic hazard assessments;
- The use of ANN means the analyst has less control over ensuring that the functional forms accurately reflect the physical nature of seismic phenomena. While this data-driven approach is flexible, it lacks the transparency and control of parametric models that can be based on seismological understanding;
- The model assumes homoscedasticity (constant variance of residuals) across rupture parameters, which may oversimplify the treatment of variability. Introducing a heteroscedastic dispersion model might offer a more nuanced treatment of uncertainty but would increase the model's complexity;
- Although the GGMM allows for seamless expansion to include additional IMs, doing so could complicate the model further, especially with regard to overfitting or ensuring adequate training for new IMs;
- Expanding the model to include ground motion data from various tectonic settings beyond active shallow crustal earthquakes could increase its generalisability and usefulness in global seismic hazard assessments.

Regarding the developed correlation models, the following limitations and recommended future work can be drawn.

- The applicability of the models is limited to active shallow crustal tectonic regions. Future work could involve recalibrating the models to different tectonic regions, which would enhance the models' applicability to a global scale;
- The study uses a single GGMM that includes IMs of interest. While this provides consistency, it might limit the exploration of variability

that could result from using different GMMs. Incorporating additional GMMs in future studies could provide insights into how these correlations vary depending on the GMM used. This would further strengthen the reliability of the correlation models;

- This thesis presented correlation models based only on total residuals. While this provides all the necessary information for most risk assessment cases, having correlations separately for intra- and inter-event residuals can be useful for specific cases;
- Dependence of correlation coefficients on seismological and site-specific parameters can improve the accuracy and robustness of the correlation models. Therefore, this is a natural further development for contemporary correlation models, as was seen from the analyses of this thesis;
- Future research could aim to fill the gaps by developing correlation models for other IM pairs that do not exist in literature, providing an even more comprehensive toolkit for performance-based seismic analyses.

Regarding the application of GGMM and correlation models on the risk assessment of a set of seven bridge structures, the limitations and future developments are as follows.

- Future studies could explore the variability in the structural modelling parameters and their effects on resulting fragility functions, using methods such as those proposed by Gardoni et al. (2002);
- The integration of additional modelling complexity could be explored, such as foundation effects, site-specific effects, multi-support excitations, or ground motion input excitation in all three dimensions, to enhance the robustness of the results;
- The applications could be extended to other structural typologies or sites with different underlying hazard conditions. This can strengthen the conclusions drawn from this thesis;
- Extend the dynamic analyses to biaxial excitation using both available recordings in horizontal plane. Additionally, the impact of using

different horizontal component definitions in the seismic hazard analysis and ground motion selection can be explored. These further explorations could offer a more comprehensive assessment of the predictive capability of the proposed IMs;

- Practical tools for advanced ground motion selection based on the developed GGMM and correlation models could be developed, making the usage of next-generation IMs more accessible to practitioners.

These combined limitations and recommendations highlight areas where future research can build upon the contributions of this thesis to further enhance seismic risk assessment methodologies.

References

- Abadi, M., Agarwal, A., Barham, P., Brevdo, E., Chen, Z., Citro, C., Corrado, G. S., Davis, A., Dean, J., Devin, M., Ghemawat, S., Goodfellow, I., Harp, A., Irving, G., Isard, M., Jia, Y., Jozefowicz, R., Kaiser, L., Kudlur, M., Levenberg, J., Mané, D., Monga, R., Moore, S., Murray, D., Olah, C., Schuster, M., Shlens, J., Steiner, B., Sutskever, I., Talwar, K., Tucker, P., Vanhoucke, V., Vasudevan, V., Viégas, F., Vinyals, O., Warden, P., Wattenberg, M., Wicke, M., Yu, Y., & Zheng, X. (2015). TensorFlow: Large-Scale Machine Learning on Heterogeneous Systems. <https://www.tensorflow.org/> Software available from tensorflow.org.
- Abarca, A., Monteiro, R., O'Reilly, G., Zuccolo, E., & Borzi, B. (2021). Evaluation of intensity measure performance in regional seismic risk assessment of reinforced concrete bridge inventories. *Structure and Infrastructure Engineering*, 19(6), 760–778. <https://doi.org/10.1080/15732479.2021.1979599>
- Abarca, A., Monteiro, R., & O'Reilly, G. J. (2022). Simplified methodology for indirect loss-based prioritization in roadway bridge network risk assessment. *International Journal of Disaster Risk Reduction*, 74(December 2021), 102948. <https://doi.org/10.1016/j.ijdrr.2022.102948>
- Abrahamson, N. A., & Silva, W. J. (1997). Empirical response spectral attenuation relations for shallow crustal earthquakes. *Seismological Research Letters*, 68(1), 94–109. <https://doi.org/10.1785/gssrl.68.1.94>
- Abrahamson, N., Atkinson, G., Boore, D., Bozorgnia, Y., Campbell, K., Chiou, B., Idriss, I. M., Silva, W., & Youngs, R. (2008). Comparisons of the NGA Ground-Motion Relations. *Earthquake Spectra*, 24(1), 45–66. <https://doi.org/10.1193/1.2924363>

- Abrahamson, N. A., & Al Atik, L. (2010). Scenario spectra for design ground motions and risk calculation. *Proc. of the 9th US National and 10th Canadian Conference on Earthquake Engineering*. Oakland, Canada.
- Abrahamson, N. A., & Silva, W. (2008). Summary of the Abrahamson & Silva NGA ground-motion relations. *Earthquake Spectra*, 24(1), 67–97. <https://doi.org/10.1193/1.2924360>
- Abrahamson, N. A., & Youngs, R. R. (1992). A stable algorithm for regression analyses using the random effects model. *Bulletin of the Seismological Society of America*, 82(1), 505–510. <https://doi.org/10.1785/BSSA0820010505>
- Afshari, K., & Stewart, J. P. (2016). Physically parameterized prediction equations for significant duration in active crustal regions. *Earthquake Spectra*, 32(4), 2057–2081. <https://doi.org/10.1193/063015EQS106M>
- Ahdi, S. K., Mazzoni, S., Kishida, T., Wang, P., Nweke, C. C., Kuehn, N. M., Contreras, V., Rowshandel, B., Stewart, J. P., & Bozorgnia, Y. (2020). Engineering characteristics of ground motions recorded in the 2019 ridgecrest earthquake sequence. *Bulletin of the Seismological Society of America*, 110(4), 1474–1494. <https://doi.org/10.1785/0120200036>
- Akkar, S., Sandikkaya, M. A., & Ay, B. Ö. (2014). Compatible ground-motion prediction equations for damping scaling factors and vertical-to-horizontal spectral amplitude ratios for the broader Europe region. *Bulletin of Earthquake Engineering*, 12(1), 517–547. <https://doi.org/10.1007/s10518-013-9537-1>
- Akkar, S., Sandikkaya, M. A., Şenyurt, M., Azari Sisi, A., Ay, B. Ö., Traversa, P., Douglas, J., Cotton, F., Luzi, L., Hernandez, B., & Godey, S. (2014). Reference database for seismic ground-motion in Europe (RESORCE). *Bulletin of Earthquake Engineering*, 12(1), 311–339. <https://doi.org/10.1007/s10518-013-9506-8>
- Akkar, S., & Özen, Ö. (2005). Effect of peak ground velocity on deformation demands for SDOF systems. *Earthquake Engineering & Structural Dynamics*, 34(13), 1551–1571. <https://doi.org/10.1002/eqe.492>
- Ancheta, T., Darragh, R., Stewart, J., Seyhan, E., Silva, W., Chiou, B., Wooddell, K., Graves, R., Kottke, A., Boore, D., Kishida, T., & Donahue, J. (2013). *PEER NGA-West2 Database, PEER Report 2013-03* (tech. rep.). Pacific Earthquake Engineering Research Center,

- University of California. Berkeley, California. https://peer.berkeley.edu/sites/default/files/2013_03_ancheta_7.3.2020.pdf
- Ang, A. H.-S., & Tang, W. H. (1975). *Probability Concepts in Engineering Planning and Design: Decision, risk and reliability*. John Wiley & Sons. Hoboken, NJ. <https://books.google.it/books?id=tuRDAQAAIAAJ>
- Aristeidou, S., & O'Reilly, G. J. (2024). Exploring the Use of Orientation-Independent Inelastic Spectral Displacements in the Seismic Assessment of Bridges. *Journal of Earthquake Engineering*, 28(12), 3515–3538. <https://doi.org/10.1080/13632469.2024.2343067>
- Aristeidou, S., Shahnazaryan, D., & O'Reilly, G. J. (2024). Artificial neural network-based ground motion model for next-generation seismic intensity measures. *Soil Dynamics and Earthquake Engineering*, 184, 108851. <https://doi.org/10.1016/j.soildyn.2024.108851>
- Aristeidou, S., Shahnazaryan, D., & O'Reilly, G. J. (2025). Correlation Models for Next-Generation Amplitude and Cumulative Intensity Measures using Artificial Neural Networks. *Earthquake Spectra*, 41(1), 851–875. <https://doi.org/10.1177/87552930241270563>
- Aristeidou, S., Tarbali, K., & O'Reilly, G. J. (2023). A Ground Motion Model for Orientation-Independent Inelastic Spectral Displacements from Shallow Crustal Earthquakes. *Earthquake Spectra*, 39(3), 1601–1624. <https://doi.org/10.1177/87552930231180228>
- ASCE. (2017). *Minimum design loads for buildings and other structures (ASCE 7-16)*. American Society of Civil Engineers. Reston, VI.
- ASCE/SEI 7-16. (2018). *Minimum Design Loads for Buildings and Other Structures*. American Society of Civil Engineers.
- Aslani, H. (2005). *Probabilistic earthquake loss estimation and loss disaggregation in buildings* [Doctoral dissertation, Stanford University] [Department of Civil and Environmental Engineering. John A. Blume Earthquake Engineering Center].
- Atik, L. A., Abrahamson, N., Bommer, J. J., Scherbaum, F., Cotton, F., & Kuehn, N. (2010). The Variability of Ground-Motion Prediction Models and Its Components. *Seismological Research Letters*, 81(5), 794–801. <https://doi.org/10.1785/gssrl.81.5.794>
- Avşar, Ö., & Özdemir, G. (2013). Response of Seismic-Isolated Bridges in Relation to Intensity Measures of Ordinary and Pulselike Ground

- Motions. *Journal of Bridge Engineering*, 18(3), 250–260. [https://doi.org/10.1061/\(ASCE\)BE.1943-5592.0000340](https://doi.org/10.1061/(ASCE)BE.1943-5592.0000340)
- Bahrampouri, M., Bozorgnia, Y., Mazzoni, S., & Campbell, K. (2023). *Use of Inelastic Response Spectra in Seismic Hazard Analysis and Design* (tech. rep. No. GIRS-2023-01). University of California, Los Angeles. <https://doi.org/10.34948/N38G6K>
- Baker, J., Bradley, B., & Stafford, P. (2021). *Seismic Hazard and Risk Analysis* (1st ed.). Cambridge University Press. <https://doi.org/10.1017/9781108425056>
- Baker, J. W. (2011). Conditional Mean Spectrum: Tool for Ground-Motion Selection. *Journal of Structural Engineering*, 137(3), 322–331. [https://doi.org/10.1061/\(ASCE\)ST.1943-541X.0000215](https://doi.org/10.1061/(ASCE)ST.1943-541X.0000215)
- Baker, J. W., & Bradley, B. A. (2017). Intensity Measure Correlations Observed in the NGA-West2 Database, and Dependence of Correlations on Rupture and Site Parameters. *Earthquake Spectra*, 33(1), 145–156. <https://doi.org/10.1193/060716EQS095M>
- Baker, J. W., & Chen, Y. (2020). Ground motion spatial correlation fitting methods and estimation uncertainty. *Earthquake Engineering and Structural Dynamics*, 49(15), 1662–1681. <https://doi.org/10.1002/eqe.3322>
- Baker, J. W., & Cornell, C. A. (2005a). A vector-valued ground motion intensity measure consisting of spectral acceleration and epsilon. *Earthquake Engineering and Structural Dynamics*, 34(10), 1193–1217. <https://doi.org/10.1002/eqe.474>
- Baker, J. W., & Cornell, C. A. (2005b). *Vector-valued ground motion intensity measures for probabilistic seismic demand analysis* (tech. rep. No. 150). John A. Blume Earthquake Engineering Center. Stanford University. California.
- Baker, J. W., & Cornell, C. A. (2006a). Correlation of response spectral values for multicomponent ground motions. *Bulletin of the Seismological Society of America*, 96(1), 215–227. <https://doi.org/10.1785/0120050060>
- Baker, J. W., & Cornell, C. A. (2006b). Spectral shape, epsilon and record selection. *Earthquake Engineering & Structural Dynamics*, 35(9), 1077–1095. <https://doi.org/10.1002/eqe.571>

- Baker, J. W., & Cornell, C. A. (2006c). Which spectral acceleration are you using? *Earthquake Spectra*, 22(2), 293–312. <https://doi.org/10.1193/1.2191540>
- Baker, J. W., & Jayaram, N. (2008). Correlation of spectral acceleration values from NGA ground motion models. *Earthquake Spectra*, 24(1), 299–317. <https://doi.org/10.1193/1.2857544>
- Baker, J. W., & Lee, C. (2018). An Improved Algorithm for Selecting Ground Motions to Match a Conditional Spectrum. *Journal of Earthquake Engineering*, 22(4), 708–723. <https://doi.org/10.1080/13632469.2016.1264334>
- Bakouregui, A. S., Mohamed, H. M., Yahia, A., & Benmokrane, B. (2021). Explainable extreme gradient boosting tree-based prediction of load-carrying capacity of FRP-RC columns. *Engineering Structures*, 245, 112836. <https://doi.org/10.1016/j.engstruct.2021.112836>
- Bazzurro, P., & Cornell, C. A. (2002). Vector-valued Probabilistic Seismic Hazard Analysis (VPSHA). *Proceedings of the 7th US National Conference on Earthquake Engineering*. Boston, MA.
- Beyer, K., & Bommer, J. J. (2006). Relationships between median values and between aleatory variabilities for different definitions of the horizontal component of motion. *Bulletin of the Seismological Society of America*, 96(4A), 1512–1522. <https://doi.org/10.1785/0120050210>
- Bianchini, M., Diotallevi, P. P., & Baker, J. W. (2009). Prediction of inelastic structural response using an average of spectral accelerations. *Proceedings of the 10th international conference on structural safety and reliability (ICOSSAR09)*. Osaka, Japan.
- Bindi, D., Pacor, F., Luzi, L., Puglia, R., Massa, M., Ameri, G., & Paolucci, R. (2011). Ground motion prediction equations derived from the Italian strong motion database. *Bulletin of Earthquake Engineering*, 9(6), 1899–1920. <https://doi.org/10.1007/s10518-011-9313-z>
- Bodenmann, L., Baker, J. W., & Stojadinović, B. (2023). Accounting for path and site effects in spatial ground-motion correlation models using Bayesian inference. *Natural Hazards and Earth System Sciences*, 23(7), 2387–2402. <https://doi.org/10.5194/nhess-23-2387-2023>
- Bojórquez, E., Iervolino, I., Reyes-Salazar, A., & Ruiz, S. E. (2012). Comparing vector-valued intensity measures for fragility analysis of steel frames in the case of narrow-band ground motions. *Engineering*

- Structures*, 45, 472–480. <https://doi.org/10.1016/j.engstruct.2012.07.002>
- Bommer, J. J., & Acevedo, A. B. (2004). The use of real accelerograms as input to dynamic analysis. *Journal of Earthquake Engineering*, 8(sup001), 43–91. <https://doi.org/10.1080/13632460409350521>
- Bommer, J. J., & Martínez-Pereira, A. (1999). The effective duration of earthquake strong motion. *Journal of Earthquake Engineering*, 3(2), 127–172. <https://doi.org/10.1080/13632469909350343>
- Boore, D. M. (2010). Orientation-independent, nongeometric-mean measures of seismic intensity from two horizontal components of motion. *Bulletin of the Seismological Society of America*, 100(4), 1830–1835. <https://doi.org/10.1785/0120090400>
- Boore, D. M., Stewart, J. P., Seyhan, E., & Atkinson, G. M. (2014). NGA-West2 equations for predicting PGA, PGV, and 5% damped PSA for shallow crustal earthquakes. *Earthquake Spectra*, 30(3), 1057–1085. <https://doi.org/10.1193/070113EQS184M>
- Boore, D. M., Stewart, J. P., Skarlatoudis, A. A., Seyhan, E., Margaris, B., Theodoulidis, N., Scordilis, E., Kalogerias, I., Klimis, N., & Melis, N. S. (2021). A Ground-Motion Prediction Model for Shallow Crustal Earthquakes in Greece. *Bulletin of the Seismological Society of America*, 111(2), 857–874. <https://doi.org/10.1785/0120200270>
- Boore, D. M., Watson-Lamprey, J., & Abrahamson, N. A. (2006). Orientation-independent measures of ground motion. *Bulletin of the Seismological Society of America*, 96(4 A), 1502–1511. <https://doi.org/10.1785/0120050209>
- Borzi, B., Ceresa, P., Franchin, P., Noto, F., Calvi, G. M., & Pinto, P. E. (2015). Seismic Vulnerability of the Italian Roadway Bridge Stock. *Earthquake Spectra*, 31(4), 2137–2161. <https://doi.org/10.1193/070413EQS190M>
- Bozorgnia, Y., Abrahamson, N. A., Al Atik, L., Ancheta, T. D., Atkinson, G. M., Baker, J. W., Baltay, A., Boore, D. M., Campbell, K. W., Chiou, B. S., Darragh, R., Day, S., Donahue, J., Graves, R. W., Gregor, N., Hanks, T., Idriss, I. M., Kamai, R., Kishida, T., Kottke, A., Mahin, S. A., Rezaeian, S., Rowshandel, B., Seyhan, E., Shahi, S., Shantz, T., Silva, W., Spudich, P., Stewart, J. P., Watson-Lamprey, J., Wooddell, K., & Youngs, R. (2014). NGA-West2 research project.

- Earthquake Spectra*, 30(3), 973–987. <https://doi.org/10.1193/072113EQS209M>
- Bozorgnia, Y., Hachem, M. M., & Campbell, K. W. (2010). Ground motion prediction equation ("Attenuation Relationship") for inelastic response spectra. *Earthquake Spectra*, 26(1), 1–23. <https://doi.org/10.1193/1.3281182>
- Bradley, B. A. (2010). A generalized conditional intensity measure approach and holistic ground-motion selection. *Earthquake Engineering & Structural Dynamics*, 39(12), 1321–1342. <https://doi.org/10.1002/eqe.995>
- Bradley, B. A. (2011a). Correlation of significant duration with amplitude and cumulative intensity measures and its use in ground motion selection. *Journal of Earthquake Engineering*, 15(6), 809–832. <https://doi.org/10.1080/13632469.2011.557140>
- Bradley, B. A. (2011b). Empirical equations for the prediction of displacement spectrum intensity and its correlation with other intensity measures. *Soil Dynamics and Earthquake Engineering*, 31(8), 1182–1191. <https://doi.org/10.1016/j.soildyn.2011.04.007>
- Bradley, B. A. (2012). The seismic demand hazard and importance of the conditioning intensity measure. *Earthquake Engineering & Structural Dynamics*, 41(11), 1417–1437. <https://doi.org/10.1002/eqe.2221>
- Bradley, B. A., & Baker, J. W. (2014). Ground motion directionality in the 2010–2011 Canterbury earthquakes. *Earthquake Engineering and Structural Dynamics*, 44(3), 371–384. <https://doi.org/10.1002/eqe.2474>
- Bradley, B. A., Burks, L. S., & Baker, J. W. (2015). Ground motion selection for simulation-based seismic hazard and structural reliability assessment. *Earthquake Engineering & Structural Dynamics*, 44(13), 2321–2340. <https://doi.org/10.1002/eqe.2588>
- Bradley, B. A., Dhakal, R. P., MacRae, G. A., & Cubrinovski, M. (2009). Prediction of spatially distributed seismic demands in specific structures: Ground motion and structural response. *Earthquake Engineering & Structural Dynamics*, 39, 501–520. <https://doi.org/10.1002/eqe.954>
- Bray, J. D., & Rodriguez-Marek, A. (2004). Characterization of forward-directivity ground motions in the near-fault region. *Soil Dynamics*

- and Earthquake Engineering*, 24(11), 815–828. <https://doi.org/10.1016/j.soildyn.2004.05.001>
- Burks, L. S., & Baker, J. W. (2014). Validation of ground-motion simulations through simple proxies for the response of engineered systems. *Bulletin of the Seismological Society of America*, 104(4), 1930–1946. <https://doi.org/10.1785/0120130276>
- Caltrans. (2010). *Caltrans Seismic Design Criteria Version 1.6*. California Department of Transportation (tech. rep. No. November). Sacramento, CA.
- Caltrans. (2019). *Caltrans Seismic Design Criteria Version 2.0* (tech. rep.). State of California. Sacramento, California. <https://dot.ca.gov/programs/engineering-services/manuals/seismic-design-criteria>
- Campbell, K. W., & Bozorgnia, Y. (2007). *Campbell-Bozorgnia NGA Ground Motion Relations for the Geometric Mean Horizontal Component of Peak and Spectral Ground Motion Parameters* (tech. rep.). Pacific Earthquake Engineering Research Center, University of California. Berkeley, California.
- Campbell, K. W., & Bozorgnia, Y. (2008). NGA ground motion model for the geometric mean horizontal component of PGA, PGV, PGD and 5% damped linear elastic response spectra for periods ranging from 0.01 to 10 s. *Earthquake Spectra*, 24(1), 139–171. <https://doi.org/10.1193/1.2857546>
- Campbell, K. W., & Bozorgnia, Y. (2014). NGA-West2 Ground Motion Model for the Average Horizontal Components of PGA, PGV, and 5% Damped Linear Acceleration Response Spectra. *Earthquake Spectra*, 30(3), 1087–1115. <https://doi.org/10.1193/062913EQS175M>
- Campbell, K. W., & Bozorgnia, Y. (2019). Ground Motion Models for the Horizontal Components of Arias Intensity (AI) and Cumulative Absolute Velocity (CAV) Using the NGA-West2 Database. *Earthquake Spectra*, 35(3), 1289–1310. <https://doi.org/10.1193/090818EQS212M>
- CEN. (2005). Eurocode 8: Design of Structures for Earthquake Resistance - Part 2: Bridges (EN 1998–2:2005). Brussels, Belgium.
- Chandramohan, R., Baker, J. W., & Deierlein, G. G. (2016). Quantifying the influence of ground motion duration on structural collapse capacity using spectrally equivalent records. *Earthquake Spectra*, 32(2), 927–950. <https://doi.org/10.1193/122813EQS298MR2>

- Chen, T., & Guestrin, C. (2016). XGBoost: a scalable tree boosting system. *Proceedings of the 22nd ACM SIGKDD International Conference on Knowledge Discovery and Data Mining*, 785–794. New York, USA. <https://doi.org/10.1145/2939672.2939785>
- Chiou, B. S., & Youngs, R. R. (2008). An NGA model for the average horizontal component of peak ground motion and response spectra. *Earthquake Spectra*, 24(1), 173–215. <https://doi.org/10.1193/1.2894832>
- Chopra, A. K. (2014). *Dynamics of Structures - Theory and Applications to Earthquake Engineering* (Fourth Ed.). Pearson Education Limited.
- Cordova, P. P., Deierlein, G. G., Mehanny, S. S., & Cornell, C. A. (2000). Development of a two-parameter seismic intensity measure and probabilistic assessment procedure. *The second US-Japan workshop on performance-based earthquake engineering methodology for reinforced concrete building structures*, (20), 187–206. Hokkaido, Japan.
- Cornell, C. A., Jalayer, F., Hamburger, R. O., & Foutch, D. A. (2002). Probabilistic Basis for 2000 SAC Federal Emergency Management Agency Steel Moment Frame Guidelines. *Journal of Structural Engineering*, 128(4), 526–533. [https://doi.org/10.1061/\(ASCE\)0733-9445\(2002\)128:4\(526\)](https://doi.org/10.1061/(ASCE)0733-9445(2002)128:4(526))
- Cornell, C. A., & Krawinkler, H. (2000). Progress and challenges in seismic performance assessment. *PEER Center News*, 3(2), 1–2.
- Cornell C. Allin. (1968). Engineering Seismic Risk Analysis. *Bulletin of the Seismological Society of America*, 58(5), 1583–1606.
- Danciu, L., Nandan, S., Reyes, C., Basili, R., Weatherill, G., Beauval, C., Rovida, A., Vilanova, S., Sesetyan, K., Bard, P.-Y., Cotton, F., Wiemer, S., & Giardini, D. (2021). *The 2020 update of the European Seismic Hazard Model: Model Overview* (tech. rep. No. EFEHR Technical Report 001, v1.0.0). <https://doi.org/https://doi.org/10.12686/a15>
- Dávalos, H., Heresi, P., & Miranda, E. (2020). A ground motion prediction equation for filtered incremental velocity, FIV3. *Soil Dynamics and Earthquake Engineering*, 139, 106346. <https://doi.org/10.1016/j.soildyn.2020.106346>
- Dávalos, H., & Miranda, E. (2019). Filtered incremental velocity: A novel approach in intensity measures for seismic collapse estimation.

- Earthquake Engineering & Structural Dynamics*, 48(12), 1384–1405.
<https://doi.org/10.1002/eqe.3205>
- Dávalos, H., & Miranda, E. (2020). Evaluation of FIV3 as an Intensity Measure for Collapse Estimation of Moment-Resisting Frame Buildings. *Journal of Structural Engineering*, 146(10), 1–14. [https://doi.org/10.1061/\(asce\)st.1943-541x.0002781](https://doi.org/10.1061/(asce)st.1943-541x.0002781)
- Dávalos, H., & Miranda, E. (2021). A Ground Motion Prediction Model for Average Spectral Acceleration. *Journal of Earthquake Engineering*, 25(2), 319–342. <https://doi.org/10.1080/13632469.2018.1518278>
- Del Gaudio, C., De Martino, G., Di Ludovico, M., Manfredi, G., Prota, A., Ricci, P., & Verderame, G. M. (2017). Empirical fragility curves from damage data on RC buildings after the 2009 L'Aquila earthquake. *Bulletin of Earthquake Engineering*, 15(4), 1425–1450. <https://doi.org/10.1007/s10518-016-0026-1>
- Derras, B., Bard, P. Y., & Cotton, F. (2014). Towards fully data driven ground-motion prediction models for Europe. *Bulletin of Earthquake Engineering*, 12(1), 495–516. <https://doi.org/10.1007/s10518-013-9481-0>
- Derras, B., Bard, P. Y., & Cotton, F. (2016). Site-condition proxies, ground motion variability, and data-driven GMPEs: Insights from the NGA-West2 and RESORCE data sets. *Earthquake Spectra*, 32(4), 2027–2056. <https://doi.org/10.1193/060215EQS082M>
- Dhanya, J., & Raghukanth, S. T. (2018). Ground Motion Prediction Model Using Artificial Neural Network. *Pure and Applied Geophysics*, 175(3), 1035–1064. <https://doi.org/10.1007/s00024-017-1751-3>
- Douglas, J. (2022). Ground motion prediction equations 1964–2021. Retrieved December 4, 2023, from <http://www.gmpe.org.uk/gmpereport2014.html>
- Duncan, J. M., & Mokwa, R. L. (2001). Passive Earth Pressures: Theories and Tests. *Journal of Geotechnical and Geoenvironmental Engineering*, 127(3), 248–257. [https://doi.org/10.1061/\(asce\)1090-0241\(2001\)127:3\(248\)](https://doi.org/10.1061/(asce)1090-0241(2001)127:3(248))
- Eads, L., & Miranda, E. (2013). *Seismic collapse risk assessment of buildings: effects of intensity measure selection and computational approach* [Doctoral dissertation, Stanford University]. <https://purl.stanford.edu/cn733sv2623>

- Eads, L., Miranda, E., & Lignos, D. G. (2015). Average spectral acceleration as an intensity measure for collapse risk assessment. *Earthquake Engineering & Structural Dynamics*, 44(12), 2057–2073. <https://doi.org/10.1002/eqe.2575>
- Enke, D. L., Tirasirichai, C., & Luna, R. (2008). Estimation of Earthquake Loss due to Bridge Damage in the St. Louis Metropolitan Area. II: Indirect Losses. *Natural Hazards Review*, 9(1), 12–19. [https://doi.org/10.1061/\(ASCE\)1527-6988\(2008\)9:1\(12\)](https://doi.org/10.1061/(ASCE)1527-6988(2008)9:1(12))
- Fayaz, J., Dabaghi, M., & Zareian, F. (2020). Utilization of Site-Based Simulated Ground Motions for Hazard-Targeted Seismic Demand Estimation: Application for Ordinary Bridges in Southern California. *Journal of Bridge Engineering*, 25(11). [https://doi.org/10.1061/\(asce\)be.1943-5592.0001634](https://doi.org/10.1061/(asce)be.1943-5592.0001634)
- Fayaz, J., Medalla, M., & Zareian, F. (2020). Sensitivity of the response of Box-Girder Seat-type bridges to the duration of ground motions arising from crustal and subduction earthquakes. *Engineering Structures*, 219, 110845. <https://doi.org/10.1016/j.engstruct.2020.110845>
- Fayaz, J., Xiang, Y., & Zareian, F. (2021). Generalized ground motion prediction model using hybrid recurrent neural network. *Earthquake Engineering & Structural Dynamics*, 50(6), 1539–1561. <https://doi.org/10.1002/eqe.3410>
- Feng, R., Wang, X., Yuan, W., & Yu, J. (2018). Impact of seismic excitation direction on the fragility analysis of horizontally curved concrete bridges. *Bulletin of Earthquake Engineering*, 16(10), 4705–4733. <https://doi.org/10.1007/s10518-018-0400-2>
- Feng, R., Yuan, W., & Sextos, A. (2021). Probabilistic loss assessment of curved bridges considering the effect of ground motion directionality. *Earthquake Engineering and Structural Dynamics*, 50(13), 3623–3645. <https://doi.org/10.1002/eqe.3525>
- Fontara, I.-K. M., Kostinakis, K. G., Manoukas, G. E., & Athanatopoulou, A. M. (2015). Parameters affecting the seismic response of buildings under bi-directional excitation. *Structural Engineering and Mechanics*, 53(5), 957–979. <https://doi.org/10.12989/sem.2015.53.5.957>
- Gardoni, P., Der Kiureghian, A., & Mosalam, K. M. (2002). Probabilistic Capacity Models and Fragility Estimates for Reinforced Concrete Columns based on Experimental Observations. *Journal of Engineer-*

- ing Mechanics*, 128(10), 1024–1038. [https://doi.org/10.1061/\(ASCE\)0733-9399\(2002\)128:10\(1024\)](https://doi.org/10.1061/(ASCE)0733-9399(2002)128:10(1024))
- GEM. (2022). The OpenQuake-engine User Manual. *Global Earthquake Model (GEM) OpenQuake Manual for Engine version 3.18.0*. <https://doi.org/10.13117/GEM.OPENQUAKE.MAN.ENGINE.3.18.0>
- Gentile, R., & Galasso, C. (2021). Hysteretic energy-based state-dependent fragility for ground-motion sequences. *Earthquake Engineering & Structural Dynamics*, 50(4), 1187–1203. <https://doi.org/10.1002/eqe.3387>
- Giannopoulos, D., & Vamvatsikos, D. (2018). Ground motion records for seismic performance assessment: To rotate or not to rotate? *Earthquake Engineering & Structural Dynamics*, 47(12), 2410–2425. <https://doi.org/10.1002/eqe.3090>
- Hancock, J., & Bommer, J. J. (2006). A State-of-Knowledge Review of the Influence of Strong-Motion Duration on Structural Damage. *Earthquake Spectra*, 22(3), 827–845. <https://doi.org/10.1193/1.2220576>
- Haselton, C. B., & Baker, J. W. (2006). Ground motion intensity measures for collapse capacity prediction: Choice of optimal spectral period and effect of spectral shape. *8th US National Conference on Earthquake Engineering*, 15, 8830–8839. <https://api.semanticscholar.org/CorpusID:124847110>
- Haykin, S. S. (2009). *Neural networks and learning machines*. Pearson.
- HAZUS. (2003). *Multi-hazard loss estimation methodology - earthquake model*. FEMA-National Institute of Building Sciences. Washington, DC, USA.
- Heresi, P., Dávalos, H., & Miranda, E. (2018). Ground motion prediction model for the peak inelastic displacement of single-degree-of-freedom bilinear systems. *Earthquake Spectra*, 34(3), 1177–1199. <https://doi.org/10.1193/061517EQS118M>
- Huang, C., & Galasso, C. (2019). Ground-motion intensity measure correlations observed in Italian strong-motion records. *Earthquake Engineering & Structural Dynamics*, 48(15), 1634–1660. <https://doi.org/10.1002/eqe.3216>
- Huang, C., Tarbali, K., & Galasso, C. (2020). A region-specific ground-motion model for inelastic spectral displacement in northern Italy

- considering spatial correlation properties. *Seismological Research Letters*, 92(3), 1979–1991. <https://doi.org/10.1785/0220200249>
- Huang, Q., Gardoni, P., & Hurlebaus, S. (2010). Probabilistic Seismic Demand Models and Fragility Estimates for Reinforced Concrete Highway Bridges with One Single-Column Bent. *Journal of Engineering Mechanics*, 136(11), 1340–1353. [https://doi.org/10.1061/\(ASCE\)EM.1943-7889.0000186](https://doi.org/10.1061/(ASCE)EM.1943-7889.0000186)
- Huang, Y. N., Whittaker, A. S., & Luco, N. (2009). Orientation of maximum spectral demand in the near-fault region. *Earthquake Spectra*, 25(3), 707–717. <https://doi.org/10.1193/1.3158997>
- Husid, R. (1969). Características de terremotos. Análisis general. *Revista IDIEM*, 8(1), 21–42.
- Iervolino, I., Manfredi, G., & Cosenza, E. (2006). Ground motion duration effects on nonlinear seismic response. *Earthquake Engineering & Structural Dynamics*, 35(1), 21–38. <https://doi.org/10.1002/eqe.529>
- Jalayer, F., Beck, J. L., & Zareian, F. (2012). Analyzing the Sufficiency of Alternative Scalar and Vector Intensity Measures of Ground Shaking Based on Information Theory. *Journal of Engineering Mechanics*, 138(3), 307–316. [https://doi.org/10.1061/\(asce\)em.1943-7889.0000327](https://doi.org/10.1061/(asce)em.1943-7889.0000327)
- Jalayer, F., Franchin, P., & Pinto, P. E. (2007). A scalar damage measure for seismic reliability analysis of RC frames. *Earthquake Engineering & Structural Dynamics*, 36(13), 2059–2079. <https://doi.org/10.1002/eqe.704>
- Japan Road Association. (2012). *Specifications for highway bridges*. Tokyo, Japan.
- Kaka, S. I., & Atkinson, G. M. (2004). Relationships between Instrumental Ground-Motion Parameters and Modified Mercalli Intensity in Eastern North America. *Bulletin of the Seismological Society of America*, 94(5), 1728–1736. <https://doi.org/10.1785/012003228>
- Kaklamanos, J., Baise, L. G., & Boore, D. M. (2011). Estimating unknown input parameters when implementing the NGA ground-motion prediction equations in engineering practice. *Earthquake Spectra*, 27(4), 1219–1235. <https://doi.org/10.1193/1.3650372>
- Kalakonas, P., & Silva, V. (2022). Earthquake scenarios for building portfolios using artificial neural networks : part I — ground motion

- modelling. *Bulletin of Earthquake Engineering*, (0123456789). <https://doi.org/10.1007/s10518-022-01598-3>
- Kalkan, E., & Kunnath, S. K. (2006). Effects of Fling Step and Forward Directivity on Seismic Response of Buildings. *Earthquake Spectra*, 22(2), 367–390. <https://doi.org/10.1193/1.2192560>
- Kaviani, P., Zareian, F., & Taciroglu, E. (2014). Performance-Based Seismic Assessment of Skewed Bridges. *Pacific Earthquake Engineering Research Center (PEER)*, (January), 161. <https://doi.org/10.13140/2.1.1586.0007>
- Kazantzi, A. K., & Vamvatsikos, D. (2015). Intensity measure selection for vulnerability studies of building classes. *Earthquake Engineering & Structural Dynamics*, 44(15), 2677–2694. <https://doi.org/10.1002/eqe.2603>
- Kiefer, J., & Wolfowitz, J. (1952). Stochastic Estimation of the Maximum of a Regression Function. *The Annals of Mathematical Statistics*, 23(3), 462–466. <https://doi.org/10.1214/aoms/1177729392>
- Kilanitis, I., & Sextos, A. (2019). Impact of earthquake-induced bridge damage and time evolving traffic demand on the road network resilience. *Journal of Traffic and Transportation Engineering (English Edition)*, 6(1), 35–48. <https://doi.org/10.1016/j.jtte.2018.07.002>
- Kingma, D. P., & Ba, J. (2014). Adam: A Method for Stochastic Optimization. *3rd International Conference on Learning Representations, ICLR 2015*, 1–15. <http://arxiv.org/abs/1412.6980>
- Kohrangi, M., Bazzurro, P., Vamvatsikos, D., & Spillatura, A. (2017). Conditional spectrum-based ground motion record selection using average spectral acceleration. *Earthquake Engineering & Structural Dynamics*, 46(10), 1667–1685. <https://doi.org/10.1002/eqe.2876>
- Kohrangi, M., Kotha, S. R., & Bazzurro, P. (2018). Ground-motion models for average spectral acceleration in a period range: Direct and indirect methods. *Bulletin of Earthquake Engineering*, 16(1), 45–65. <https://doi.org/10.1007/s10518-017-0216-5>
- Kohrangi, M., Papadopoulos, A. N., Bazzurro, P., & Vamvatsikos, D. (2020). Correlation of spectral acceleration values of vertical and horizontal ground motion pairs. *Earthquake Spectra*, 36(4), 2112–2128. <https://doi.org/10.1177/8755293020919416>
- Kohrangi, M., Vamvatsikos, D., & Bazzurro, P. (2016). Implications of intensity measure selection for seismic loss assessment of 3-D buildings.

- Earthquake Spectra*, 32(4), 2167–2189. <https://doi.org/10.1193/112215EQS177M>
- Kohrangi, M., Vamvatsikos, D., & Bazzurro, P. (2019). Pulse-like versus non-pulse-like ground motion records: Spectral shape comparisons and record selection strategies. *Earthquake Engineering & Structural Dynamics*, 48(1), 46–64. <https://doi.org/10.1002/eqe.3122>
- Kotha, S. R., Bindi, D., & Cotton, F. (2017). Site-corrected magnitude- and region-dependent correlations of horizontal peak spectral amplitudes. *Earthquake Spectra*, 33(4), 1415–1432. <https://doi.org/10.1193/091416EQS150M>
- Kotha, S. R., Weatherill, G., Bindi, D., & Cotton, F. (2020). A regionally-adaptable ground-motion model for shallow crustal earthquakes in Europe. *Bulletin of Earthquake Engineering*, 18(9), 4091–4125. <https://doi.org/10.1007/s10518-020-00869-1>
- Lin, T., Haselton, C. B., & Baker, J. W. (2013a). Conditional spectrum-based ground motion selection. Part I: Hazard consistency for risk-based assessments. *Earthquake Engineering & Structural Dynamics*, 42(12), 1847–1865. <https://doi.org/10.1002/eqe.2301>
- Lin, T., Haselton, C. B., & Baker, J. W. (2013b). Conditional spectrum-based ground motion selection. Part II: Intensity-based assessments and evaluation of alternative target spectra. *Earthquake Engineering & Structural Dynamics*, 42(12), 1867–1884. <https://doi.org/10.1002/eqe.2303>
- Lin, Y., He, X., & Igarashi, A. (2022). Influence of directionality of spectral-compatible Bi-directional ground motions on critical seismic performance assessment of base-isolation structures. *Earthquake Engineering and Structural Dynamics*, 51(6), 1477–1500. <https://doi.org/10.1002/eqe.3624>
- Luco, N., & Cornell, C. A. (2007). Structure-specific scalar intensity measures for near-source and ordinary earthquake ground motions. *Earthquake Spectra*, 23(2), 357–392. <https://doi.org/10.1193/1.2723158>
- Mackie, K. R., Cronin, K. J., & Nielson, B. G. (2011). Response sensitivity of highway bridges to randomly oriented multi-component earthquake excitation. *Journal of Earthquake Engineering*, 15(6), 850–876. <https://doi.org/10.1080/13632469.2010.551706>

- Mackie, K. R., Wong, J.-M., & Stojadinović, B. (2010). Post-earthquake bridge repair cost and repair time estimation methodology. *Earthquake Engineering & Structural Dynamics*, 39(3), 281–301. <https://doi.org/10.1002/eqe.942>
- Mangalathu, S., Jeon, J.-S., Padgett, J. E., & DesRoches, R. (2017). Performance-based grouping methods of bridge classes for regional seismic risk assessment: Application of ANOVA, ANCOVA, and non-parametric approaches. *Earthquake Engineering & Structural Dynamics*, 46(14), 2587–2602. <https://doi.org/10.1002/eqe.2919>
- McCulloch, W. S., & Pitts, W. (1943). A logical calculus of the ideas immanent in nervous activity. *The Bulletin of Mathematical Biophysics*, 5(4), 115–133. <https://doi.org/10.1007/BF02478259>
- Mehdizadeh, M., Mackie, K. R., & Nielson, B. G. (2017). Scaling Bias and Record Selection for Quantifying Seismic Structural Demand. *Journal of Structural Engineering*, 143(9), 1–12. [https://doi.org/10.1061/\(asce\)st.1943-541x.0001855](https://doi.org/10.1061/(asce)st.1943-541x.0001855)
- Miranda, E., & Bertero, V. V. (1994). Evaluation of Strength Reduction Factors for Earthquake-Resistant Design. *Earthquake Spectra*, 10(2), 357–379. <https://doi.org/10.1193/1.1585778>
- Močkus, J. (1975). On bayesian methods for seeking the extremum, 400–404. https://doi.org/10.1007/3-540-07165-2_55
- Monteiro, R., Zelaschi, C., Silva, A., & Pinho, R. (2019). Derivation of Fragility Functions for Seismic Assessment of RC Bridge Portfolios Using Different Intensity Measures. *Journal of Earthquake Engineering*, 23(10), 1678–1694. <https://doi.org/10.1080/13632469.2017.1387188>
- Muntasir Billah, A., & Shahria Alam, M. (2014). Seismic fragility assessment of highway bridges: a state-of-the-art review. *Structure and Infrastructure Engineering*, 11(6), 804–832. <https://doi.org/10.1080/15732479.2014.912243>
- Nafeh, A. M. B., O'Reilly, G. J., & Monteiro, R. (2020). Simplified seismic assessment of infilled RC frame structures. *Bulletin of Earthquake Engineering*, 18(4), 1579–1611. <https://doi.org/10.1007/s10518-019-00758-2>
- Nassar, A. A., & Krawinkler, H. (1991). *Seismic demands for SDOF and MDOF systems* (tech. rep. No. 95). Stanford University. https://stacks.stanford.edu/file/druid:qt582bc4669/TR95_Nassar.pdf

- Newmark, N., & Hall, W. (1982). *Earthquake spectra and design*. Earthquake Engineering Research Institute.
- Omrani, R., Mobasher, B., Sheikhhakbari, S., Zareian, F., & Taciroglu, E. (2017). Variability in the predicted seismic performance of a typical seat-type California bridge due to epistemic uncertainties in its abutment backfill and shear-key models. *Engineering Structures*, 148, 718–738. <https://doi.org/10.1016/j.engstruct.2017.07.018>
- O'Reilly, G. J. (2021a). Limitations of $Sa(T_1)$ as an intensity measure when assessing non-ductile infilled RC frame structures. *Bulletin of Earthquake Engineering*, 19(6), 2389–2417. <https://doi.org/10.1007/s10518-021-01071-7>
- O'Reilly, G. J. (2021b). Seismic intensity measures for risk assessment of bridges. *Bulletin of Earthquake Engineering*, 19(9), 3671–3699. <https://doi.org/10.1007/s10518-021-01114-z>
- O'Reilly, G. J., & Monteiro, R. (2019). On the efficient risk assessment of bridge structures. *COMPDYN 2019 - 7th international conference on computational methods in structural dynamics and earthquake engineering*, 473–483. Crete Island, Greece. <https://doi.org/10.7712/120119.6933.18933>
- Otárola, K., Fayaz, J., & Galasso, C. (2022). Fragility and vulnerability analysis of deteriorating ordinary bridges using simulated ground-motion sequences. *Earthquake Engineering and Structural Dynamics*, 51(13), 1–26. <https://doi.org/10.1002/eqe.3720>
- Otárola, K., Gentile, R., Sousa, L., & Galasso, C. (2023). Impact of ground-motion duration on nonlinear structural performance: Part I: spectrally equivalent records and inelastic single-degree-of-freedom systems. *Earthquake Spectra*, 39(2), 829–859. <https://doi.org/10.1177/87552930231155502>
- Otárola, K., Sousa, L., Gentile, R., & Galasso, C. (2023). Impact of ground-motion duration on nonlinear structural performance: Part II: site- and building-specific analysis. *Earthquake Spectra*, 39(2), 860–888. <https://doi.org/10.1177/87552930231155506>
- Oyarzo-Vera, C., & Chouw, N. (2008). Effect of earthquake duration and sequences of ground motions on structural responses. *Proceedings of the 10th International Symposium on Structural Engineering for Young Experts, ISSEYE 2008*, (August), 1881–1886. Changsha, China.

- Petrini, L., Maggi, C., Priestley, M. J., & Calvi, G. M. (2008). Experimental verification of viscous damping modeling for inelastic time history analyzes. *Journal of Earthquake Engineering*, 12(SUPPL. 1), 125–145. <https://doi.org/10.1080/13632460801925822>
- Picard, R. R., & Cook, R. D. (1984). Cross-Validation of Regression Models. *Journal of the American Statistical Association*, 79(387), 575–583. <https://doi.org/10.1080/01621459.1984.10478083>
- Pinho, R., Monteiro, R., Casarotti, C., & Delgado, R. (2009). Assessment of continuous span bridges through nonlinear static procedures. *Earthquake Spectra*, 25(1), 143–159. <https://doi.org/10.1193/1.3050449>
- Porter, K. (2003). An Overview of PEER's Performance-Based Earthquake Engineering Methodology. *Proc. Ninth International Conference on Applications of Statistics and Probability in Civil Engineering (ICASP9)*.
- Poulos, A., & Miranda, E. (2023). Modification of Ground-Motion Models to Estimate Orientation-Dependent Horizontal Response Spectra in Strike-Slip Earthquakes. *Bulletin of the Seismological Society of America*, 113(6), 2718–2729. <https://doi.org/10.1785/0120230084>
- Poveda, J., & O'Reilly, G. J. (2025). Influence of Ground Motion Record Selection on Higher Modes: A Comparison of UHS and CS Approaches. *Third Croatian Conference on Earthquake Engineering (3CroCEE)*. Split, Croatia.
- Priestley, M. J. N., Seible, F., & Calvi, G. M. (1996). *Seismic design and retrofit of bridges*. John Wiley & Sons. <https://doi.org/10.1002/9780470172858>
- Qian, J., & Dong, Y. (2020). Multi-criteria decision making for seismic intensity measure selection considering uncertainty. *Earthquake Engineering and Structural Dynamics*, 49(11), 1095–1114. <https://doi.org/10.1002/eqe.3280>
- Raghunandan, M., & Liel, A. B. (2013). Effect of ground motion duration on earthquake-induced structural collapse. *Structural Safety*, 41, 119–133. <https://doi.org/10.1016/j.strusafe.2012.12.002>
- Rivera-Figueroa, A., & Montejo, L. A. (2022). Spectral matching RotD100 target spectra: Effect on records characteristics and seismic response. *Earthquake Spectra*, 38(2), 1570–1586. <https://doi.org/10.1177/87552930211049259>

- Romstad, K., Kutter, B., Maroney, B., Vanmarcke, E., Griggs, M., & Chai, Y. (1995). *Experimental measurements of bridge abutment behavior* (tech. rep. No. UCD STR 95 1). Dept. of Civil and Environmental Engineering. University of California, Structural Engineering Group, Davis, CA.
- Rupakhetty, R., & Sigbjörnsson, R. (2009). Ground-motion prediction equations (GMPEs) for inelastic response and structural behaviour factors. *Bulletin of Earthquake Engineering*, 7(3), 637–659. <https://doi.org/10.1007/s10518-009-9105-x>
- Rupakhetty, R., & Sigbjörnsson, R. (2013). Rotation-invariant measures of earthquake response spectra. *Bulletin of Earthquake Engineering*, 11(6), 1885–1893. <https://doi.org/10.1007/s10518-013-9472-1>
- Sarieddine, M., & Lin, L. (2013). Investigation Correlations between Strong-motion Duration and Structural Damage. *Structures Congress 2013*, 2926–2936. <https://doi.org/10.1061/9780784412848.255>
- Scott, M. H., & Fenves, G. L. (2006). Plastic Hinge Integration Methods for Force-Based Beam–Column Elements. *Journal of Structural Engineering*, 132(2), 244–252. [https://doi.org/10.1061/\(asce\)0733-9445\(2006\)132:2\(244\)](https://doi.org/10.1061/(asce)0733-9445(2006)132:2(244))
- Scott, M. H., & Ryan, K. L. (2013). Moment-rotation behavior of force-based plastic hinge elements. *Earthquake Spectra*, 29(2), 597–607. <https://doi.org/10.1193/1.4000136>
- SEAOC. (1995). *Vision 2000: Performance-based seismic engineering of buildings*. Sacramento, California.
- Sedaghati, F., & Pezeshk, S. (2023). Machine learning–based ground motion models for shallow crustal earthquakes in active tectonic regions. *Earthquake Spectra*, 39(4), 2406–2435. <https://doi.org/10.1177/87552930231191759>
- Sengupta, A., Quadery, L., Sarkar, S., & Roy, R. (2016). Influence of Bidirectional Near-Fault Excitations on RC Bridge Piers. *Journal of Bridge Engineering*, 21(7). [https://doi.org/10.1061/\(asce\)be.1943-5592.0000836](https://doi.org/10.1061/(asce)be.1943-5592.0000836)
- Shahi, S. K., & Baker, J. W. (2014). NGA-West2 models for ground motion directionality. *Earthquake Spectra*, 30(3), 1285–1300. <https://doi.org/10.1193/040913EQS097M>
- Shamsabadi, A., Rollins, K. M., & Kapuskar, M. (2007). Nonlinear Soil–Abutment–Bridge Structure Interaction for Seismic Performance-

- Based Design. *Journal of Geotechnical and Geoenvironmental Engineering*, 133(6), 707–720. [https://doi.org/10.1061/\(asce\)1090-0241\(2007\)133:6\(707\)](https://doi.org/10.1061/(asce)1090-0241(2007)133:6(707))
- Shome, N., Cornell, C. A., Bazzurro, P., & Carballo, J. E. (1998). Earthquakes, Records, and Nonlinear Responses. *Earthquake Spectra*, 14(3), 469–500. <https://doi.org/10.1193/1.1586011>
- Somerville, P. G., Smith, N. F., Graves, R. W., & Abrahamson, N. A. (1997). Modification of Empirical Strong Ground Motion Attenuation Relations to Include the Amplitude and Duration Effects of Rupture Directivity. *Seismological Research Letters*, 68(1), 199–222. <https://doi.org/10.1785/gssrl.68.1.199>
- Sousa, L., Silva, V., Marques, M., & Crowley, H. (2016). On the treatment of uncertainties in the development of fragility functions for earthquake loss estimation of building portfolios. *Earthquake Engineering & Structural Dynamics*, 45(12), 1955–1976. <https://doi.org/10.1002/eqe.2734>
- Sousa, R., Almeida, J. P., Correia, A. A., & Pinho, R. (2020). Shake Table Blind Prediction Tests: Contributions for Improved Fiber-based Frame Modelling. *Journal of Earthquake Engineering*, 24(9), 1435–1476. <https://doi.org/10.1080/13632469.2018.1466743>
- Spillatura, A., Kohrangi, M., Bazzurro, P., & Vamvatsikos, D. (2021). Conditional spectrum record selection faithful to causative earthquake parameter distributions. *Earthquake Engineering & Structural Dynamics*, 50(10), 2653–2671. <https://doi.org/10.1002/eqe.3465>
- Stafford, P. J., Sullivan, T. J., & Pennucci, D. (2016). Empirical correlation between inelastic and elastic spectral displacement demands. *Earthquake Spectra*, 32(3), 1419–1448. <https://doi.org/10.1193/020515EQS021M>
- Stewart, J., Taciroglu, E., Wallace, J., Ahlberg, E., Lemnitzer, A., Rha, C., Tehrani, P., Keowen, S., Nigbor, R., & Salamanca, A. (2007). *Full Scale Cyclic Testing of Foundation Support Systems for Highway Bridges. Part II : Abutment Backwalls* (tech. rep. No. UCLA SGEL 2007/02). University of California, Los Angeles, CA.
- Tarbali, K. (2017). *Ground Motion Selection for Seismic Response Analysis* (Publication No. April) [Doctoral dissertation, University of Canterbury].

- Tarbali, K., & Bradley, B. A. (2015). Ground motion selection for scenario ruptures using the generalised conditional intensity measure (GCIM) method. *Earthquake Engineering & Structural Dynamics*, 44(10), 1601–1621. <https://doi.org/10.1002/eqe.2546>
- Tarbali, K., Bradley, B. A., & Baker, J. W. (2019). Ground motion selection in the near-fault region considering directivity-induced pulse effects. *Earthquake Spectra*, 35(2), 759–786. <https://doi.org/10.1193/102517EQS223M>
- Tarbali, K., Bradley, B. A., & Baker, J. W. (2023). Effect of near-fault directivity pulses on ground-motion intensity measure correlations from the NGA-West2 data set. *Earthquake Spectra*, 39(4), 2263–2280. <https://doi.org/10.1177/87552930231199059>
- Torbol, M., & Shinozuka, M. (2014). The directionality effect in the seismic risk assessment of highway networks. *Structure and Infrastructure Engineering*, 10(2), 175–188. <https://doi.org/10.1080/15732479.2012.716069>
- Tothong, P., & Cornell, C. A. (2006). An empirical ground-motion attenuation relation for inelastic spectral displacement. *Bulletin of the Seismological Society of America*, 96(6), 2146–2164. <https://doi.org/10.1785/0120060018>
- Tothong, P., & Luco, N. (2007). Probabilistic seismic demand analysis using advanced ground motion intensity measures. *Earthquake Engineering and Structural Dynamics*, 36(13), 1837–1860. <https://doi.org/10.1002/eqe.696>
- Trifunac, M. D., & Brady, A. G. (1975). A study on the duration of strong earthquake ground motion. *Bulletin of the Seismological Society of America*, 65(3), 581–626. [https://doi.org/10.1016/0148-9062\(76\)90487-3](https://doi.org/10.1016/0148-9062(76)90487-3)
- Vamvatsikos, D. (2013). Derivation of new SAC/FEMA performance evaluation solutions with second-order hazard approximation. *Earthquake Engineering & Structural Dynamics*, 42(8), 1171–1188. <https://doi.org/10.1002/eqe.2265>
- Vamvatsikos, D., & Cornell, C. A. (2002). Incremental dynamic analysis. *Earthquake Engineering and Structural Dynamics*, 31(3), 491–514. <https://doi.org/10.1002/eqe.141>
- Vamvatsikos, D., & Cornell, C. A. (2005). Developing efficient scalar and vector intensity measures for IDA capacity estimation by incorpo-

- rating elastic spectral shape information. *Earthquake Engineering & Structural Dynamics*, 34(13), 1573–1600. <https://doi.org/10.1002/eqe.496>
- Vamvatsikos, D., & Cornell, C. A. (2006). Direct estimation of the seismic demand and capacity of oscillators with multi-linear static pushovers through IDA. *Earthquake Engineering and Structural Dynamics*, 35(9), 1097–1117. <https://doi.org/10.1002/eqe.573>
- Vidic, T., Fajfar, P., & Fischinger, M. (1994). Consistent inelastic design spectra: Strength and displacement. *Earthquake Engineering and Structural Dynamics*, 23(5), 507–521. <https://doi.org/10.1002/eqe.4290230504>
- Villar-Vega, M., Silva, V., Crowley, H., Yepes, C., Tarque, N., Acevedo, A. B., Hube, M. A., Gustavo, C. D., & María, H. S. (2017). Development of a Fragility Model for the Residential Building Stock in South America. *Earthquake Spectra*, 33(2), 581–604. <https://doi.org/10.1193/010716EQS005M>
- Wilson, P., & Elgamal, A. (2006). Large scale measurement of lateral earth pressure on bridge abutment back-wall subjected to static and dynamic loading. *Proceedings of the New Zealand Workshop on Geotechnical Earthquake Engineering*, 307–315. University of Canterbury, Christchurch, New Zealand.
- Wooddell, K. E., & Abrahamson, N. A. (2014). Classification of main shocks and aftershocks in the NGA-West2 database. *Earthquake Spectra*, 30(3), 1257–1267. <https://doi.org/10.1193/071913EQS208M>
- Wu, Y. F., Li, A. Q., & Wang, H. (2019). Inelastic displacement spectra for Chinese highway bridges characterized by single-degree-of-freedom bilinear systems. *Advances in Structural Engineering*, 22(14), 3066–3085. <https://doi.org/10.1177/1369433219857845>
- Zafarani, H., & Soghrat, M. R. (2023). Ground Motion Models for Non-Spectral Intensity Measures Based on the Iranian Database. *Journal of Earthquake Engineering*, 27(13), 3786–3806. <https://doi.org/10.1080/13632469.2022.2150334>
- Zafarani, H., & Soghrat, M. R. (2024). An Empirical Spectral Ground-Motion Model for Iran Using Truncated Iranian Strong-Motion Database Enriched by Near-Field Records. *Journal of Earthquake Engineering*, 28(4), 922–945. <https://doi.org/10.1080/13632469.2023.2226223>

- Zengin, E., & Abrahamson, N. A. (2021). A procedure for matching the near-fault ground motions based on spectral accelerations and instantaneous power. *Earthquake Spectra*, 37(4), 2545–2561. <https://doi.org/10.1177/87552930211014540>
- Zhu, M., McKenna, F., & Scott, M. H. (2018). OpenSeesPy: Python library for the OpenSees finite element framework. *SoftwareX*, 7, 6–11. <https://doi.org/10.1016/j.softx.2017.10.009>

Appendix A. Influence of database subset selection on correlation coefficients

This appendix briefly examines what is the main cause of difference between the cross-correlation coefficients proposed here and the ones available in the literature. With that, more general conclusions can be outlined on the importance of different decisions when developing correlation models.

In Figure A.1 four different NGA-West2 GMMs were used with the same filtering criteria. The filtering criteria are the ones actually used in this study. It can be clearly seen that the correlations obtained from the different GMMs give very similar results. Therefore, we can safely say that the correlation results are not biased by the use of a single GMM and that the ASO24 model is also in line with the others.

The same records and same GMM as BB17 was used to calculate the correlations and compared with the BB17 model itself in Figure A.2. The BB17 model used the NGA-West2 database and is very close to BJ08 model. The results, as expected, are very close. The figures in this appendix constitute strong evidence that the difference comes from the filtering (i.e., subset selection) of the database and not from the background GMM adopted.

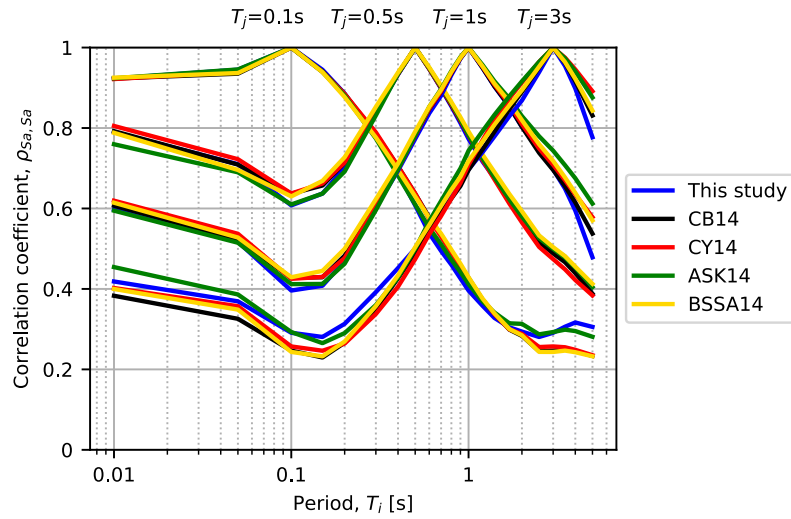


Figure A.1. Comparison of correlation coefficients derived from utilising each of the four NGA-West2 GMMs and the one employed for this study

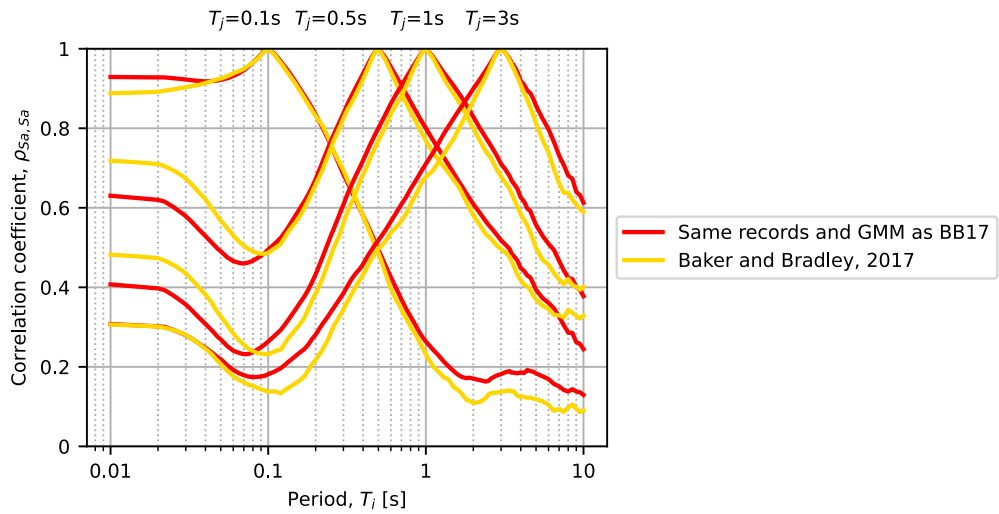


Figure A.2. Correlations proposed by BB17, and the ones calculated here with the same GMM (i.e., CY14) and the same ground motion records

Appendix B. Target and selected intensity measure distributions from the different ground motion selection cases

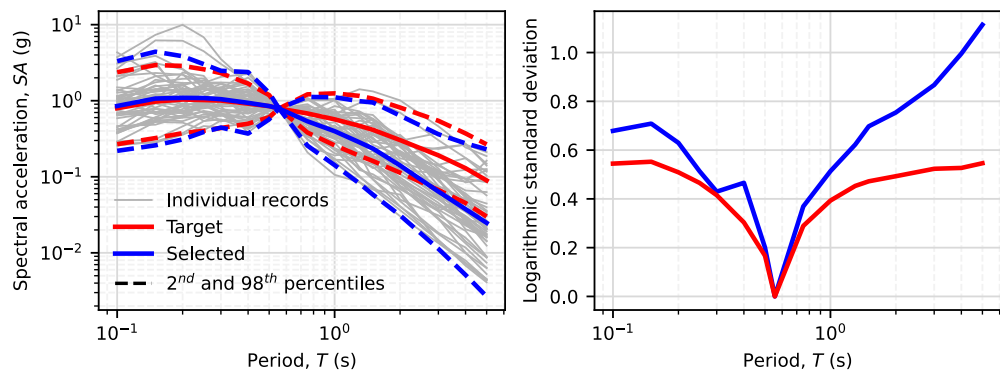


Figure B.3. Sa spectrum and comparison of the target and selected dispersions. Case 0. Bridge 1. IM level 4

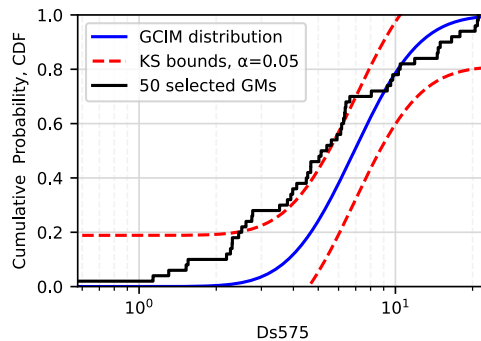


Figure B.4. Ds_{575} theoretical and empirical cumulative distribution function (CDF). Case 0. Bridge 1. IM level 4

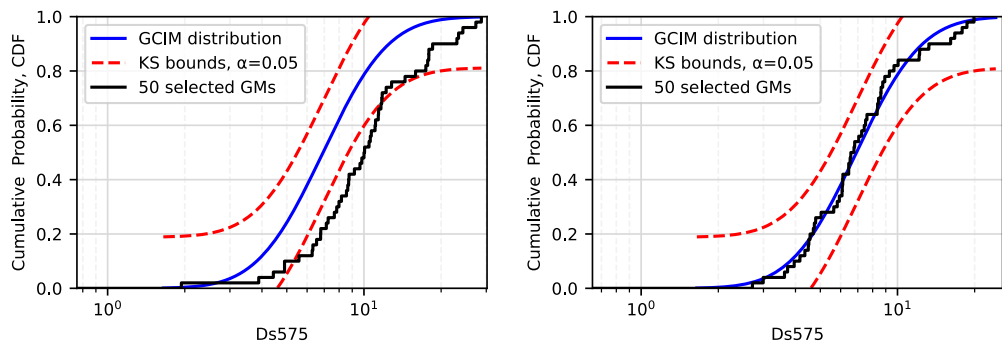


Figure B.5. Ds_{575} theoretical and empirical CDF. Case 1 (left) and 2 (right). Bridge 1. IM level 4